CAVITATION BUBBLE DYNAMICS FOR BIOMEDICAL APPLICATIONS: SHOCKWAVE AND ULTRASOUND BUBBLE INTERACTION SIMULATION

FONG SIEW WAN

(B.Eng. (Hons.), M. Eng.) NUS

A THESIS SUBMITTED

FOR THE DEGREE OF DOCTOR OF PHILOSOPHY

About this thesis

This is a compilation of work done for my degree of Doctor of Philosophy under the National University of Singapore Graduate School of Integrative Sciences and Engineering (NGS) from August 2003 to August 2007. I was under the Agency for Science, Technology and Research (A*STAR) Graduate Scholarship, and was attached to the Institute of High Performance Computing (IHPC), A*STAR throughout my candidature. My supervisors are Prof Khoo Boo Cheong from the Department of Mechanical Engineering of the National University of Singapore (NUS), and Dr Evert Klaseboer from IHPC. My thesis committee consists of both of my supervisors and A/Prof Lim Ping from the Mathematics Department in NUS. This thesis was examined by Prof John R. Blake from the School of Mathematics, University of Birmingham, Prof Sheryl M. Gracewski from the Department of Mechanical Engineering and Biomedical Engineering, University of Rochester, and Dr Richard Manasseh from CSIRO Manufacturing and Materials Technology (Australia). The oral examination has taken place via teleconferencing on the 6th of March 2008 with Prof Gracewski and Dr Manasseh as examiners. NGS nominated Prof Andrew Nee from NUS as moderator.

Acknowledgement

I would like to express my heart-felt gratitude towards Dr Evert Klaseboer from the Institute of High Performance Computing (IHPC) for his patience and effort in guiding me through my candidature and the thesis. Also, I wish to thank Prof Khoo Boo Cheong from the National University of Singapore (NUS) for all his invaluable support and ingenious suggestions. I want to thank Dr Hung Kin Chew, my former supervisor, for his help in the early days of my research work at IHPC.

I am also grateful for the help from other staff members of IHPC, especially Dr Cary Turangan. At the same time, I wish to acknowledge the support from all laboratory members of Impact Mechanics Lab, Dynamics Lab 1, and Fluid Mechanics Lab 1. Without their help, the experiments presented here would not be possible. Also, the financial support for this research work from the Agency of Science, Technology and Research is gratefully acknowledged.

Lastly, a big ‘thank you’ to my partner, Asst Prof Claus-Dieter Ohl, for the technical advice and emotional support he has given me through out the trying period of thesis writing. I also want to thank my parents for being so understanding and caring all the time.

Contents

Abstract

Medical treatments involving the use of shockwaves and ultrasound are gaining popularity. When these strong sound waves are applied, cavitation bubbles are generated in nearby tissues and bodily fluids. This thesis aims to study the complex bubbles' interactions with the tissues and among themselves. Simulations are done using the Boundary Element Method (BEM) which has computational efficiency advantage as compared to other numerical methods.

Firstly, the interaction between a shockwave and a bubble is modeled and verified against experimental results. A temporally inverted lithotripter shockwave is tested. This waveform has the potential benefit of minimizing collateral damages to close-by tissues or blood vessels. Next, the non-spherical bubble dynamics near a biomaterial in a medical ultrasound field is investigated. Complex bubble behaviors are observed; for certain cases, the bubble jets towards the biomaterials, and in other conditions it forms high speed jets away from the materials. Also, the model is extended to study a microbubble's interaction with high intensity pulsed ultrasound proposed for tissue cutting (histotripsy). In medical applications, multiple bubbles are often involved. To provide better understanding of multiple bubble interaction, an experimental study using high speed photography of spark-generated bubbles is performed. Corresponding numerical simulations are done to compare and highlight the details of the complex fluid dynamics involved. Good agreement between the experimental data and the 3D BEM results are obtained.

The thesis concludes with discussions on its scientific contributions, some new development in acoustic bubble applications (for example microbubble contrast agents for cancer treatment), and hazards involved in the use of ultrasound in medical therapy. It ends with a conclusion and some suggestions for future work.

List of Tables

List of Figures

Figure **Page**

Chapter 1

Introduction to acoustic bubble dynamics

The study of sound wave interaction with bubbles in a fluid is of interest to a wide-ranging field of science. From sonochemistry and medical applications such as fragmentation of kidney stones, to industrial processes like ultrasonic cleaning and defense technology involving the use of sonar for undersea exploration, the interaction of the bubbles and the acoustic field is of importance. The bubbles involved could be gas or vapor bubbles, or ‘cavities’ formed as the liquid is ‘torn apart’ by tension forces. Nevertheless, these bubbles are oscillating (non-equilibrium), and affecting the fluid and the surrounding acoustic field in a complex manner. For instance, the bubble-liquid interface would continue to change shape and size, pressure and temperature in the bubble and its surrounding liquid would fluctuate rapidly, and complex phenomena such as thermal diffusion and acoustic streaming may occur.

This chapter begins with a brief review of the history of bubble dynamics studies. Then more specifically, a short outline of some important acoustic bubble work is given. The role of bubbles in some common medical applications is described. And lastly, the scope and objectives of this thesis are presented with brief summaries of the contents of the chapters to come.

1.1 Brief review of previous work on bubble dynamics

The study of bubble dynamics was initially motivated by the damages sustained in ship propellers. Lord Rayleigh (Rayleigh, 1917) pioneered the study by giving a theoretical description to a spherically collapsing bubble. The asymmetric collapse of a bubble leading to the development of a high speed jet from one side of the bubble surface to its opposite side with the eventual penetration of the surface was first suggested by Kornfeld and Suvorov (1944). Using specially prepared bubbles, Naude and Ellis (1961) and Benjamin and Ellis (1966) were able to confirm the postulation experimentally. Since then, the role of collapsing bubbles in causing damage to solid surfaces has motivated a large number of scientific investigations.

Using high speed photography, the jetting of an oscillating bubble near a solid boundary was studied in detail by Benjamin and Ellis (1966), Gibson (1968), Lauterborn and Bolle (1975), Lauterborn (1982), Lauterborn and Vogel (1984) Tomita and Shima (1990), and Soh (1991) among others. These bubbles are typically generated by high voltage electrical spark discharge or using a pulsed laser. Accurate photographic records of bubble shape and jet evolution as shown in Fig. 1.1 were obtained.

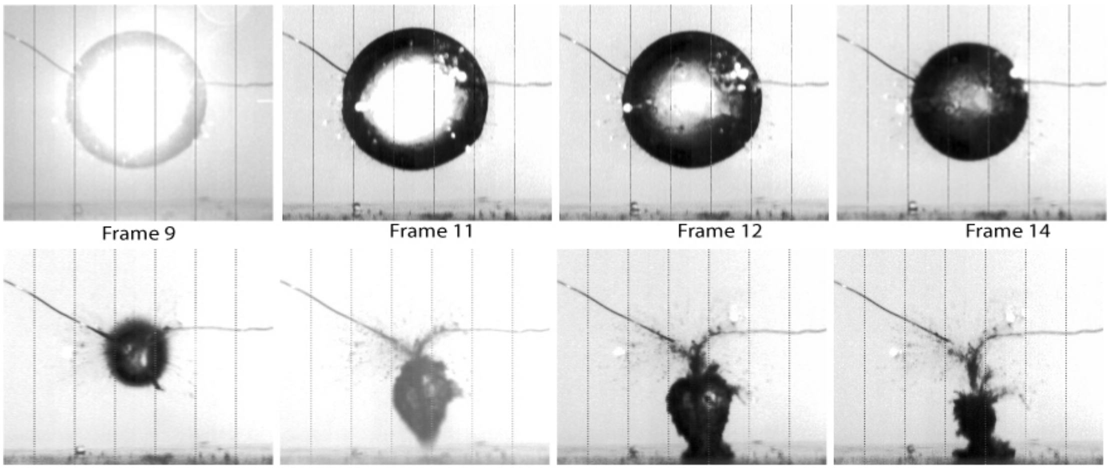

Fig. 1.1 High speed photographic recording of the collapse of a spark bubble of maximum radius (taken from frame 11), R_{max}, of 3.9 mm near a solid boundary. The frame rate used is 12500 frames per second (fps) and the corresponding frame numbers from the first frame showing the initial spark are given below the pictures. The bubble is initially located 7.8 mm away from the solid boundary below. A penetrating high speed jet is observed moving towards the wall (from Frame 19 to 23). The experiment was performed by the author.

When the bubble collapses near a free surface, however, the jet formed is directed away from the free surface (as oppose to moving towards the solid boundary). Experimental works on this phenomenon were done by Gibson (1968), Chahine (1977), Gibson and Blake (1980), Blake and Gibson (1981), and Robinson et al (2001). It was also reported that the water-air interface formed a water plume after the collapse of the bubble beneath it.

The flexibility of the nearby boundary seems to determine the direction of the reentrant bubble jets. For a completely flexible surface like the free surface, the jet is directing away from the surface; while for a non-flexible solid surface, the jet is directing towards it. Therefore it leads one to wonder what will happen if the surface has flexibility that is in between these two extremes. Gibson and Blake (1982), and Blake and Gibson (1987) studied both experimental and analytically the bubble dynamics near a rubber-coated solid boundary. They noticed that during the collapse, the bubble contracted more rapidly from the sides toward the axis of symmetry, formed an “hourglass” shape bubble (a similar phenomenon is reported in Fig. 6.3 in Chapter 6. It is termed “mushroom-shape” bubble in that figure), and eventually split into two bubbles. Tomita and Kodama (2003), and Shima et al (1989) also used composite surfaces (using a rubber plate and foam rubber) to study the interaction, and reported the same perturbation on the sides of the bubbles which led to bubble splitting and jetting. Experiments by Brujan et al (2001a, b), however, made use of a polyacrylamide gel (PAA) as the elastic boundary. The laser-generated bubble of Brujan et al (2001a, b) was found to exhibit complex interactions with this nearby interface. They reported “mushroom” shaped bubble formation, bubble splitting, and the elevation and repulsion of the elastic boundary. Recently, Turangan et al (2006) introduced a spark bubble next to a stretched elastic membrane. Similar complex bubble and interface behaviors were reported.

Apart from experimental observations, theoretical and analytical studies on bubble dynamics near the different types of boundary were performed too. The first fully numerical paper which studied the phenomenon of a cavitation bubble collapsing near a solid (rigid) boundary is by Plesset and Chapman (1971). Lauterborn and Bolle (1975) compared their experimental results with numerical calculations based on Plesset and Chapman (1971), and reported remarkable agreement. Following these initial studies, more analytical works have been performed. These include studies done by Guerri et al (1981), Prosperetti (1982), Cerone and Blake (1984), Taib et al (1984), Blake et al (1986), Zhang et al (1993), and Klaseboer et al (2005). In some of these works, the Boundary Element Method (BEM) was utilized to solve the equations involved. More details about this numerical method will be given in Chapter 2 on numerical modeling.

As for the modeling of an oscillating bubble collapsing near a free surface, a series of papers by Blake and co-workers (Blake and Gibson (1981), Blake (1988), Cerone and Blake (1984), Blake and Gibson (1987) etc.) detailed the theoretical formulation and the BEM implementation. A number of other numerical studies were done to study this problem. Starting with the classical textbook of Cole (1948) treating the bubble with the method of images, Best (1991), Wilkerson (1992), Wang et al (2003), and Klaseboer et al (2005) studied underwater explosions using axisymmetric and three dimensional (3D) BEM. Jetting phenomena and formation of toroidal shape bubbles were successfully simulated.

There are relatively limited numerical works involving flexible surfaces. Apart from the mentioned study from Blake and Gibson (1987), Duncan and Zhang (1991) coupled BEM and a Finite Difference Method to study the fluid motion of an oscillating bubble near a spring-backed surface. Later, this model was extended by Duncan et al (1996) to incorporate a Finite Element model of the composite structure. Recently, Klaseboer and Khoo (2004a, b) developed a full BEM scheme to simulate the bubble-elastic boundary interaction. Simulation results from this model have been successfully compared to experimental data from Turangan et al (2006). It has also been extended to model various biomaterials as described in Chapter 4 on ‘Ultrasonic bubbles near biomaterials’.

1.2 Background on acoustic bubble dynamics

Apart from the presence of a nearby boundary (either solid or free surface), the bubble jetting phenomenon is also observed when the bubble interacts with a strong sound wave, such as lithotripsy shockwave or high intensity focused ultrasound (HIFU). This phenomenon is commonly studied because of its importance in lithotripsy treatment for the fragmentation of kidney stones, and ultrasonic cleaning for the electronic industry. For a comprehensive review on acoustic bubbles, the reader is advised to refer to the book by Leighton (1994).

1.2.1 Shockwave bubble interaction

Most studies on shockwave bubble interaction involve a single bubble (two or three dimensional), and a planar or focused shockwave. The shockwaves are often generated by a lithotripter (either with spark discharge or using piezo-electric transducer) or focused piezo-electric transducers in a disc or cylindrical shape. The use of a disc-shaped quasi two dimensional (2D) bubble to study shockwave bubble interaction was first suggested by Brunton (1966). He introduced a bubble in the liquid between two transparent plates, and then allowed the bubble to be hit by a planar shockwave. An extension of the idea was used by Dear and Field (1988). They added 12 % gelatin to the water between the plates so as to allow better control of the position and size of the cavities. Very high speed jets up to 400 m/s were measured when the millimeter-sized cavities were subjected to strong shocks of 0.26 GPa. In another similar setting, a stronger planar shock of 1.88 GPa was used by Bourne and Field (1999) to study the role of hydrodynamic and adiabatic heating in ignition associated with the shock bubble interaction. Kodama and Takayama (1998) attached bubbles to a gelatin surface and allowed them to interact with a spherical shockwave of 10.2 ± 0.5 MPa to understand the destructive effect of jet penetration on nearby biological tissue specimens. They generated the spherical shocks using micro-explosives of silver-azide pellets. More recently, full 3D studies of shockwave bubble interactions were performed by Ohl and Ikink (2003), and Sankin et al (2005) among others. Both groups used a clinical lithotripter transducer to generate shockwaves of strength between 20 to 40 MPa which interacted with gas bubbles (for Ohl and Ikink (2003)) or laser generated bubbles (for Sankin et al (2005)). High speed jetting of bubbles in the direction of travel of the shockwaves was reported.

The difficulties in generating shockwaves and the stringent high speed photography requirements for experimental study of shockwave bubble interaction can be mitigated by numerical simulations. By numerical calculations, it is possible to study the phenomena in great details without being limited by temporal or spatial resolution of the experimental diagnostics. Ding and Gracewski (1996) utilized the Arbitrary Lagrangian-Eulerian (ALE) method to study the interaction of a strong shockwave with a stationary bubble in an axisymmetric configuration. Jamaluddin (2004) also did a similar set of simulations using the Free Lagrange method (FLM). The author will compare the results from these two studies with that from BEM simulations in Chapter 3 on shockwave bubble interactions. These apart, Ball et al (2000) implemented a 2D FLM code to generate simulation results which were set to the initial conditions from Bourne and Field (1992, 1999). The simulations successfully captured many important phenomena such as shock transmission inside the bubble and the prediction of local heating of the bubble content.

1.2.2 Bubble in an ultrasound field

One of the most impressive photographs of a jetting bubble is from Crum (1979). A small bubble of 3 mm was placed on a pulsating table of 60 Hz, and was photographed using stroboscopic illumination. Blake et al (1999) modeled the phenomena observed using BEM whereby the influence of the oscillating table was incorporated into the reference pressure in the Bernoulli equation (more details about modeling ultrasound field this way can be found in Chapter 2) by adding a modified gravitational term associated with the sinusoidal table displacement. Other studies involving standing ultrasound waves include the research on microstreaming from bubble oscillation (e.g. Elder (1959), Marmottant and Hilgenfeldt (2004), and Tho et al (2007)), light emission from the bubble due to high amplitude driving waves (sonoluminescence)(e.g. Brenner et al (2002)), and chemical reactions triggered in acoustic waves (sonochemistry)(e.g. Suslick (1998)). Since they are not examined in detail in this thesis and are relevant only as subjects for future studies, they are included in a brief manner for the completeness of discussion.

When a stationary bubble is trapped in a weak oscillating ultrasound field, it will undergo shape oscillations. The bubble oscillates in different modes, causes streaming flow in the surrounding liquid, but does not collapse with a jet. Kolb and Nyborg (1956) were the first to study this phenomenon. Elder (1959) extended their work by classifying the streaming patterns observed. Liu et al (2002) made use of the streaming in the liquid caused by this acoustic bubble for the mixing of liquid in micro-channels. Also for microfluidic devices, Marmottant and Hilgenfeldt (2004) suggested the use of the flow field to transport particles. More recently, Tho et al (2007) used micro-PIV (particle imaging velocimetry) technique to photograph the microstreaming patterns in single and multiple bubble systems to great accuracy. Some numerical works on this topic include that from Davidson and Riley (1971), Wu and Du (1997), and Longuet-Higgins (1998).

When the ultrasound field applied is of higher amplitude, it may cause the collapse of the existing bubbles in the liquid. The violent bubble collapse results in conversion of the kinetic energy of the liquid motion into the heating of the bubble contents. As a result, high local temperatures and pressures are created. These local sites serve as hotspots for driving chemical reactions which require extreme conditions. The chemistry induced by the bubble collapse has been extensively studied by Flynn (1964), Neppiras (1980), Mason & Lorimer (1988), Suslick (1988), and Suslick (1998).

The concentration of energy in the acoustic bubble under certain conditions causes the emission of light. This phenomenon, first observed by Frenzel and Schultes (1934), is known as sonoluminescence. Single Bubble Sonoluminescence (SBSL) involves the trapping of a stationary bubble in the node of a standing acoustic field. Many experiments and numerical studies have been reported, and interested readers are advised to refer to articles by Barber and Putterman (1992), Gaitan et al (1992), Ohl et al (1998), and Brennen et al (2002) for more information. When the light emission involves many short-lived bubbles in an acoustic field, the phenomenon is known as Multi-bubble Sonoluminescence (MBSL).

When the ultrasound field is generated by a focused transducer, the phenomena obtained are different from those mentioned previously. High amplitude sound waves generated this way could be used to create cavitation bubbles (Brujan et al (2005), Parlitz et al (1999)). Brujan et al (2005) used a disc shape piezo transducer to generate an ultrasonic bubble next to the elastic PAA material for the study of their complex interaction. Lauterborn’s group (Parlitz et al, 1999) has studied the formation of bubble streams generated by the focus piezo devices when they are driven with continuous waves. Ikeda et al (2006) proposed to replace shockwaves used in lithotripsy with pulsed ultrasound of different frequencies for better control of the forced collapse of the cavitation bubbles near the renal stones. More discussions on the use of this type of ultrasound waves in medical applications are given in the following section.

1.3 Bubbles in biomedical applications

Cavitation bubbles are believed to play a part in numerous biomedical applications. Most notably is the use of shockwave for the fragmentation of kidney stones as mentioned. This procedure is termed Extracorporeal Shockwave Lithotripsy (ESWL). High intensity shockwaves are focused on the renal stones and are applied in repetitions up to 1000 or even 3000 times until the stones are comminuted (Chaussy et al 1980). Although there are arguments on the exact mechanisms responsible for the destruction of the renal calculi (Delius and Brendel (1988), Gracewski et al (1993), Howard and Sturtevant (1997), and Lokhandwalla and Sturtevant (2000)), it is widely believed that cavitation bubbles play an important role in the stones' disintegration (Coleman et al (1987), Crum (1988), Kodama and Takayama (1998), and Zhu et al (2002)). This is because, as mentioned in Section 1.2.1, when a shockwave hits a pre-existing bubble or a bubble that is produced by previous lithotripter generated pulses, a high speed jet is generated within the bubble in the direction of the shockwave propagation. This jet is capable of penetrating the opposite bubble surface and impacts upon the renal stones. The stress forces imposed on the stones are deemed to be part of the mechanisms that causes the breakup of the stones.

Apart from ESWL, acoustic energy in the form of ultrasound is also commonly used for various medical treatments, for example, to mention just a few, in ultrasound-assisted lipoplasty, phacoemulsification, brain tumor surgery, muscle and bone therapies, and drug delivery into the eye (intraocular) or through the skin (transdermal). Each of these treatments is related to the motivation behind the simulations performed in Chapter 4, as they involve the interaction of an ultrasonic bubble near various biomaterials (for instance fat, cornea, skin, muscle, cartilage, brain and bone). Brief descriptions for them are given in the following paragraphs.

Lipoplasty (also commonly known as liposculpture, liposuction or suction lipectomy) is a surgical technique for the permanent removal of undesirable or excessive fat deposits located beneath the surface of the skin (Ehrlich and Schroeder, 2004). In recent years, the traditional suction-vacuuming technique is gradually being replaced by the safer ultrasound-assisted procedure (also known as Ultrasound-Assisted Lipoplasty, UAL (Cooter et al, 2001)). The surgeon inserts an ultrasonically vibrating probe under the patient’s skin via an incision into the area from which the excessive fat is to be removed. The fat cells are believed to be ruptured and ‘emulsified’ by the collapsing cavitation bubbles near or in them.

Another well-known situation in which such a probe is used is in phacoemulsification, the procedure used to emulsify the dense nucleus of the optical lens so as to remove them by vacuum during cataract surgery (Snell and Lemp, 1998). The advantage of this minimally invasive procedure over traditional eye surgery is that only a very small incision at the side of the eye is required for inserting the probe (the same incision is used to remove the old lens and insert the new artificial one). However, cavitation is also known to cause collateral damage to the cornea. Hence various studies have been performed to control the extent of cavitation to increase its effectiveness while minimizing the undesirable side-effects (FDA (1996), and Anis (1999)).

The use of focused ultrasound in contrast to single shockwave allows the control of concentrated cavitation in regions near the surface of the targeted stone (Ikeda et al, 2006). Again the competing objectives of maximizing damage to the stone (by increasing the strength of the ultrasound) and minimizing collateral damages have motivated various studies to improve on the design of the lithotripter (Zhong and Zhou (2001) and Sokolov et al (2001)).

An understanding of the dynamics of acoustic cavitation is also important in brain tumor surgery. A procedure which is known as ‘ultrasonic aspiration’ is performed by making use of the ultrasound vibration to break the tumor into small pieces which are then aspirated out (Brock et al, 1984). The jetting effect of the collapsing cavitation bubbles is believed to be responsible for the break down of the tumor.

Instead of a beneficial role, transient cavitation is an undesirable side-product in several medical treatments, such as the use of ultrasound for bone growth stimulation (Duarte, 1983), and muscle injury therapy (Jarvinen et al, 2005). It is argued that cavitation is partly responsible for ultrasound-induced lesions (Chavrier et al, 2000).

The cavitation mechanism is also utilized to enhance transdermal (Langer, 2000), and intraocular (Zderic et al, 2004) drug delivery. In the former, cavitation is speculated to be one of the releasing mechanisms responsible for sonophoresis (enhanced drug transport through skin, Langer (2000)). For the latter, both stable and transient bubbles are thought to be playing a role in enhancing the permeability of the cornea (Zderic et al, 2004).

Another important use of ultrasound is in biomedical imaging. A special type of microbubble, known as Ultrasound Contrast Agent (UCA), is used. These bubbles have high echogenicity, i.e. the ability to reflect sound waves, which enhances the backscattering of ultrasound. UCAs are of micron-size, and are coated with thin shells of protein, lipid or polymer. During the imaging process, they are injected intravenously for the imaging of blood flow, tissue and organ delineation and perfusion. Their usage is especially important in the imaging of blood flow in organs because the acoustic impedance difference between the bodily fluid, such as blood and the surrounding tissues is low; but the enhanced backscattering from the gas in the microbubbles allows the spatial and temporal imaging of blood flow, and thus provides a non-invasive method for quantitative analysis, and visualization of the system for diagnostic purposes (Feinstein (2004), and Lepper et al (2004)).

Recently, the microbubble contrast agent has also been used for therapeutic procedures, for example thrombosis and vascular plaques treatments (Unger et al. (1981), Tachibana and Tachibana (1995), and Tsutsui et al (2006)), drug and gene deliveries ((Taniyaman et al (2002), Li et al (2003), and Bekeredjian et al (2005)). More interestingly, when these bubbles are coated with targeting ligands (antibodies and peptides), they attach themselves only to specific cells (a technique that has been successfully applied as discussed in Unger et al (2003), Klibanov (1999), and Lanza et al (1996)). This technique can be used for preferential enhancement of the ultrasound signal at the diseased area, diagnosis of cancerous tissues, and even therapeutic procedures such as targeted drug/gene delivery and selective destruction of the cancerous cells. For these therapies, a stronger ultrasound wave, such as high amplitude pulsed ultrasound, is generally required. This kind of sound wave is proposed to be used to replace the use of shockwaves in lithotripsy (Ikeda et al 2006), and also in Xu et al (2005) for the highly localized removal of tissues. Both Ikeda et al (2006) and Xu et al (2005) claim that the new methods could minimize collateral damages on the nearby tissues.

1.4 Scope and objectives of this thesis

There are two main objectives of this thesis. Firstly, it strives to provide an understanding of the role of cavitation bubbles in acoustic fields which are commonly found in biomedical applications. Secondly, it aims to introduce BEM as an effective and efficient computational tool for the simulation involving acoustic bubbles. Single or multiple bubbles dynamics are studied either numerical, experimental, or a combination of both. Results from simulations are compared with other established methods and experimental data so as to validate the model. Further discussions and analysis of results are given to provide physical understanding to the phenomena observed.

After this introductory chapter, the theory behind the potential flow model and the numerical implementation involving the Boundary Element Method (BEM) are presented in Chapter 2. The assumptions involved in the model are described and the non-dimensionalization of parameters is made clear. Other aspects of BEM modeling and implementation which are pertaining to specific chapters are given in the chapters themselves for the ease of reading and referencing.

Chapter 3 begins by validating the BEM model against established methods in the modeling of shockwave bubble interaction, namely the Arbitrary Lagrangian-Eulerian (ALE) (Ding and Gracewski, 1996) and the Free Lagrange (FLM) (Jamaluddin, 2004) methods. Both ALE and FLM take into account the compressibility of the fluid and are capable of accounting for the shockwave reflection from the bubble. Despite of its simplicity as a potential flow theory model, the BEM simulations manage to capture the bubble shape and size changes, as well as other physical parameters such as the maximum jet velocity.

The BEM model is then extended to model the interaction of a lithotripter shockwave with a cavitation bubble which has been studied experimentally by Sankin et al (2005). Detailed quantitative comparison on the bubble shape changes, and qualitative analysis for experimental measurements such as the collapse time and impact pressure are performed. With the validations from numerical and experimental results, simulations are performed on the interaction of a temporally inverted shockwave with a stationary bubble. The motivation of using this form of alternative shockwave for lithotripsy treatment stems from the possibility of reducing collateral damage to the surrounding cells or vessels because of the suppression of rebounding bubble's expansion. Interesting results on maximum bubble size obtained, collapse time, and especially the jet velocity are discussed.

The fourth chapter is based on a paper by Fong et al (2006) which studies the complex interaction of a cavity near a biomaterial in an ultrasound field. This numerical paper is valuable as cavitation bubbles are often found in the vicinity of biomaterials such as fat, cornea, and skin during medical treatments involving the use of ultrasonic probes. A diverse range of possible responses between the bubble and the biomaterial is reported. For example, high speed jets from the collapsing acoustic bubble could be directing towards or away from the biomaterials in different cases. Even bubble splitting events with jets in opposite directions are found.

Apart from cavitation and gas bubbles, ultrasound contrast agent microbubbles are considered in Chapter 5. Recent developments see the use of these bubbles for drug delivery and cancer treatment. A strong and focused ultrasound pulse is used instead of the weak continuous wave as described in Chapter 4. Collapse of these microbubbles is induced by the strong pulses in the vicinity of the diseased cells for the delivery of treatment DNA or proteins, or the destruction of cancerous cells by mechanical forces. Thus, the author modified the BEM code to simulate the event of strong pulsed ultrasound waves as described in Xu et al (2005) interacting with microbubbles of various initial sizes. The effects of intensity and bubble size variations for several parameters of interest (such as bubble shape, jet velocity) are discussed.

Chapter 6 is on multiple spark bubbles experiment and the corresponding BEM simulations. Interesting interactions between two or three bubbles of different initial positions, sizes and time of initiation are detailed. For instance, a high speed jet of 180 m/s is observed when a bubble that is collapsing near another bubble which is generated slightly earlier. This phenomenon is termed ‘catapult’ effect and is important as another way of generating high speed jets with bubbles (apart from the mentioned ones when a single bubble collapses near a solid boundary or interacts with a strong pressure wave).

The last chapter, Chapter 7, gives a summary of the contributions of this thesis. It also contains the discussion on new developments in biomedical applications involving acoustic bubbles. It ends with discussions on possible hazards in use and suggestions for future code expansions.

1.5 Author's contributions

This thesis is a collection of work on soundwave bubble interaction done by the author with help and contributions from others in the team. The experimental example shown in Fig. 1.1 was performed by the author. In the second chapter, the model and BEM code on bubble dynamics, both axisymmetric and 3D, are described. They were developed over a period of about ten years by colleagues in the same scientific group. The author's contribution to the modeling rests mainly on the addition of a shockwave or an ultrasound wave to the existing BEM model.

In the third chapter, the author, under the supervision and guidance of Dr. Evert Klaseboer and Prof Boo Cheong Khoo, pioneered the simulation of strong shockwave bubble interaction using BEM. The comparison to other compressible codes, ALE and FLM, is done successfully by the author. An extension of this work is in the second part of this chapter, Section 3.2, where a study mainly done by Dr Evert Klaseboer and other co-authors in the paper Klaseboer et al (2007) is described. The author was involved in active scientific discussion with the other co-authors of the paper, and she also contributed to the writing up of the paper. Since the implementation of an inverted shockwave was more challenging, the author fully concentrated on this work instead which is described in Section 3.3. A scientific paper is currently being written on this work.

For the fourth chapter, the author originated the ideal of modeling biomaterials with an existing elastic fluid model. The ultrasound field is also added by the author to the pre-existing model. All simulations and write up of the paper are done by the author in consultation with her supervisors. The fifth chapter on pulsed ultrasound interaction with microbubble, the author suggests the modeling and modifies the code accordingly. The analysis and writing is done by the author with scientific advice from her supervisors and Dr Claus-Dieter Ohl.

Chapter 5 is devoted to the study of a microbubble contrast agent interacting with a high intensity pulsed ultrasound wave. The simulations are done solely by the author. The results are recently published (Fong et al, 2008).

The chapter on bubble dynamics experiments show results from the author, as well as some others performed by mechanical engineering students under the advice and supervision of the author. The students' contributions are noted, where appropriate, throughout the chapter. This novel method of generating spark bubble for the study of bubble dynamics is developed by the author and a final year student, Geok Pei Ong. The method is further extended to study multiple bubble interaction with the help of another student, Deepak Adikhari. Other students the author has supervised or helped in setting up their experiments include Kelly Siew Fong Lew, Daan Martens, Hui Shan Xu, and Benny Teo. The experiments with Hui Shan Xu and Benny Teo involve the generation of focused ultrasound using a bowl-shaped transducer. The author designed and set up the initial experiments with the students. The experiments involving the use of ultrasound by the author are still ongoing and therefore not included in this thesis. Another experiment that the author helped to set up together with an attachment student, Rahman Dadvand from the University of Tabriz, Iran, involves a spark bubble near a perforated wall. On one side of the wall (with a hole) where the bubble is, the fluid is water; on the other side, the fluid is air. As the hole size increases, the bubble behavior changes; for holes that are smaller that the diameter of the bubble, the bubble collapses towards the wall, and for holes that are bigger than the diameter of the bubble, it collapses away from the wall. In both cases, a water jet is observed on the free surface side of the wall.

Chapter 2

Numerical modeling using the Boundary Element Method (BEM)

For all the simulations in this thesis, an incompressible fluid is considered. The Laplace equation is assumed to be valid in the fluid domain. An adiabatic bubble is added to the fluid assuming either a stationary or a non-equilibrium initial stage. After that, the numerical equations used to model a weak ultrasound field are described in details. This acoustic model is used in Chapter 4 to study the interaction of a bubble near a biomaterial which is modeled as an elastic fluid. In Section 2.2, details about non-dimensionalizing the equations, as commonly applied in fluid dynamics numerical studies, are described. In the last section, Section 2.3, the Boundary Element Method implementations for both an axisymmetric and a 3D model are presented.

2.1 Physics of the problem

2.1.1 The fluid model

As mentioned, the fluid is considered to be incompressible. This consideration can be justified knowing that compressibility can be modeled by adding a term $\left(1-\frac{1}{c}\frac{dR}{dt}\right)$ to the Rayleigh-Plesset equation, and c is the speed of sound in water (Young, 1989). In general, when the velocity of the bubble wall, dR/dt, is much lower than c (~1500 m/s) (for example the jet speed when a bubble collapses near a solid boundary is about 100 m/s), the compressibility assumption is valid. However, in some cases in this thesis, the bubble velocity exceeds 1500 m/s. Thus these jet speeds are accurate only as a first order approximation. With the incompressibility assumption, the divergence of velocity is zero and thus the continuity equation is reduced to

$$\nabla \bullet \underline{v} = 0\,, \tag{2.1}$$

where $\underline{v}$ is the velocity vector. Furthermore, the fluid is assumed to be irrotational with viscous effects being ignored. This is justified because the Reynolds number *Re* is typically very high, rendering the flow to be essentially inertia-controlled. For example in the spark bubble experiments and simulations, a typical maximum bubble size $R_{\max}$ is 3 mm, the collapse time t_c is about 0.3 ms (see eqn. (3.15) on Rayleigh collapse time), then $Re = 2v_r R_{\max} / \upsilon = 2R_{\max}^2 / (\upsilon * t_c)$ is 60000 since viscosity of water υ is about 10^{-6} m^2/s, and the velocity of the bubble wall, v_r, is equaled to $R_{\max} / t_c$. For the micron-sized bubble simulations in this thesis, a typical bubble radius is 1 μm. The corresponding Rayleigh collapse time is 0.1 μs. Thus *Re* is 20, which is still above the limit of *Re* = 1. Also, in these cases, the timescale for diffusion of vorticity is very small and therefore there is no time for the development of a boundary layer. With the irrotational assumption, a potential Φ which obeys the following equation is introduced:

$$\underline{v} = \nabla \Phi\,. \tag{2.2}$$

Combining eqns. (2.1) and (2.2), the potential flow approximation model can be expressed using the Laplace equation

$$\nabla^2 \Phi = 0\,. \tag{2.3}$$

2.1.2 The boundary and initial conditions

Since the flow is incompressible and irrotational, the following unsteady Bernoulli equation is valid everywhere in the fluid

$$p = p_{ref} - \rho \frac{D\Phi}{Dt} + \frac{1}{2}\rho|\underline{v}|^2 , \tag{2.4}$$

where p is the pressure, p_{ref} is a reference pressure (taken to be equal to atmospheric pressure, $p_{ATM} = 10^5$ Pa, unless otherwise stated), ρ is the liquid density (in all cases, water is the surrounding fluid and its density, ρ, is taken to be 1000 kg/m^3), t denotes time, and the material derivative D/Dt is equal to $\partial/\partial t + \underline{v} \cdot \nabla$. It is noted that the gravitational field effect has been ignored. This is justifiable by considering the Froude number in the cases involved. The Froude number (F_r) is defined to be the ratio between the inertia forces and the gravitational forces, such that

$$F_r = \frac{v_r^{\ 2}}{gL} = \frac{v_r}{gt_c} , \tag{2.5}$$

where g is the gravitational acceleration, L, the length scale is equal to $v_r\ t_c$. But $v_r \equiv U_{ref} = \sqrt{\frac{p_{ref}}{\rho}}$, and $L = R_{\max}$, thus,

$$F_r = \frac{p_{ref}}{g \cdot \rho \cdot R_{\max}} . \tag{2.6}$$

For a typical bubble of R_{max} = 3 mm, and g = 10 m/s^2, F_r is found to be 3.3x10^3. For the small 1 μm bubble, F_r is even higher (F_r = 9.9x10^6). This high number confirms the fact that the gravitational forces are of much less significant than the governing inertia forces (Turangan et al, 2006).

The surface tension, σ, is also neglected because the typical Weber number (*We*) is rather large. It can be calculated as follows:

$$\begin{aligned} We &= \frac{\rho v_r^{\,2} L}{\sigma} = \frac{\rho v_r^{\,3} t_c}{\sigma} \\ &= \frac{R_{\max} \cdot p_{ref}}{\sigma} \end{aligned} . \tag{2.7}$$

With the numerical values for the parameters as mentioned and taking σ to be $70\text{x}10^{-3}$ N/m, *We* is found to be $4.3\text{x}10^{3}$. This certainly shows the dominant importance of the inertia forces over surface tension. Although for a 1 μm bubble, *We* is as low as 1.43. However, it is shown in the simulations in Fong et al. (2008) whereby the surface tension is incorporated in to the model, the difference in terms of jet velocity and translational movement of the lowest node is minimal. Nevertheless, both gravity and surface tension can be easily incorporated into eqn. (2.10) if need be (Blake et al (1987), and Klaseboer et al (2005)).

A bubble is introduced into this liquid. For simplicity, the gas inside the bubble is assumed to behave adiabatically. Together with the ideal gas law and the assumption of a uniform gas pressure p_g, the following equation describes the gas pressure inside the bubble:

$$p_g = p_{g,0}\left(\frac{V_0}{V}\right)^{\gamma}, \tag{2.8}$$

where the subscript '0' denotes in the initial values, and *V* is the volume of the bubble. The ratio of the specific heats γ has been empirically approximated to be 1.25 for explosives like TNT (Cole, 1948) and is defined to be 1.4 for an ideal diatomic gas (Fermi, 1956).

The total pressure inside the bubble is expressed as

$$p_b = p_v + p_g . \tag{2.9}$$

In most of the cases mentioned in this thesis, the vapour pressure p_v could be ignored because it is several magnitudes smaller than the gas pressure p_g. With eqn. (2.4), the following equation is valid on the bubble's surface:

$$\rho \frac{D\Phi}{Dt} = p_{ref} - p_v - p_{g,0}\left(\frac{V_0}{V}\right)^{\gamma} + \frac{1}{2}\rho\left|\underline{v}\right|^2 . \tag{2.10}$$

Eqn. (2.10) is utilized to update Φ on the surface of the bubble for the next time step. Then from the Boundary Element equations (see Section 2.3), the normal component of the velocity vector, $\frac{\partial \Phi}{\partial n}$, can be determined. With these values, the position of the bubble boundary can be found by

$$\frac{D\underline{x}}{Dt} = \nabla\Phi , \tag{2.11}$$

where $\underline{x}$ is the position vector of the boundary.

2.1.3 Modeling an explosion (non-equilibrium) bubble

In Section 3.2, the interaction of a lithotripter shockwave with an already oscillating bubble is considered. The shockwave impinges on the bubble at various $R_{00} / R_{\max}$, where R_{00}, and $R_{\max}$ denote the bubble radius at the moment of shockwave impact and maximum bubble radius respectively. Thus apart from setting the initial value for $R_{00} / R_{\max}$, we need a formulation for the initial velocity potential for the corresponding R_{00}, $\Phi(R_{00})$.

As mentioned in the previous section, the gas inside the bubble is assumed to behave adiabatically and therefore eqn. (2.8) holds. Also, it is supposed that for laser generated bubbles from the experiments in Sankin et al (2005) to which the numerical simulations in Section 3.2 are compared to, γ, the ratio of specific heats, is the same as that of oscillating underwater explosion bubbles, i.e. $\gamma = 1.25$ (Cole, 1948). The bubble in this case is far from boundaries (either free surface or solid structures), and free from other disturbances (such as gravity (see Section 2.1.2 for reason supporting this assumption)). It will oscillate spherically prior to the interaction with the shockwave. Continuity of mass of the fluid around the spherical expanding bubble requires that the radial fluid velocity v_r depends on the radial co-ordinate r (with its origin in the center of the bubble) as $r^2 v_r = R^2 dR/dt$, where R and dR/dt denote the bubble radius and bubble wall velocity at time t, respectively. Thus the velocity potential becomes

$$\Phi = -\frac{R^2}{r}\frac{dR}{dt}. \tag{2.12}$$

The motion of a spherically oscillating bubble can be described with the Rayleigh-Plesset equation (Brennen, 2005). Applying the unsteady Bernoulli equation at the bubble surface, using eqn. (2.12) and setting the fluid pressure to the internal pressure of the bubble, p_b (it is assumed that $p_b = p_g$ in eqn. (2.8) because the internal pressure originates mainly from the bubble's non-condensable gas contents, therefore $p_v = 0$), the simplest form of the Rayleigh-Plesset equation (also commonly known as Rayleigh equation) is obtained as follows

$$\frac{p_b - p_{ref}}{\rho} = \frac{3}{2}\left(\frac{dR}{dt}\right)^2 + R\frac{d^2R}{dt^2}, \tag{2.13}$$

From eqn. (2.8), again considering $p_b = p_g$, an analytical solution of eqn. (2.13) exists, which relates dR/dt to R as (Brennen, 1995)

$$\frac{3}{2}\left(\frac{dR}{dt}\right)^2 = \frac{p_{ref}}{\rho}\left(\frac{R_0^3}{R^3} - 1\right) - \frac{p_{g,0}}{\rho(\gamma - 1)}\left(\frac{R_0^{3\gamma}}{R^{3\gamma}} - \frac{R_0^3}{R^3}\right), \tag{2.14}$$

where $p_{g,0}$ is the internal pressure at initial bubble radius R_0 (R_0 relates to the initial bubble volume, V_0 by $V_0 = \frac{4}{3}\pi R_0^3$). This equation automatically satisfies the initial condition $dR/dt = 0$ at $R = R_0$. When the bubble reaches its maximum radius $R = R_{\max}$, the velocity becomes $dR/dt = 0$ again, thus:

$$\frac{R_0^3}{R_{\max}^3} - 1 = \frac{p_{g,0}}{p_{ref}} \frac{1}{\gamma - 1} \left(\frac{R_0^{3\gamma}}{R_{\max}^{3\gamma}} - \frac{R_0^3}{R_{\max}^3} \right). \tag{2.15}$$

Using eqn. (2.12), the potential on the surface of an oscillating bubble with radius R_{00} can be determined by setting $r = R = R_{00}$ and substituting dR/dt from eqn. (2.14), the initial velocity potential $\Phi(R_{00})$ can be determined as

$$\Phi(R_{00}) = \pm R_{00} \sqrt{\frac{2p_{ref}}{3\rho} \left(\frac{R_0^3}{R_{00}^3} - 1 \right) - \frac{2p_{g.0}}{3\rho(\gamma - 1)} \left(\frac{R_0^{3\gamma}}{R_{00}^{3\gamma}} - \frac{R_0^3}{R_{00}^3} \right)}. \tag{2.16}$$

The positive sign in eqn. (2.16) is for a collapsing bubble and the negative sign is for an expanding bubble when the shockwave hits.

It is noted that in the simulations, a dimensionless parameter ε (often referred to as the strength parameter in bubble dynamics) is used. It is defined as

$$\varepsilon = p_{g,0} / p_{ref}. \tag{2.17}$$

Of the three dimensionless parameters ε (as in eqn. (2.17)), and $R_0 / R_{\max}$ and γ in eqn. (2.15), only two can be chosen independently. In fact, eqn. (2.15) is used to calculate R_0 in the numerical model, assuming the other parameters are given.

2.1.4 Modeling weak ultrasound

The simplified acoustic wave models used in this thesis are able to describe the physics involved. The linearity of the ultrasound wave is assumed as normally done in studies involving the medical applications mentioned although these sound waves are intrinsically non-linear. Also, reflection, shear wave propagation and scattering effects are ignored. Therefore, the ultrasound waves can be described by a time-varying pressure field. This pressure perturbation is incorporated into the reference pressure term, p_{ref}, in the unsteady Bernoulli's equation of eqn. (2.10). At any time step, p_{ref} is taken to be equal to the pressure on the elements as the wave travels across the bubble at a certain speed. Since eqn. (2.10) is valid on the bubble surface, the sound waves' temporal effect is captured. The various shockwave models used in the simulations in this thesis are described in details in the later chapters. The ultrasound and the elastic fluid model used in Chapter 4 are presented here.

The pressure due to the ultrasound in fluid in the absence of the bubble can be written as:

$$p_{ref}(t) = p_{ATM}[1 - A\sin(2\pi ft)], \tag{2.18}$$

where p_{ATM} represents the static pressure of the liquid, $p_{ATM}A$ is the amplitude of the pressure perturbation, A is the dimensionless pressure amplitude, f is the frequency of the pressure perturbation, and t represents time. It is assumed that $p_{ref}(t)$ only depends on time and not on the spatial coordinates. This is valid because the wave lengths of the ultrasound used in the set of simulations in Chapter 4 are much larger than the typical bubble size in consideration. For example, in one of the applications, brain tumor surgery, an ultrasound wave of 500 kHz is typically used. The wave length of this ultrasound is 3 mm. However the bubbles involved (which vibrate in their resonance frequency of 500 kHz) are 6 μm in radii. Thus the bubbles do not experience much of a pressure gradient across their surfaces. This justifies the decision not to consider spatial variation of pressure. In contrast, the spatial variation becomes important and is incorporated into the models described in Chapter 3 and 5.

It is noted that if A has a positive value and the pressure perturbation starts at $t = 0$, then $p_{ref}(t)$ will decrease first. This will cause the bubble to expand. Otherwise, if A has a negative value, then $p_{ref}(t)$ will increase first, causing the bubble to shrink.

Another important parameter that is used in the simulations is the resonance frequency of a bubble, f_0. The relationship between the initial bubble radius R_0 and f_0 is derived by Minnaert (1933) by considering the bubble as a simple harmonic oscillator neglecting surface tension and assuming small oscillations

$$f_0 = \frac{1}{2\pi R_0}\sqrt{\frac{3\gamma p_{g,0}}{\rho}} \,. \tag{2.19}$$

The frequency ratio f / f_0 is used in the simulations and discussions because it is deemed that this ratio largely determines the oscillatory behavior of the bubble (Brujan (2004), Sato et al (1994), Krasovitski and Kimmel (2001), Fong et al (2006)).

2.1.5 Modeling an elastic fluid

This model is largely based on Klaseboer and Khoo (2004a, 2004b), and Fong et al (2006). In the model two fluids separated by a common interface are considered. Viscosity is neglected and the fluid-fluid interface is initially at rest. One of the fluids (Fluid 1) is water, where a bubble with initial radius, R_0, is located. The other fluid, Fluid 2, has some elastic properties incorporated. This elastic fluid is used to represent the various biomaterials such as fat, skin, cornea, brain, muscle, cartilage, or bone. Also, to make the biomaterial model more realistic, the elastic fluid's density is changed according to the values obtained from literature. In Fig. 2.1, the parameters used in the simulation are described. It is noted that the distance between the center of the bubble and the fluid-fluid interface is denoted as *H*.

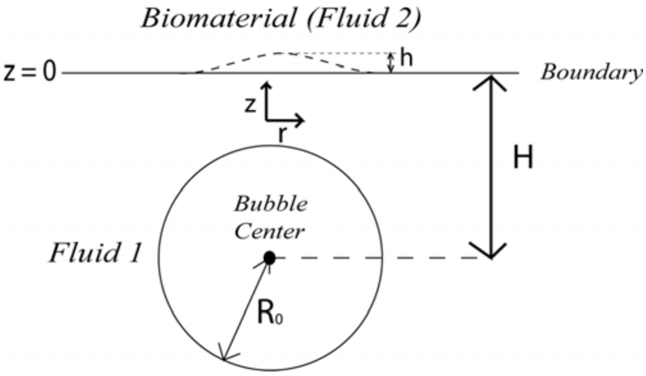

Fig. 2.1. A bubble immersed in Fluid 1 that is in contact with a biomaterial (Fluid 2) used in numerical simulations. The *z*-axis and *r*-axis directions are as indicated (r=0 is the axis of symmetry). The initial distance between the center of the bubble and the fluid-fluid interface is termed 'H' and 'h' is the elevation of the fluid-fluid interface with respect to its initial horizontal equilibrium position.

The model is based on Potential Flow theory and therefore two velocity potentials, Φ_1 and Φ_2, are introduced to Fluid 1 and 2 respectively. Both liquids are irrotational and incompressible. Therefore $\nabla^2\Phi_1 = 0$ and $\nabla^2\Phi_2 = 0$, and the subsequent velocity vectors can be derived as $\underline{v}_1 = \nabla\Phi_1$ and $\underline{v}_2 = \nabla\Phi_2$. As in Section 2.1.2, the Bernoulli equation can be applied to Fluid 1 (at the Fluid-Fluid interface), and the pressure p_1 can be expressed as:

$$p_1 = p_{ref}(t) - \rho_1 \frac{D\Phi_{i1}}{Dt} + \frac{1}{2}\rho_1 |\underline{v}_1|^2 . \tag{2.20}$$

Here $Dx/Dt = \partial x/\partial t + \underline{v}_1 \bullet \nabla x$ represents the material derivative with respect to velocity $\underline{v}_1$. The subscript '*i*' in the potential refers to the fluid-fluid interface, and ρ_1

is the density of water. Similarly, the Bernoulli equation is also valid in Fluid 2. However, since the interface between the two fluids is common to both, the interface movement due to Fluid 1 must be considered. From Klaseboer and Khoo (2004a, 2004b) it is argued that the comparable equation for Fluid 2 is

$$p_2 = p_{ref}(t) - \rho_2 \frac{D\Phi_{i2}}{Dt} + \rho_2 \underline{v}_2 \bullet \left(\underline{v}_1 - \frac{1}{2}\underline{v}_2 \right). \tag{2.21}$$

With eqn. (2.21), the model is designed such that the nodes of the discretization of the fluid-fluid interface move with the velocity of Fluid 1.

The elasticity of Fluid 2 is expressed by considering the elasticity modulus (Young's modulus) *E*, the Poisson ratio ν , and the elevation of the fluid-fluid interface with respect to its initial equilibrium position *h* (see Fig. 2.1). Following Klaseboer and Khoo (2004a, 2004b), *h* is related to the pressure difference between the fluids such that

$$p_1 - p_2 = \frac{E}{2\left(1-\upsilon^2\right)R_0} h , \tag{2.22}$$

The bubble in Fluid 1 is modeled as described in Section 2.1.2. It is assumed to be in equilibrium at $t = 0$ with an initial radius R_0. Therefore the ratio of the specific heats of the bubble's contents γ is taken to be 1.4, which is the value for an ideal diatomic gas. The γ value is different from that in Section 2.1.3 where γ = 1.25 because the bubbles here are stationary bubbles, naturally presiding in Fluid 1 whereas in Section 2.1.3, the bubbles are non-equilibrium bubbles generated using a laser. These laser bubbles probably have content properties closer to that of explosion bubbles which have γ = 1.25.

2.2 Dimensionless equations

To facilitate numerical calculations and eliminate the need to mention physical units in the discussion, the equations mentioned in Section 2.1 are made dimensionless. For distances, the scaling factor used is the maximum bubble radius, $R_{\max}$, which is taken to be the radius of the bubble at its maximum size. For all pressure terms, they are scaled with $p_0 = p_{ref} - p_v$, where p_{ref} is the reference pressure (taken to be equaled to atmospheric pressure, 0.1 MPa), and p_v is the vapor pressure. In most simulation cases in this thesis, p_v is considered to be negligible because normally p_v is at least several orders of magnitude smaller than p_{ref}. However, in the simulation for comparisons with spark bubbles experiments presented in Chapter 6, due to this special method of bubble generation, p_v is found to be as large as 0.5 bar. Thus it is taken into consideration in those calculations performed in Chapter 6. The scaling factor for time, t_0, is given by

$$t_0 = R_{\max}\sqrt{\frac{\rho}{p_0}}\,. \tag{2.23}$$

The potential is scaled with

$$\Phi_0 = R_{\max}\sqrt{\frac{p_0}{\rho}}\,. \tag{2.24}$$

Due to the relation $\underline{v} = \nabla\Phi$ the scaling factor for the velocity is $v_0 = \dfrac{\Phi_0}{R_{\max}}$. With these non-dimensionalizing factors, eqn. (2.10) which is valid on the bubble surface is reduced to

$$\frac{D\Phi'}{Dt'} = 1 - \varepsilon\left(\frac{V'_0}{V'}\right)^{\gamma} + \frac{1}{2}\left|\underline{v}'\right|^2\,. \tag{2.25}$$

In the above and subsequent equations, variables with a prime (') refer to dimensionless variables.

In the ultrasound model mentioned in Section 2.1.4, both f and f_0 in the frequency ratio are made dimensionless with $1/t_0$. Since the factors cancel out, $f/f_0 \equiv f'/f'_0$.

Eqns. (2.20), (2.21) and (2.22) are combined to give the following dimensionless form:

$$\frac{D}{Dt'}\left(\Phi'_{i2} - \alpha\Phi'_{i1}\right) = \underline{v}'_2 \bullet \left(\underline{v}'_1 - \frac{1}{2}\underline{v}'_2\right) - \frac{\alpha}{2}\left|\underline{v}'_1\right|^2 + \alpha\kappa^* h'. \tag{2.26}$$

The parameter determining the elasticity of Fluid 2, κ^*, is given by

$$\kappa^* = \frac{E}{2\left(1-\upsilon^2\right)p_{g,0}}, \tag{2.27}$$

and the density ratio of the two fluids, α, is expressed as

$$\alpha = \frac{\rho_1}{\rho_2}. \tag{2.28}$$

Eqn. (2.26) gives the relationship between the two potentials above and below the fluid-fluid interface and can be considered as a boundary condition for the problem. Another boundary condition is such that the normal velocities at this fluid-fluid interface should be equal but opposite (since the normal vector is pointing in opposite direction for the two fluids), thus:

$$\frac{\partial\Phi'_1}{\partial n} = -\frac{\partial\Phi'_2}{\partial n}, \tag{2.29}$$

with $\partial/\partial n = \underline{n} \bullet \nabla$, where $\underline{n}$ is the normal derivative on the bubble boundary and directed away from the boundary. With the Bernoulli equation which can be applied on the bubble surface given as

$$p_b = p_{g,0}\left(\frac{V_0}{V}\right)^{\gamma} = p_{ref}(t) - \rho_1 \frac{D\Phi_b}{Dt} + \frac{1}{2}\rho_1 \left|\underline{v}_b\right|^2 \text{ (as in Section 2.1.2),} \qquad (2.30)$$

where Φ_b , v_b refer to the values of Φ and v on the bubble surface, and the equivalent dimensionless equation can be written with eqns. (2.19) to (2.22) as

$$\frac{D\Phi'_{b1}}{Dt'} = -\left(\frac{V'_0}{V'}\right)^{\gamma} + 1 - A\sin\left(\sqrt{3\gamma}\frac{f'}{f'_0}t'\right) + \frac{1}{2}\left|\underline{v}'_b\right|^2, \qquad (2.31)$$

where $f'_0 = \dfrac{\sqrt{3\gamma}}{2\pi}$.

2.3 Boundary Element Method and numerical implementation

The Laplace equation is an elliptic equation and the potential anywhere in the fluid domain can always be computed provided that the potential is known on the boundary of the bubble. The boundary element formulation, which relates Φ and $\frac{\partial \Phi}{\partial n}$ on the surface of the bubble, *S*, can be written as (Brebbia and Dominguez (1989), Pozrikidis (2005)):

$$c(\underline{x})\Phi(\underline{x}) + \int_S \Phi(\underline{y}) \frac{\partial G(\underline{y},\underline{x})}{\partial n} dS = \int_S G(\underline{y},\underline{x}) \frac{\partial \Phi(\underline{y})}{\partial n} dS \ . \tag{2.32}$$

Eqn. (2.32) is the Boundary Element equation where $\underline{x}$ is a fixed point and $\underline{y}$ is the integration variable, both are located on *S*. The solid angle at location $\underline{x}$ is represented by $c(\underline{x})$ and *G* is the Green function or kernel function defined in a three-dimensional (or axisymmetrical) domain as:

$$\mathrm{G}(\underline{\boldsymbol{y}},\underline{\boldsymbol{x}}) = \frac{1}{|\underline{\boldsymbol{x}} - \underline{\boldsymbol{y}}|} \ . \tag{2.33}$$

The non-dimensionalized form of eqn. (2.32) is given as

$$\mathrm{c}(\underline{\boldsymbol{x}}')\Phi'(\underline{\boldsymbol{x}}') + \int_{\mathrm{S}'} \Phi'(\underline{\boldsymbol{y}}') \frac{\partial \mathrm{G}'(\underline{\boldsymbol{y}}',\underline{\boldsymbol{x}}')}{\partial \mathrm{n}} \mathrm{dS}' = \int_{\mathrm{S}'} \mathrm{G}'(\underline{\boldsymbol{y}}',\underline{\boldsymbol{x}}') \frac{\partial \Phi'(\underline{\boldsymbol{y}}')}{\partial \mathrm{n}} \mathrm{dS}' \ . \tag{2.34}$$

As for the two fluids model as depicted in Section 2.1.5, the Boundary Element Method can be applied for Fluid 1 to relate between the potential and the normal velocity on the boundaries and is valid for any point on the fluid-fluid interface or the bubble interface:

$$c\,\Phi'_1 = \int_{b+i} \left(G' \frac{\partial \Phi'_1}{\partial n} - \Phi'_1 \frac{\partial G'}{\partial n} \right) dS \ , \tag{2.35}$$

where the integral is over both the bubble surface and fluid-fluid interface "*b*+*i*". In eqn. (2.32) G is the Green function and c represents the solid angle at the point on the surface under consideration. A similar equation can be obtained for Fluid 2,

$$(4\pi - c)\Phi'_2 = \int_i \left(G' \frac{\partial \Phi'_2}{\partial n} + \Phi'_2 \frac{\partial G'}{\partial n} \right) dS \, . \tag{2.36}$$

The term $4\pi - c$ appears in eqn. (2.36) because the solid angle is viewed from Fluid 2. The plus sign that appears in eqn. (2.36) is due to the fact that the normal vector points in the opposite direction in Fluid 2. In eqn. (2.36), the integral is now only performed on the fluid-fluid interface "*i*". More details about the method can be found in Klaseboer and Khoo (2004a and 2004b).

2.3.1 The axisymmetric implementation

The surface of the bubble is represented with N nodes. The number of nodes on the bubble surface is N = 51 for all cases simulated using the axisymmetric formulation. For each node, eqn. (2.34) relates this particular node to all the other nodes. An axisymmetric formulation as described in Wang et al (1996a and 1996b) is used. The integrations are performed with a linear representation of the potential and the normal velocity. A system of equations with size NxN is then obtained with influence matrices $\underline{\underline{\boldsymbol{G}}}$ and $\underline{\underline{\boldsymbol{H}}}$ and vectors $\underline{\Phi'}$ and $\underline{\frac{\partial \Phi'}{\partial n}}$ representing the potential and its normal derivative at each node:

$$\underline{\underline{\boldsymbol{G}}} \cdot \underline{\frac{\partial \Phi'}{\partial n}} = \underline{\underline{\boldsymbol{H}}} \cdot \underline{\Phi'} \, . \tag{2.37}$$

The new potential at the next time step can be determined using the potential and velocities at the current time step. The right hand side of the system of equations in eqn. (2.37) is now known and it can be solved for the unknown normal velocity $\frac{\partial \Phi'}{\partial n}$ at each node using Gauss elimination. The velocity vector $\underline{\boldsymbol{v}}'$ can be determined with this normal velocity and the potential distribution along the surface of the bubble to evaluate the tangential velocity. The position vector of a node on the bubble surface $\underline{\boldsymbol{x}}'$ can be updated for each time step using eqn. (2.11).

The initial condition at the bubble surface which is initially at rest is:

$$\Phi' = 0 \qquad at \quad t' = 0 \,. \tag{2.38}$$

A fixed time step which is reasonable in terms of computational accuracy and efficiency is chosen to a particular set of simulations. Smoothing is done to prevent numerical surface instabilities at every 10 time steps (Klaseboer and Khoo, 2004a).

2.3.2 The three dimensional implementation

The 3D model used for simulations in Chapter 6 was developed by Wang et al (2001), Wang et al (2003), and Klaseboer et al (2005). The grid on the bubble surface consists of triangular cells. The initial meshing is usually formed using an icosahedron as a first level (Fig. 2.2). This shape has 20 equally sized equilateral triangles and 12 nodes. All of these nodes lie on the surface of a sphere. Each triangle is taken to be a single element (with 3 nodes). Then the mesh is refined by dividing each of the original triangles into smaller ones and projecting the new nodes on the spherical surface. The number of times the original triangles is subdivided is termed the ‘level’ of meshing. For instance, the level 3 mesh divides the original triangle into 9 sub-triangles.

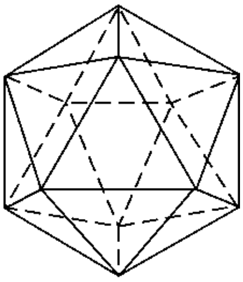

Fig. 2.2 The icosahedron used for representing the level 0 bubble mesh. It has 20 equally sized equilateral triangles and 12 nodes.

In the 3D simulations presented in this thesis, the level of mesh used is 5 as shown in Fig. 2.3. There are 500 elements and 252 nodes in total. In fact the number of elements for a particular level of mesh n is given as $N_t = 20n^2$. Also, the total number of nodes can be calculated from $N_n = 10n^2 + 2$.

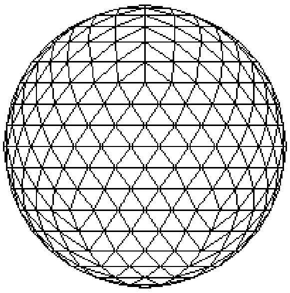

Fig. 2.3 The level 5 mesh with 500 elements and 252 nodes.

As the bubble surface advances, the internode distances can become highly irregular and the mesh greatly distorted. A methodology known as the Elastic Mesh Technique (EMT) developed by Wang et al (2003) is used in the code to counter this problem.

This mesh optimization technique is based on the assumption that the segments of the mesh are elastic (as if elastic springs are attached at each side of a triangular mesh element). The mesh is not advanced by the material velocity as commonly done in front tracking simulations (Harris (1992), Zhang and Duncan

(1994), Zhang et al (2001)). Instead an optimum shift velocity v_{EMT} is used. This shift velocity is calculated by minimizing the total elastic energy stored in every segment of the mesh at every time step. In doing so, the same number of nodal points is maintained (there is no need for mesh refinement as suggested by Zhang et al (2001)) together with the regularity of the mesh. This is effective in ensuring uniform mesh distribution at the beginning of the simulation up to the point when the jet has been largely developed and just before its impact. After that, the material velocity $\mathbf{v}$ is applied so that the node density becomes higher at the jet tip which leads to a better resolution of the flow physics in this region which has a large velocity gradient.

A varying time step scheme based on the Bernoulli equation (similar to that of Harris (1992) and Zhang et al (2001)) is implemented. By iteratively solving the matrix equations resulting from the varying time step scheme, the normal velocity on the bubble can be calculated. Then the potential and the normal velocity on each node are known. Although the normal vector can be determined easily on each triangular element, the normal vector on the nodes has to be approximated. As each node is surrounded by several triangular elements with different normal vector, a weighted average based on Zhang et al (2001) is used:

$$\mathbf{n} = \frac{\sum_i \frac{\mathbf{n}_i}{\Delta_i}}{\sum_i \frac{1}{\Delta_i}}. \tag{2.39}$$

The normal vectors of the surrounding elements $\mathbf{n}_i$ are averaged with the inverse of their area Δ_i. The inverse of the area is used because it is a better weighted average than the area itself; a small element will be nearer to the desired node and therefore yield a larger influence than the larger elements around.

After this, the velocity vector at any node can be found with the help of the potential of its neighbouring nodes in a similar way as the normal vector. The detailed procedure has been described in Zhang et al (2001); an estimation for the gradient of the potential (or velocity) can be made from the potential of the nodes of each element surrounding a particular node. A weighted average scheme similar to eqn. (2.41) is then applied to find the velocity $\mathbf{v}$ at each node.

Apart from imposing a limit on the time step size, a least-squares smoothing scheme is also applied. It is applied at every 10 time steps until the jet impact. Detailed explanation of this smoothing scheme can be found in Zhang et al (2001).

Chapter 3

Numerical simulations of shockwave bubble interaction

In this chapter, the results for BEM simulation of shockwave bubble interaction are presented. Firstly the shockwave is modeled as a pressure pulse, as described in Section 3.1.2. The simulation results are compared to that from the Free-Lagrange Method (FLM) and the Arbitrary Lagrangian-Eulerian Method (ALE). For further validation of the code, simulations are performed for comparison to the experiments of Sankin et al (2005) in Section 3.2. A real lithotripter shockwave is modeled based on experimental readings. The interaction of this shockwave with a non-equilibrium (oscillating) laser bubble is studied. The advantages of using BEM for the simulation of bubble lithotripter shockwave interaction are also discussed.

After the validations, the code is modified to model an alternative shock waveform known as an inverted shockwave (a shock with its tensile component that comes before the compressive part). Firstly, the interaction between an inverted shockwave and a stationary bubble is studied. The strength (peak pressures) of the shockwave and the initial bubble radius are varied to study the inverted shockwave's effect on the bubble dynamics in terms of bubble shape, volume changes in time, jet velocity and Kelvin impulse. Lastly, the potential application of this alternative form of shockwave is discussed.

3.1 Shockwave interactions with a stationary bubble

3.1.1 Comparison with other numerical methods –

Arbitrary Lagrangian-Eulerian (ALE) and Free Lagrange (FLM) methods

Ding and Gracewski (1996) studied the interaction of a shockwave of strength 0.528, 1.011, and 2.06 GPa with a bubble of initial radii 0.1, 1.0, and 10.0 mm. They modeled the shockwaves as step pressure pulses and simulated the interaction using ALE. Several similar cases were again examined by Jamaluddin (2004), who carried out the simulation via the Free Lagrange Method (FLM). Considering the same set of cases, simulations using BEM are performed and the results are compared to the others.

A brief description of the ALE and FLM methodology is given as follows. Both methods involve the solving of the compressible Euler equations in a two dimensional or axisymmetric configuration, and both methods use sophisticated and computationally expensive meshing. The ALE method developed by Ding and Gracewski (1996) uses the finite volume method. They have an adaptive mesh generation technique whereby a weight function depending on the pressure gradient was used. The FLM also utilizes the finite volume method. It starts off by filling the domain with computational "particles", and then discretising the domain by constructing a Voronoi mesh. As the computation progresses, the computational "cell" are allowed to change "neighbours" so as to prevent mesh distortion. The Euler equations are solved using Godunov-type solvers (Ball et al. (2000), Howell and Ball (2002), Turangan et al. (2006)).

In comparison, the BEM model is only solving a Laplace equation which is inherently incompressible. Our model is axisymmetric and involves the use of only 51 nodes on the bubble surface. This minimal number of nodes needed attribute to the great computational efficiency obtained with BEM.

3.1.2 Modeling a single pulse (step) shockwave

The shockwave is modeled as a pressure pulse function. It moves with constant velocity U_s and a width W_s towards the bubble in the direction of the z-axis as depicted in Fig. 3.1. The bubble is initially located at z_0 with a radius R_{max}.

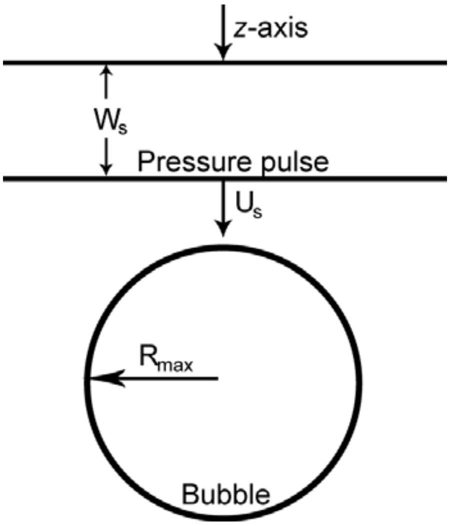

Fig. 3.1. Schematic diagram of a pressure pulse with a width W_s moving towards the bubble in the z-direction with velocity U_s. The initial bubble radius is R_{max}.

The shockwave has a constant peak pressure P_s across the width W_s. Anywhere else, the shockwave pressure is taken to be the reference pressure, p_{ref}, which is equivalent to the atmospheric pressure, i.e. 0.1 MPa. At a fixed position the shockwave profile is as shown in Fig. 3.2. The duration of the pressure pulse t_s is related to W_s as

$$W_s = U_s \cdot t_s \,. \tag{3.1}$$

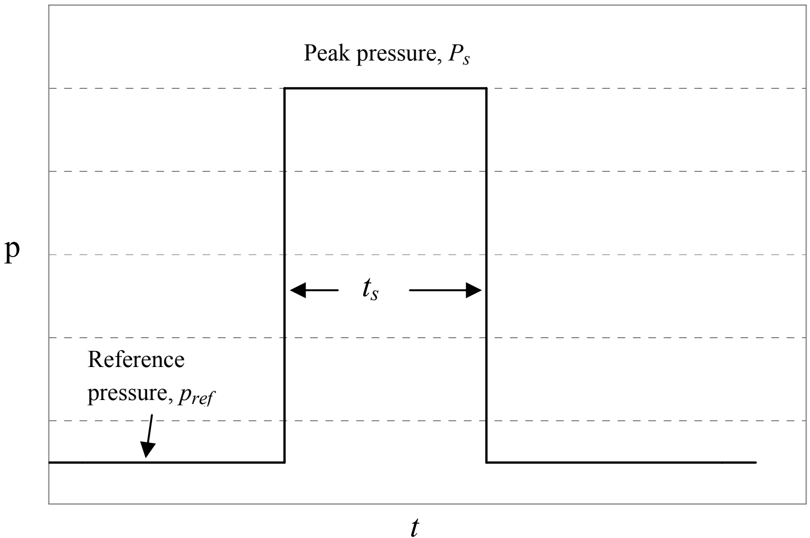

Fig. 3.2 Schematic diagram of a pressure pulse with duration t_s and peak pressure P_s as a function of time t. At all other times the pressure equals the reference pressure P_{ref}

Because of the pressure variation in time and its constant velocity U_s, the spatial variation of the traveling shockwave in the z-direction is defined. It is represented in the p_{ref} term in the unsteady Bernoulli's equation (eqn. (2.4) in Chapter 2), such that before the front of the shock reaches the bubble, $p_{ref} = p_{ATM}$ (atmospheric pressure); when the shock moves across the bubble, it is eventually submerged in the shockwave, and $p_{ref} = P_s$; and lastly, when the shock has passed, p_{ref} is again $p_{ref} = p_{ATM}$. Mathematically, p_{ref} is expressed with the following:

$$\begin{cases} p_{ref} = p_{ATM}; & z < z_0 + tU_s - W_s \\ p_{ref} = P_s; & z_0 + tU_s - W_s < z < z_0 + tU_s \\ p_{ref} = p_{ATM}; & z > z_0 + tU_s \end{cases} \tag{3.2}$$

With this spatial consideration, the current model can be seen as an extension to that used by Blake et al (1999). In their model, at any point on the bubble surface, p_{ref} is a function of time only. Recently, the model from Blake et al (1999) is also extended to include the spatial consideration similar to the formulation described in this section in Calvisi et al (2007).

In order to model with spatial consideration, the speed of the shockwave, U_s, must be known. It is in fact related to the amplitude of the shock, P_s. First of all, a parameter called particle velocity behind the shock is calculated. It is computed with consideration of the shock amplitude, and is then used to obtain the shock speed (Flores and Holt, 1981). It is assumed that the Tait equation of state applies in the fluid domain (in this case, the fluid is water). The density of the fluid behind the shock, ρ^*, is given by

$$\rho^* = \left(\frac{P_S}{B} + 1\right)^{1/n} \rho_{Rd} \tag{3.3}$$

where $\rho_{Rd} = 999.96\,\text{kg/m}^3$ is the water reference density at zero pressure, and B and n are constants with values of $3.31\text{x}10^8$ and 7, respectively.

Then as proposed by Flores and Holt (1981), the post-shock water particle velocity, u^*, can be calculated from

$$u^* = u_u + \sqrt{\left(\frac{\rho^* - \rho_u}{\rho^* \rho_u}\right)(P_s - P_u)}\ , \tag{3.4}$$

where the subscript u refers to the pre-shock condition. For all simulations in this thesis, the water is stationary. Therefore $u_u = 0.0$ m/s and $P_u = p_{ref} = 0.1$ MPa.

It is known that for most solids and liquids, the shock velocity U_s is near-linearly proportional to the velocity of the material (relative to the undisturbed medium) behind the shock u^*, provided that there is no phase change or existence of porosity (Howell and Ball, 2002). This is certainly the case for water. The near-linear relation of experimental shock data is given in the form

$$U_s = a_k + A_k u^* \tag{3.5}$$

where a_k is the local isentropic sound velocity and A_k is the shock density ratio parameter. For water $a_k = 1480$ m/s and the linear fit of U_s versus u^* for $u^* < 3.5$ km/s gives A_k = 1.815 (based on shock Hugoniot data as found in Marsh (1980)). For a weak pressure disturbance under atmospheric conditions, the wave speed in water approaches the local sound velocity, which is $U_s = a_k \approx 1480 \ \ \mathrm{m/s}$ (Leighton, 1994). But for a very strong shock, like the case to be presented in Section 3.2 whereby P_s = 0.528 GPa, u^* reaches a value of 259 m/s, and therefore, U_s = 1950 m/s, or U'_s = 195.0 (where U'_s is nondimensionalised as will be described shortly in eqn (3.8)). In the simulations in Section 3.1, this value of U'_s is used.

3.1.3 Non-dimensionalizing the shockwave model equations

As mentioned in Chapter 2, the equations are non-dimensionalized to facilitate numerical calculation and the subsequent discussions. For the parameters involved in describing the shockwaves, the following dimensionless parameters are used to non-dimensionalize eqn. (3.2):

$$P'_s = P_s / p_{ref} \tag{3.6}$$

$$W'_s = W_s / R_{\max} \tag{3.7}$$

$$U'_s = U_s / v_0 , \tag{3.8}$$

where v_0 is equal to $\sqrt{p_{ref} / \rho}$. The resultant non-dimensionalized eqn. (3.2) is as follows:

$$\begin{cases} p'_{ref} = 1 & ; \ z' < z'_0 + t'U'_s - W'_s \\ p'_{ref} = P'_s & ; \ z'_0 + t'U'_s - W'_s < z' < z'_0 + t'U'_s \\ p'_{ref} = 1 & ; \ z' > z'_0 + t'U'_s \end{cases} \tag{3.9}$$

In eqn. (3.8), U'_s is independent of the maximum bubble radius R_{max} and only depends on U_s. Since it is mentioned in Section 3.1.2 that $U_s = a_k \approx 1950 \, ms^{-1}$,

U'_s therefore assumes the value U'_s = 195. Also, the parameter z'_0 is chosen as $z'_0 = -1.0$, so that $t' = 0$ coincides with the time the pulse first hits the bubble.

3.1.4 Interaction of a 0.528 GPa pressure pulse (shockwave) with a bubble of radius 1.0 mm

In this particular case, a pressure pulse with profile as depicted in Fig. 3.2 is simulated to interact with a stationary bubble. The shock strength, also known as the peak pressure, P_s, is equal to 0.528 GPa, and the initial bubble radius is 1.0 mm. The shock width, W_s, is set to a very large value with respect to the bubble size, i.e. $W'_s =$ 1000. As the pressure pulse travels from top to bottom, eventually it strikes the upper surface of the bubble. This strong pressure perturbation causes a large momentum to be imparted to the gas-water interface of the bubble surface. This creates a high pressure region in the water around the impact location. The immediate difference in pressure between this water region and the gas inside the bubble, forces the bubble boundary to form an accelerating jet in the traveling direction of the pulse.

Fig. 3.3 depicts the BEM simulation results on the bubble evolution as a result of its interaction with the pressure pulse on the left, together with the FLM results from Jamaluddin (2004) on the right. Again, it is noted that $t' = 0$ is set to be the time when the pulse first hits the bubble. Prior to that, the velocity anywhere on the bubble surface is identically zero as the bubble is stationary.

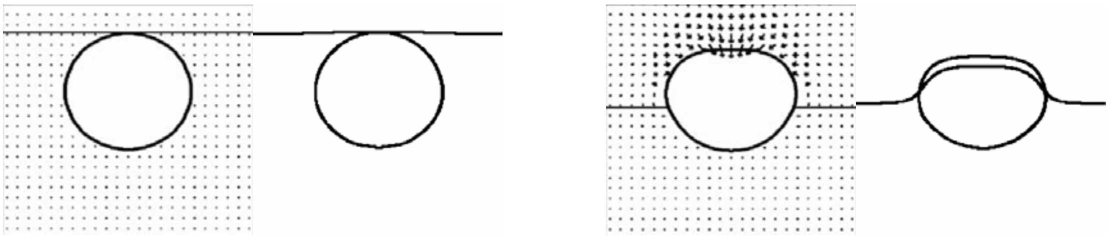

(i) 0 μs 0 μs (ii) 0.66 μs 0.6 μs

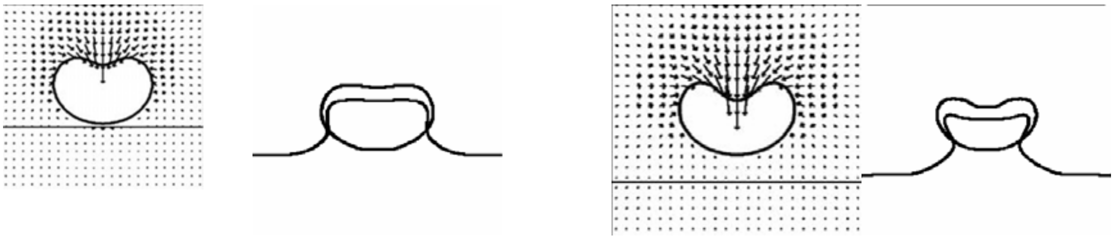

(iii) 1.1 μs 1.0 μs (iv) 1.32 μs 1.2 μs

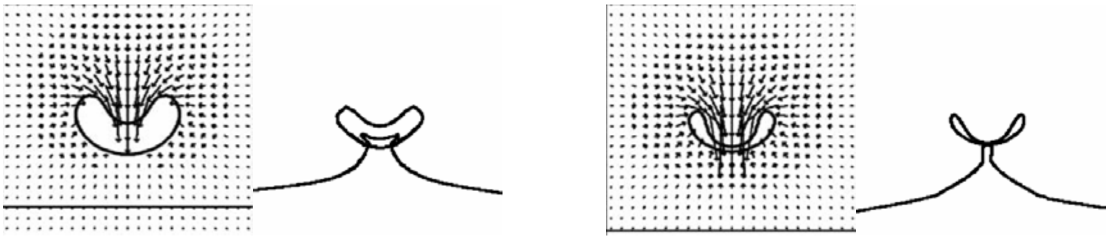

(v) 1.57 μs 1.4 μs (vi) 1.79 μs 1.6 μs

Fig. 3.3 BEM and FLM simulation of the interaction of a very wide pressure pulse of 0.528 GPa with a bubble of radius 1.0 mm. The figures on the left of the pair with velocity vectors plots (represented by the arrows) are from the BEM simulation; while the ones on the right of the pair are FLM results taken from Jamaluddin (2004). The line represents the shock front which moves from top to bottom (is horizontal for the BEM simulations). The time for the respective frames is indicated below the figures. The dimensionless parameters for the shockwave are: $P'_s = 5280$, $W'_s = 1000$ and $U'_s = 195$. The top bubble surface moves first and it accelerates to form a high speed jet of 2 km/s upon impact.

In the FLM method in Fig. 3.3 (figures on the right), the pressure pulse front represents the Mach contour front, whereas for the BEM method, the horizontal line represents the pulse front. Due to the lower acoustic impedance of air in comparison with water, the transmitted shock inside the bubble propagates slower than the pressure pulse front. This phenomenon is captured correctly by FLM simulations. But because the BEM model is an incompressible model, this feature is not reproduced.

At t = 0 μs in Fig 3.3(i), the pressure pulse touches the upper surface of the bubble. The pulse travels from top to the bottom of the frame in the z-axis direction (see Fig. 3.1). About 0.66 μs later (Fig. 3.3(ii)), the pressure pulse has traveled to the middle part of the bubble. The top surface of the bubble is then flattened by the fluid behind the shock which is responding to the pressure pulse. The next figure, Fig. 3.3(iii), shows the bubble profile when the pressure pulse has completely passed the bubble. Since the shock width, W_s, is much larger than the bubble size, the bubble is then completely immersed in a very high pressure environment ($p_{ref} = P_s = 0.528$ GPa). Due to the fluid inertia, a high speed jet begins to develop from the top surface of the bubble towards its bottom surface. The jet becomes more prominent from Fig. 3.3(iv) to (v). At $t = 1.79$ μs, the bubble continues to contract and the jet has almost touched the opposite surface of the bubble. From this series of figures, it is clear that although the BEM model does not model the propagation of waves inside the gas body, highly similar bubble profiles are obtained. However, possibly due to the lack of reflection and other shock related phenomena, the jet from the top bubble surface impacts slightly later in the BEM model; jet impact occurs at 1.6 μs for the FLM method, but at 1.79 μs for the BEM method.

In Fig. 3.3, the figures on the left of the pair (BEM simulations) show velocity vector plots (represented by the arrows) as well. Similar plots are also presented by Jamaluddin (2004), and are in good agreement with the left side figures of Fig. 3.3 (not reproduced here). As the shock travels from top to bottom, the velocity vectors behind the shock respond as the fluid is perturbed and has picked up speed. Highest speed indicated by the longest velocity vectors is observed around the region near the jet tip. In short, despite its simplicity, the results of BEM simulation are very similar to that of FLM and ALE in terms of the bubble shape (for ALE results, the reader can refer to Ding and Gracewski (1996)). The velocity plots compare favorably well with that from FLM (not shown here) too.

For a quantitative comparison, the jet velocity-time plot of the same case is examined. After the shock hits the bubble, a jet starts to develop at the top surface of the bubble. Its velocity in time is recorded for all three methods and presented in Fig. 3.4. Jamaluddin (2004) obtained the jet velocity values by taking averages of the absolute velocity of a few elements at the tip of the jet. For BEM, the velocity of a single node which is on the axis of symmetry is recorded. The trend of the results for both methods is similar; the jet velocity increases in time with an almost linear acceleration of about 1300 m/s^2. The same observation is obtained for ALE, with exception of some minor oscillations at the beginning of the simulation. However, when the jet is about to impact on the bottom surface of the bubble, the difference between BEM and FLM/ALE becomes larger. For the bubbles in FLM and ALE simulations, the jet impact occurs sooner at t = 1.6 μs, and at a higher final maximum velocity of about 2200 m/s. From the BEM simulations, it is found that the jet impact happens at t = 1.79 μs, and the velocity reaches a comparable value of 2000 m/s. This probably implies that the reflected shockwaves inside the bubble play a part in enhancing the collapse of the bubble, and therefore resulting in slightly earlier collapse with higher velocity. Nevertheless, the general trends for the bubble’s jet velocity for all three methods remain similar.

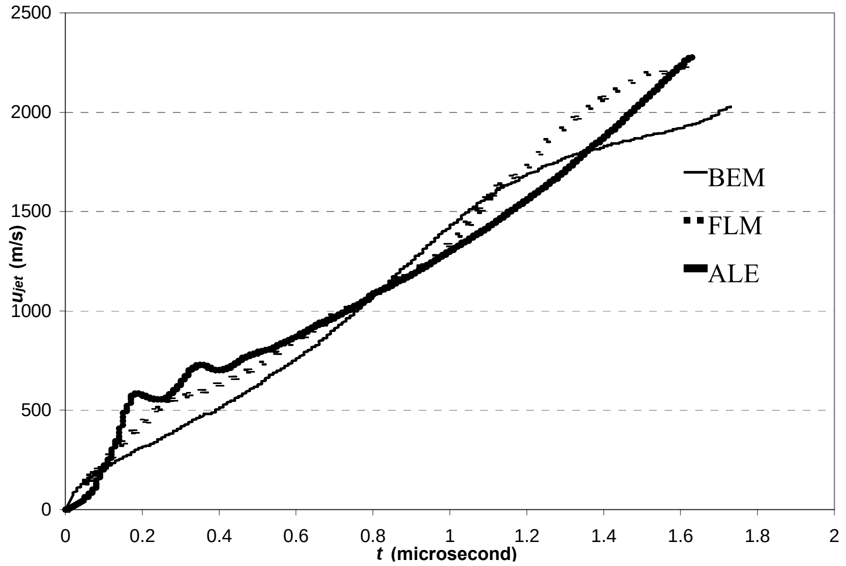

Fig. 3.4 Jet velocity, u_{jet}, vs time, t, for BEM, FLM, and ALE methods. The pressure pulse hits the bubble at t = 0 μs. Then the jet starts to develop; for ALE and FLM, it impacts upon the bottom bubble surface at about $t = 1.6$ μs. For BEM, jet impact occurs slightly later at $t = 1.79$ μs. As for the jet velocity at the moment of impact, u_{jet} reaches a maximum of about 2200 m/s for FLM and ALE, but slightly less at 2000 m/s for BEM. Nevertheless, the trends for all methods are similar.

The BEM simulation has two significant advantages over the other methods mentioned, namely the FLM and ALE methods. Firstly, the time requirement to run the same simulation (for instance the case presented in Section 3.1.4) is much less for BEM than for the other methods. On a normal personal computer, the full simulation of the case in Section 3.1.4 takes only a few minutes for BEM, whilst for FLM and ALE, it takes at least a few hours. Secondly, the storage space requirement is much less for BEM. Since only the boundaries in the model (in this case, the bubble surface) are considered, a great reduction of computational elements is achieved using BEM. For this case, the author used a total of 51 nodes for the representation of half of the bubble surface (this is sufficient since the problem is considered in axisymmetric configuration). Typically for FLM, since a full mesh of the domain is required, the number of cells used can be very large (for example about 19000 for the simulation in Section 3.1.4 (Jamaluddin, 2004)). The small number of computational elements is also the main factor contributing to the fast computing time for BEM. Furthermore, as the calculation proceeds, the number of elements remains the same for BEM simulations. For FLM, however, a high concentration of nodes is often found in the region where the shock advances. This adds to greater computational complexity which in turn leads to longer time requirement and larger storage space needed.

More results and detailed discussions on other cases have been done but are not shown here. Interested readers can refer to Klaseboer et al (2006b). After the comparison with other numerical simulation results, the BEM model is slightly modified in the next section to simulate the interaction of a lithotripter shockwave with an oscillating (non-equilibrium) bubble. The bubble shape changes in time and jet velocity readings from both experimental and numerical results will be compared and discussed.

3.2 Lithotripter shockwave interaction with a non-equilibrium bubble

In this section, the dynamic interaction of a shockwave, which is modeled as a pressure pulse with realistic pressure profile from a lithotripter, with an expanding or collapsing bubble is investigated numerically. This model is an extension of the model used in the previous section and will be presented in detail in Section 3.2.1 and 3.2.2. The results are compared with experimental observations of lithotripter shockwaves impinging on laser induced bubbles as presented in Sankin et al (2005). The jet impacts the opposite surface of the bubble in the direction of the shockwave and emits an intense pressure wave, which was measured experimentally and compared to various parameters in the numerical results. It is found that the experimental peak pressure is related to numerical variables such as the jet velocity and the Kelvin impulse (all at the moment of jet impact). The key observation in this section is that the most intense collapse is occuring for a bubble having intermediate size (not the maximum size), and that this happens when the collapse time of the bubble is approximately equal to the time scale of the compressive portion of the shockwave. The main advantage in computational efficiency of the BEM code is retained in this extended model.

3.2.1 Modeling of a lithotripter shockwave

The shockwaves generated by a lithotripter used in kidney stone removal treatment have typical profiles as depicted in Fig. 3.5. The lithotripter shockwave consists of firstly a high peak pressure compressive wave, and then a negative pressure tensile wave. For this particular case, the compressive wave has a maximum pressure of 39 MPa and lasts for about 1 μs, and the tensile wave has a minimum of -8 MPa and duration of about 2 μs.

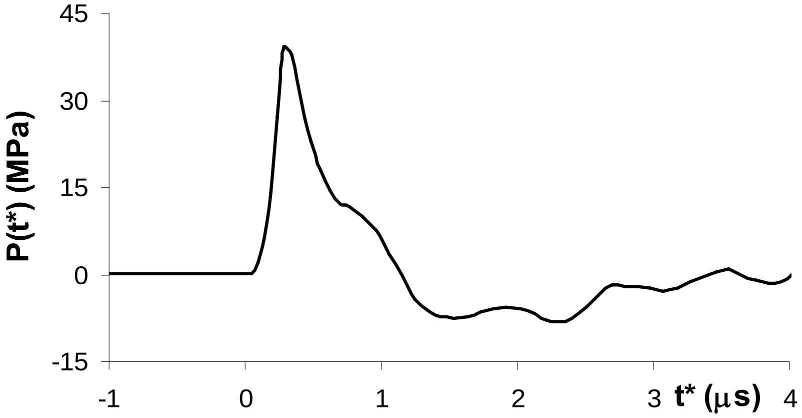

Fig. 3.5 Average-smoothed experimental shockwave profile from Sankin et al (2005), pressure P(t*) as a function of time, t* with peak pressure 39 MPa. The pulse has approximately a 1 μs compressive wave followed by a 2 μs tensile wave of -8 MPa. The secondary oscillations in the profiles are due to reflections.

The shockwave as shown in Fig. 3.5 is incorporated into the model with both temporal and spatial considerations as mentioned in Section 3.1.2. The difference between these two models is that instead of a constant shock pressure P_s, a realistic time-varying pressure, *P(t*)* is used. The values in *P(t*)* are obtained from the experimental observations such as that found in Fig. 3.5. It is incorporated into the reference pressure term p_{ref} in the unsteady Bernoulli's equation (eqn (2.4) in Chapter 2) again such that p_{ref} (z, t) = P(t*) with

$$t^* = t - z/U_s + R_0/U_s, \tag{3.10}$$

where U_s is the velocity of sound in water, which is taken to be 1480 m/s as the shock is moderate in strength (see Section 3.1.2), and z is the distance on the z-axis as depicted in Fig. 3.1. Also if $t^* < 0$, the reference pressure $P(z,t)$ is set to be equal to p_{ATM}. The absolute time is set to $t = 0$ when the front of the shockwave hits the bubble.

3.2.2 Modeling of an oscillating (non-equilibrium) bubble

When the shockwave impinges on an oscillating bubble at $t = 0$ μs, the radius of the bubble at that moment is taken to be R_{00}. Note that this radius differs from the initial radius for a stationary bubble like that mentioned in Section 3.1 in such that R_{00} might not be the minimum or maximum bubble radius. Therefore in the following section, the shockwaves are considered to hit the bubble ($t = 0$ μs) at various R_{00} with non-dimensionalization provided by $R_{\max}$ (maximum bubble radius which a bubble would have obtained if no shockwave was present), i.e. $R_{00} / R_{\max}$. Also apart from setting the initial value for $R_{00} / R_{\max}$, we need a formulation for the initial velocity potential for the corresponding R_{00}, $\Phi(R_{00})$. This is because at this instance, the bubble is not stationary, i.e. $\Phi(R_{00}) \neq 0$. Instead it is already moving with a certain velocity because the bubble could be in its 'E' (expanding) or 'C' (collapsing) phase. The derivation for $\Phi(R_{00})$ is found in eqn. 2.16. For the simulations performed here,

ε is taken to be 100 (thus assuming $p_{g,0} = 100\,\text{bar}$), $R_0 / R_{\max}$ is calculated to be equal to 0.1485 with eqn. 2.15. All bubbles studied in Section 3.2 have maximum radii, $R_{\max}$ = 300 μm. This $R_{\max}$ is chosen because it is the bubble size generated with the laser energy level as set by Sankin et al. (2005). The result is probably valid for bubbles between a few micron to a few millimeter because as pointed out in Section 2.1, a 1 μm bubble is perhaps the lower limit of the BEM model, and for larger bubbles, other forces like gravity and buoyancy might play a part in the bubble dynamics.

3.2.3 Comparison of bubble shapes and collapse times with experimental results

Figs. 3.6 to 3.11 show experimental and numerical results of the lithotripter shockwave given in Fig. 3.5 impinging on bubbles with $R_{00}/R_{\max}$ ~0.50, ~0.65, and ~1.0 (R_{00} and $R_{\max}$ denote the bubble radius at the moment of shockwave impact and maximum bubble radius respectively). The letter 'E' in the figures stands for an initial expanding bubble and 'C' denotes a collapsing bubble. The collapse time is defined to be the time taken for the bubble to collapse from its maximum size to the moment of jet impact. Selected experimental frames are shown (for the complete sequence, one can refer to Sankin et al (2005)). Several general trends of bubble dynamics are observed. Firstly, all bubbles eventually develop high speed jets in the direction of the propagation of the shockwave, in this case, in the upwards direction. They are forced to collapse by the strong shockwave that travels across them. Also, for a bubble of a certain size, the collapse time for this bubble in its 'E' (expansion) phase is longer than that when it is in its ‘C’ (collapse) phase. Lastly, a smaller bubble has the tendency to collapse earlier than the larger ones (see also Fig. 3.12).

When the shockwave impinges on an ‘E’ (expanding) bubble, the bubble shape changes are documented experimentally in Fig. 3.6(a) (from Sankin et al, 2005) and numerically in Fig. 3.6(b). Both figures show the development of a flat and broad jet in the direction of propagation of the shockwave. The bubble shapes (t = 1.20, 1.29, and 1.32 μs) in the simulation diagram show clearly how the thick jet develops. Also, it is noticed that the bubble center translates in the shockwave propagation direction as well.

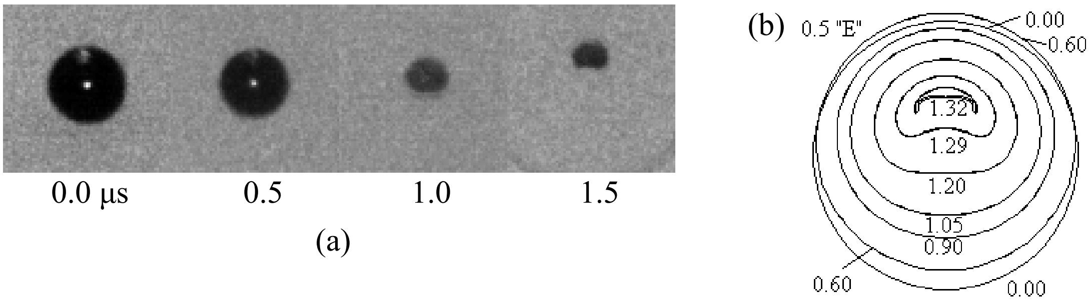

Fig. 3.6 An oscillating bubble with R_{00}/R_{max} = 0.53 in its ‘E’ (expansion) phase. The shockwave is coming from below. (a) Experimental results taken from Sankin et al (2005). It shows the bubble from t = 0 to 1.5 μs. (b) Numerical results of the bubble shape with the corresponding time in μs indicated on each profile. Both experimental and numerical results show the development of a flat broad jet and the translation of bubble center.

The corresponding observation for a bubble of similar initial bubble size (R_{00}/R_{max} = 0.5), but in its ‘C’ (collapsing) phase instead, is presented in Fig. 3.7. Again the final bubble shows a much flattened profile; for the simulation this happens at 0.96 μs, and the corresponding experimental observation at 1.0 μs after the shockwave hits the bubble. This collapse time is much shorter than that observed for the corresponding ‘E’ bubble; the bubble collapses at 1.5 μs for experiment and 1.32 μs for simulation results are shown in Fig. 3.6. It is noted that the secondary shockwaves from the bubble collapse in the experiment is seen in the last frame.

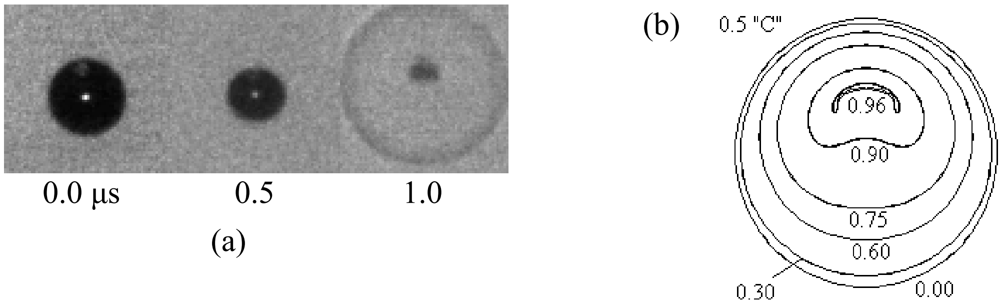

Fig. 3.7 An oscillating bubble with $R_{00}/R_{max} = 0.5$ in its 'C' (collapse) phase. (a) Experimental results taken from Sankin et al (2005). It shows the bubble from t = 0 to 1.0 μs (with an interframe rate of 0.5 μs). The last frame shows a secondary shockwave from the bubble collapse (b) Numerical results of the bubble shape with the corresponding time in μs indicated on each profile. Again as in Fig. 3.6, both experimental and numerical result show the development of a flat broad jet and the translation of bubble center in the direction of shockwave propagation (upwards).

In the next two figures (Fig. 3.8 and 3.9), a bubble with $R_{00}/R_{max} = 0.65$ is considered. For both cases, the bubble collapses with a flat and broad jet as in the previous examples. Fig. 3.8 shows an 'E' bubble which collapses with a flat broad jet at $t = 1.77$ μs for simulation results and 1.5 μs for the corresponding experimental result. The final shape of the bubble is similar to that in Fig. 3.6.

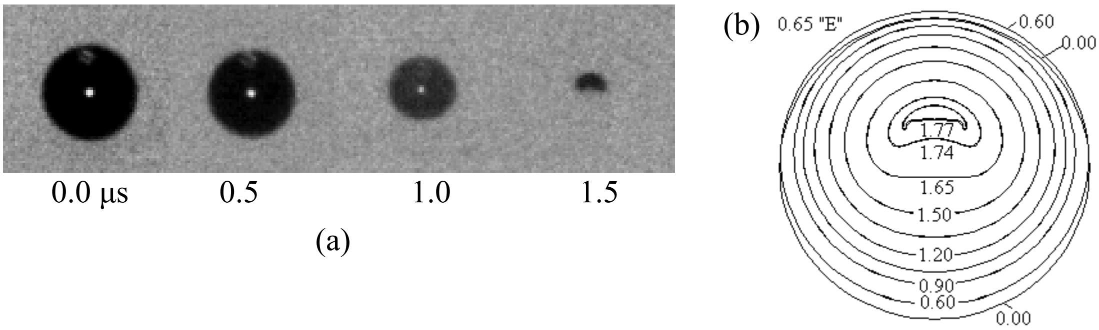

Fig. 3.8 An oscillating bubble with $R_{00}/R_{max} = 0.65$ in its 'E' (expansion) phase. (a) Experimental results taken from Sankin et al (2005). It shows the bubble from t = 0 to 1.5 μs (with an interframe rate of 0.5 μs). (b) Numerical results of the bubble shape with the corresponding time in μs indicated on each profile. Both experimental and numerical results show the development of a flat broad jet.

Fig. 3.9 shows a 'C' bubble with the same size ($R_{00}/R_{max} = 0.65$) when it is hit by the shockwave of Fig. 3.5. It develops a slightly rounder jet than that of the corresponding 'E' bubble in Fig. 3.8. Also, a shorter collapse time is observed. For this 'E' bubble, it collapses at $t = 1.77$ μs, whereas for the 'C' bubble, it takes 1.32 μs.

Similar translational movement of the bubble center is observed for the bubbles of different R_{00}/R_{max}.

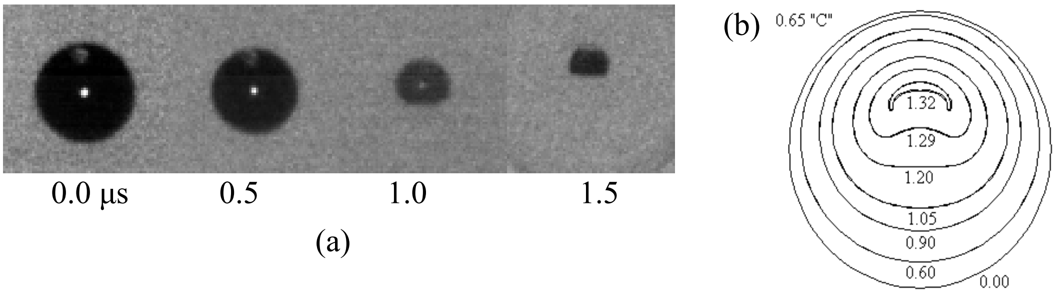

Fig. 3.9 An oscillating bubble with R_{00}/R_{max} = 0.65 in its 'C' (collapse) phase. (a) Experimental results taken from Sankin et al (2005). It shows the bubble from t = 0 to 1.5 µs (with an interframe rate of 0.5 µs). (b) Numerical results of the bubble shape with the corresponding time in µs indicated on each profile. Again as in Fig. 3.8, both experimental and numerical results show the development of a flat broad jet.

When the shock hits a bubble at its maximum size (R_{00}/R_{max} = 1.0) as shown in Fig. 3.10, it takes a much longer time of 4 µs for the bubble to collapse. According to Sankin et al (2005), in general, the larger the size of the bubble when the shockwave impacts, the longer it takes to collapse. Besides, there is clearly a jet developing at about t = 3.5 µs (t = 3.45 µs for the simulation results in Fig. 3.10(b)). But at the final moment of collapse, the jet becomes so broadened that the bubble appears flattened out (last frame of Fig. 3.10(a) and bubble profile at t = 3.51 µs for Fig. 3.10 (b)).

It is noted that for previous cases with R_{00}/R_{max} = 0.5 or 0.65, the compressive part of the shockwave of Fig. 3.5 which lasts only about 1 µs, has completely passed the bubbles before their final collapses. In other words, they experience part of the tensile component of the shock as the jets develop and impact on the other surfaces on the bubbles. As for the R_{00}/R_{max} = 1 bubble however, it experiences the full tensile part of the shock (lasting about 2-3 µs) before its final collapse at t = 4 µs (or t = 3.51 µs for the simulation). This could be the reason behind the peculiar final shape of the bubble.

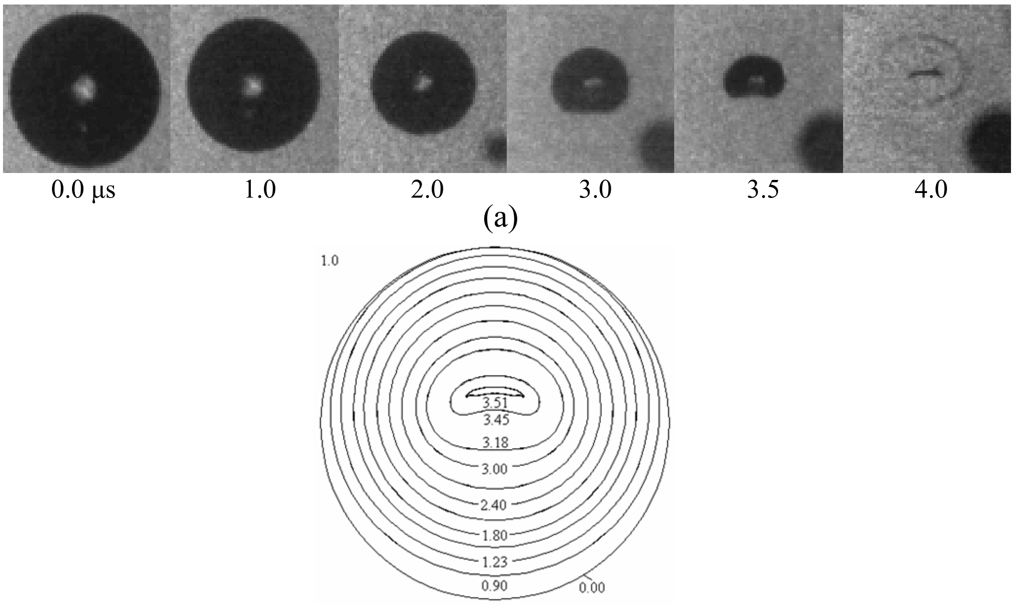

(b)

Fig. 3.10 An oscillating bubble with $R_{00}/R_{max} = 1$. (a) Experimental results taken from Sankin et al (2005). It shows selective frames of the bubble from t = 0 to 4 μs. (b) Numerical results of the bubble shape with the corresponding time in μs indicated on each profile. A very flattened disc-like bubble is observed both (a) experimental and (b) numerically.

For a bubble with very small R_{00}/R_{max}, no experimental results are available. This is probably because of the temporal constraints as it is difficult to align the equipment to enable the shockwaves to hit the bubbles at those instances as the bubbles are growing/collapsing extremely rapidly. From numerical simulation, it is seen that a rather thin jet is formed and impacts on the opposite surface of the bubble at t = 0.48 μs. It has been mentioned in Section 3.1.2 that shockwave speed, U_s, is taken to be 1480 m/s (Leighton, 1994). Thus it takes the shockwave $2 \cdot R_0 / U_s$, i.e. 0.64 μs, to move across the bubble. Since the bubble has already collapsed at t = 0.48 μs, it has not experienced the tensile component of the shock which happens after 1 μs. This is possibly the reason behind the different in final collapse shape of the bubble as compared to all previously discussed cases (from Figs. 3.6 to 3.10).

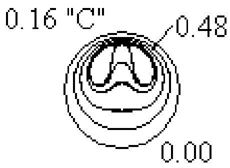

Fig. 3.11 An oscillating bubble with R_{00}/R_{max} = 0.16 in its 'C' (collapse) phase. The bubble shapes with the corresponding time in μs indicated on the first and last profiles.

Apart from the bubble shapes, the collapse times of the bubbles in various initial conditions of R_{00}/R_{max} are also studied. Experimental results from Sankin et al (2005) are plotted together with numerical simulation values in Fig. 3.12. They show very close resemblance. Three important observations are obtained: firstly, for each group of the bubble ('E' or 'C' bubbles), the larger the value of R_{00}/R_{max}, the longer the collapse time. Secondly, the 'C' bubbles are collapsing faster then the 'E' bubbles of the same normalized size in R_{00}/R_{max}. Thirdly, the difference in collapse time for an 'E' and 'C' bubble pair of same R_{00}/R_{max}, is about 0.5 μs for a large range of values of R_{00}/R_{max}. It is also noted that no values for small R_{00}/R_{max} are available from Sankin et al (2005) because of experimental limitations in the use of laser bubble. These bubbles suffer non-spherical distortion at their early stages (also in late stages) of oscillation. However, numerical results are available even for a bubble with minimum value of R_{00}/R_{max} i.e. $R_{00}/R_{max} = 0.1485$. These data form a closed loop, where the curves of 'E' and 'C' bubbles join at the left bottom and right top corners of the graph. Also plotted on the same graphs are results from Rayleigh-Plesset model of the oscillating bubbles (dashed red lines). In this model the pressure experienced on the bubble surface is uniform (no spatial difference) because only temporal variation of the pressure wave is considered. It is seen that the results match that from the BEM simulation rather well. For 'E' bubbles with $R_{00}/R_{max} > 0.6$, the Rayleigh-Plesset collapse times are slightly larger than that from the BEM simulation. Similar increase in collapse times is observed for 'C' bubbles with $R_{00}/R_{max} > 0.8$. On the other hand, for 'C' bubbles with $R_{00}/R_{max} < 0.8$, the collapse times obtained from the Rayleigh-Plesset model is slightly lower than that calculated with BEM simulations. Similar decrease is observed for 'E' bubbles with $R_{00}/R_{max} < 0.6$. Nevertheless, the difference in collapse times between the two models is less than 4.5%. This suggests that the simple Rayleigh-Plesset model is sufficient in predicting the collapse time of the oscillating bubble when hit by a lithotripter shockwave. However, the BEM model has the added advantage of being able to provide other information about the jet development and jet velocity.

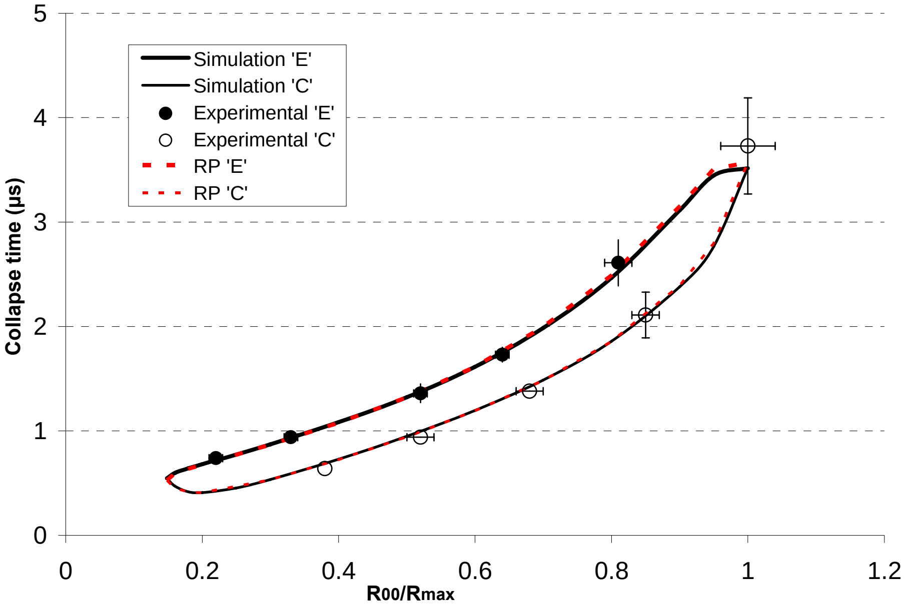

Fig. 3.12 Collapse time for bubbles with various normalized bubble radius (R_{00}/R_{max}). Experimental results from Sankin et al are plotted with circles (filled circles for 'E' and empty circles for 'C' bubbles). Numerical simulation values are plotted in thick and thin lines for 'E' and 'C' bubble respectively. Also plotted in thick and thin dashed lines for 'E' and 'C' bubbles from Rayleigh-Plesset simulations. Each of these curves is plotted from 14 data points. Results shows that the larger the value of R_{00}/R_{max}, the longer is the bubble's collapse time. Also, a 'C' bubble always collapses faster than an 'E' bubble of the same initial size. Similar trends are shown by the Rayleigh-Plesset (RP) model. Slight differences between the models are observed. For the larger bubbles ('E' bubbles, $R_{00}/R_{max} > 0.6$, 'C' bubbles, $R_{00}/R_{max} > 0.8$), the RP model predicts a longer collapse times. But for small bubbles ('E' bubbles, $R_{00}/R_{max} < 0.6$, 'C' bubbles, $R_{00}/R_{max} < 0.8$), the collapse times for the RP model are lower than that from the BEM simulations.

3.2.4 Comparison between experimental pressure measurements and numerical results

Since jet impact from the collapsing bubbles is believed to be one of the important mechanisms in breaking up kidney stones during lithotripsy treatments, the jet velocity and pressure pulse resulting from these bubbles are of interest. Sankin et al (2005) measured the peak pressure shortly after jet impact by using a needle hydrophone which was placed along the central axis of the shockwave source at a distance of 1.1 mm above the source's focus. Results were obtained for the various R_{00}/R_{max}, and were plotted as shown in Fig. 3.13.

As mentioned in the previous section, the collapsing 'C' bubbles tend to have shorter collapse time as compared to the 'E' bubbles of the same R_{00}/R_{max}. These 'C' bubbles also seem to be collapsing more violently than the counterpart 'E' bubbles (of the same R_{00}/R_{max}) because the pressure at impact measured (in Fig. 3.13) is much higher. One noteworthy observation from Fig. 3.13 is that the maximum value of the peak pressure is obtained for a bubble of $R_{00}/R_{max} = 0.7$, and not at the lowest or highest R_{00}/R_{max} values. For example, for the 'C' bubble, the peak pressures for lowest and highest R_{00}/R_{max} of 0.4 and 1.0 respectively, they are only about 60% of the peak pressure measured at $R_{00}/R_{max} = 0.7$.

The numerical model used assumes incompressibility of the liquid. Therefore it is not possible to calculate directly the pressure caused by shock emission from the jet impact. But the pressure measured is related to how violent the collapse is, which is in turn related to the jet velocity and the Kelvin impulse values (details about the parameter Kelvin impulse are given in the later paragraphs in this section). The numerical results for both parameters are presented in Fig. 3.14 and 3.15, respectively. Both figures show strong resemblance to the peak pressure figure (Fig. 3.13).

In Fig. 3.14, jet velocity of the jet tip just at the moment before it impacts on the opposite bubble wall is shown. In general, the jet velocities calculated are very high. The maximum value of 1260 m/s is obtained for a ‘C’ bubble with R_{00}/R_{max} = 0.5. Even the minimum jet velocity reaches a value of 410 m/s, for an ‘E’ bubble of R_{00}/R_{max} = 0.95. Also, similar to the peak pressure data, jet velocity for ‘C’ bubbles are higher than that of its corresponding ‘E’ bubbles of the same R_{00}/R_{max}, except for the cases whereby R_{00}/R_{max} < 0.2. This is probably due to the fact that when the bubbles are small, i.e. R_0/R_{max} is less than 0.2, the collapse time difference between ‘E’ and ‘C’ bubbles are proportionally larger. For example, a ‘C’ bubble of R_{00}/R_{max} = 0.2, collapses after 0.41 μs; whilst a corresponding ‘E’ bubble collapses only after 0.68 μs. This means that the ‘E’ bubble has about 1.6 times longer for the development and acceleration of jets before the final impact. Therefore it is able to achieve a higher jet velocity than the ‘C’ bubble. However for the larger bubbles, the difference in collapse time between the ‘C’ and ‘E’ bubbles is only 15 to 20%. Therefore the propensity of the already collapsing ‘C’ bubbles to collapse more violently than the corresponding ‘E’ bubbles dominates. As a result, higher jet velocity values are obtained by the ‘C’ bubbles.

Another interesting parameter for accessing the physics of the bubble collapse is known as the Kelvin impulse. The impulse vector **K** is defined as the integral of the potential Φ on the bubble surface *S* multiplied by the fluid density, ρ, and the normal vector **n** at this surface (Pearson et al. 2004):

$$\mathbf{K} = \rho \int_S \Phi \mathbf{n} dS \,. \tag{3.12}$$

Physically this parameter gives the impulse that is required to be applied over the surface of the bubble in order to generate the flow field during the jet formation and the subsequent jet impact. Therefore, it is related to the jet speed and the broadness of the jet radius. For a spherically oscillating bubble, however, the Kelvin impulse vector is zero because the flow field is uniform on the bubble surface and $\int_S \mathbf{n} dS = \mathbf{0}$. Also, since the simulations done here are under axisymmetric configuration, the Kelvin impulse vector has only a component in the z-direction. Thus, it is taken to be a scalar with value $K = |\mathbf{K}|$.

Non-dimensionalized Kelvin impulse (K') values are used in Fig. 3.15. It is obtained by dividing K with $R_{\max}^3 \sqrt{p_{ref}\rho}$. The ‘C’ bubbles generally give a higher value of K' than their corresponding ‘E’ bubbles. Exception occurs again for R_{00}/R_{max} < 0.2. The maximum value is obtained for $R_{00}/R_{max} = 0.7$ for a ‘C’ bubble. Although the peak pressure is not directly proportional to K', K' exhibits a trend that is very similar to the peak pressure data of Fig. 3.13. Therefore K' can potentially be utilized to predict the pressure measurement qualitatively.

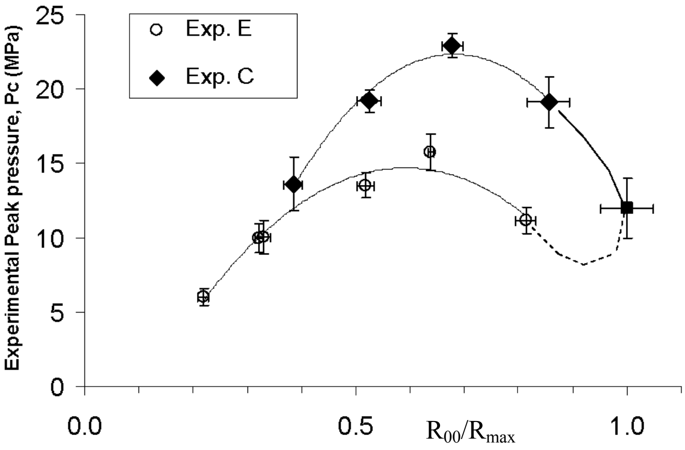

Fig. 3.13 Measured peak pressure due to the jet impact P_c for the various ‘E’ and ‘C’ bubbles with different R_{00}/R_{max}. The figure is reproduced from Sankin et al (2005).

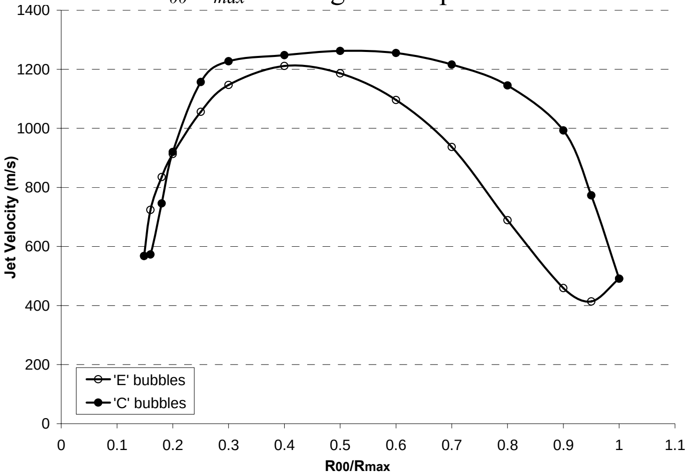

Fig. 3.14 Jet velocities of the ‘E’ and ‘C’ bubbles with various R_{00}/R_{max} from BEM simulations. ‘C’ bubbles of $R_{00}/R_{max} > 0.2$ collapse with higher jet velocity than ‘E’ bubbles and vice versa for bubbles with $R_{00}/R_{max} < 0.2$. Maximum jet velocity of about 1260 m/s is obtained for a ‘C’ bubble of $R_{00}/R_{max} = 0.5$.

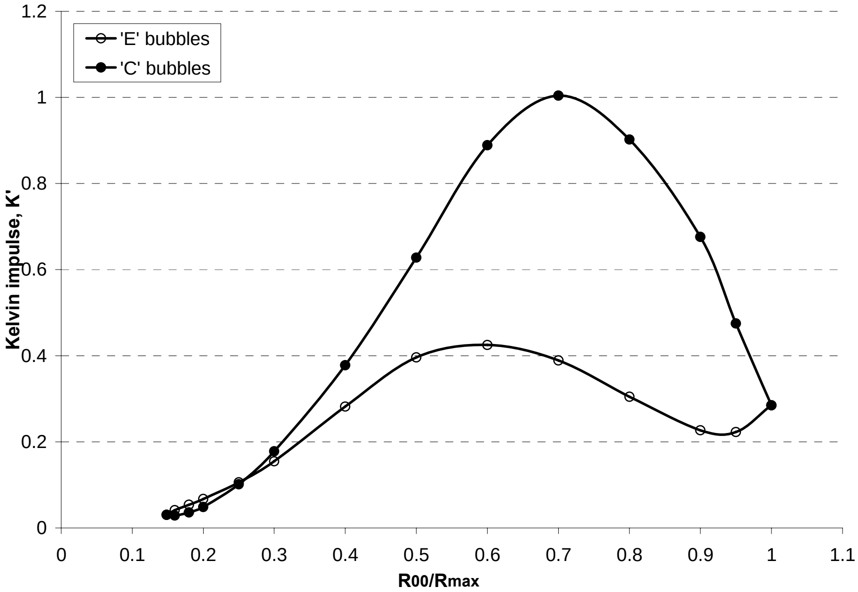

Fig. 3.15 The dimensionless Kelvin impulse, K’, at the moment of jet impact for various R_{00}/R_{max}. The maximum K’ occurs at $R_{00}/R_{max} = 0.7$ for a ‘C’ bubble.

3.2.5 Discussion

3.2.5.1 Other types of bubbles

In Section 3.2, the bubble studied is an oscillating bubble with a bubble strength of ε = 100. It is therefore interesting to compare the interaction of the same lithotripter shockwave on a stationary bubble, or a bubble with higher ε. The stationary bubble is modeled with setting ε = 1.0. As discussed in eqn. (2.15), this will set the initial internal gas pressure, $p_{g,0}$, equal to that of the reference pressure, $p_{ref,}$ and thus the bubble will stay at rest for $t \leq 0$.

To compare meaningfully with the oscillating bubble cases, the results obtained are non-dimensionalized with $R_{\max} = 300$ μm. It is found that for a particular value of $R_{00}/R_{\max}$, the collapse time and the dimensionless Kelvin impulse, *K'* of the non-oscillating bubble takes on the average value of the corresponding 'C' and 'E' bubbles. For instance, a stationary bubble of $R_{00}/R_{\max} = 0.5$ ($R_{00} = 150$ μm) collapses after 1.11 μs while its corresponding 'C' and 'E' bubbles collapse at t = 0.95 and 1.32 μs, respectively. It is also noted that for very small bubbles (i.e. those with $R_{00}/R_{\max}$ close to zero), their collapse time tend towards zero. As for the *K'* curve, again the stationary bubbles of certain $R_{00}/R_{\max}$, tend to take on the average values of that of its 'C' and 'E' corresponding bubbles.

Therefore it is concluded that simulation results from modeling a stationary bubble are average values from the simulations that consider oscillating bubbles. This is important as it is very often that a stationary bubble is modeled in simulation due to its simplicity, but in realistic situations the bubbles might be oscillating. Some insights can still be obtained from the simplified stationary bubble results.

The parameter ε, bubble strength, is set to an arbitrary value of 100 in all the simulations presented in previous sections. Deriving from eqn. (2.11) and taking the maximum peak pressure as obtained from G.N. Sankin through private communication to be 4.5 MPa, the value of ε and $R_{00}/R_{\max}$ are set to be 3906 and 0.0413. This high value of ε is deemed unrealistic because it would probably suggest that a shockwave is emitted in both expansion and collapse phase of the oscillating bubble, and no such emission was picked up by experimental measurements of Sankin et al (2005). Nevertheless to analyze the effect of ε, a set of simulations with ε = 3906 and $R_{00}/R_{\max}$ = 0.0413 is performed. It is found that both collapse time and the K' graphs for 'C' and 'E' bubbles for both ε = 100 and ε = 3906, overlap almost exactly. The only mismatch is found for 'C' bubbles with $R_{00}/R_{\max} < 0.2$. In these cases, the pressure in the tiny bubbles is so large (390.6 MPa) that the shockwave has little influence on the bubble dynamics and thus the bubbles collapse spherically rather than with a jet. With these results, it is concluded that in general the value of ε is not critically influencing the numerical results of shockwave-bubble interaction.

3.2.5.2 Advantages and validity of BEM in bubble lithotripter shockwaves simulations

The main advantages of BEM, as mentioned in Section 3.1.4, are its computational efficiency and storage space requirement. These benefits are retained in the simulation involving lithotripter shockwave bubble interaction. A full simulation of a particular case of $R_{00}/R_{\max}$ 'C' and 'E' bubbles only takes a few minutes. The number of nodes on the bubbles also remains constantly 51.

The reader might be concerned about the use of potential flow approximation which does not take into account the compressibility of the fluid in the modeling of shockwave bubble interaction. It is true that the shockwave phenomena cannot be modeled using the potential theory. Nevertheless, the shockwave can be considered as a pressure perturbation because the bubble dynamics involved in its interaction with the shock is still primarily inertia driven. From the validations obtained by comparing the BEM results with those from other numerical methods which model compressibility, and the experimental data from Sankin et al (2005), it can be said that fluid compressibility and bubble's internal shockwave are of weak secondary importance. More discussions and details of the simulation performed in Section 3.2 can be found in Klaseboer et al (2007).

3.3 Interactions of a stationary bubble with inverted shockwaves

For the normal shockwaves used in lithotripsy treatment, there is a compressive component of high intensity followed by a tensile part of relatively long duration as depicted in Fig. 3.5. This shockwave causes the bubbles that are generated either by a previous shock or are pre-existing in the fluid or tissues, to collapse violently with a very high speed jet. This phenomenon is much discussed in the previous section. However it is noticed that the collapse time of the bubbles are generally shorter than the duration of the shockwave. They have collapsed either before the arrival of the tensile part of the shock or in the early phase of the tensile wave. Thus, these bubbles after the initial collapse and their likely subsequent fragmentation will rebound typically as clusters of bubbles. This rebound bubble cluster will also eventually collapse, usually only a few hundred microseconds later (Church (1989), Coleman et al (1992), Zhong et al (1997b, 1999)), and may cause great collateral damage to the nearby tissue (Castensen et al (1990)).

To minimize collateral damage and to maximize treatment efficiency (fewer number of shock used in a single session), the use of an inverted shockwave has been proposed (Zhong et al (2001), Bailey et al (1999), Loske and Prieto (2002)). This shock has a leading tensile wave, which is followed immediately by a much stronger compressive wave. The tensile component will cause the existing gas pockets or small bubbles to expand, but the compressive wave will force the bubbles to collapse violently, and greatly suppress further bubble growth. This type of shockwave can be generated using a pressure release reflector which is inserted into an electrohydraulic lithotripter (Bailey et al, 1998) or by changing the piezoelectric circuit (Loske et al, 2002).

There are few numerical simulations of bubble interactions with an inverted shockwave. In two successive publications, Bailey et al. (1998, 1999) studied the effect of acoustic inversion on the pressure distribution and cavitation field. They also applied a single bubble model to compare the measured bubble dynamics. They found that the inverted shockwave greatly shortened bubble collapse duration, and yet the pressure emitted from the bubble cluster is the same as that from a cluster which is driven with a standard pressure pulse. In the same year, Zhu and Zhong (1999) did a numerical study of the combination of waveforms to generate an inverted shockwave for the interaction with a stationary bubble using the Gilmore formulation (Gilmore, 1952). They also found that the inverted shockwave significantly decreased the re-expansion of the bubble following its initial collapse, and thus may alleviate the risk for vascular expansion. In this section, the author will extend the BEM model that has been previously describe to study the interaction of an inverted shockwave of varying strength with a stationary bubble of different initial sizes. Bubble profile evolution, collapse time, jet velocity and Kelvin impulse of the interaction are presented. These parameters, however, could not be obtained from the previous mentioned spherical symmetric bubble models of Bailey et al. (1998, 1999) and Zhu and Zhong (1999).

3.3.1 Inverted shockwave

The shockwave model used is based on Church (1989). Church proposed to model a typical lithotripter shock wave by considering its time history $P^*(t)$ to be

$$P^*(t) = 2P^+ e^{-\alpha t}\cos(2\pi f t + \pi/3), \qquad (3.14)$$

where P^+ is the peak pressure, α is the decay constant (taken to be 1.15x10^6), and f is the frequency which is determined by the negative pulse duration of the shockwave. In the simulation, the time varying pressure $P^*(t)$ from eqn. (3.14) is incorporated into the reference pressure term p_{ref} of the unsteady Bernoulli's equation such that $p_{ref}(z, t) = P^*(t)$. The velocity of the shockwave is then taken to be negative. This converts a normal lithotripter shockwave into an inverted lithotripter shock. An additional distance factor is added to eqn. (3.10) to ensure that the absolute time is set to $t = 0$ when the pressure starts to decrease smoothly, and such that the waveform crosses zero pressure at about $t = 7$ μs before the arrival of the positive peak pressure.

The pressure profiles of the three waveforms used in this study are presented in Fig. 3.16. The shockwaves used have different peak positive pressures, P^+. The strongest of them, Inverted Lithotripsy Shockwave 1 (ILSW1), has $P^+ = 39$ MPa. This value is taken because it is a common pressure strength generated by a clinical lithotripter as discussed in section 3.2.1. The peak negative pressure, P^-, of this shock has a value of -4 MPa. To study the effect of varying the shock strength in terms of its peak positive and negative pressures on a bubble, two other shockwaves of lower strength as shown in Fig. 3.16 are used. These waves have a P^+ of 17 and 5 MPa, with the corresponding P^- of -1.7 and -0.5 MPa, respectively. For the ease of discussion, they are denoted as ILSW2 and ILSW3.

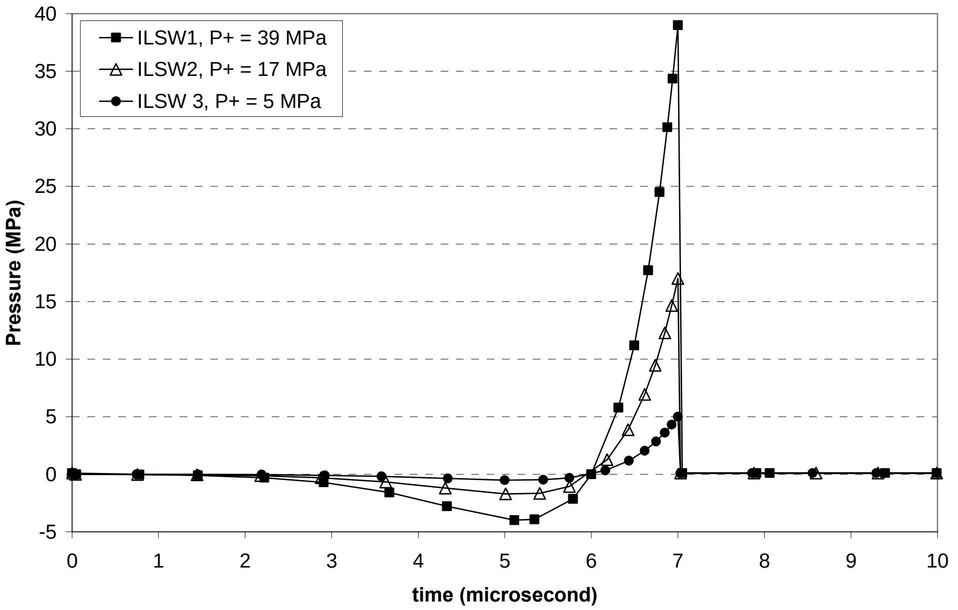

Fig. 3.16 Pressure profile of the three inverted shockwaves used in simulations. They are generated based on the theoretical lithotripsy shockwave formulation from Church (1989). The inverted shocks have peak positive pressures, P^+, of 39, 17, and 5 MPa as indicated in the legends; the corresponding peak negative pressures (P^-) are -4, -1.7, and -0.5 MPa. In the discussion, these waves are termed ILSW1, ILWS2 and ILSW3 respectively.

3.3.2 Interaction of an inverted shockwaves of 39 MPa (ILSW1) with stationary bubbles

Stationary bubbles of initial sizes, R_0, of 1, 10 and 100 μm are simulated to interact with the three waveforms presented in Fig. 3.16. The equivalent radius, R, (calculated from bubble volume, V, such that, $V = \frac{4}{3}\pi R^3$) is plotted against time for all three bubbles interacting with ILSW1 (P^+ = 39 MPa, P^- = -4 MPa). It is noted that the initial tensile component of ILSW1 creates a region of low pressure in the fluid surrounding the bubbles and thus causes the bubbles to expand. All three bubbles of different initial sizes expand to their maximum sizes after about 6.7 μs (Fig. 3.17). At this point in time, they have already experienced part of the compressive component of the shockwave which stops their expansion. As seen in Fig. 3.16, the compressive wave lasts a very short duration of only about 1 μs. Soon after it passes, the bubbles collapse. The forced collapse of the bubble caused by a varying pressure such as ILSW1, is now compared with that of a Rayleigh collapse driven by a constant overpressure. The Rayleigh collapse time (Rayleigh, 1917), t_c, is given to be:

$$t_c = 0.91 \cdot R_{\max} \sqrt{\frac{\rho}{P_s^*}}\,, \tag{3.14}$$

where P_s^* is the effective positive pressure experienced by the bubbles. An estimation of this constant overpressure, P_s^*, is done with the following equation:

$$P_s^* = \frac{t_+}{t_c} \cdot P_{avg} + (1 - \frac{t_+}{t_c}) \cdot p_{ref}\,, \tag{3.15}$$

where P_{avg} is the average pressure of the positive part of the pressure wave, and $\frac{t_+}{t_c}$ denotes the proportion of pressure contribution from the compressive wave (see t_+ in Fig. 3.17). Then

eqn. (3.14) gives the time duration of the positive component

$$t_+ = \frac{1}{12 \cdot f}\,. \tag{3.16}$$

Since it is set in the simulation that f = 83.3 kHz, t_+ is equal to 1.0004 μs. Then with eqn. (3.18), the value of P_{avg} can be obtained using the P^+ for ILSW1. Similar calculation is done for ILSW2, ILSW3, and ILSW4 for data in Fig. 3.20.

$$P_{avg} = \frac{1}{t_+} \int_0^{t_+} 2P^+ e^{-\alpha t} \cos(2\pi f t + \pi/3) \;\; dt\,. \tag{3.17}$$

The collapse time is then obtained by successive iteration of eqns. (3.15) and (3.16).

Thus the calculated collapse time, t_c, for the 1, 10 and 100 μm initial radii bubble is 1.40, 1.50 and 2.50 μs respectively. From the simulation, the collapse time (from the bubble's maximum size to the time of jet impact) is slightly shorter. For the 1, 10, and 100 μm bubble, it is 1.25, 1.35 and 2.45 μs. The difference can be attributed to the overestimation of the effective pressure P_s^*. This is due to the assumption that the bubbles experience the full extent of the compressive wave in its collapse phase. However, it is seen in Fig. 3.17 that the bubbles start to collapse only shortly after the pressure has started to rise from zero. The average compressive pressure, P_{avg}, is calculated from eqn. (3.18) with t_+ taken from the moment that the pressure becomes zero from negative. Therefore a lower P_{avg} would be obtained if t_+ is taken from the moment the bubbles start their collapse phases.

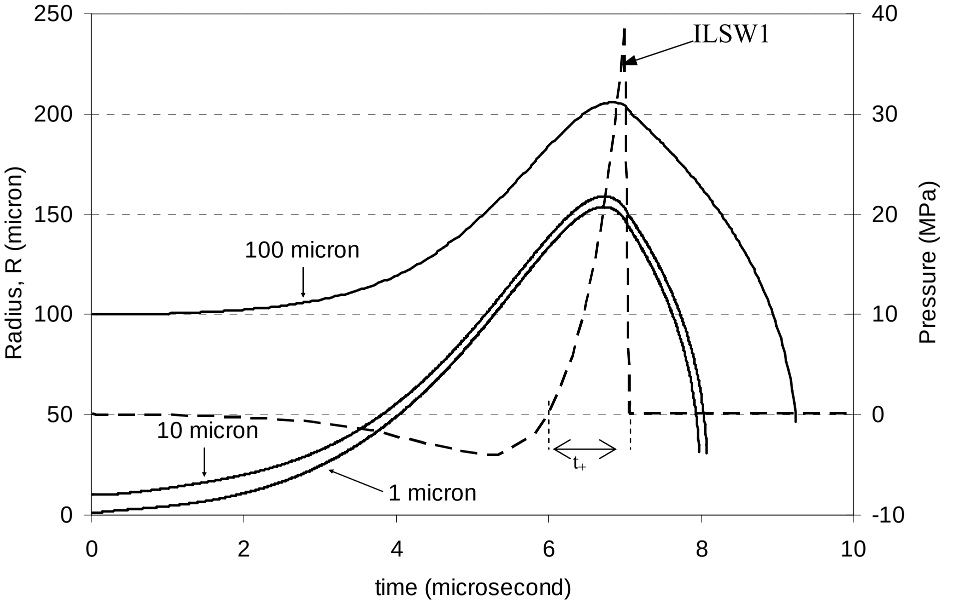

Fig. 3.17 Equivalent radius, R, versus time for bubbles of 1, 10, and 100 μm (initial bubble radii) interacting with an inverted shockwave (ILSW1) of 39 MPa peak positive pressure (P^+), and -4 MPa peak negative pressure (P^-). All bubbles expand to large sizes that are multiples of their initial sizes, and experience inertial collapse after their expansions are stopped by the compressive component of ILSW1.

The bubble shape changes in the collapse phase for the same set of simulations are shown in Fig. 3.18. All bubbles grow to a very large maximum size (the dashed line plots in Fig. 3.18) after about 6.7 μs from the instant when the shockwaves hit them. The 1 and 10 μm initial radii bubbles expand to 154 and 159 μm in radii respectively. The large bubble of 100 μm, on the other hand, reaches a maximum size of 206 μm. They then collapse with translational movement of the bubble center about

50 μm from its initial position in the direction of the traveling shockwave. This is due to the fact that the upper surfaces of the bubbles move downwards in a much slower manner than the bottom surfaces which accelerate upwards. The final bubble for all three cases obtains a peculiar shape whereby the bottom sides of the bubbles seem to move faster than the center (Fig 3.19). This might cause the bubbles to break up. Nevertheless, the bottom surfaces of these bubbles still move with a high speed (about 1000 m/s for the 1 and 10 μm bubble; and about 500 m/s for the 100 μm bubble) which might eventually develop into high speed jets.

In the following sections, the results of the interaction of the all three shockwaves (ILSW1, ILSW2, and ILSW3) with the bubbles of different initial sizes will be discussed. Their collapse time, maximum radius (R_{max}) obtained, jet velocity, and Kelvin impulse after interacting with the inverted shocks will be studied.

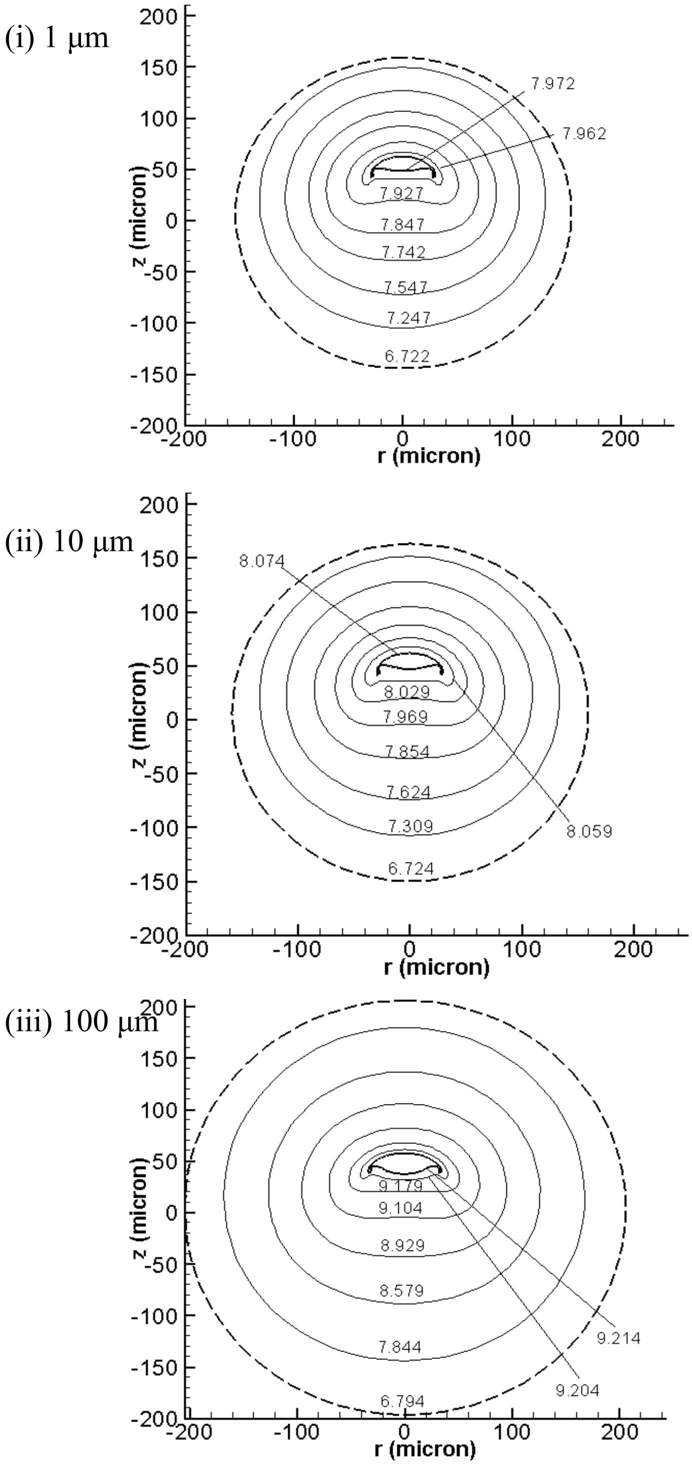

Fig. 3.18 Shape profiles of the bubbles of different initial sizes, R_0, equal to 1, 10, and 100 μm interacting with ILSW1 (Peak positive pressure, P^+ = 39 MPa). Also on each profile, the corresponding time in μs is noted. It is observed that all three bubbles expand to a large maximum radius, R_{max} of over 150 μm at about 6.7 μs and then collapse to a flattened bubble.

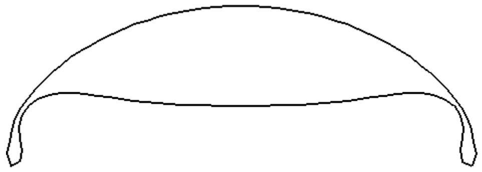

Fig. 3.19 The final collapsing shape of the 1 μm bubble as shown in Fig. 3.18. The bottom surface moves with high speed towards the upper surface (about 1000 m/s for this 1 μm bubble. Larger bubbles of radii 10 and 100 μm, collapse with jet speed of about 1000 and 500 m/s, repectively).

3.3.3 Maximum radius R_{max} and collapse time

The maximum radii, R_{max}, obtained by the bubbles as a result of their interactions with the tensile wave are documented in Fig. 3.20. Also besides each data point for a certain bubble size and amplitude P_s^*, the collapse time from simulation, and the Rayleigh collapse time, t_c (see eqn. (3.15) to (3.19)) are shown. It is noticed that the tensile component of the shockwaves causes the bubbles to expand from its initial size to a much larger R_{max}. This is especially true for small bubbles of 1 and 10 μm whereby even a weak P^- = -0.5 MPa from ILSW3 can cause them to expand to over 50 μm ($R_{max,1\mu m}$ = 56 μm, $R_{max,\ 10\mu m}$ = 65 μm). This is 56 and 65 times their original radii respectively. In this case, the large bubble of 100 μm also expands to a 133 μm maximum radius. But this is only 1.3 times its original size. For a stronger inverted shock like ILSW2 with P^- = -1.7 MPa, the bubbles expand even more than that when they interact with ILSW1. Both 1 and 10 μm bubbles grow to maximum radii of 101 and 108 μm, respectively. The 100 μm bubble reaches a maximum size of 163 μm in radius. When the strength of the negative part of the shockwaves continues to increase to ILSW1, the bubbles expand well above 150 μm as discussed in detail in the previous section. The 100 μm bubble even expands to over 200 μm in radius.

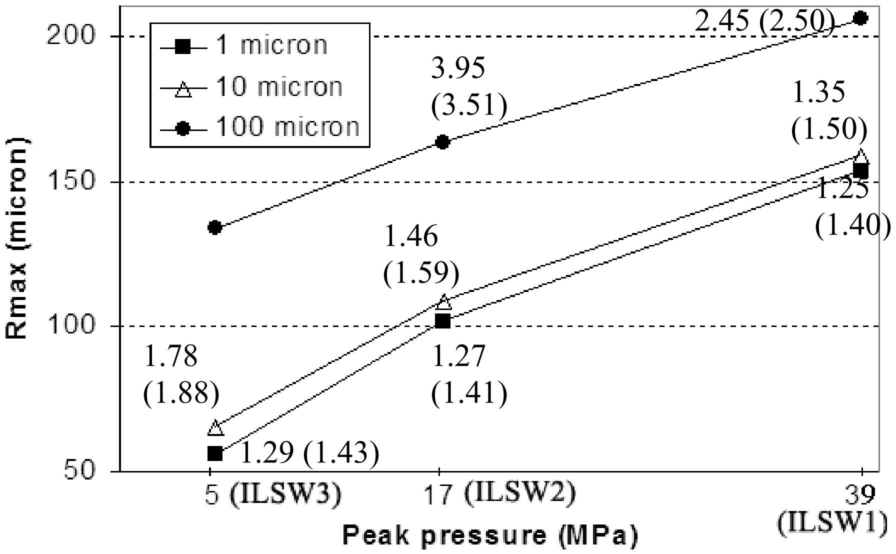

Fig. 3.20 Maximum radius R_{max} for the various initial size bubbles (1, 10, and 100 μm) interacting with inverted shockwaves of three different strengths (ILSW1, ILSW2, ILSW3). Also indicated next to the data points are the simulated collapse time and (estimated Rayleigh collapse time, t_c). It is noted that the 100 μm bubble does not collapse immediately after interacting with ILSW3. It rebounds from its minimum and continues to oscillate (see Fig. 3.21).

After the passing of the tensile component, the compressive part of the shockwaves will stop the expansion of the bubbles and cause them to collapse as also mentioned in the previous section for the particular cases involving ILSW1. Since the collapse time, t_c is proportional to R_{max}, t_c is higher for a bubble with a larger initial radius. For instance, it is calculated that it takes 3.51 μs for the 100 μm initial radius bubble to collapse under ILSW2, but for the 1 and 10 μm bubbles, they take 1.59 and 1.41 μs, respectively. The simulated results show a collapse time slightly different in magnitude but similar in trend. The 100 μm bubble takes 3.95 μs to collapse, whereas the 1 and 10 μm bubbles require only 1.27 and 1.46 μs, respectively. The discrepancies lie on the underestimation of the effective positive pressure P^*_s as experienced by the bubbles as discussed in Section 3.3.2.

In summary, it is found that the shockwave limits the duration of bubble expansion to that of the tensile wave. Although small bubbles can expand to approximately 150 times that of their initial radius, large bubbles reach comparable sizes too. In the next section, the focus is turned to the collapse and the jetting thereafter.

3.3.4 Jet velocity and Kelvin impulse

When considering the degree of destruction caused by cavitation activities, it is important to assess the jet velocity and probably also the Kelvin impulse at the moment of jet impact.

Fig. 3.22(a) shows the maximum jet velocity of the bottom node of the bubbles of various initial sizes (1, 10, and 100 μm) interacting with ILSW1, ILSW2, and ILSW3. There is no data available for the 100 μm bubble interacting with ILSW3 because it does not collapse initially but rather rebounds from its minimum size and oscillates for several periods (Fig. 3.21). In the subsequent periods, the 100 μm bubble attains a peculiar shape as shown in Fig. 3.21(a) and (b) for its third and fourth periods respectively. For the small bubbles of 1 and 10 μm, very high speed jet velocities are recorded. For interaction with ILSW1 (peak pressure P^+ = 39 MPa), ILSW2 (P^+ = 17 MPa) and ILSW3 (P^+ = 5 MPa), a 1 μm initial radius bubble reaches a maximum jet velocity of 1100, 1400 and 1200 m/s respectively. Similarly high velocities are obtained for the 10 μm bubble (960 m/s for ILSW1 and ILSW3, and 1300 m/s for ILSW2). For the large bubble of initial size 100 μm, when it collapses under ILSW1 and ILSW2, it obtains a maximum jet velocity of 520 and 590 m/s respectively.

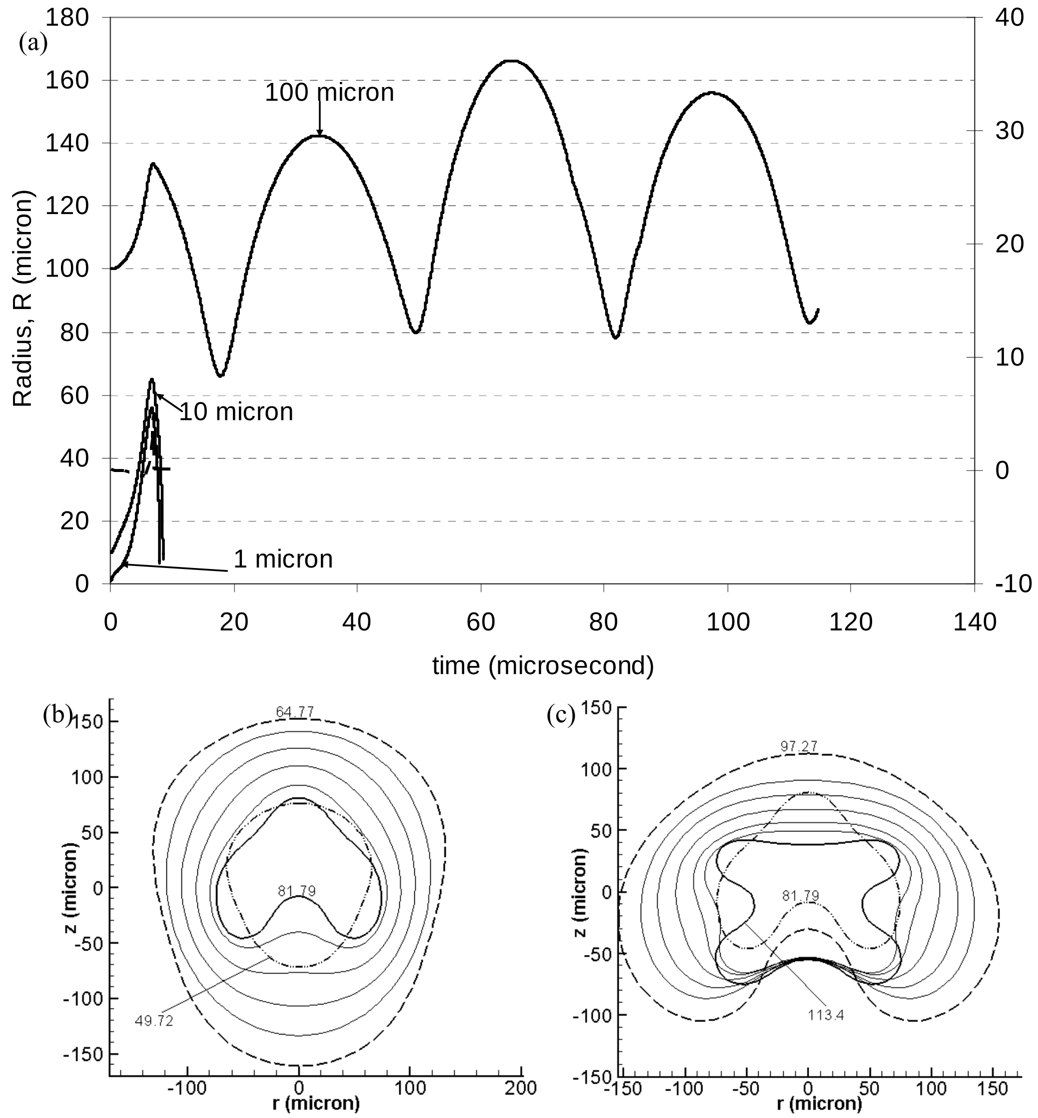

Fig. 3.21 (a) Equivalent radius, *R*, versus time for bubbles of 1, 10, and 100 μm (initial bubble radii) interacting with an inverted shockwave (ILSW3) of 5 MPa peak positive pressure (P^+), and -0.5 MPa peak negative pressure (P^-). All bubbles expand to large sizes that are multiples of their initial sizes. The 100 μm bubble does not collapse but oscillates with a peculiar shape (see Fig. 3.21(b) for period three and (c) for period four after the passing of the shockwave.

It is noticed that when the bubbles are hit by ILSW2, they reach higher maximum jet velocities than when they are interacting with the stronger shockwave of ILSW1. This may be explained by considering the Kelvin impulse, *K*, as shown in Fig. 3.22(b). It is noticed that all the bubbles of different sizes seem to obtain rather similar Kelvin impulse values for their interaction with a particular inverted shock. When hit by ILSW3, all bubbles have *K*'s close to $3\text{x}10^{-10}$ kg m/s at the moment just before jet impact. Interacting with ILSW2 and ILSW1, they have *K*'s of about

60x10^{-10} and 450x10^{-10} kg m/s respectively. Since a higher value of K means a higher jet speed or a broader jet (Klaseboer et al, 2007), in this case, when the shockwave peak pressure increases from 5 to 17 MPa, the increase in *K*'s coincide with the increase in maximum jet velocities recorded for the 1 and 10 μm bubbles. However, as the shockwave's positive peak pressure P^+ increases to 39 MPa, the maximum jet velocities obtained for all bubbles decrease. Broadening of jets is observed. For instance, both 1 and 10 μm bubbles have a jet radius of 12 μm at the moment of collapse when they interact with ILSW2, but the jet radius increases to 27 μm for both cases when the bubbles are hit by ILSW1.

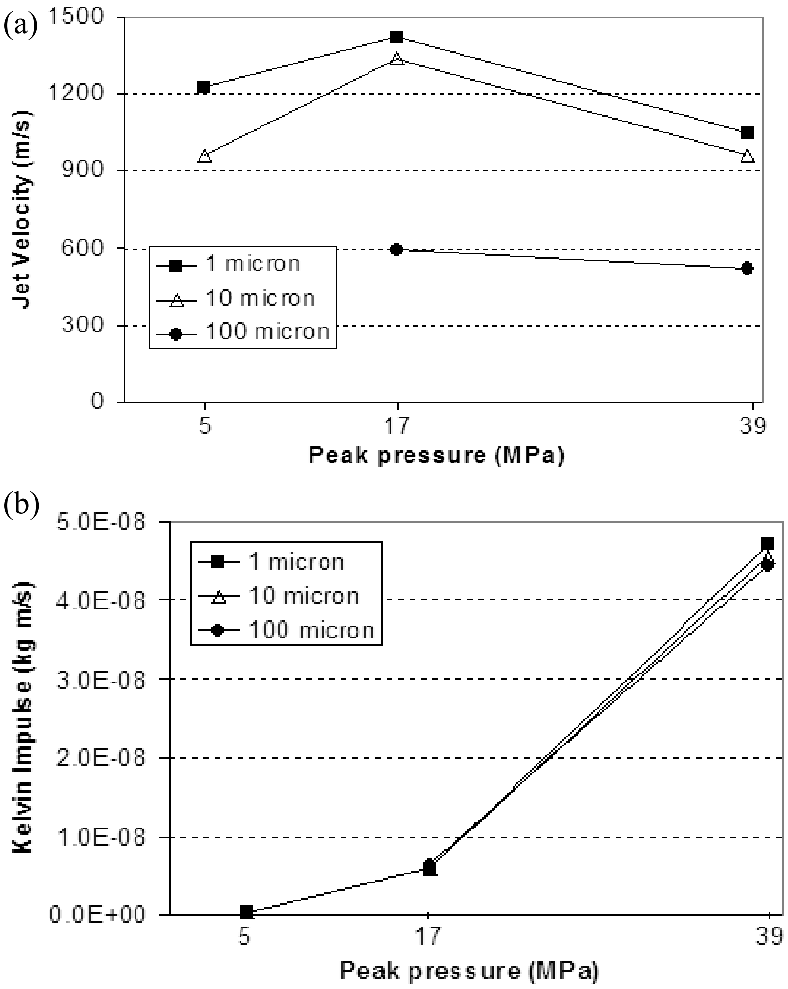

Fig. 3.22 (a) The maximum jet velocity from the bottom node as the bubbles collapse under the compressive component of different magnitudes. (b) The Kelvin impulse recorded at the moment just before jet impact for the similar set of bubbles and shockwaves.

3.3.5 Discussion and conclusion

The inverted shockwaves presented in Section 3.3 have the same acoustic energy as their counterparts of same pressure amplitude and pulse duration as produced by the standard lithotripter. The standard lithotripsy pulse, like the one measured by Sankin et al (2005) in Fig. 3.5, has a sharp-rising, high pressure amplitude compressive component which is followed by a much lower in amplitude, negative pressure wave. When the positive pressure hits the existing bubbles (either stationary or oscillating) in the fluid, they will collapse from their initial size violently with a high speed jet as discussed in Section 3.1 and 3.2. Although not examined in this thesis, it is shown in numerous studies (Bailey et al (1999), Zhu and Zhong (1999), Zhong et al (2001)) that the ensuing negative tensile wave will cause these collapsed bubbles to rebound. The growth and collapse cycle is then driven by the inertia of the surrounding fluid and lasts far longer (usually a few hundreds microseconds) than the lithotripter pulse. Thus the rebounded bubble(s) can grow to a large size before the pressure difference across the gas/water interface forces the bubble(s) to collapse. This often leads to severe collateral damages in the surrounding tissues. However, if the shockwave shape is inverted, i.e. the negative tensile wave comes before the positive compressive wave, the bubble will expand to a large size initially but the expansion will be stopped by the compressive component and the bubble will collapse. There is no ensuring negative pressure to trigger the rebound of bubbles and thus less collateral damage is made possible.

This form of inverted lithotripsy shockwaves is studied in Section 3.3. Three inverted shocks with different peak positive (P^+) and peak negative pressures (P^-), namely 39 and -4 MPa (ILSW1), 17 and -1.7 MPa (ILSW2), 5 and -0.5 MPa (ILSW3), are simulated to interact with bubbles of initial radii 1, 10, and 100 μm. It is found that the tensile component causes the small bubbles to expand to large sizes between 50 to 200 μm in radius. However, further expansion is suppressed, and the bubbles are forced to collapse. All bubbles collapse in a few microseconds after the interaction with the high positive compressive waves, except for the case of the 100 μm bubble interacting with the weak shock of ILSW3. In this exception, the large bubble does not collapse with a high speed jet but rather rebounds from its minimum volume and continues to oscillate for several periods.

It is noteworthy that although further expansion of bubbles after the passing of the inverted shockwaves is suppressed (at least for all small bubbles between 1 and 10 μm in radius), one must not ignore the initial large expansion and the subsequently violent forced collapse. These small bubbles expand to several tens and hundreds times of their initial radius before being stopped by the compressive wave. Also when they collapse, they form flat broad jets as shown in Fig. 3.19. The jet velocities obtained are still relatively high (compared to its standard lithotripsy shockwave counterparts of equal amplitude and pulse duration). Together with the large jets, these bubbles may still be capable of causing damage to the kidney stones. It is therefore concluded that the inverted lithotripter shockwave is potentially useful for kidney stone fragmentation with the advantage of minimizing collateral damages to the nearby tissue.

Chapter 4

Ultrasonic bubbles near biomaterials

This section details the numerical study of the interaction of a stationary bubble with a nearby biomaterial in an ultrasound field. These biomaterials are involved in various medical treatments using ultrasound as mentioned in Section 1.3. But due to the high frequencies and small spatial scale, it is difficult to observe the complex interaction between the ultrasonic bubble and the biomaterials. Therefore numerical simulations are performed. A range of frequencies is used to study the bubble behavior in terms of its growth and collapse shapes, and the maximum jet velocity obtained.

4.1 Modeling biomaterials and the acoustic bubble

A BEM model of two fluids is used in the simulation whereby one of the fluids has some elasticity and is used to represent the various biomaterials. The other fluid in which the bubble is located is assumed to be a Newtonian fluid, and in all the simulations presented in this chapter, it is taken to be water. Details about the model are described in Section 2.1.5, and its relating non-dimensionalization and other parameters used in the program is detailed in Section 2.2. The two important parameters used to model the biomaterials are κ^* and α. The parameter κ^* is related to the Young's modulus, E, and the Poisson ratio, υ, of the biomaterials by eqn. (2.27) in Chapter 2; whereas α denoted the density ratio of the two fluids in the model as depicted in eqn. (2.28) in Chapter 2.

The mechanical properties of the biomaterials modeled (as presented in Table 4.1) are obtained from various studies[*]. It is noted that the quantification of the Young's moduli of biomaterials is highly challenging, and the numbers reported in the literature often vary greatly, depending upon measurement method, rate of excitation, applied strain and sample size. But the trend reported is consistent (for example, fat tissue has a Young's modulus much lower than that of cartilage). Furthermore, the composite nature of the materials and the variety of measurement techniques used render the values obtained at best averages. Nevertheless, since the purpose of this study is to provide insights to acoustic bubble biomaterial interaction, a sufficiently representative value is acceptable. From the density, Young's Modulus, and Poisson ratio values of the biomaterials listed in Table 4.1, the input parameters for our program, κ^* and α, are calculated using eqn. (2.27) and eqn. (2.28). It is noted that α is close to 1 ($\alpha \approx 1$) for all of the cases simulated except for the case of the bone. However, κ^* changes significantly for the different materials.

---

[*] Fat's Young's modulus (YM) and Poisson ratio (PR) are from Nightingale et al (2003), and its density is from Martin et al (1994). Skin's YM and PR are from Zheng et al (1999), and its density from Lask et al. (1997). Cornea's YM, PR, and density are from Power et al (2001). Brain's parameters are from Trosseille et al (1992). Muscle's YM and PR are from Duck (1990), and its density is from Payne et al (2005). Cartilage's YM and PR are from Patil et al (1996), and its density is from Shapiro et al (2001). Bone's parameters are from Duarte (1983).

Table 4.1. Mechanical properties of the biomaterials used in the simulations. The values are obtained from references (Duarte (1983), Nightingale et al (2003), Martin et al (1994), Zheng et al (1999), Lask et al (1997), Power et al (2001), Patil et al (1996), Shapiro et al (2001), Trosseille et al (1992), Payne et al (2005), Duck (1990)). It is noted that the high Young's Modulus of the bone causes numerical difficulties in our simulation. Since bone is considered a hard material, we have replaced the parameters with that of a solid wall.

No	Material	Density (kg/m^3)	Young's Modulus (kPa)	Poisson ratio	α	κ^*
1	Adipose tissue (fat)	950	5.6	0.45	1.05	0.037
2	Skin	1100	22.6	0.45	0.909	0.1288
3	Cornea	1400	47	0.49	0.714	0.2209
4	Brain	1000	240	0.495	1.0	1.589
5	Muscle (across fibers)	1060	790	0.45	0.943	4.673
6	Cartilage (coastal)	1300	5000	0.4	0.769	22.89
7	Bone	2000	14000000	0.43	0.001	100.0

The stationary gas bubble is placed in the Newtonian fluid (Fluid 1 in Fig. 2.1 in Chapter 2). Its distance from the biomaterials, H, (refer to Fig. 2.4) is set to be $H = 1.5 * R_0$ (in non-dimensionalized terms, $H' = H / R_0 = 1.5$). The value 1.5 is used for all the simulations done in this chapter. It is chosen so that the bubble is not too far from the biomaterial (in order that the influence of the boundary on the bubble is still reasonably significant), and the bubble is not too near the biomaterial so as to allow room for the translational movement of the bubble (a bubble which has moved too close to the boundary can lead to numerical instability in the simulation). The bubble is stationary at $t' = 0$ when the sound field is applied. The initial radius of the bubble is taken to be $R_0' = 1$. The interface of the biomaterial is assumed to be flat and at rest initially. The material is assumed to extend to infinity. The fluid in which the bubble resides (water) is assumed to extend to minus infinity. The dimensionless amplitude of the wave, A, is chosen to be 0.8 for all the simulations as also used in Sato et al

(1994). The frequencies that are used, f / f_0, range from 0.25 to 2.0. The discussion here will focus on bubbles that are driven below, at, and above their resonance frequencies, i.e. $f / f_0 = 0.5$, 1.0 and 1.5.

4.2 Influence of frequency

The profiles of the bubble evolution and biomaterial boundary behavior are investigated and discussed in detail in this section for a selection of the materials mentioned in Table 4.1. High sensitivity of the bubble behavior to the different types of biomaterials is observed. The bubble will oscillate, and in some occasions, it will form a jet or split into two smaller bubbles. The corresponding reaction of the biomaterials varies too; in some cases, it hardly moves (for example cartilage and bone). In certain cases, it is 'attracted' towards the bubble (although close proximity of the bubble and the material prevents the simulation from proceeding after a while). The result in the last case is observed to bear some similarities to the development of jet-like ejection of the material into the fluid as reported in Brujan et al (2001a, and 2001b). Incidentally, the above-mentioned experiments of Brujan et al (2001a, and 2001b) were performed with non-equilibrium bubbles and not with ultrasound; a successful comparison of those experiments with a numerical model based on the same theory as described here was given in Klaseboer and Khoo (2004b). For a more direct comparison of the present work involving ultrasound on the bubble with the experiments on a non-equilibrium bubble, more assumptions and relations will have to be established, which is beyond the scope of the present work. It is noted that the radius R' mentioned in the figures is the dimensionless equivalent radius which is calculated from the dimensionless volume, V', of the bubble, $R' = \sqrt[3]{V'(3/4\pi)}$.

4.2.1 Sound field frequency, $f / f_0 = 1.0$

The first case, labeled as Case 1 (Fig. 4.1), depicts the profiles of a bubble near an adipose tissue (or fat, $\kappa^* = 0.037$) at different instances (Fig. 4.1(a)), together with its equivalent radius R' versus time graph which quantities the bubble profiles with time (Fig. 4.1(b)). The three dimensional structure of the bubble corresponds to the final profile (Fig. 4.1(c)) just before jet impact. In the first period of oscillation, the bubble expands (from $t' = 0.000$ to $t' = 1.937$) pushing back the fat tissue and then contracts almost spherically (from $t' = 1.951$ to $t' = 3.013$) to a very small size ($R' \approx 0.45$) and the fat boundary is ‘attracted’ towards the bubble. In the second period, it expands from its minimum size (‘P1’ in Fig. 4.1(a) and (b)) until it reaches its maximum size as shown with the dashed-lined profile (‘P2’) which is larger than its maximum size in the first oscillation. The boundary is pushed back. After that, the bubble enters its second collapse phase. Its profile at the end of the second oscillation period is drawn with a solid line (‘P3’) with the corresponding point of the radius (R') versus time plot. The jet formed is directed away from the interface as shown in Fig. 4.1(a) ($t' = 6.707$, solid line). Similar jet formation is often observed in a cavitation bubble collapse near a free surface or gas-water interface with a consequential water plume into the gaseous medium (Wang et al, 1996a). However, instead of the hump formed on the fluid interface as a counter reaction to the jet formation within the bubble (like for the free surface), the adipose tissue seems to be ‘attracted’ towards the bubble because of its elastic nature.

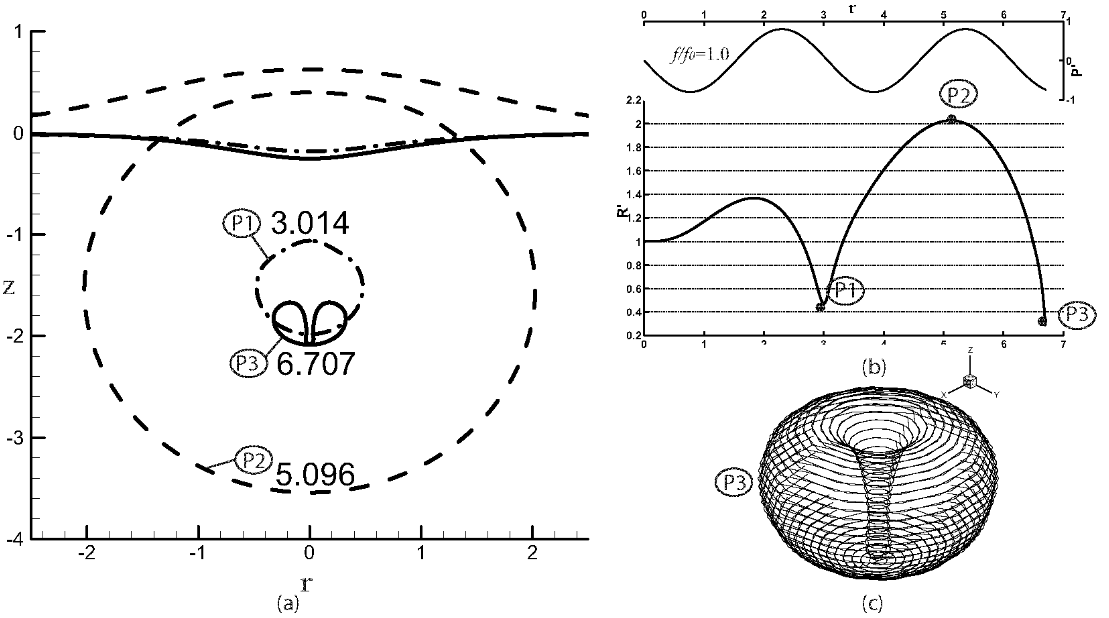

Fig. 4.1 Case 1: A bubble near a fat tissue boundary (κ*= 0.037) in a sound field ($f\,/\,f_0$= 1.0). (a) The dimensionless t' is as indicated near each history profiles. (b) The corresponding profiles (‘P1’, ‘P2’ and ‘P3’) are indicated on the R' vs t' graph. The pressure oscillation of the sound wave is indicated on the top (p' vs t' graph). (c) The 3D visualization of the bubble is based on the solid line profile (‘P3’) at t' =6.707.

For Case 2 involving skin (Fig. 4.2), however, the jet formed is directed towards the interface as is often observed for the cavitation bubble near a rigid boundary (Blake and Gibson, 1987) or a bubble collapsing in an ultrasound field near a solid wall (Sato et al, 1994). From t' = 0.000 to t' = 1.909, the bubble expands spherically. It collapses (t' = 2.082 to t' = 3.016) with slight elongation on the part of the bubble which is nearest to the skin (‘P1’ in Fig. 4.2(a) and (b)). The skin moves a little towards the bubble. During its second expansion (t' = 3.017 to t' = 5.021), the bubble grows to a much larger size (‘P2’ in Fig. 4.2(a) and (b)) than it ever does during the first period of oscillation pushing back the skin interface. The bubble then contracts (t' = 5.022 to t' = 6.819) and moves towards the skin with the latter advancing towards it as well. Then a jet is formed and it penetrates the (opposite) bubble wall eventually (‘P3’).

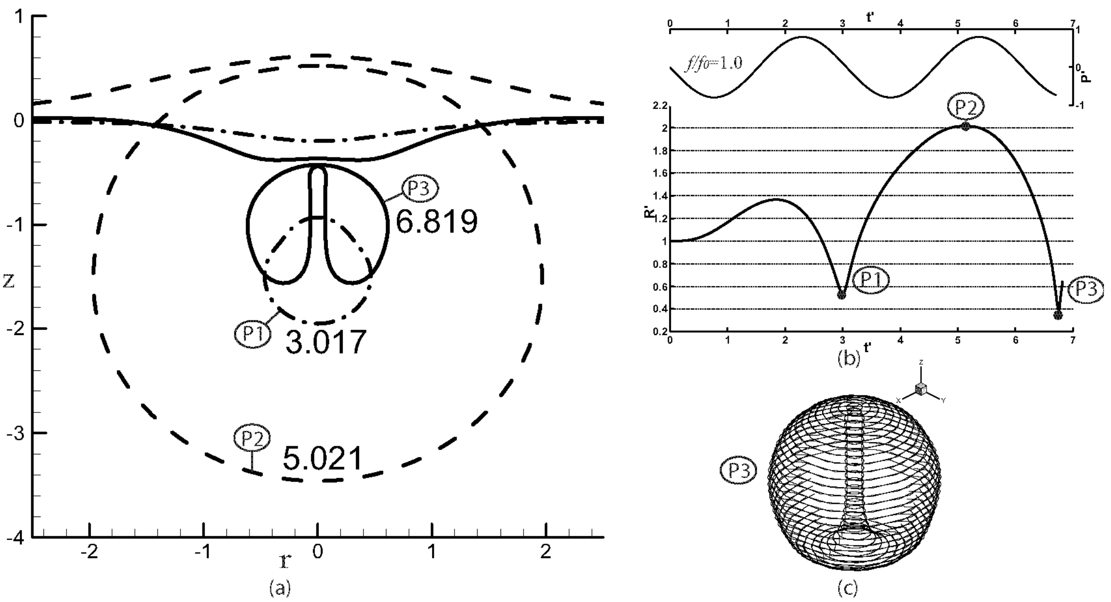

Fig. 4.2 Case 2: A bubble near a skin boundary (κ*= 0.1288) in a sound field ($f\,/\,f_0$= 1.0). (a) The dimensionless t' is as indicated near each history profiles. (b) The corresponding profiles (‘P1’, ‘P2’ and ‘P3’) are also shown on the R' vs t' graph. The pressure oscillation of the sound wave is indicated on the top (p' vs t' graph). (c) The 3D visualization of the bubble is based on the solid line profile (‘P3’) at t' =6.819.

Similarly for Case 3 of a bubble near the cornea (Fig. 4.3), the jet formed is directed towards the cornea. This is probably because both cornea and skin biomaterials are significantly stiffer, i.e. the Young’s moduli for cornea and skin are about 5 and 10 times higher than that of fat, and slightly denser than fat. In its first period of oscillation, the bubble expands (t' = 0.000 to t' = 1.909) and contracts (t'= 1.924 to t' = 3.032) almost spherically. During the bubble’s second period (t' = 3.033 to t' = 5.101), it moves slightly towards the interface (‘P1’ in Fig. 4.3(a) and (b)), and expands to a large volume (‘P2’). The cornea boundary is ‘attracted’ towards the bubble initially before being pushed back when the bubble expands to its maximum size. Then the bubble collapses from t' = 5.102 to t' = 6.835 with a dimensionally thicker jet towards the cornea (‘P3’). The cornea bulges towards the collapsing bubble considerably.

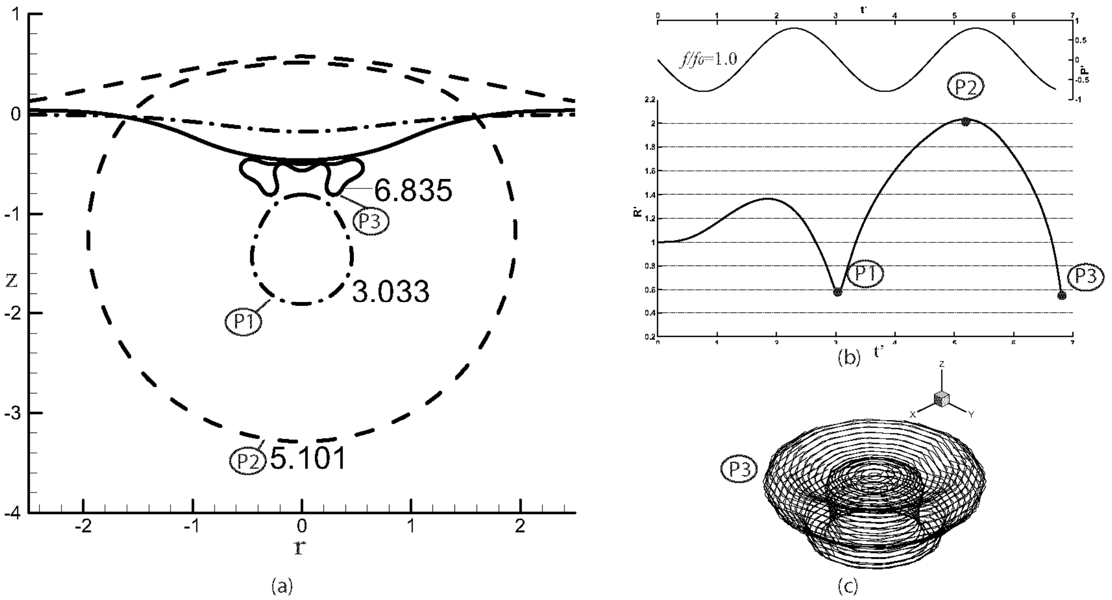

Fig. 4.3 Case 3: A bubble near a cornea boundary (κ*= 0.2209) in a sound field ($f\,/\,f_0$= 1.0). (a) The dimensionless t' is as indicated near each history profiles. (b) The corresponding profiles ('P1', 'P2' and 'P3') are depicted on the R' vs t' graph. The pressure oscillation of the sound wave is indicated on the top (p' vs t' graph). (c) The 3D visualization of the bubble is based on the solid line profile ('P3') at t' =6.835.

When a bubble oscillates near a brain-like tissue boundary (Case 4), it behaves very differently from all the previous cases investigated. This could be related to the density of the brain tissue which is the same as that of water (Fluid 1). In the first oscillation period, it expands (t' = 0.000 to t' = 1.767) spherically, and then collapses from t' = 1.782 to t' = 3.043 with 'pinches' observed on the side of the bubble ('P1' in Fig. 4.4(a) and (b)). The brain interface moves towards the bubble during this period. In its second period of expansion, it grows to a large size (R' > 2 at 'P2' in Fig. 4.4(b)). The boundary is pushed back only marginally as compared to the previously mentioned cases because brain tissue is stiffer (κ* = 1.589) than that of fat, skin, and cornea (κ* = 0.037, 0.1288, and 0.2209, respectively). After that, the bubble collapses and breaks into two with the top bubble being much larger than the bottom one ('P3') in Fig. 4.4(a). Note that the stand-alone data of 'P3' in Fig. 4.4(b) pertains only to the top bubble. In spite of its stiffness, the brain boundary bulges towards the bubble very significantly, even more severe than that in the previous fat, skin and cornea cases. No jet is observed for the first two periods of oscillation.

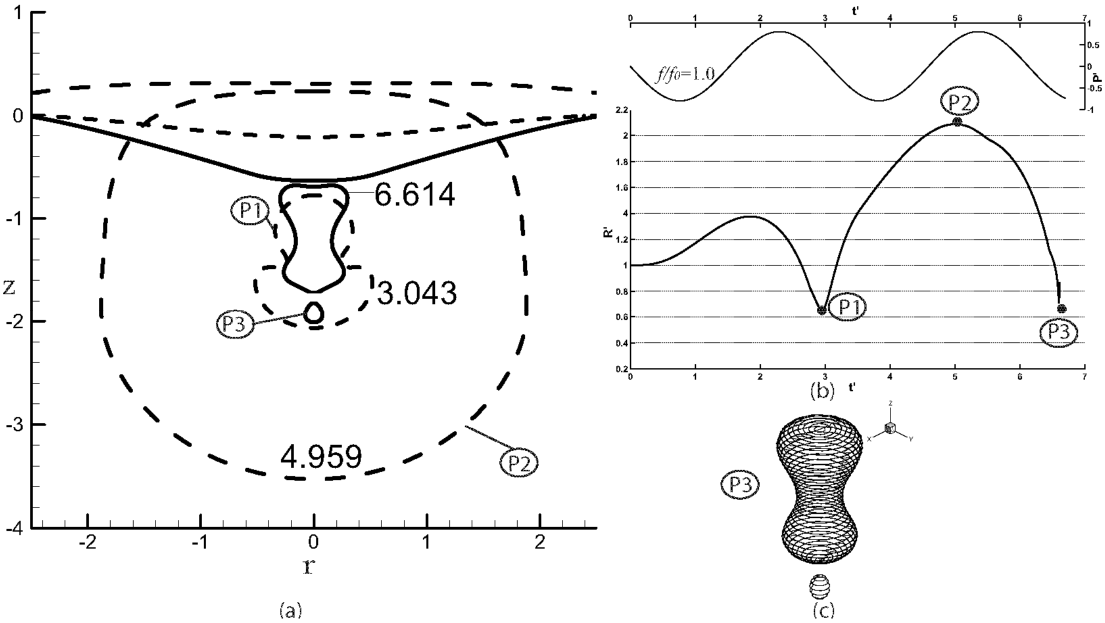

(a) (c)

Fig. 4.4 Case 4: A bubble near a brain-like tissue boundary (κ*= 1.589) in a sound field (f/f_0 = 1.0). (a) The dimensionless t' is as indicated near each history profiles. (b) The corresponding profiles (‘P1’, ‘P2’ and ‘P3’) are shown on the R' vs t' graph. The R' at the square ‘P3’ is calculated only with the volume of the top large bubble. The pressure oscillation of the sound wave is indicated on the top (p' vs t' graph). (c) The 3D visualization of the bubble is based on the solid line profile (‘P3’) at t' =6.614.

For the case involving the muscle tissues (Case 5 in Fig. 4.5), after expanding almost spherically, the bubble starts to pinch at the side towards the end of its first period (‘P1’ in Fig. 4.5(a) and (b)). After that, the bubble moves towards the interface and eventually gets very close to the muscle boundary in its second expansion phase from t' = 2.965 to t' = 4.817, and thereby pushing back the boundary as it expands. Then it splits into two in this (second) expansion phase. (This is very different from Case 4 for the brain boundary where the bubble splitting occurs during the second collapse phase.) Eventually opposite-directed jets are formed at the bottom and top of the upper and lower bubbles, respectively (‘P2’) as depicted in Fig. 4.5(a) and 6(b). (Again in Fig. 4.5(b) depicting R' versus t', the dotted distribution shortly after ‘P1’ pertains to the upper bubble only.)

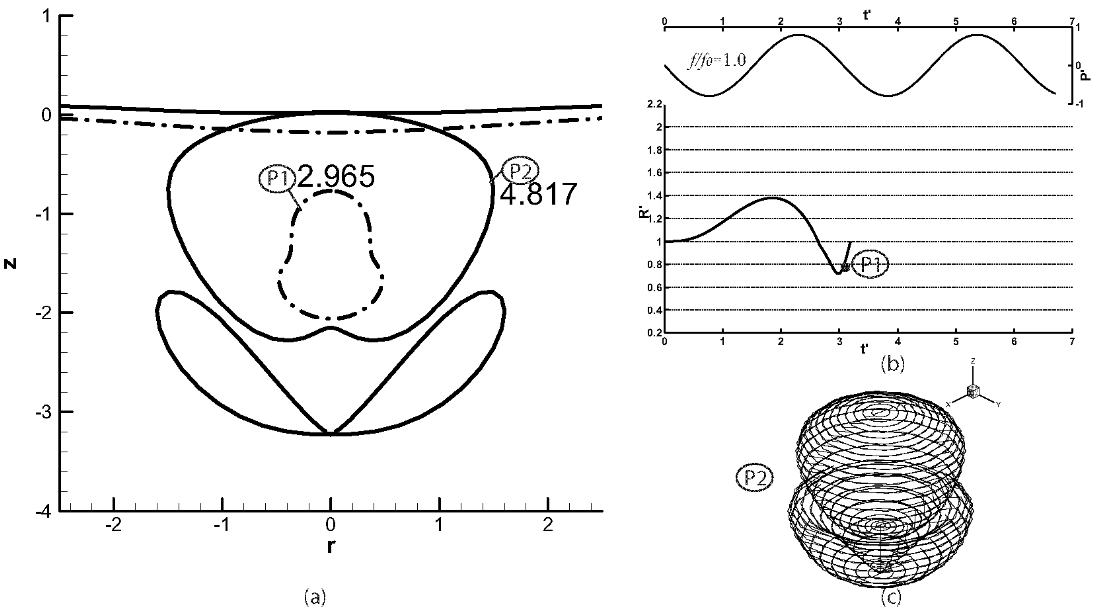

Fig. 4.5 Case 5: A bubble near a muscle boundary (κ*= 4.673) in a sound field ($f\,/\,f_0$= 1.0). (a) The dimensionless t' is as indicated near each history profiles. (b) The profile 'P1' is shown on the R' vs t' graph. The pressure oscillation of the sound wave is indicated on the top (p' vs t' graph). (c) The 3D visualization of the bubble is based on the solid line profile ('P2') at t' =4.817.

The behavior of a bubble near cartilage is presented in Fig. 4.6 (Case 6). Since the biomaterial is relatively much harder or stiffer as compared to the previous cases, it is expected not to move much as the bubble evolves to its maximum size ('P2' in Fig. 4.6(a) and (b)) and thereafter. Then the bubble breaks into two at t' = 3.152, with the top bubble being much larger then the bottom bubble. In its second period of oscillation, two opposite penetrating jets are observed in the top and bottom bubbles directing towards and away from the interface, respectively, and depicted as 'P3' as shown in Fig. 4.6(a). The numerical code is able to handle the event of breaking up of the bubble into two, and their consecutive behaviors. The reader can refer to Klaseboer and Khoo (2004a) for details on the numerics.

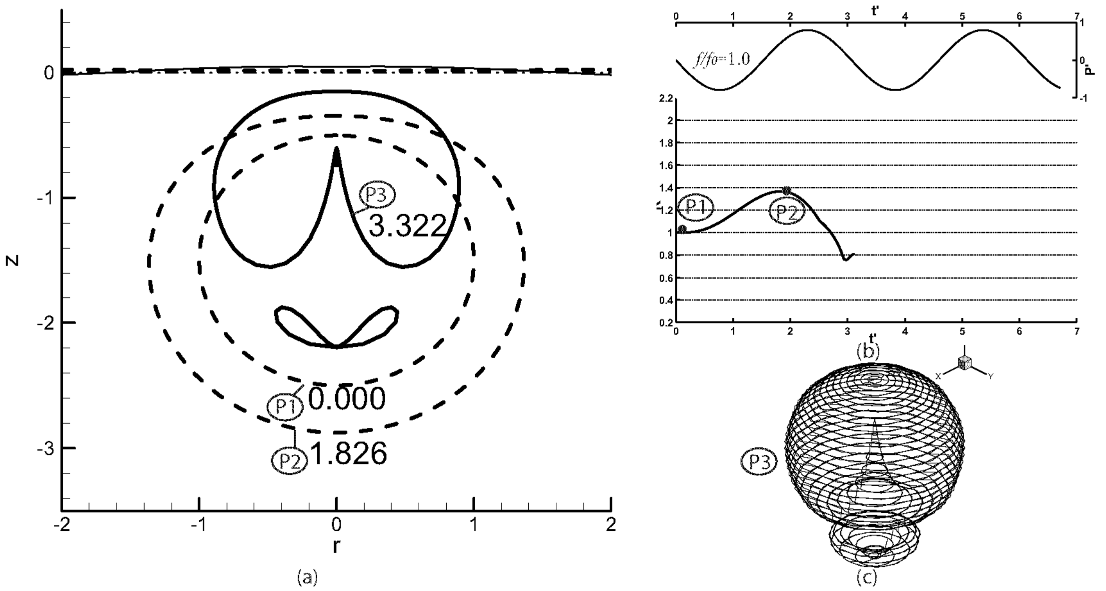

Fig. 4.6 Case 6: A bubble near a cartilage boundary (κ*= 22.89) in a sound field ($f\,/\,f_0$= 1.0). (a) The dimensionless t' is as indicated near each history profiles. (b) The corresponding profiles ('P1' and 'P2') are also shown on the R' vs t' graph. The dashed line curve is drawn with R' calculated from only the volume of the larger bubble which is nearer to the boundary. The pressure oscillation of the sound wave is indicated on the top (p' vs t' graph). (c) The 3D visualization of the bubble is based on the solid line profile ('P3') at t' =3.322.

When a bubble is placed near a solid wall which approximates a bone material (Case 7), it expands spherically from t' =0.000 to t' =1.919 to its maximum size ('P2' in Fig. 4.7(a) and (b)). Then it collapses with a jet that penetrates its opposite wall ('P3'). This is a common observation for a bubble collapsing next to a rigid boundary (Blake and Gibson, 1987). At $t' \approx 3.327$, the induced jet is on the verge of impacting on the opposite side of the bubble surface which will lead to the formation of a toroidal shape bubble.

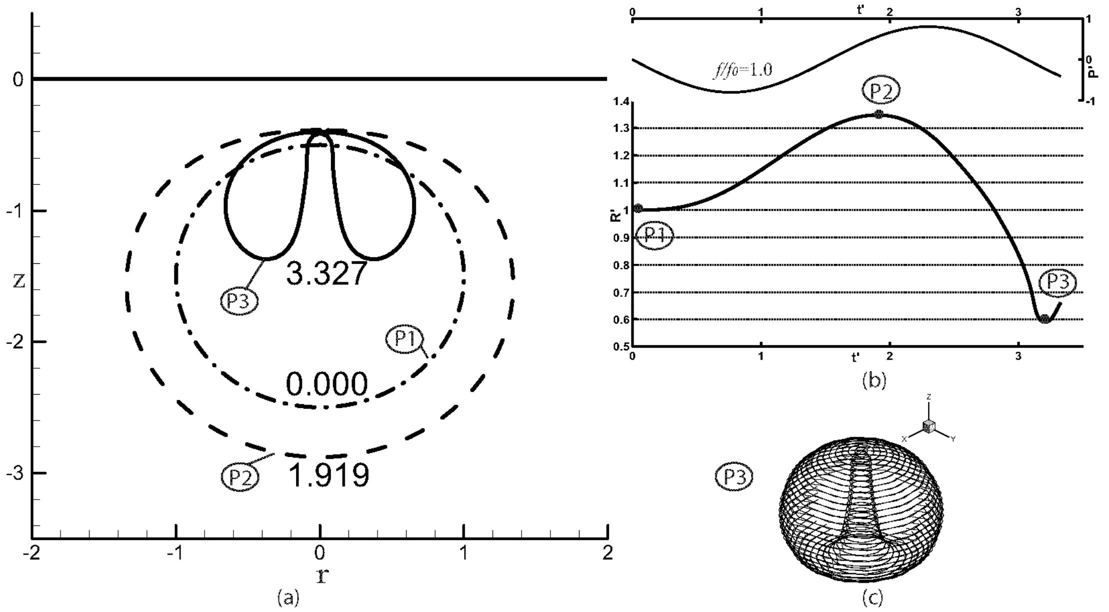

Fig. 4.7 Case 7: A bubble near solid wall which approximates a bone material in a sound field ($f / f_0 = 1.0$). (a) The dimensionless t' is as indicated near each history profiles. (b) The corresponding profiles ('P1', 'P2' and 'P3') are also shown on the R' vs t' graph. The pressure oscillation of the sound wave is indicated on the top (p' vs t' graph). (c) The 3D visualization of the bubble is based on the solid line profile ('P3').

4.2.2 Sound field frequency, $f / f_0 = 0.5$

For comparison, simulations for a bubble near the same set of biomaterials for sound waves with dimensionless frequencies (f / f_0) of 0.5 (here) and 1.5 (in Section 4.2.3) are performed. For Case 8 at $f / f_0 = 0.5$ (fat boundary), there is no penetrating jet developed in the first two periods of oscillation (see Fig. 4.8). Although the bubble is seemingly pinched at the middle towards the end of its first period of oscillation ('P3' at $t' = 4.504$, solid line), it does not break into two. The fat boundary is attracted to the bubble as the latter contracts to its minimum size. In the second period, a jet directed away from the interface is observed. However, the jet does not impact on the opposite side of the bubble wall. The bubble traverses away from the initial quiescent boundary while the latter evolves and indicates a movement towards the bubble.

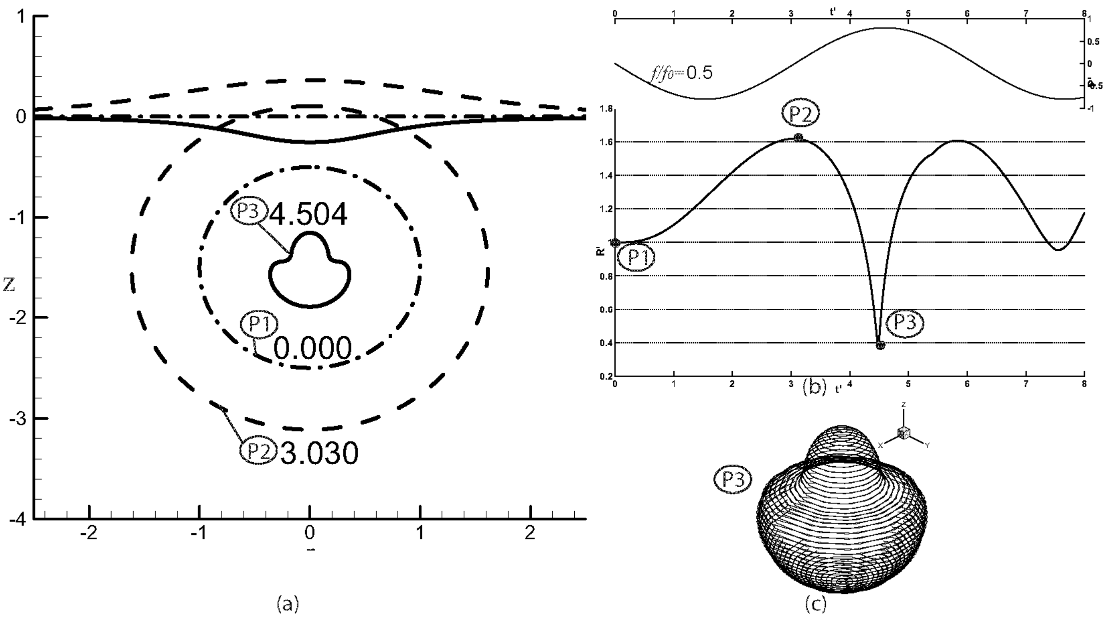

Fig. 4.8 Case 8: A bubble near a fat boundary (κ*= 0.037) in a sound field (f / f_0= 0.5). (a) The dimensionless *t′* is as indicated near each history profiles. (b) The corresponding profiles (‘P1’, ‘P2’ and ‘P3’) are shown on the *R′* vs *t′* graph. The pressure oscillation of the sound wave is indicated on the top (*p′* vs *t′* graph). (c) The 3D visualization of the bubble is based on the solid line profile (‘P3’) at *t′* =4.504.

Compared to the fat boundary just mentioned, for the bubble near the skin and the cornea (f / f_0 = 0.5), a slower jet is observed. The bubble collapses with a jet towards the skin interface, similar to that of Case 2 (Fig. 4.2) and not shown here. The typical history profiles of the bubble for the cornea (Case 9) are shown in Fig. 4.9. The bubble moves towards the boundary while developing a jet towards it (‘P3’ at *t′* = 4.585, solid line). The cornea boundary advances towards the bubble. But in the second period, the jet does not develop further as the bubble expands. This is very unlike Case 3 for the cornea boundary at f / f_0 = 1.0 where a broader extent jet is observed to develop fully in the second period.

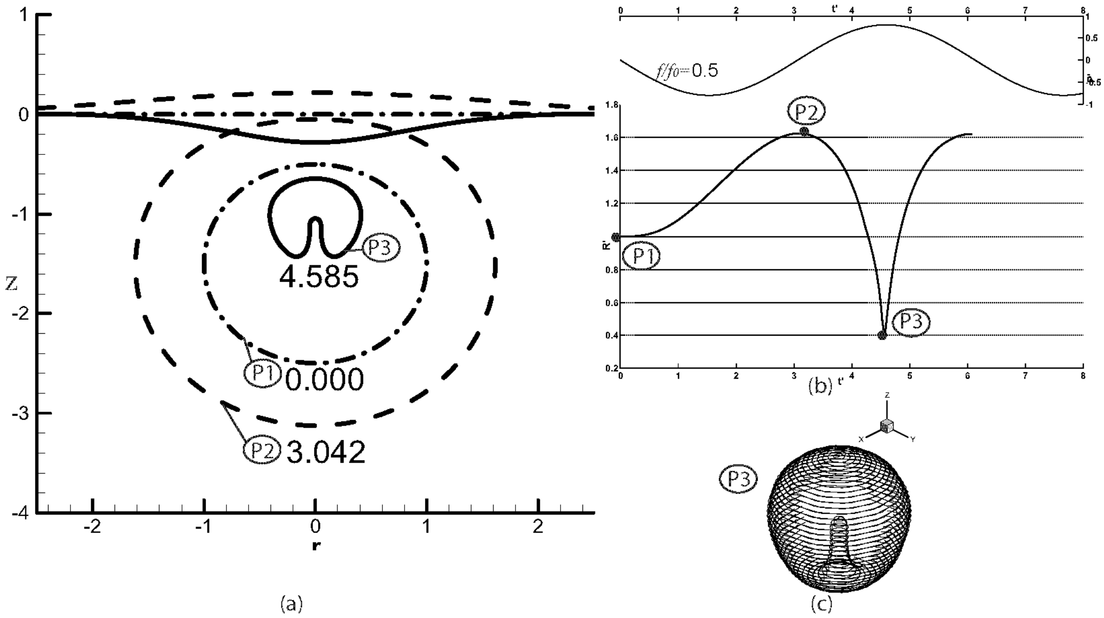

Fig. 4.9 Case 9: A bubble near a cornea boundary (κ*= 0.2209) in a sound field ($f\,/\,f_0$= 0.5). (a) The dimensionless t' is as indicated near each history profiles. (b) The corresponding profiles ('P1', 'P2' and 'P3') are shown on the R' vs t' graph. The pressure oscillation of the sound wave is indicated on the top (p' vs t' graph). (c) The 3D visualization of the bubble is based on the solid line profile ('P3') at t' =4.585.

When the bubble is placed near the brain and muscle however (only the case for the former is presented in Case 10 Fig. 4.10), it splits into two with the top bubble (the one nearer to the biomaterial) larger than the bottom bubble. There is no jet formation leading to the collapses of the bubbles after they have split ('P3' in Fig. 4.10(a) and (b)). The brain boundary moves towards the bubble even as the latter breaks into two entities. On the other hand, the muscle boundary, being stiffer, moves only marginally towards the split bubble (not shown here).

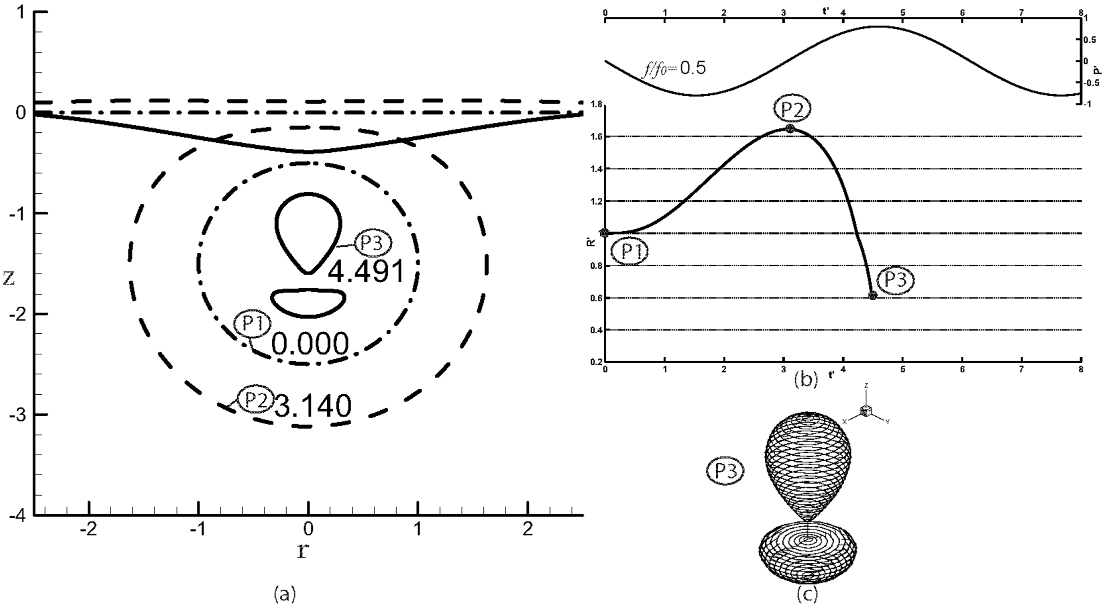

Fig. 4.10 Case 10: A bubble near a brain boundary (κ*= 1.589) in a sound field (f / f_0 = 0.5). (a) The dimensionless t' is as indicated near each history profiles. (b) The corresponding profiles (‘P1’, ‘P2’ and ‘P3’) are shown on the R' vs t' graph. The pressure oscillation of the sound wave is indicated on the top (p' vs t' graph). (c) The 3D visualization of the bubble is based on the solid line profile (‘P3’) at t' =4.491.

For very stiff boundaries like cartilage and bone, a bubble-induced jet is developed and is directing towards the boundaries (similar to Fig. 4.7 for a bubble near the bone with f / f_0 = 1.0). For the bubble near the cartilage boundary the formation of a jet towards the boundary in this case is very unlike the counterpart of f / f_0 = 1.0 where the bubble splits into two parts first to be followed by two opposing jets (Fig. 4.5).

4.2.3 Sound field frequency, $f / f_0 = 1.5$

The history profiles of the bubble in a sound field of f / f_0 = 1.5 are rather different from the earlier ones at f / f_0 = 1.0 and 0.5. For the first three cases of the bubble placed in the vicinity of fat, skin, and cornea at f / f_0 = 1.5, no penetrating jet is observed during the first two periods of oscillation (although a jet is initially formed for the case of skin, it does not develop fully to penetrate through the opposite bubble wall). However, for the case of brain, a penetrating jet is seen at the end of the second period (see Fig. 4.11(a)); this is very different from the counterparts at $f / f_0 = 1.0$ (Case 4) and $f / f_0 = 0.5$ (Case 10) where no jet is observed.

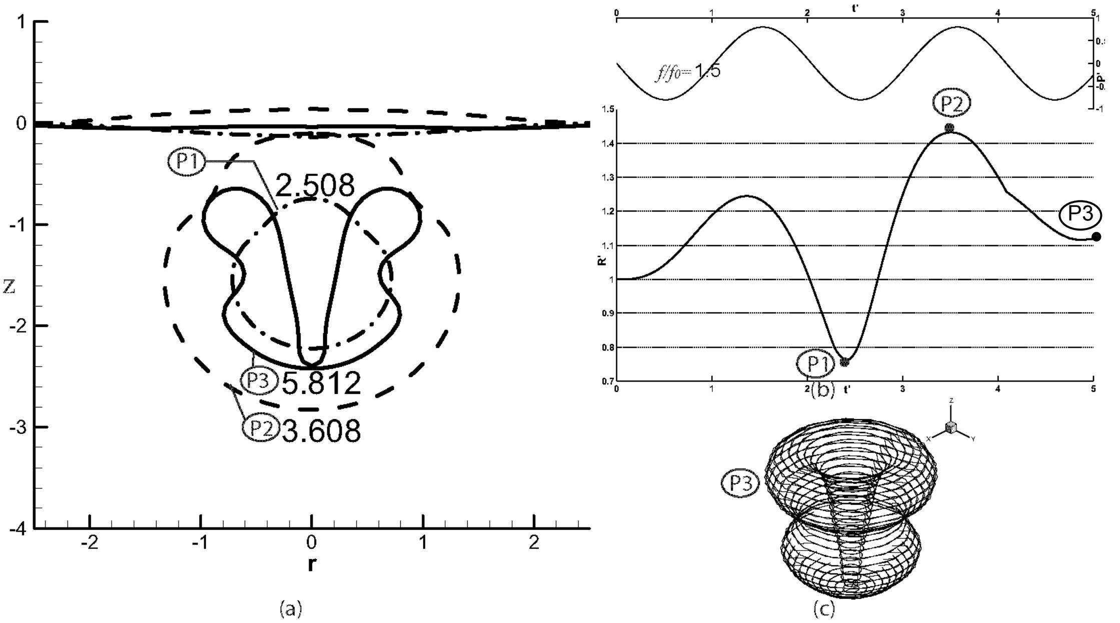

(a) (c)

Fig. 4.11 Case 11: A bubble near a brain boundary (κ*= 1.589) in a sound field ($f / f_0 = 1.5$). (a) The dimensionless t' is as indicated near each history profiles. (b) The corresponding profiles ('P1', 'P2' and 'P3') are shown on the R' vs t' graph. The pressure oscillation of the sound wave is indicated on the top (p' vs t' graph). (c) The 3D visualization of the bubble is based on the solid line profile ('P3') at $t' = 5.812$.

For the cases of muscle and cartilage (Case 12), the bubble elongates towards the boundary quite profoundly at the beginning of its second oscillation period as shown in Fig.4.12 (a) and (b) ('P1'). Then the bubble expands to its maximum size with pinching in the middle Section ('P2' at $t' = 3.605$, dashed profile) is observed. After that, the top boundary of the bubble moves very closely to the interface with additional pinching near its lower portion ('P3' $t' = 4.640$, solid line). The topological behavior of the bubble surface is very different from the counterpart at $f / f_0 = 1.0$ (Case 6).

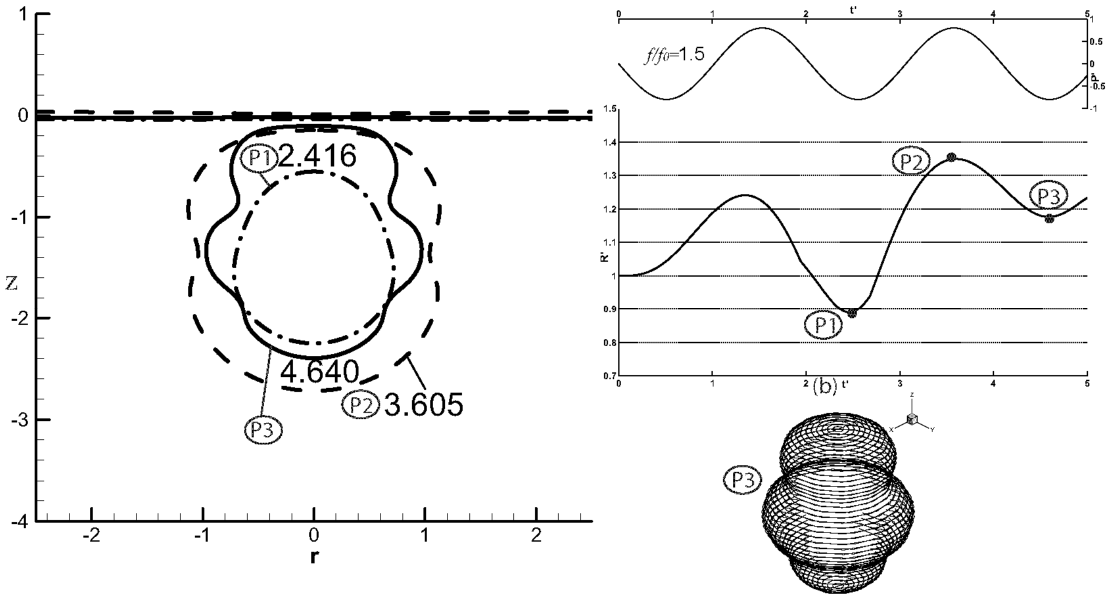

(a) (c)

Fig. 4.12 Case 12: A bubble near a coastal cartilage boundary (κ*= 22.89) in a sound field ($f\,/\,f_0$ = 1.5). (a) The dimensionless *t'* is as indicated near each history profiles. (b) The corresponding profiles ('P1', 'P2' and 'P3') are shown on the *R'* vs *t'* graph. The pressure oscillation of the sound wave is indicated on the top (*p'* vs *t'* graph). (c) The 3D visualization of the bubble is based on the solid line profile ('P3') at *t'* =4.640.

4.2.4 Jet velocity and translational movement of the bubble

The penetrating jet phenomenon is observed in several cases for the bubble in an ultrasound field of $f\,/\,f_0$ = 1.0. It is closely related to the frequency of the sound wave. In this case, the driving frequency of the sound wave is the same as the bubble's natural frequency. As a result, the phase difference between the bubble's oscillation and the sound wave is $\pi/2$ (Leighton, 1994) as can be seen in Figs. 3b, 4b, 5b, 6b, 7b and 8b. This promotes the bubble growth. The radius *R'* is re-plotted in Fig. 4.13 whereby a large dimensionless equivalent radius *R'* of close to 1.4 is obtained in the first period of oscillation; in the second period, the maximum *R'* even exceeds 2.0. Figure 4.13 seems to indicate that, while the shapes of the bubbles can be very different, the volume-time oscillations are quite similar for all the Cases 1 to 7.

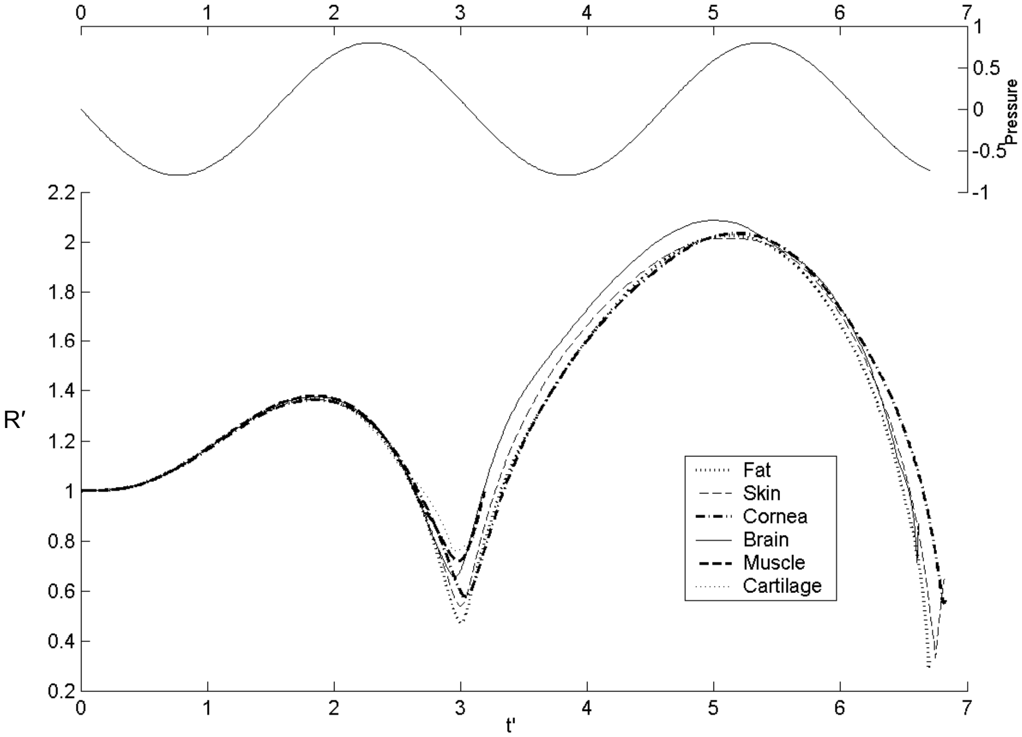

Fig. 4.13 The variation of bubble radius, R', with time (t'). The pressure variation of the sound wave (f / f_0= 1.0, A= 0.8) is plotted on top with a secondary y-axis on the right.

When the bubble collapses with a jet, the variation of the maximum jet velocity (as it originates from one Section of the bubble surface and evolves towards the opposite wall of the bubble) is shown in Fig. 4.14. This velocity is obtained from the locality on the bubble boundary which is on or nearest to the tip of the jet and which will eventually penetrate the bubble. A very high speed jet of up to 980 m/s is observed as the bubble collapses near the fat boundary (Case 1). Interestingly, this jet is directed away from the biomaterial, similar to that formed in a bubble near a free surface (Wang et al, 1996a). However the bubble center traverses slightly away from the initial quiescent boundary as opposed to the movement of the bubble towards the free surface (Brennen, 2005) during the collapse. This could be due to the momentum transfer from the elastic fat boundary which is 'attracted' towards the bubble as the bubble collapses.

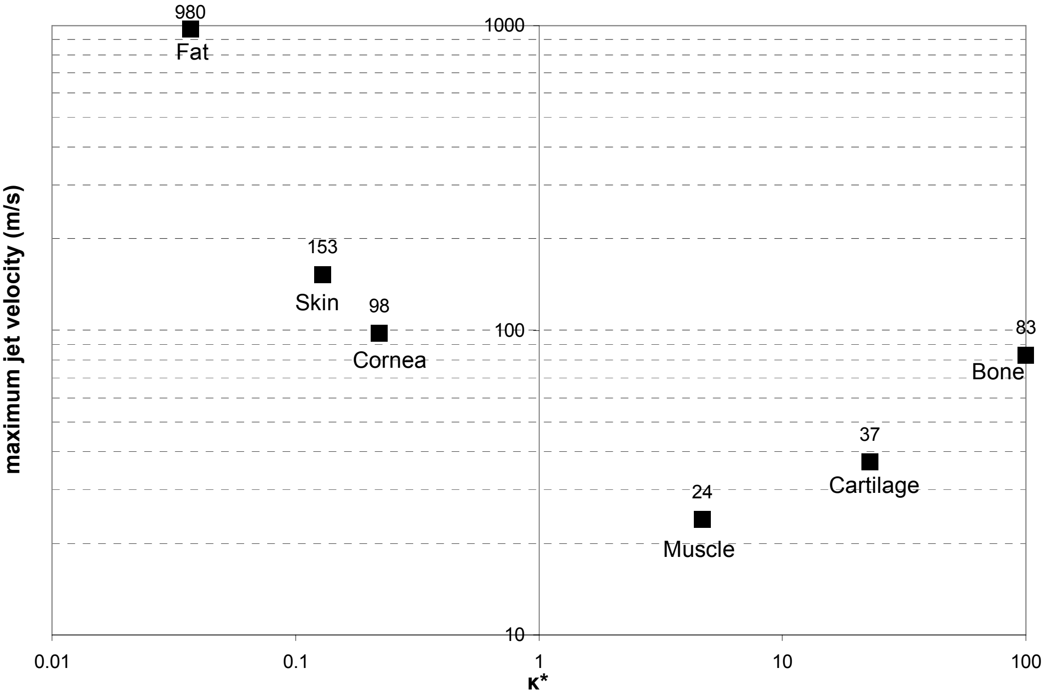

Fig. 4.14 Maximum jet velocity for a bubble collapsing near various biomaterials in an ultrasound field of $f / f_0 = 1.0$.

For the cases of a bubble near skin, cornea and bone boundaries (Case 2, 3 and 7), the jet formed is directed towards the boundary. The maximum velocities of these jets, however, are about ten times lower than that of the previous case. For the jet in a bubble near the skin boundary, the maximum velocity of the impinging jet is 153 m/s. As for the cases of the cornea and bone, even lower maximum velocities of 98 and 83 m/s are observed, respectively.

Before the bubble collapses near the muscle or cartilage boundaries (Case 5 and 6), it splits up into two with opposing jets formed pertaining to both split bubbles. The jet develops more rapidly for the bottom bubbles in both cases. This bottom bubble is smaller in size and the jet impinges the opposite wall of the bubble away from the (interface) boundary before the jet pertaining to the top bubble develops fully which is directed towards the boundary. In Fig. 4.14, the maximum jet velocities obtained are for the bottom bubbles. For Case 5, this value is 24 m/s and for Case 6, it is 37 m/s. In all these cases (Case 2 to 7), the bubble traverses away from the horizontal boundary initially, but moves towards the latter as the jet develops. A similar observation of the translational movement of the bubble center is obtained for Case 4 (brain). The bubble moves away from the initial quiescent brain boundary and then towards it when the bubble splits up into two.

When the sound field is changed to that of $f / f_0 = 0.5$, in all the biomaterial cases, except for Case 8 (fat), the bubble initially traverses away from the boundary and then towards it as it expands in the second period. In Fig. 4.15, the variations of the evolution of R' with t' for the different biomaterials at $f / f_0 = 0.5$ are given for comparison. As observed, the maximum bubble radius read in the first period is about the same as for the second period, unlike that found for $f / f_0 = 1.0$ where the phenomenon occurs in the same period. Also, the maximum radius obtained for $t' < 7.0$ is only about 1.6 (Fig. 4.15), which is lower than that of bubbles in a sound field of $f / f_0 = 1.0$ (Fig. 4.13).

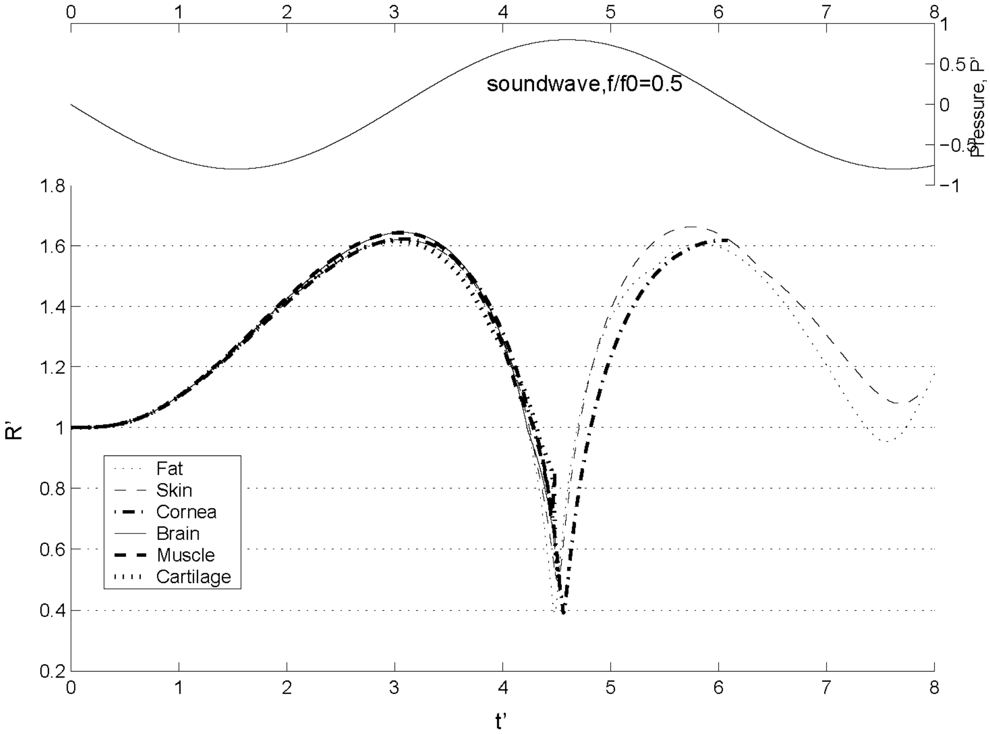

Fig. 4.15 The variation of bubble radius, R', with time (t'). The pressure variation of the sound wave ($f / f_0 = 0.5$, A= 0.8) is plotted on top with a secondary y-axis on the right.

As for maximum jet velocity, the only two cases where a jet is observed in the collapsing bubbles for $f/f_0 = 0.5$ are for the bubble near the cartilage or bone materials. The maximum jet velocity for the case involving cartilage is very high at about 900 m/s. This suggests that very severe damage can be sustained by the cartilage when the acoustic bubble collapses next to it. For the case of the bone boundary, the maximum velocity recorded is much lower at about 141 m/s. For the sound field of $f/f_0 = 1.5$, the maximum jet velocity obtained for the case of a bubble near the brain-like material is about 25 m/s. Even for a bubble near the bone, its maximum jet velocity is only 12 m/s.

It is noted that the brain boundary, in the case of $f/f_0 = 1.5$, displaces much less as compared to the previous $f/f_0 = 1.0$ or $f/f_0 = 0.5$ cases. Furthermore, the translational movement of the bubble center for this sound field is generally less than that of $f/f_0 = 0.5$ and 1.0. Also, as seen in Fig. 4.16, the variation of R' is almost in phase with that of the sound wave. The maximum radius achieved at about 1.3 to 1.4 is comparatively lower that the counterparts at $f/f_0 = 1.0$ and $f/f_0 = 0.5$. It is apparent that the maximum R' is obtained at the resonant frequency of $f/f_0 = 1.0$ irrespective of the different types of nearby boundary.

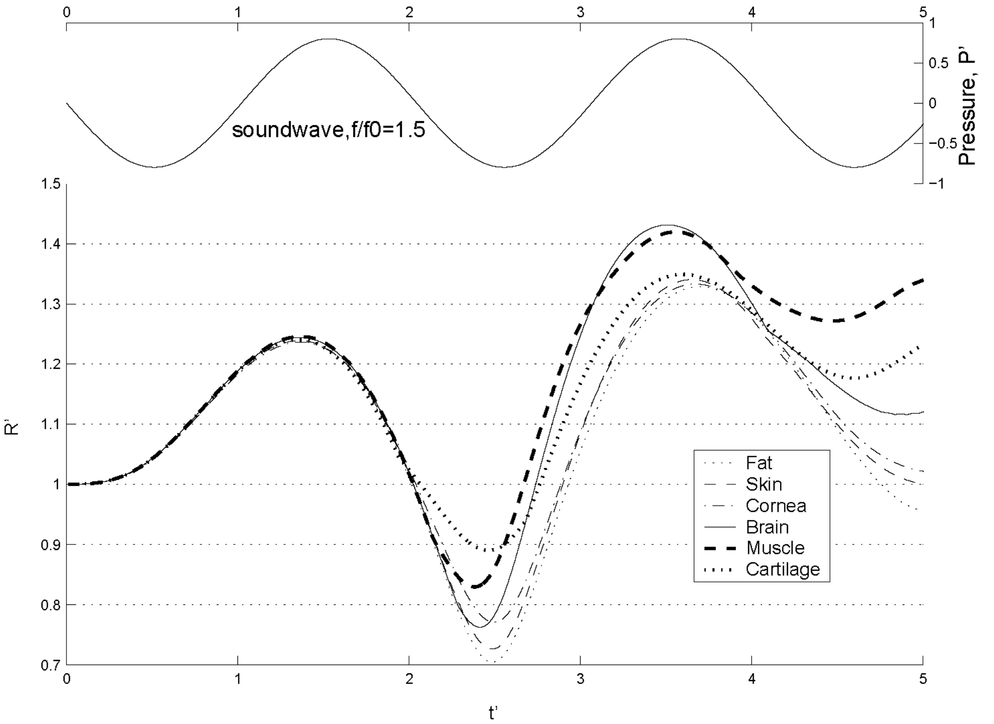

Fig. 4.16 The variation of bubble radius, R', with time (t'). The pressure variation of the sound wave ($f\,/\,f_0$= 1.5, A= 0.8) is plotted on top with a secondary y-axis on the right.

Chapter 5

Acoustic microbubble simulations

The interaction of a microbubble contrast agent with a strong pulsed ultrasound field is studied numerically in this chapter. The response of the bubble, in terms of its profiles at different time, the maximum bubble radius obtained, the oscillation time, the jet velocity, and its translational movement, is studied. Also the effect of increasing the intensity of the ultrasound waves is examined. Lastly, the importance of initial bubble radius on the acoustic bubble dynamics is considered.

5.1 Introduction of the study of microbubbles in sound fields

Microbubbles are used as contrast agents in medical imaging. When interacting with high intensity acoustic waves, the microbubbles can collapse with a high speed jet (Bourne and Field, 1999). The jet from the collapsing bubbles will create high shear stress on the cell membranes and eventually rupture them (Brujan, 2004). This could lead to possible drug delivery via sonoporation (Miller et al (2002), Ohl et al (2006)) or cell death (Prentice et al, 2005a). A similar bubble collapse phenomenon involving shockwave bubble interaction has been previously studied by several researchers such as Ding and Gracewski (1996), Jamaluddin (2004), and Klaseboer et al. (2006b). However, recent development in clinical treatment has seen renewed interest focusing largely on the use of the pulsed ultrasound; this is possibly motivated by the intent to minimize collateral damage on the nearby tissues caused by strong shockwaves (Ikeda et al, 2004). Therefore, it is essential to establish the basic phenomena concerning microbubble pulsed ultrasound interactions as presented in this chapter, for a better understanding of the physics involved, and for future improvement in clinical treatments.

5.1.1 Pulsed ultrasound profiles

The pulsed ultrasound profiles used here are based on those reported experimentally by Xu et al. (2005). They use focused pulsed ultrasound to mechanically remove tissue in a localized, controlled manner for clinical treatments. Various intensities of sound waves as shown in Fig. 5.1 are used, namely 1000, 3000, 5000, and 9000 W/cm^2 as indicated on the figure. These ultrasound waves are generated using a single-element transducer. The main frequency of the pulses is 0.8 Mhz. Xu et al. (2005) postulate that transient cavitation is the primary mechanism of the tissue erosion process. This is because they detected acoustic signals caused by the existence of the cavitation bubbles when there is effective tissue erosion. Since the sound waves used by Xu et al. (2005) are strong enough to cause the collapsing cavitation bubbles to cut through tissues, they are deemed suitable to be used as a driving force for the forced collapse of the microbubble contrast agents in the cancer treatment procedure mentioned (targeted drug delivery with cell destruction by collapsing microbubbles). Four pulses of different strengths as shown in Fig. 5.1 are used in the simulations. In this chapter, they are referred to as Pulse 1 (for the 1000 W/cm^2 ultrasound), Pulse 2 (3000 W/cm^2), Pulse 3 (5000 W/cm^2), and Pulse 4 (9000 W/cm^2) for ease of referral.

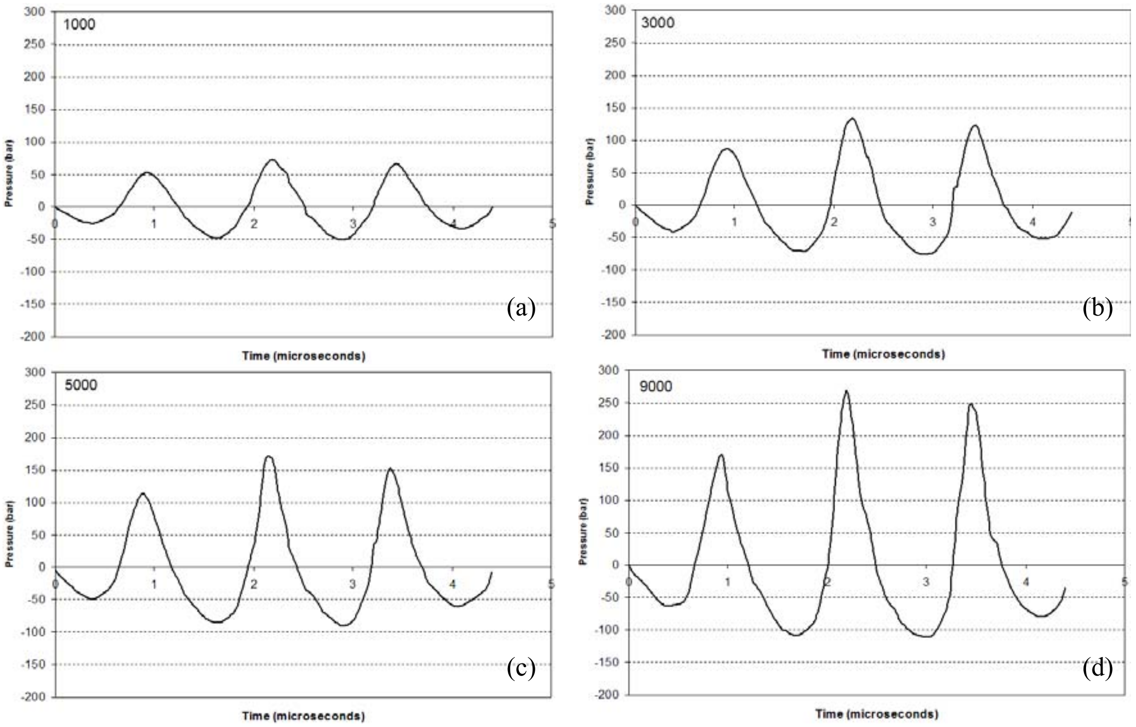

Fig. 5.1 Pulsed ultrasound with various intensities as indicated, (a) 1000, (b) 3000, (c) 5000, and (d) 9000 W/cm^2 as used in Xu et al (2005) and the simulations in this section. It is noted that all the sound waves start off with a tensile part that will cause the bubbles to expand before they are forced to collapse by the compressive component of the waves.

The modeling of these pulsed ultrasound waves is similar to that mentioned in chapter 3. Both spatial and temporal considerations are taken into account. In all the simulations in this chapter, the pulsed ultrasound is set to hit the bubble from the bottom surface, and then travels across the bubble to the top.

5.1.2 The microbubbles

The term ‘microbubble’ is generally used to indicate ultrasound contrast agent which is basically a small gas bubble with a thin membrane. Often heavy gases, such as sulphur hexafloride, are used. But in some cases, an air core is utilized (for example in Levovist Ultrasond Contrast Agent (UCA) from Schering). The use of heavy gases is arguably preferred because these gases are less water-soluble so they are less likely to dissolve which impairs echogenicity (McCulloch et al., 2000). Also with slow gas diffusion, the microbubbles are likely to last longer in circulation. The thin membrane enclosing the gas core is usually made of albumin, galactose, lipid, or polymers (Lindner, 2004). For example the commercially available ultrasound contrast agent Optison has octafluoropropane as it content, and it is enclosed in albumin.

Because of the existence of the shells, the microbubbles remain stable in solution for a certain period of time, from a few minutes to a few hours. If left unattended, they gradually dissolve due to gas diffusion or dissolution of the membrane. However, if a strong acoustic field is present, these bubbles could be driven to expand to multiple times of their original sizes (as to be presented in later sections). In this case, the bubble dynamics is mainly inertially-controlled, and the bubbles behave more like cavitation bubbles. Thus, in our model of the microbubble, the thin membrane is not considered to be important. It is noted that this is unlike the case for the study of microbubble oscillations in a sinusoidal ultrasound field intended for bio-imaging purposes. When the microbubbles oscillate gently in the ultrasound, the surface tension due to their usually tens of nanometer thick membrane is important in influencing the bubble dynamics, e.g. the resonance frequency (Khismatullin, 2004). Yet in the case of strong sound waves, the extremely rapid expansion and subsequent even more rapid collapse of the microbubbles, render the membrane effect to be of secondary importance. In fact, as shown in various experiments using strong pressure waves (Wolfrum et al (2002), Prentice et al (2005b)), these microbubbles collapse violently with a high speed jet, similar to that of a cavitation bubble collapsing after being hit by a shockwave (refer to Chapter 3 on "Shockwave bubble interaction"). Therefore, it is considered reasonable in this study to ignore the damping effect due to the membrane and to model the microbubble as a stationary gas bubble with internal pressure of 1 bar.

5.2 Interaction of a microbubble with pulsed ultrasound of intensity 1000 W/cm^2

The size of the microbubble contrast agents available commercially is fairly well-controlled and uniform. They are usually found within the range between 1 to 4 μm. This small size allows them to flow easily through the blood circulation (being smaller than the red blood cells), and even the micro-circulation systems to the site of interest. Therefore in this section, the interaction of a single microbubble of typical sizes (with slightly wider range between 1 to 10 μm) with Pulse 1 (denoting the pulsed ultrasound of 1000 W/cm^2 as shown in Fig. 5.1) is presented.

Firstly a microbubble 1 μm in radius is considered. This stationary bubble is hit by a sound wave like Pulse 1. The traveling wave is modeled as described in Section 3.2.1 (the only difference being the function P(t*), in Section 3.2.1, it depicts the pressure variation of a shockwave (Fig. 3.5), while here it represents a pulsed ultrasound as shown in Fig. 5.1). As the tensile part of the waves passes the bubble, the bubble expands and grows to about 25 times that of its initial radius, to a maximum radius, R_{max}, of 25.9 μm as shown and indicated by the dashed line profile in Fig. 5.2. After that, the bubble enters its collapse phase. The subsequent profiles in the collapse phase with the time for each profile in microseconds are also shown in Fig. 5.2. A jet in the direction of travel of the sound wave (upwards) is formed, and causes the collapse of the bubble at t = 1.229 μs from the initial contact (t = 0 μs) of the sound wave and the bottom surface of the bubble (the sound wave travels from bottom to top).

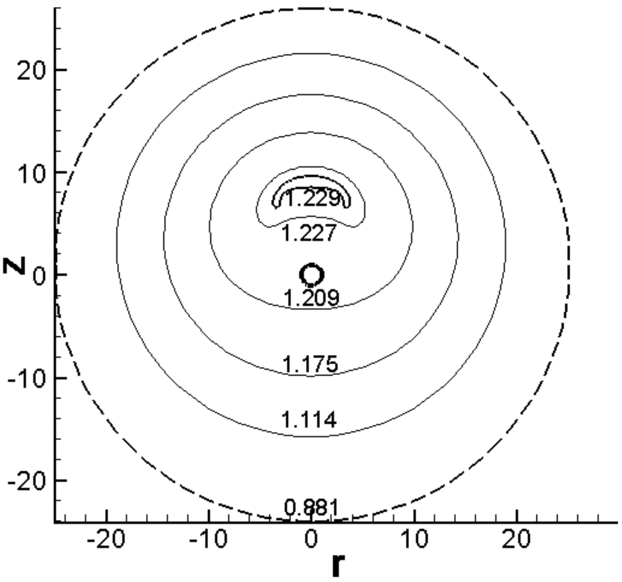

Fig. 5.2 The microbubble profiles with initial radius of 1 μm when it is hit by the pulsed ultrasound of intensity 1000 W/cm^2 (Pulse 1). It expands from its initial size (thick solid line at the center of the plot) to its maximum radius, R_{max} = 25.9 μm, at t = 0.881 μs (dotted line). Then the bubble collapses with a jet at t = 1.229 μs. The formation of the jet is shown with the respective bubble profiles at different time (in μs) which is indicated next to the profiles.

All the bubbles between 1 to 10 μm in radii, collapse with similar shapes. They expand to a large size before collapsing with a jet in the direction of the pulsed ultrasound. The maximum bubble radius, R_{max}, obtained for these bubbles is in the range between 25 to 30 μm. The oscillation time, t_{osc}, which is defined to be from t = 0 μs to the collapse of the bubble (or its first minimum after a maximum size), is found to be between 1.2 to 1.4 μs for the range of microbubbles considered. As shown in Fig. 5.3, all the bubbles of these sizes collapse within the first cycle of Pulse 1. This is significant because it could mean that if the strong jet from the collapsing bubble is the main mechanism for tissue erosion or cell membrane rapture, a single cycle ultrasound should be sufficient. The removal of redundant further cycles might serve to reduce collateral damages to the healthy cells in the vicinity.

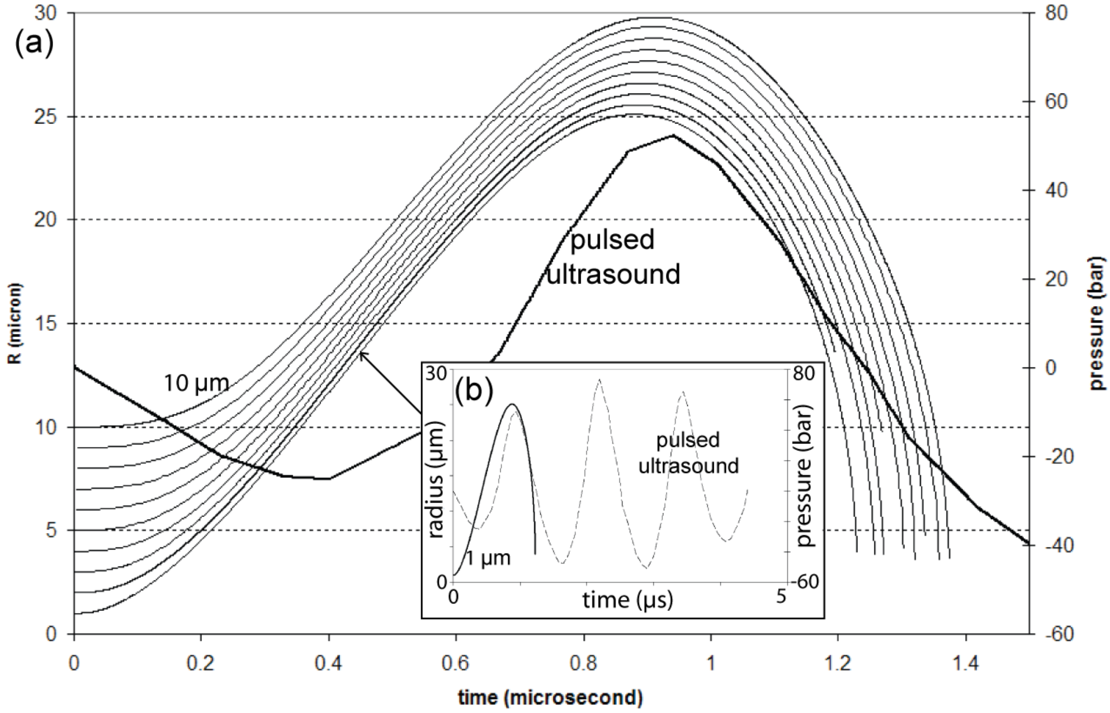

Fig. 5.3 (a) Variation of bubble radius in time for microbubbles of radii between 1 to 10 µm inclusively. Also indicated is the pressure variation in time of the pulsed ultrasound wave of 1000 W/cm^2 (with *y*-axis on the right). The bubbles obtain maximum radii between 25 to 30 µm and collapse between 1.2 to 1.4 µs. The collapse times are within the first cycle of the pulsed ultrasound wave as shown in (b) where the complete pulsed ultrasound wave is plotted together with the 1 µm bubble's radius variation in time.

Also it is noted that, the larger the initial bubble radius, the longer the oscillation time, t_{osc}, before the bubble collapses as indicated in Fig. 5.3(a). This is because the larger bubble takes longer to expand to its maximum size. In fact all of the bubbles are still expanding while already being subjected to the compressive component of the sound wave. Another important thing to discuss is the collapse time, t_c. The value of t_c from its maximum radius (R_{max}) to jet impact is greater for bubbles with larger initial radius because for a given driving pressure, P^+, the bubble collapse time measured, t_c, is found to be proportional to R_{max} (see section 5.3).

The bubble translates in the direction of the sound waves as it collapses. Most of the bubbles have moved a distance of about 8 µm at the moment of jet impact. Furthermore, the high speed jets formed attain velocities (v_{jet}) ranging from 1050 m/s for the 1 µm bubble to about 1400 m/s for the 10 µm bubble.

5.3 The effect of increasing the intensity of the pulsed ultrasound

Sound intensity is defined as sound power per unit area. Considering the ultrasound waves here as planar progressive waves, the intensity of the waves, I, is proportional then to the square of the amplitude of the pressure waves (A),

$$I = \frac{A^2}{Z}, \tag{5.1}$$

where Z is the acoustic impedance. Therefore, when it is increased, the maximum positive and negative pressures of the pulsed ultrasound also increase (as shown in Fig. 5.1). Since all bubbles between 1 to 10 μm collapse within the first cycle of the sound waves, only the pressure amplitudes (both positive and negative) of this cycle are considered in this section. As shown in Table 5.1, as the intensity of the sound waves increases from 1000 W/cm^2 to 9000 W/cm^2, the negative pressure increases in magnitude from -25 bar to -62 bar. This negative tensile wave is responsible for the expansion of the microbubbles. As provided in Table 5.1, the range of maximum radius obtained for the bubbles between 1 to 10 μm also increases with the rise in the amplitude of the negative pressure. For the pulsed ultrasound of intensity 1000 W/cm^2 (denoted as Pulse 1) as discussed in the previous section, R_{max} is 25.1 μm for a bubble with initial radius of 1 μm and 29.8 μm for the 10 μm initial radius bubble. When the negative pressure is increased from -25 to -39 bar for Pulse 2, the range of R_{max} for the same variation of initial bubble radii increases to between 31.2 to 35.7 μm. When the negative component of Pulse 3 almost doubles from that of Pulse 1 to -48 bar, the maximum radii range increases significantly to between 34.8 and 39.3 μm. Further on, the bubbles expand to between 40.5 to 44.7 μm in radii before collapsing when they are hit by Pulse 4 with a maximum negative pressure of -62 bar.

Table 5.1 Peak pressures (negative and positive) of the first cycle of the pulsed ultrasound waves of different intensity and their effects on the collapse time and the maximum radii of the microbubbles of initial radii between 1 to 10 μm. The lower bond is set by the columns under 1 μm bubble, and the upper bond is given by the values for 10 μm bubbles. All other bubbles (between 2 to 9 μm) have t_{osc} and R_{max} between these two bonds.

Intensity of pulsed ultrasound (W/cm^2)	Peak negative pressure (bar) of the first cycle	Peak positive pressure (bar) of the first cycle	Oscillation time, t_{osc} (μs)		Maximum radius, R_{max} (μm)	
			1 μm	10 μm	1 μm	10 μm
1000 (Pulse 1)	-25	52	1.23	1.37	25.1	29.8
3000 (Pulse 2)	-39	86	1.21	1.31	31.2	35.7
5000 (Pulse 3)	-48	112	1.20	1.30	34.8	39.3
9000 (Pulse 4)	-62	169	1.23	1.32	40.5	44.7

On the other hand, the oscillation time (t_{osc}) of the microbubbles for a given initial bubble radius for the various pulsed ultrasound amplitudes remains fairly invariant (Table 5.1). They range between 1.20 and 1.37 μs. When the compressive component of the first pulse passes the bubbles, they collapse in the direction of travel of the sound wave. A very high speed jet of about 1000 m/s (see Table 5.2) is observed for the microbubbles of various sizes. Both the intensity and the initial bubble radius are important factors in determining the jet velocity. For example, the small 1 μm bubble records maximum jet speeds between 1270 and 1366 m/s for the various sound waves in Table 5.2; while for the 10 μm bubble, it is between 813 and 1466 m/s.

The decrease of the maximum jet velocity obtained with increasing pulsed ultrasound intensity seems counter-intuitive. However, this can be explained by considering the Kelvin impulse. For a 1 μm bubble, its Kelvin impulse calculated is progressively higher when it is impacted by pulsed ultrasound waves of increasing intensity. For instance as shown in Table 5.2, $K = 0.131\times10^{-6}$ kg ms^{-1} at the moment of collapse when it is hit by Pulse 1; but when it is impacted by Pulse 4, *K* is about 10 times larger, i.e. $K = 1.22\times10^{-6}$ kg ms^{-1}. The Kelvin impulses, *K*, for the 10 μm bubble is also increasing along with the intensity of the sound waves. For example, at the moment of jet impact when the 10 μm bubble is hit by Pulse 1, its Kelvin impulse is $K = 0.101 \times 10^{-6}$ kg ms^{-1}. However, then it is interacting with Pulse 4, K is about 10 times larger, i.e. $K = 1.03 \times 10^{-6}$ kg ms^{-1}.

Table 5.2 Maximum jet velocities and Kelvin impulse for the microbubbles of initial radii 1 and 10 μm. The maximum jet velocity decreases with increasing pulse intensity (more significantly with increasing initial bubble radius). The Kelvin impulse, however, increases with increasing pulse intensity. This signifies the broadening of jet radius with increasing pulsed ultrasound intensities.

Intensity of pulsed ultrasound (W/cm^2)	Maximum jet velocity, v_{jet} (m/s)		Kelvin impulse (μg ms^{-1})	
	1 μm	10 μm	1 μm	10 μm
1000 (Pulse 1)	1366	1466	0.131	0.101
3000 (Pulse 2)	1274	1397	0.418	0.388
5000 (Pulse 3)	1279	1224	0.597	0.50
9000 (Pulse 4)	1270	813	1.22	1.03

Since the Kelvin impulse is a measure of both the jet speed and its broadness, the result signifies that although the jet speed does not vary much, the increase in the sound waves' intensity has the effect of broadening the jet tip (as depicted in Fig. 5.4). In this particular case, both bubbles expand spherically, and they start to collapse, an obvious flattening of the bottom surface is noticed at about 1.2 μs. The flattened bottom surfaces eventually develop into thick jets. The stronger is the sound wave, a thicker but slower jet is formed. The radius of the jet, R_{jet}, for the bubble interacted with Pulse 1 (Fig. 5.4(a)), has doubled from about 3 μm, to about 6.5 μm for the one with Pulse 4 (Fig. 5.4(b)). This could lead to a broad-based and more effective tissue erosion or cell rupture as mentioned. It is noted that both bubbles The broad jet is formed as the bubbles collapse.

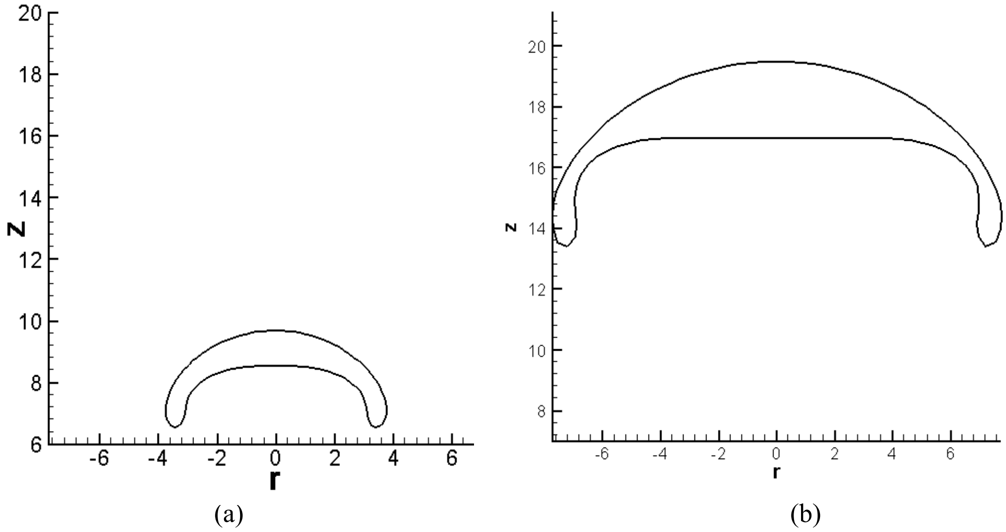

Fig. 5.4 The bubble profile at its moment of collapse for a 1 μm bubble interacted with (a) Pulse 1 (pulsed ultrasound of intensity 1000 W/cm^2), and (b) Pulse 4 (pulsed ultrasound of intensity 9000 W/cm^2). The jet tip is much wider with the radii of the jets, R_{jet}, doubling from (a) 3 μm to (b) about 6.5 μm.

Another physical quantity shown in Table 5.3 is the translational movement of the equivalent bubble center or its centroid. The center of a 1 μm bubble translates as much as 8.11 μm in the direction of the sound wave when it is hit by Pulse 1. When the same interacts with Pulse 4, the distance moved almost doubles to 15.24 μm. For all the bubbles in the size range of 1 to 10 μm, the increase in sound intensity has the effect of causing further translation of the bubble center especially in the collapse phase of the bubble evolution. This is perhaps directly related to the fact that the higher intensity sound waves cause the bubble to obtain greater R_{max} as discussed in Table 5.1. As seen in Fig. 5.5, for the case of a 1 μm bubble interacting with Pulse 1, the bubble center hardly moves at the expansion phase. As seen from the line with dotes which indicates the position of bubble center, the translational movement happens mainly in the collapse phase. Both top and bottom surface movements are obtained from the top and bottom nodes on the *z*-axis. During the expansion phase, both surfaces move away (radially outwards) from the initial position of the bubble ($z = 0$). The bubble centroid moves little from its initial position as seen in Fig. 5.5 during the bubble's expansion.

Table 5.3 Translation of the bubble center from its initial position in the direction of the pulsed ultrasound waves for the microbubbles of initial radii between 1 to 10 μm. The lower bond is set by the columns under 1 μm bubble, and the upper bond is given by the values for 10 μm bubbles. All other bubbles (between 2 to 9 μm) have values between these two bonds.

Intensity of pulsed ultrasound (W/cm^2)	Translation of the bubble center at the moment of collapse (μm) from its initial position	
	1 μm	10 μm
1000 (Pulse 1)	8.11	8.19
3000 (Pulse 2)	11.05	11.76
5000 (Pulse 3)	12.53	13.50
9000 (Pulse 4)	15.24	17.09

The bottom surface of the bubble starts to collapse before that of the top surface at t = 0.85 μs. The top surface starts moving toward the bubble center at t = 0.91 μs. With more time for translational movement and a high acceleration at the last moment of collapse, the bottom surface moves relatively more towards the top surface then vice versa. This results in a net translational movement of the bubble centroid as seen in Fig 5.5 for t between 0.8 and 1.2 μs when the jet impact occurs in the bubble.

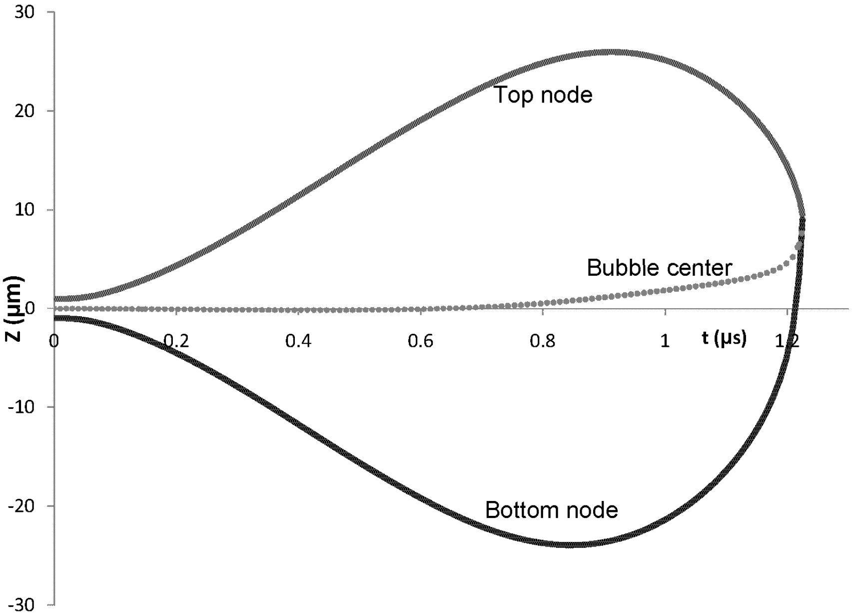

Fig. 5.5 Positions of the top and bottom nodes as a bubble of 1 μm radius is impacted by a pulsed ultrasound wave of 1000 W/cm^2 (Pulse 1). The translation of the bubble center is indicated as squares on line. It is seen that the movement during the collapse phase is mainly due to the movement of the bottom surface in the direction of positive z.

5.4 The effect of the initial size of the microbubbles

It is noted that even for very small initial bubbles of radii 0.1 μm (at the limit of validity of our model because surface tension effects have been ignored), the oscillation time is similar to that of the bubbles in the range between 1 to 10 μm in radius. For instance, when a 0.1 μm bubble interacts with Pulse 1, its oscillation time, t_{osc}, is 1.22 μs. The maximum radius obtained, about 24 μm, is close to that of the larger bubbles too (between 25.1 to 29.8 μm, Table 5.1). In Fig. 5.6, the profiles of the 0.1 μm bubble at different times during the collapse phase are shown. The bubble seems to be flattened as seen in the profile for t = 1.2147 μs. It achieves a final jet velocity, v_{jet}, of 1128 m/s.

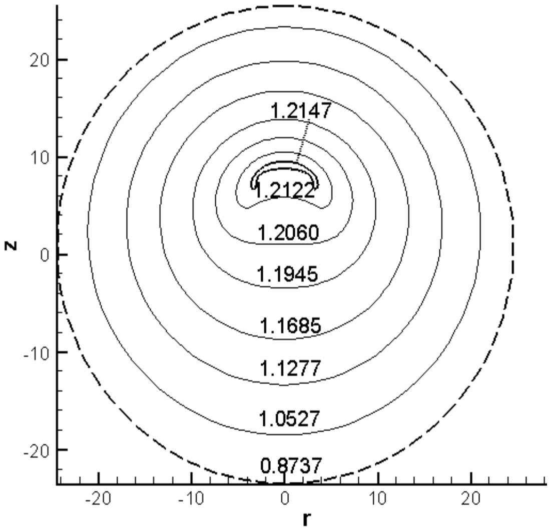

Fig. 5.6 The profiles of a 0.1 μm bubble in its collapse phase after being hit by Pulse 1 (1000 W/cm^2 pulsed ultrasound as shown in Fig. 5.1). The time (in μs) for each profile is indicated next to it. The bubble expands to about 24 μm, and collapses at around t = 1.2 μs.

It is also noted that the profile of the bubble collapse as shown in Fig. 5.6 does bear resemblances to that of the 1 μm bubble as shown in Fig. 5.2 in terms of the broad timing, general bubble shapes, and bubble dimension. This observation has an important implication: if and when the microbubble contrast agents break into smaller bubbles after their collapse, the subsequent pulses may cause these very small bubbles to expand to considerable sizes, and bring about unwanted collateral damage to the surrounding tissues. For instance, the 0.1 μm bubble which can be remnants from the original bubble having been broken up (Fig. 5.6), and can readily expand to 240 times of its initial 0.1 μm size when hit by Pulse 1 (pulsed ultrasound of 1000 W/cm^2). Moreover, the maximum radius obtained of about 24 μm is comparable to that of a 1 μm bubble with $R_{\max} \approx 26\mu\text{m}$.

On the other hand, increasing the initial bubble size beyond 10 μm has substantial influence on the subsequent bubble behaviors. As described in previous sections (Sections 5.2 and 5.3), for the bubbles between 1 to 10 μm in radii, they will collapse with a high speed jet within the first cycle of Pulse 1. As the initial bubble size increases, for example a 20 μm bubble, it will oscillate one period before collapsing in the second oscillation period as shown in Fig. 5.7.

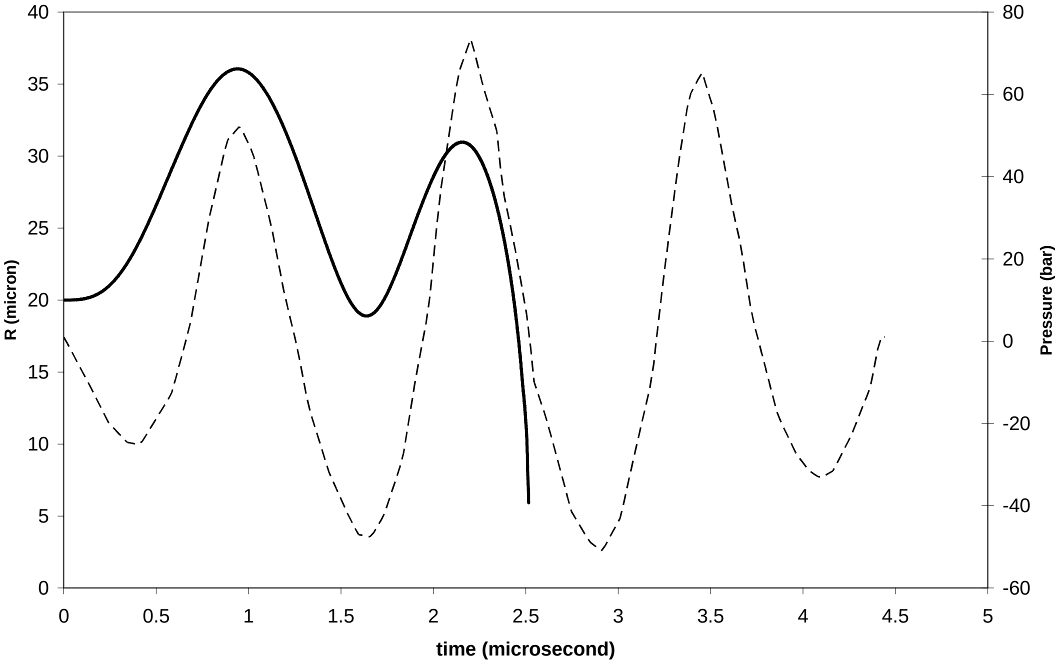

Fig. 5.7 The radius versus time curve (left *y*-axis) for a 20 μm bubble in a pulsed ultrasound field as indicated by the pressure profile in dotted line (right *y*-axis). The bubble grows to a maximum radius of 36 μm in the first period of its oscillation. It collapses only at the end of its second oscillation period which coincides with the second cycle of the ultrasound waves (Pulse 1).

Bubbles in the initial radius range between 20-28 μm exhibit a similar radius versus time curve as that shown in Fig. 5.7. Because of the longer oscillation time before collapse (with consequential more energy input from the pulsed ultrasound wave) and the greater maximum radius attained, bubbles between 20 and 28 μm in initial radius therefore collapse with a much higher jet velocity of over 2000 m/s as compared to bubbles of 1 to 10 μm (see Table 5.2). For instance, the 20 μm bubble collapses at t_{osc} = 2.51 μs with v_{jet} = 2764 m/s.

For a bubble of even larger initial radius at 30 μm interacting with Pulse 1, the bubble eventually still collapses but only after three periods of oscillation as indicated in Fig. 5.8(b). Fig. 5.8(a) shows the maximum bubble radius obtained in dashed line (corresponding point A in Fig 5.8(b)) of about 45 μm. In the final collapse from point B to C (Fig. 5.8(b)), the bubble develops several jets and is likely to break into several small bubbles after point C in Fig 5.8(a).

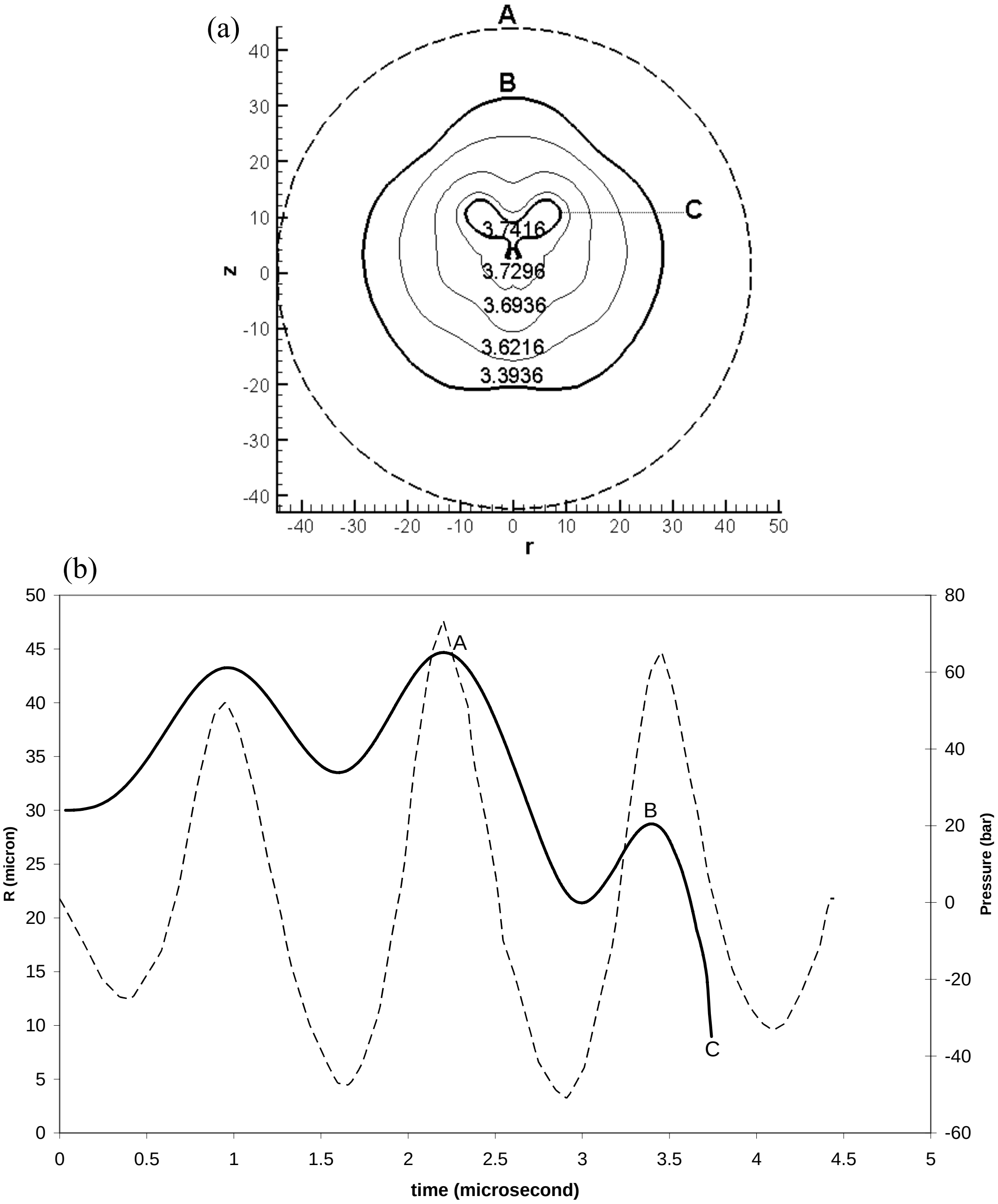

Fig. 5.8 (a) Profiles of a 30 μm bubble interacting with Pulse 1 (pulsed ultrasound of 1000 W/cm^2). The dashed line profile corresponds to the point **A** in (b) the bubble radius *R*, versus time curve (thick line, left *y*-axis). Also shown is the Pulse 1 pressure variation in time (dotted line, right *y*-axis). The final collapse from point **B** to **C** with the timing indicated is shown in (a). The final stage, the bubble developed multiple jets and is likely to break into several smaller bubbles.

In fact, as observed in previous sections, for microbubbles of ranges of size range between 0.1 and 30 μm, the maximum radius obtained has increased correspondingly. It is interesting to investigate the bubble dynamics with initial bubble radii that are even larger than the mentioned range interacting with the same pressure pulse (Pulse 1). For bubble of initial sizes between 40 to 100 μm, they primarily oscillate in the presence of Pulse 1. As depicted in Fig. 5.9, these bubbles do not collapse with a high speed jet. Instead they continue to oscillate after the passing of full three cycles of the imposed pulsed ultrasound waves as shown in Fig. 5.9(b). Also noted in Fig. 5.9(a) is the fact that the oscillation amplitude of the bubbles seems to be moderated as the initial bubble size increases. For example, within the time considered or equivalent to the passing of the pulsed ultrasound waves in Fig. 5.9(a), the 40 μm bubble oscillates between a maximum radius of 54 μm and a minimum of 34 μm. For the 100 μm bubble, however, the bubble gradually grows from its initial radius of 100 μm, to only about 110 μm when the final pulse passes the bubble. In fact, the bubble radius versus time in Fig. 5.9(a) appears as a series of 'perturbations' depicted within a drawn circle in the plot of Fig. 5.9(b). For a long period after this initial 'perturbation', the bubble continues to oscillate, way beyond the duration of Pulse 1 (about 5 μs). It is found that this 100 μm initial bubble continues to oscillate in its resonance frequency, f_0, given by Minnaert (1933) (mentioned in Chapter 2 (eqn. (2.16)), and repeated here for continuity of discussion) to be

$$f_0 = \frac{1}{2\pi R_0}\sqrt{\frac{3\gamma p_0}{\rho}}\,, \tag{5.3}$$

where R_0 is the initial bubble radius, γ is the ratio of specific heat of the gas content in the bubble (taken to be 1.4 because the gas is assumed to be ideal), p_0 is the atmospheric pressure, and ρ is the density of the fluid (in this case water). As an approximation, (5.3) can be simplified to

$$f_0 \approx \frac{3}{R_0}. \tag{5.4}$$

Therefore, the 100 μm bubble has a resonance frequence, f_0 = 30 kHz. The corresponding period is therefore T_0 = 33 μs. From Fig. 5.9(b), it is seen that the period of oscillation after the passing of the pulsed ultrasound is about 32 μs. This is indeed close to the theoretical calculation mentioned.

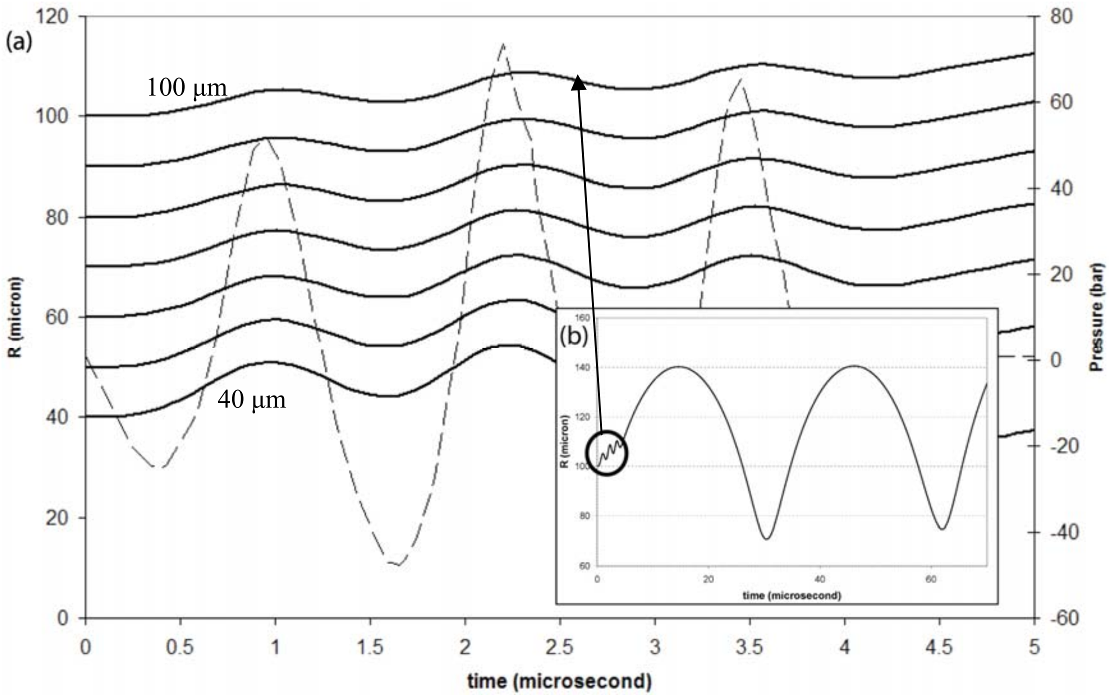

Fig. 5.9 (a) Oscillations of 40 to 100 μm bubble as a result of interaction with a pulsed ultrasound field (Pulse 1, 1000W/cm^2). The thick lines from bottom to top indicates the radius *R* variation in time for bubbles of 40, 50, 60, 70, 80, 90, and 100 μm in initial radii (left *y*-axis). Also shown is the Pulse 1 profile in dashed line with the corresponding pressure on the right *y*-axis. (b) Oscillation of a 100 μm bubble subjected to Pulse 1. The circled portion corresponds to the respective curve of the 100 μm bubble in (a) as pointed by the arrow. After the passing of the pulsed ultrasound, the bubble continues to oscillate in its resonance frequency of about 30 kHz (with a corresponding period of 33 μs).

If the bubbles are initially very large (much greater than 100 μm), they are hardly perturbed by the pulsed ultrasound waves. The bubble simply oscillates very ‘gently’ under the imposed sound fields of Pulse 1 to 4. Since no damping is included in the model, this oscillation will go on forever.

5.5 Conclusion

As the microbubble contrast agents are becoming more readily available, research on their use in more clinical procedures are being explored and developed. One ongoing area of research work is in the use of these bubbles for targeted drug delivery and cancer treatment. Strong ultrasound waves are utilized for cell sonoporation (so that macromolecular drugs or genes can enter the cells) or remote destruction of the microbubbles after they are attached to the diseased area. This procedure has the advantages of being non-invasive, can be easier monitored via bioimaging, and potentially economical.

To understand how this concept can be utilized, a numerical study is performed on the interaction of microbubbles of typical sizes (between 1 to 10 μm in radius) with pulsed ultrasound waves as used by Xu et al (2005). It is found that all the bubbles collapse within the first cycle of the pulsed ultrasound (which consists of three cycles). The maximum bubble radii obtained lie between 25 to 30 μm. When the intensity of the sound waves is increased (from Pulse 1 of 1000 W/cm^2 to Pulse 4 of 9000 W/cm^2), the bubbles expand to larger sizes before collapsing. However, the oscillation time remains fairly similar, this is because the increase in expansion time is offset by the decrease in the collapse time due to the higher positive pressure. Also, the maximum jet velocity obtained is not much affected by the increase in sound intensity. Nevertheless, the enhancement of tissue erosion by the increased intensity ultrasound as reported in Xu et al (2005) could possibly be explained by the broadening of jet radius from Pulse 1 to Pulse 4 or observed as an increase of the calculated Kelvin impulse. Also when exposed to the stronger intensity pulsed ultrasound waves, the further the bubbles translate in the direction of propagation of the waves. Thus, this movement of the bubbles to closer proximity to the cells, together with the widening of jet could well explain the more effective tissue ‘cutting’ due to higher shear stress generated with the higher ultrasound intensity.

If a microbubble has very small initial bubble radius for example 0.1 μm, it expands to about the same maximum bubble radius and collapses with similar oscillation time cycles as the 1-10 μm initial bubble radius. This is significant because potential bubble fragments arising from collapsed microbubbles could be induced by subsequent sound waves to expand to large sizes and collapse violently to cause collateral damage. For larger initial bubbles of between 20 to 30 μm in radius, however, the bubbles oscillate one or two more periods before collapsing. Because of the greater energy input from the sound waves, their collapse is even more violent than the previous smaller bubbles. However, if the initial bubbles are even larger at O(100 μm), they are hardly perturbed even by the strongest sound waves of Pulse 4.

Lastly it is mentioned that although these microbubbles are often operating/placed near tissues or organs in clinical settings, the nearby biomaterials are not modeled in this present study. The presence of biomaterial subjected to the pulsed ultrasound and response of the biomaterial to the dynamics of the bubble behavior which in turn affect the bubble behavior is likely to be a complex coupled interaction, and a subject for future studies. Lastly, the reader is referred to Fong et al (2008) for more details of the study in this chapter.

Chapter 6

Experimental observations of spark bubbles using high speed photography

In this chapter, experiments using a novel method for generating non-equilibrium spark bubbles are described. A simple setup utilizing relatively low voltages between 55 and 57 V is developed. This setup has advantages over previous works which employed high voltage for the breakdown of water (Buogo and Cannelli (2002), Soh and Willis (2003), Blake and Gibson (1981)) regarding safety and simplicity: there is no special safety measure required except for the avoidance of physical contact with the circuit when the capacitors are charged up and the water in the tank before the electrodes are short-circuited. Only a few standard electrical components, such as capacitors, switches, and wires are needed to make the circuit. Furthermore, only a slight modification is needed to generate multiple spark bubbles for the study of multiple bubble interactions which will be presented in section 6.4. One important feature of spark bubbles generated using this method is that the vapor pressure inside these spark bubbles is not negligible, as shown in Buogo and Cannelli (2002), and Lew et al (2006). From the simulations, it is found to be between 0.3 to 0.5 bar.

6.1 Experimental setup

The experimental setup consists of four main components: electrical circuit, water tank, high speed camera, and light source. Two similar circuits are used for the experiments described in section 6.3 and 6.4 respectively. For the single bubble near an elastic membrane (section 6.3), the circuit consists of a 55 V DC supply, 5300 μF capacitors (two of 1000 μF and one of 3300 μF, connected in parallel), and a 1 kΩ resistor as shown in Fig. 6.1(a). As for the multiple bubble experiments (section 6.4), a single 3300 μF capacitor, in series with a resistor of 1 kΩ, and a DC supply of 57 V (Fig. 6.1(b)), is used.

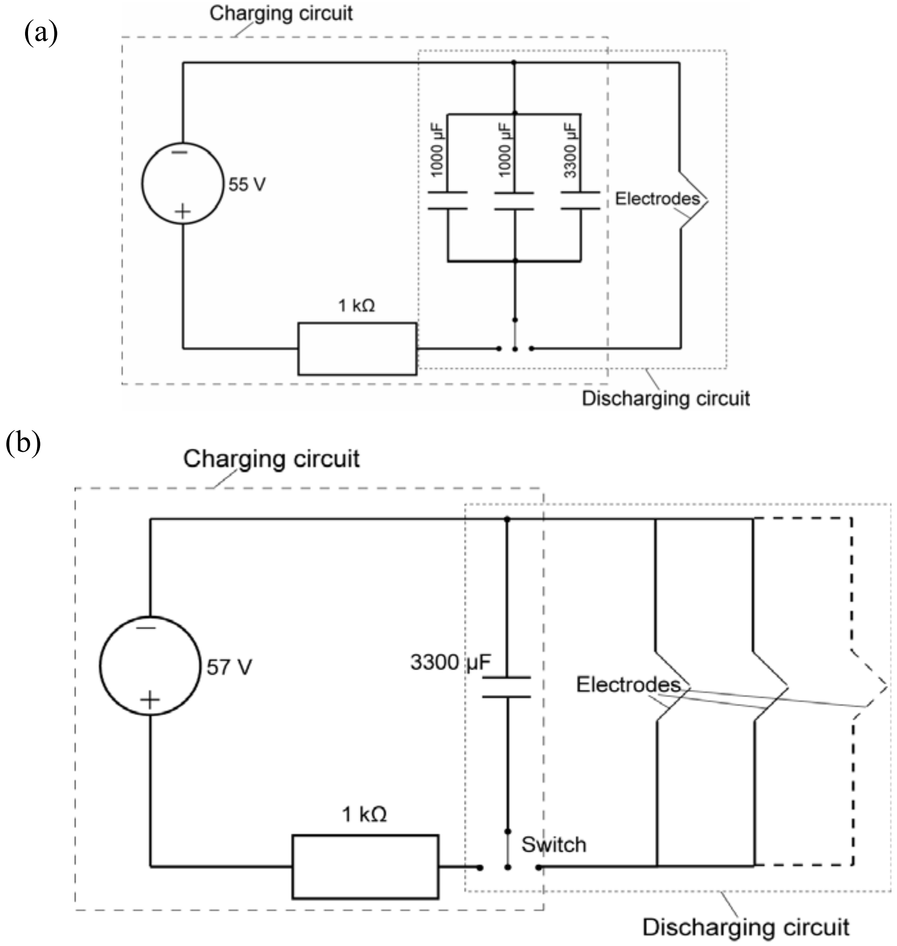

Fig. 6.1 Electrical circuits for spark bubble experiments involving (a) a bubble near an elastic membrane, and (b) multiple bubbles interactions; at the crossing of each electrode, a bubble is generated.

The tank used is an open-top transparent tank of 17x17x17 cm^3 size, in which a fixture was placed to hold a wire support. The wire support could be moved along the vertical axis of the wire fixture to a desired level and distance from the membrane, as well as incorporating multiple wire holders. At each of the wires' ends, copper-alloy electrodes (0.11 mm in diameter) are connected for the generation of a single cavitation bubble. The electrodes crossed and touched each other, and this appeared to be the best way to generate a large spark bubble. The size of the bubble produced was much larger (maximum bubble radii are from 2 to 4 mm) than the electrodes and thus their influence on the bubble's behavior was assumed to be negligible. The tank was initially filled up to about 80% with water. For the experiments involving an elastic membrane, the water is strongly degassed by boiling it and later letting it cool down to 25 °C. For the other set of experiments in section 6.4, ordinary tap water is used. The use of the different types of water has no significant influences on the results obtained.

The experiment works principally by charging the capacitors via the 'Charging circuit' in Fig. 6.1, and then discharging the electricity via the electrodes (see 'Discharging circuit' in Fig. 6.1) into the water to create the transient bubble(s). To record the events, a monochrome high speed camera (Photron Fastcam—APX Ultima Imager) with a framing rate of 12,500 frames per second (fps) and above is used. The shutter speed is set to 1/24,000 s. The camera was placed in front of the tank at a distance of approximately 45 cm. The scene is illuminated with a strong continuous spot lamp (ARRI-Arrislin) operated at an electric power of about 500 W. A white reflective board diffusely scattered the light and thus improved on the contrast of the bubble interior was used. The membrane was made from a cut rectangular piece (30 x 31.2 cm) of surgical glove. It was stretched by using two holders at the sides to a final length of 38.1 cm. Care was taken to eliminate the influence of the free surface by placing the membrane at 49.7

mm depth which was more than 10 times that of the maximum bubble radius, R_{max} (about 4 mm).

The thin copper alloy wires (the electrodes) were wound carefully to the thick copper wire used in the main circuits (Fig. 6.1). Since the electrodes were so thin, they broke off during the experiment, partly ‘vaporized’, and had to be replaced for the next experiment. When the electrodes were ‘shorted’, the intense heat and pressure due to this initial electrical discharge caused the formation of plasma at the bubble center. The bright light following that rendered the bubble shape in the first few frames of the high speed photographs indistinguishable. Nevertheless, the bubble cooled down quickly and the rest of its dynamics was able to be captured accurately and clearly. Also, the heat generated during the plasma formation caused the burning off of the electrodes. With this, the electrical discharge was stopped, and some of the initial voltage at the beginning of the discharge process remained (Lew et al, 2006).

6.2 The growth and collapse of a single spark bubble in a free field

High temperature and pressure at the contact point of the electrodes ionized the water to generate plasma and subsequently a rapidly expanding bubble. Although the content of the bubble generated using the above mentioned setup is not known exactly, it is presumed to be mainly made up of diatomic gases (for example H_2 and/or O_2) with some water vapor and hot metal vapor from the electrodes. These vapors contribute to the pressure in the bubble during the early expansion phase. In the experimental observations shown in Fig. 6.2(a), it is seen that the bubble grew to a maximum radius,

$R_{\max} \approx 3.28$ mm, and then collapsed spherically. Finally the bubble in Fig. 6.2(a) breaks into many small fragments due to the violent nature of the collapse. It is noted that p_v varies slightly from experiment to experiment.

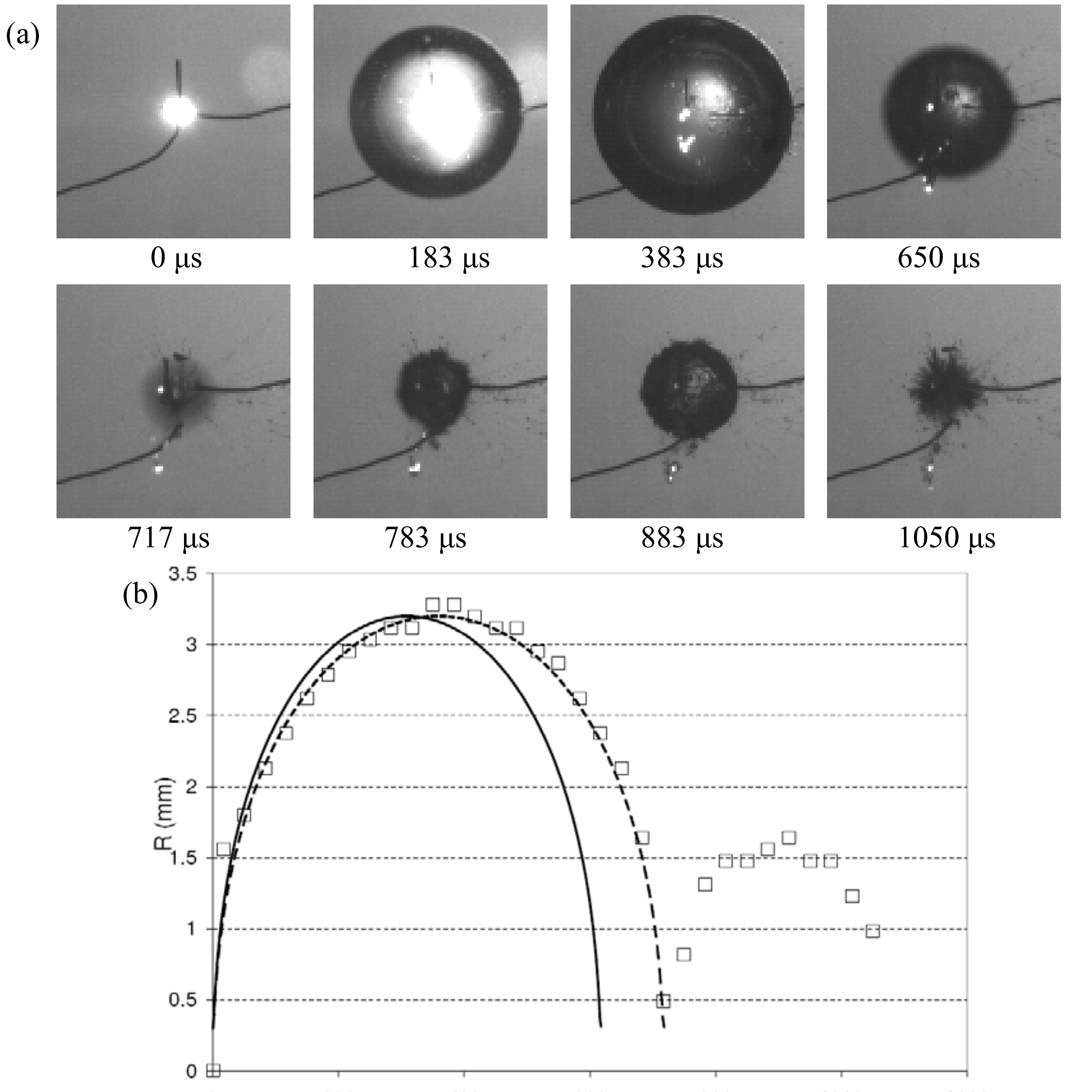

0 µs 183 µs 383 µs 650 µs

717 µs 783 µs 883 µs 1050 µs

Fig. 6.2 (a) Selected frames showing a spherical expansion and collapse of a single bubble with maximum radius $R_{\max} = 3.28$ mm (as seen in frame t = 383 µs) in a free field with the time from the start of the spark (first image). The bubble rebounds and collapses again in the last three frames (from t = 783 µs to t = 1050 µs). Pictures reproduced courtesy of Daan Martens. (b) Bubble radius-time histories: a comparison between experiment and theory. The dashed and solid lines represent the curves with vapor pressure $p_v = 0.26 \times 10^5$ and 0 Pa, respectively, and the squares represent the experimental data.

From the high speed video, the bubble radius versus time data for a single oscillation is obtained as shown in Fig. 6.2(b) (in squares). The result is compared with theoretical calculations using the Rayleigh-Plesset equation (2.10). Two solutions are plotted with $p_v = 0.26 \times 10^5$ Pa (dotted line), and $p_v = 0$ Pa (solid line) respectively. It is seen from Fig. 6.2(b) that the period of oscillation for the bubble with $p_v = 0$ Pa is significantly shorter: the bubble reaches its maximum size of 3.20 mm at 323 μs, and collapses to its minimum size at about 618 μs. But for results with $p_v = 0.26 \times 10^5$ Pa, the curve matches very well with the experimental data. In fact for all the simulations to be presented in this chapter, p_v is taken to be either 0.4×10^5 or 0.5×10^5 Pa (obtained with comparison to the time scale in experimental observations), depending on the fit with the experimental results. The bubble reaches its maximum radius at 370 μs and collapses after 720 μs. Buogo and Cannelli (2002) reported an experiment with a spark bubble of $R_{\max} \approx 35$ mm that the vapor pressure was indeed as high as $p_v = 0.3 \times 10^5$ Pa.

6.3 Spark bubble interaction with an elastic membrane

It is known that when a bubble collapses near a solid boundary, it will form a high speed jet towards the boundary. When it is near a free surface, however, the jet formed is away from the interface. The free surface develops a water plume which is opposite in direction to the jet in the bubble. If the nearby interface has elastic properties, the bubble behaviors are rather complex. Early experiments by Tomita and Kodama (2003) and Shima et al (1989) used a laser to generate a bubble near composite materials. One of the materials they used consisted of a silicone rubber plate on top of foam rubber. The elastic surface influenced the flow around the bubble as it oscillated causing it to split into two, or form a ‘mushroom’ shaped bubble, or migrate away from the compliant surface. Brujan et al (2001a and b) have also performed a series of experiments of a laser generated bubble near an elastic material. In this case, they used polyacrylamide gel as an elastic boundary. More interesting and complex bubble behaviors are observed, such as the mentioned ‘mushroom’ shaped bubble formation, bubble splitting, and elevation and repulsion of the elastic interface.

More relevant literature includes a short study by Shaw et al (1999) on the interaction of a laser bubble near a thin elastic membrane. Again phenomena such as ‘mushroom’ shape bubble formation and bubble splitting were observed. Some of the bubble profiles seen were similar to that of Brujan et al (2001a and b). Based on the experimental results to be presented here, Turangan et al (2006) performed BEM simulations using the parameters measured. Simulations results in very good agreement with experimental results were obtained. The author wish to acknowledge the effort of Ong Geok Pei in the experimental results presented in Section 6.3. She was a mechanical engineering student under the supervision of the author.

6.3.1 Growth and collapse of a spark bubble 3.0 mm away from the membrane

It is reported by Tomita and Kodama (2003) that the 'mushroom' shape bubbles were observed when the distance between the bubble center and the elastic boundary is less than one maximum bubble radius (R_{max}) away. In this experiment shown in Fig. 6.3, a spark bubble is created 3.0 mm away from the membrane (R_{max} = 4.41 mm). As seen in frame (i) at t = 0 μs, the crossing point of the electrodes (where the bubble will be initiated) is located at 3.0 mm from the membrane. Frame (ii) shows the expanding bubble at t = 640 μs. The bright spots on/near the bubble surface are possibly due to the burning of the electrodes that have been broken into small pieces.

At t = 800 μs, the bubble obtains its maximum radius, R_{max}, of 4.41 mm. Since the bubble is located less then one R_{max} away from the membrane, its bottom surface becomes flattened as its expansion is partly hampered by the membrane. The compliant membrane is, in turn, being pushed away. Then the bubble enters its collapse phase. Frame (iv) and (v) show the bubble shrinking to a smaller volume from its maximum at frame (iii). Then at t = 1200 μs (frame (vi)), both left and right sides of the lower bottom surface of the bubble seems to be forming jets that eventually cause the development of a 'mushroom' shape bubble at frame (vii). The jets meet each other, and break the bubble into two smaller bubbles at t = 1360 μs (frame (viii)).

Meanwhile, the elastic membrane moves with the bubble as it shrinks from its maximum at frame (iii) to its minimum before splitting into two bubbles at frame (vii). Then the membrane forms a hump when the bubble collapses into two at the last frame. This movement of the membrane is believed to be a repulsion back towards the bubble due to its elasticity since it was pushed away when the bubble expands to its maximum. Because of this, the momentum in the water induced by the membrane movement is transferred to the bubble in a form of perturbation that propagates from the bottom to the top of the bubble. This contributes to the formation of the ‘mushroom’ shape bubble. Apart from this, there are also clearly observable surface waves on the membrane. This waves travel from the center of the membrane where the bubble is, and then across the membrane surface towards the side clamps.

6.3.2 Growth and collapse of a spark bubble 4.16 mm away from the membrane

In this case (results shown in Fig. 6.4), the bubble is located more then one R_{max} away from the membrane as seen in frame (i). The influence of the membrane on the bubble is not significant because of the distance involved. As the bubble grows to its maximum size from frame (ii) to frame (iii), the membrane is only slightly pushed down. The bubble obtains a R_{max} of 3.2 mm at t = 400 μs (frame (iii)). Then the bubble collapses spherically from frame (iv) to frame (v). It obtains its minimum size at t = 720 μs (frame (vi)). Instead of a single bubble, it is then fragmented into many small bubbles which clump together and rebound in frame (vii). It collapses again at t = 960 μs (frame (viii)). Throughout the collapse phase, the membrane is hardly perturbed. It remains flat in its equilibrium position even at the rebound of the bubble at frame (vii).

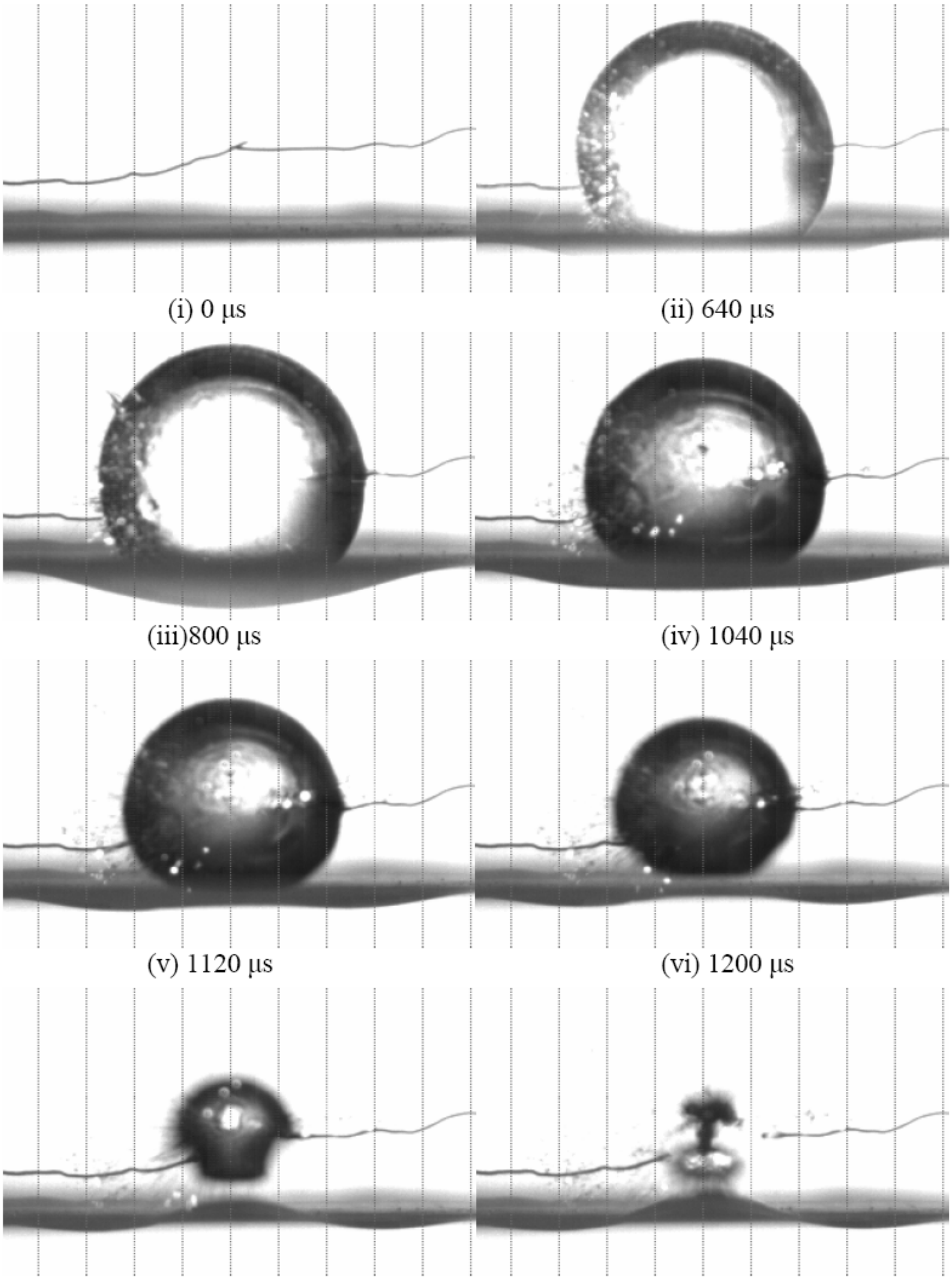

(i) 0 µs
(ii) 640 µs
(iii)800 µs
(iv) 1040 µs
(v) 1120 µs
(vi) 1200 µs
(vii) 1280 µs
(viii) 1360 µs

Fig. 6.3 Sequence of experimental result of a bubble initiated 3.0 mm above a membrane from (i) to (viii). Pictures taken from Ong (2005) and Ong et al (2005) with permission. Time was taken from the frame just before the spark was observed as t = 0 µs at (i). The corresponding time in microseconds is noted under each image. The bubble expands from (ii) to its maximum size (R_{max} = 4.41 mm) at (iii), pushing away the membrane. Then it enters its collapse phase from (iv) to (viii). The membrane moves towards the collapsing bubble. Noticeable traveling waves in the membrane are observed. No jet is formed; instead, a 'mushroom-shaped' bubble is seen in (vii) t = 1280 μs. Then the bubble splits up in two parts at (viii) t = 1360 μs. The bottom bubble is larger than the top bubble.

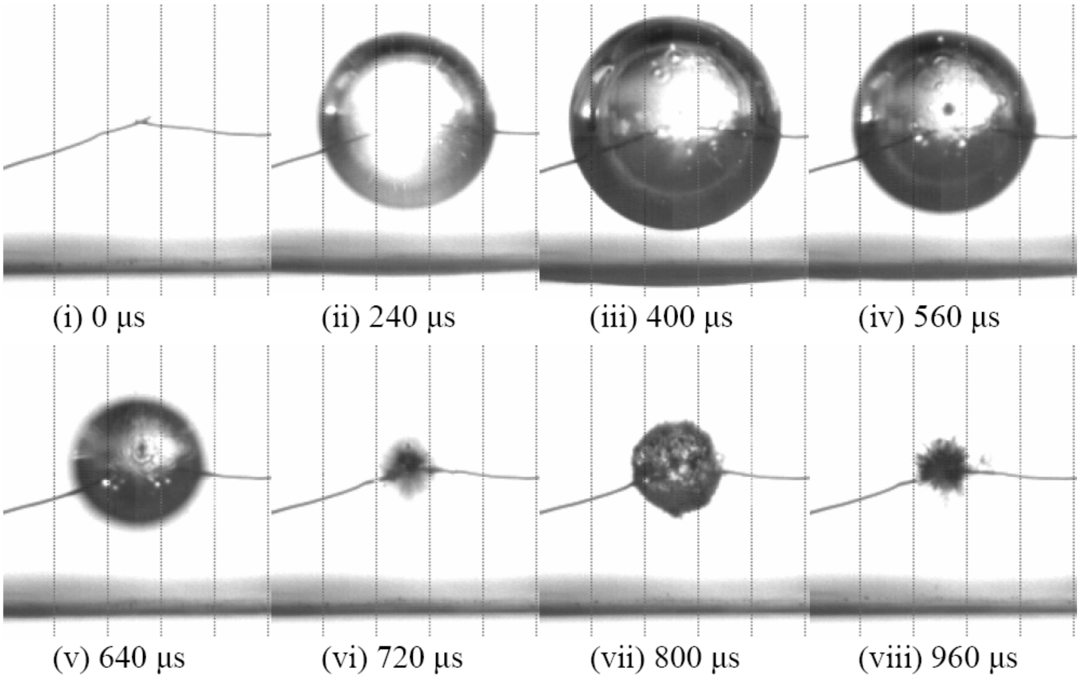

Fig. 6.4 Experimental observations of a spark bubble initiated 4.16 mm above an elastic membrane (frame (i)). Pictures taken from Ong (2005) and Ong et al (2005) with permission. The bubble obtains its maximum radius, R_{max}, of 3.2 mm at 400 μs (frame (iii)). Then the bubble collapses spherically to its minimum at frame (vi) (t = 720 μs). After that the bubble rebounds at frame (vii) (t = 800 μs), and collapses again at frame (viii) (t = 960 μs).

6.3.3 Growth and collapse of a spark bubble 2.9 mm away from the membrane

Another set of experiments with the distance between the bubble and the membrane less than R_{max} is presented in Fig. 6.5. The general behavior is similar to that presented in Fig. 6.3. Frame (i) shows the initial position of the electrodes. Initially the growth of the bubble is not visible due to the brightness of the spark. At t = 800 μs, the bubble outline is first seen. It then expands to its maximum size of R_{max} = 4.5 mm in frame (iii), after which, the bubble collapses. Frames (iv) and (v) (t = 1200 μs and t = 1280 μs respectively) show the initial stage of the collapse. Because the bubble is slightly nearer to the membrane (2.9 mm away as compared to Fig. 6.3 where the bubble is 3.0 mm away), the bottom surface of the bubble is more flattened than the previous experiment described in section 6.3.1. A ‘mushroom’ shape bubble is eventually formed (frame (vii)). However, the size of this ‘mushroom’ shape bubble is slightly larger than that described in Fig. 6.3. Also, in the last frame the bubble breaks into two bubbles of almost equal size, as compared to a larger bottom bubble and a smaller top bubble in the previous experiment.

The elastic membrane is pushed away by the expanding bubbles in frames (ii) and (iii). It moves towards the bubble as the bubble collapses. As mentioned in section 6.3.1, this causes the fluid flow around the bubble which eventually results in the formation of the ‘mushroom’ shape bubble. In the last frame, the membrane is seen to move upwards to form a hump underneath the split bubble. In conclusion, it is clear that the presence of a nearby membrane has a profound influence on the behavior of an oscillating bubble. It exhibits complex dynamics such as the formation of a ‘mushroom’ shape bubble, bubble splitting and jetting. Also, it induces a surface wave on the membrane which starts at the bottom of the expanding bubble, and travels towards the still collapsing bubble at frame (viii).

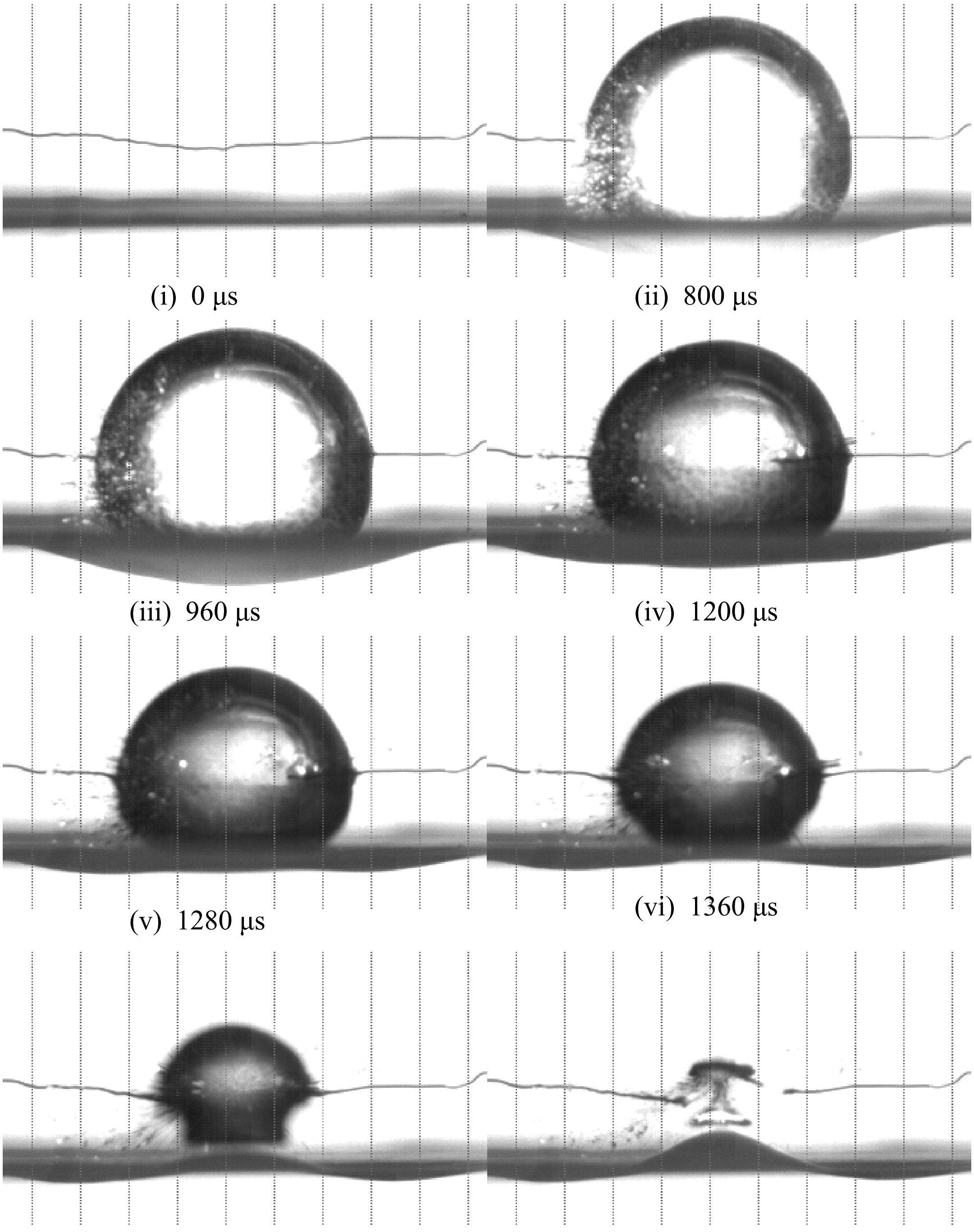

(i) 0 μs

(ii) 800 μs

(iii) 960 μs

(iv) 1200 μs

(v) 1280 μs

(vi) 1360 μs

(vii) 1440

(viii) 1520 μs

Fig. 6.5 The growth and collapse of a spark bubble which is initiated 2.9 mm above the elastic membrane (frame (i)). Pictures taken from Ong (2005) with permission. The sequence is to be interpreted from top left to bottom right (frame (i) to (viii)). The bubble grows to its maximum size at t = 960 μs, and obtains a R_{max} of 4.5 mm (frame (iii)). It collapses with a flattened bottom surface in frame (iv) and (v). The next two frames (frame (vi) and (vii)) see the formation of a 'mushroom' shape bubble. In the last frame, the bubble splits into two bubbles of almost equal size.

6.4 Multiple bubble interaction – comparison with simulation results

Using the spark discharge circuit with the modification presented in section 6.1, multiple sparks can be generated to initiate several violently oscillating bubbles at the same time. It will be shown that interesting and complex interactions between bubbles are resulting, such as jet formation, translational movement due to attraction or repulsion, and coalescence between two bubbles. The interactions between the bubbles depend on several factors: the distances between the bubbles, their relative sizes, and the spark initiation times. Because of the large number of possible combinations of these parameters, only selected and distinct cases are discussed in turn. Cases numbered 1, 2 and 3 involve bubbles that are arranged almost in-line and Cases 4 to 6 for bubbles placed in a triangular configuration. The three bubbles involved in Case 1 are created at the same instant (in phase). In Case 2 and 3, the bubbles are not in phase; Case 2 has an earlier generated center bubble which reaches a smaller maximum radius as compared to the two outer bubbles while in Case 3, the center bubble is generated later. In both Case 4 and 5, the bubbles are generated at the same instant, but for Case 5, they are placed very near each other with respect to their maximum radii. Case 6 documents the situation whereby the bubbles are created one after another, and an interesting phenomenon, termed the 'catapult' effect is observed. Here a high speed jet with a velocity of more than 180 m/s is found when the bubble is close to its maximum size. Some discussions on the coalescence of bubbles and other phenomena will be presented following the presentation of all the cases (from 1 to 6).

The geometrical arrangement and the separation distances of the bubbles in these experiments are controlled by the physical placement of the crossing points of the electrodes. The bubbles are created centered at these crossing points. The timing of the bubble generation is determined by the connection of the thin electrodes on the anode and cathode wires; the differences in the tightness of the winding of the electrode to the thicker copper wire give rise to the generation of out-of-phase bubbles. Also, the difference in bubble size is caused by the slight difference in the electrodes' contact at the respective crossing points. Nevertheless, the current experimental setup renders a fair degree of control of bubble locations and inception time. Numerical simulations using a 3D BEM program are also performed to facilitate the understanding of the flow dynamics involved. The details about the modeling and numerical methods can be found in section 2.3.2.

It is noted that some of the experiments are performed by Deepak Adhikari of the National University of Singapore (as noted in the captions of the respective figures) under the guidance of the author. The rest of the experiments and all of the simulations are done by the author.

6.4.1 Case 1: Three bubbles arranged almost in-line and in-phase

The three electrodes used for the generation of three spark induced bubbles are arranged in a linear manner as shown in Frame 1 of Fig. 6.6. The camera speed used here is 20,000 fps (frames per second) with a shutter speed of 1/20,000. In all the experimental results presented from this point onwards, the frame number as recorded with the high speed camera is indicated in the images. However, only the most interesting frames (correspondingly numbered) are shown. Frame 1 always corresponds to the frame just before the first appearance of a spark that will generate the first bubble in the experiment.

The distance between the contact points of the top and center electrodes ($l_{1,2}$), and the center and bottom electrodes ($l_{2,3}$), are 8.14 and 7.79 mm, respectively. In the simulation, coordinates of the bubbles are set to be at (in mm) (-1.17, 0.0, 8.06), (0.0, 0.0, 0.0), and (0.583, 0.0, -7.77) for the top (bubble 1), center (bubble 2), and bottom (bubble 3) bubble, respectively. These coordinates are assigned to match the locations of the bubbles in the physical experiment with the assumption that the bubbles are exactly on the same plane of $y = 0$ (the y-axis is perpendicular to the viewing plane).

The maximum bubble radii obtained for the top ($R_{max,1}$), center ($R_{max,2}$), and bottom ($R_{max,3}$) are 2.38, 3.03, and 2.69 mm, respectively. These maximum radius values are obtained by measuring the bubble radii at the frames whereby they each appear to be largest. This way of measurement is fairly accurate because the change in bubble size slows down as the bubble approaches its maximum size thus allows the camera to capture several frames for measurement and comparison. The subscripts '1', '2' and '3' refer to bubbles 1, 2 and 3. Their initial radii for the simulations ($R_{0,i}$) are 0.0940, 0.0736, and 0.0833 mm. These initial radii are calculated by considering the Rayleigh Plesset equation when the bubbles are at their maximum sizes ($R = R_{max,i}$). At this time, the velocity is equal to zero and the following equation (see (2.15) of Chapter 2) is valid:

$$\frac{R_{0,i}^3}{R_{\max,i}^3} - 1 = \frac{p_0}{p_{ref}} \frac{1}{\gamma - 1} \left(\frac{R_{0,i}^{3\gamma}}{R_{\max,i}^{3\gamma}} - \frac{R_{0,i}^3}{R_{\max,i}^3} \right), \tag{6.1}$$

where p_0 is the initial pressure (which is taken to be 362.4 bar for all simulations in this chapter based on an explosion bubble model), p_{ref} is the reference pressure (taken to be equal to atmospheric pressure, 10^5 Pa), and γ is the specific heats of the gases inside the bubble (which is taken to be equal to 1.4). Therefore by knowing $R_{max,i}$, one can easily calculate $R_{0,i}$. All bubbles are created at the same instance. The vapor pressure, p_v, is taken to be 0.5 bar in this case. The vapor pressure is determined by matching the time scale of the simulation (converting from its dimensionless form) to the experimental observations. Different vapor pressure is possible for the experiments mentioned in this chapter because of the slight difference in the spark duration used for the generation of the bubble. The spark duration is determined by the tightness of the wounding of the electrodes on the wires and the speed at which the switch for discharging the capacitor is pressed.

The bubble phenomena following their generation are highly dependent on the relative bubble size and their separations (Tomita and Shima, 1990). In this case, the bubbles are placed 2 to 3 times their maximum radii apart, with the center bubble (bubble 2) being slightly bigger in size. Bubble 1 reaches its maximum size first (Frame 11, Fig. 6.6) while the other bubbles are still expanding. It therefore collapses earlier. Due to the presence of bubble 2, its collapse is not spherical, but is affected with a jet towards bubble 2 (Frame 18 and the corresponding simulation figure of Fig. 6.6, and Frame 19 of Fig. 6.8). It is noted that the results presented in Fig. 6.8 are a continuation of that of Fig. 6.6.

The development of the jet with enhanced temporal resolution is shown in the simulation of the collapsing stage of bubble 1 in Fig. 6.7. It is noticed that the jet is directed toward the top section of the elongated bubble 2 (Fig. 6.6). The maximum velocity obtained is about 50 ms^{-1}, which is comparable to that of a bubble jetting towards a solid wall. Meanwhile the bottom section of bubble 2 is attracted (or pulled) towards the bottom bubble, bubble 3, resulting in an ellipsoidal bubble 2 at t = 746 μs (Fig. 6.6).

Before the jet impacts onto the lower interface of bubble 1, bubble 3 has expanded to its maximum radius in Frame 14 (Fig. 6.6) which is earlier than the largest bubble, bubble 2. In Fig. 6.8, the thin jet from the top bubble 1 moves towards the other two bubbles as it rebounds. Bubble 2 also moves slightly towards bubble 3 as it collapses and forms a jet towards bubble 3 (Frame 22-24, Fig. 6.8). Bubble 3 migrates vertically towards bubble 2 in Fig. 6.8, and eventually collapses with a jet towards bubble 2.

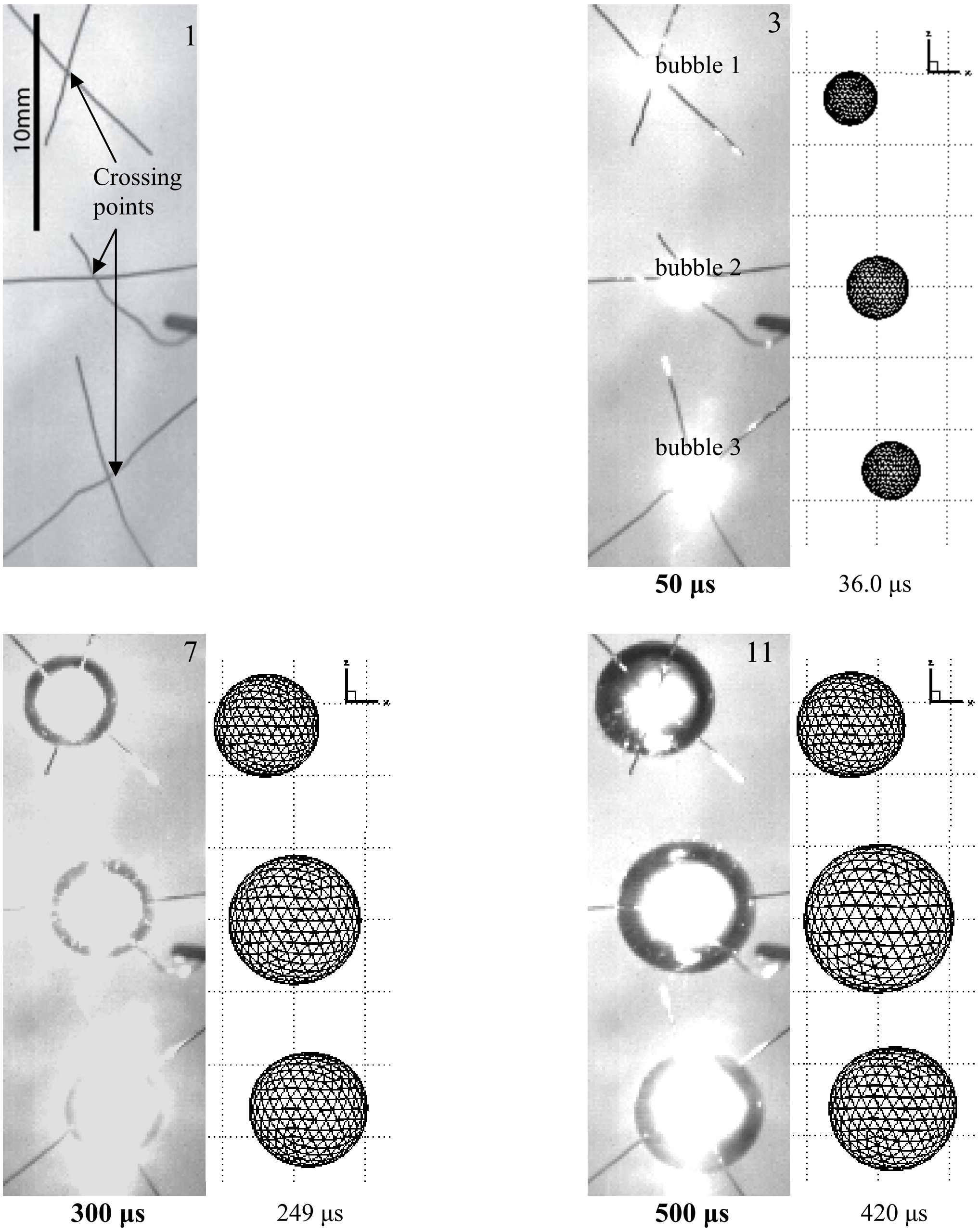

(Caption for figure on the next page)

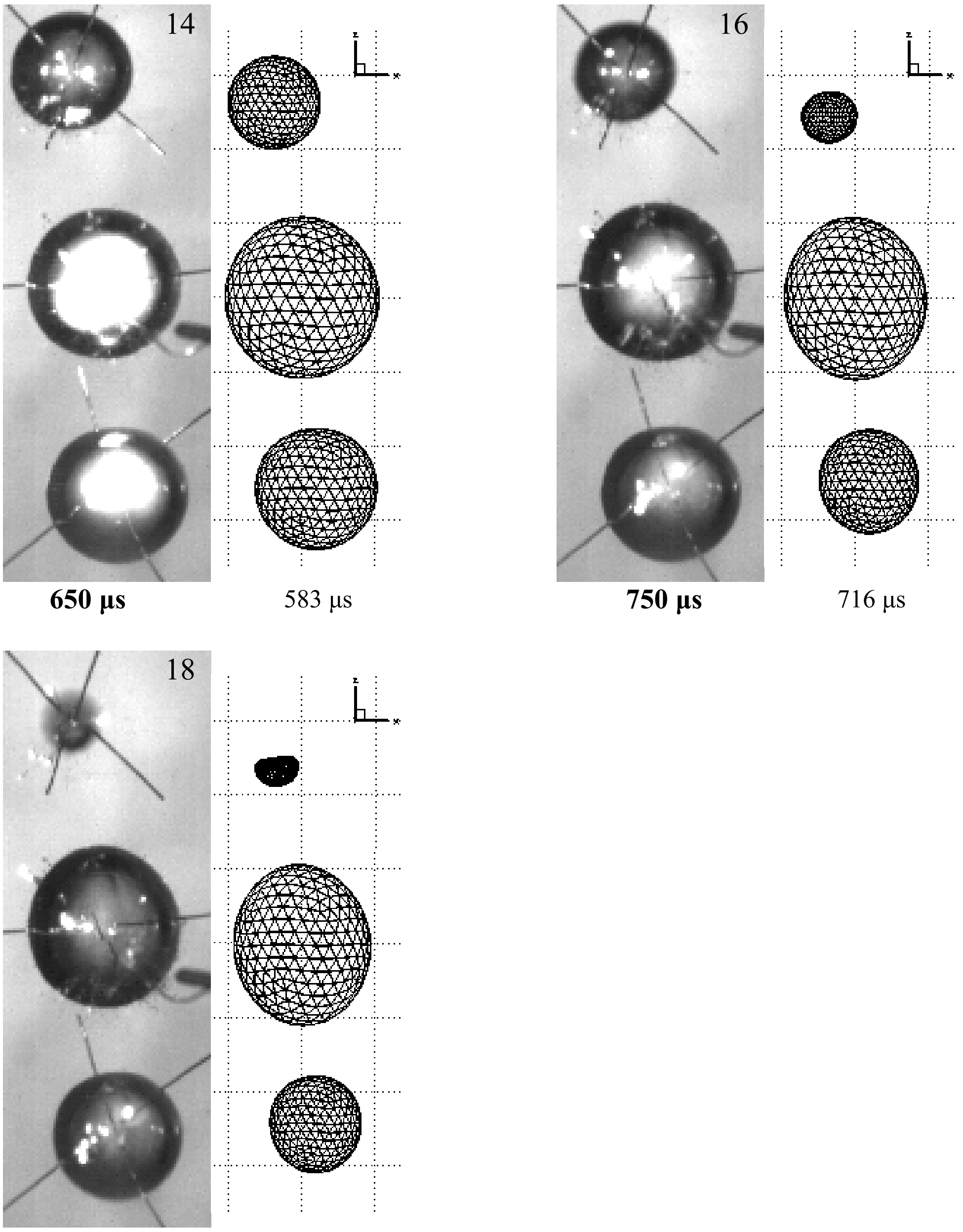

650 µs 583 µs

750 µs 716 µs

850 µs 746 µs

Fig. 6.6 Case 1: Numerical comparison with experimental results (experimental results reproduced with permission from author (Adikhari, 2006)). The three bubbles are generated at the same time. Bubble 1, being smallest in size, collapses first. It forms a jet towards bubble 2. The figures on the left of the pair are experimental observations from the high speed camera filming at 20000 frames per second. Frame 1 corresponds to the frame just before the bubbles are created, t=0 µs. The frame number and time in µs are indicated on the photographs. The bubbles are created at the 'crossing points' as indicated at Frame 1. The figures on the right of the pair are simulation results with time in µs provided. The vapor pressure, p_v, is taken to be 0.5 bar. It is noted that the last simulation result (t=746 µs) does not match exactly to the timing of Frame 18 (t=850 µs) since the former depicts an observation that should occur slightly before Frame 18 as the top bubble in Frame 18 has completely collapsed while in the simulation, the jet in the collapsing bubble has just reached its opposite wall.

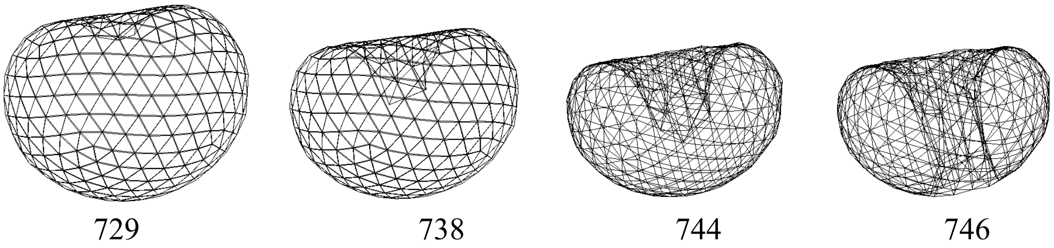

Fig. 6.7 Case 1: Final stage of collapse of the top bubble (bubble 1). Simulation results in 3D, with time (t) in μs as indicated between the subfigures from t=729 to 746 μs. The jet formed is directed towards bubble 2 (not shown here) with a maximum jet velocity of about 50 m/s.

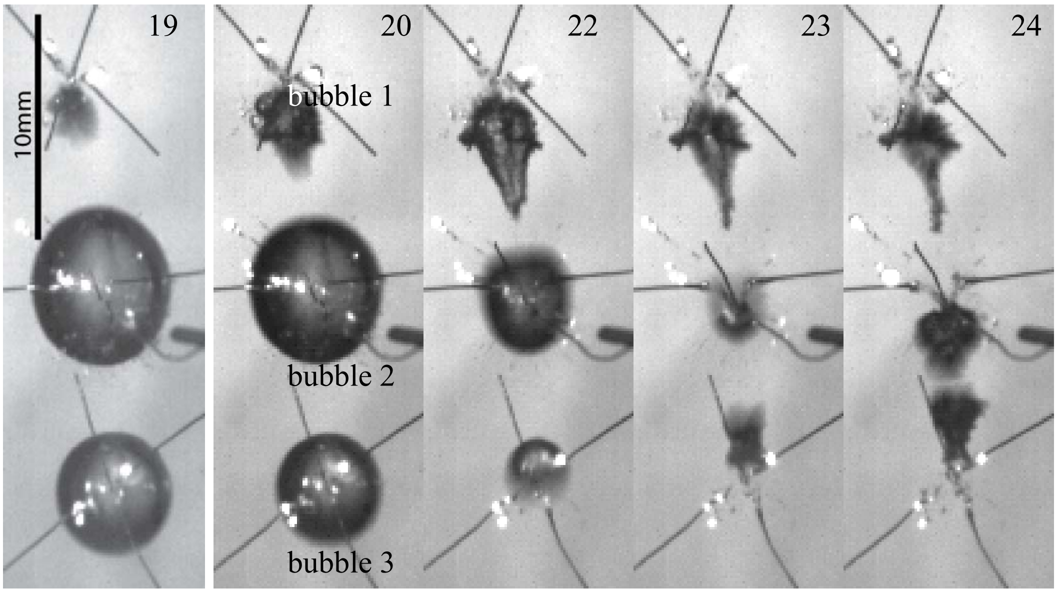

Fig. 6.8 Case 1: Experimental results after the collapse of the top bubble (reproduced with permission from author (Adikhari, 2006)). The inter-frame rate used is 20000 frames per second. The frame number continues from that in Fig. 6.6. The top bubble 1 has fully collapsed with a thin jet towards bubble 2. Bubble 3 migrates significantly towards bubble 2 as they collapse with jets towards one another.

6.4.2 Case 2: Three bubbles arranged almost in-line with center bubble created 25 μs earlier

The same arrangement of the electrodes as in Case 1 is utilized for this experiment. The distances between the contact points of the top and center electrodes

($l_{1,2}$), and that of the center and bottom electrodes ($l_{2,3}$), are 9.08 and 7.01 mm, respectively. In the numerical simulations, the coordinates of the bubbles (in mm) are (-0.332, 0.0, 9.07), (0.0, 0.0, 0.0), and (0.774, 0.0, -6.97) for the top (bubble 1), center (bubble 2), and bottom (bubble 3) bubbles. Bubble 2 is created at time $t = 0.0$ s. A slight moment later, bubble 1 and bubble 3 are generated at time, $t = 25$ μs (time obtained from experimental observation). The maximum bubble radii obtained for the top ($R_{max,1}$), center ($R_{max,2}$), and bottom ($R_{max,3}$) are 2.87, 2.65, and 2.79 mm accordingly. Camera settings are the same as that of Case 1. In the simulation, the vapor pressure, p_v, is set to be 0.5 bar.

In contrast to Case 1, the maximum size of the center bubble (bubble 2) is slightly smaller in size than the other bubbles. It has expanded to its maximum radius at Frame 12 (Fig. 6.9). Bubble 2 then starts contracting while bubble 1 and bubble 3 are still expanding. The expansion of bubble 1 and bubble 3 causes the flattening of bubble 2's top and bottom surfaces (Frame 13, Fig. 6.9). Lauterborn (1982) points out that since smaller bubbles have shorter collapse times, the highly curved parts of a bubble should therefore collapse faster. As a result, a flattened bubble like bubble 2 collapses along its equator (the part with the initially highest curvature) as observed in Fig. 6.9, and seems to break up into two parts in Frame 16 (see Fig. 6.10, frame 17).

The 'dumbbell-shaped' bubble observed in the simulation for t = 686 μs and 759 μs is also reported in other experimental settings, such as a single bubble placed between two solid walls (Shima and Sato (1980), Ishida et al (2001)), near a composite surface (Shima et al, 1989), and two simultaneously produced bubble near a rigid boundary (Tomita et al, 1994). The phenomenon for the last mentioned reference has also been simulated by Blake et al (1993). Qualitatively, it is argued that the rapid expansion of the larger bubbles (bubble 1 and bubble 3) causes the water between them and the smaller center bubble to be continuously confined or influenced by the presence of neighboring boundaries. This invariably led to the production of a flow field similar to that induced for a bubble between two rigid walls. In the sequence of breaking into two, the external liquid that rushes in at the equator of bubble 2 caused the squeezing of internal gaseous fluid at the poles.

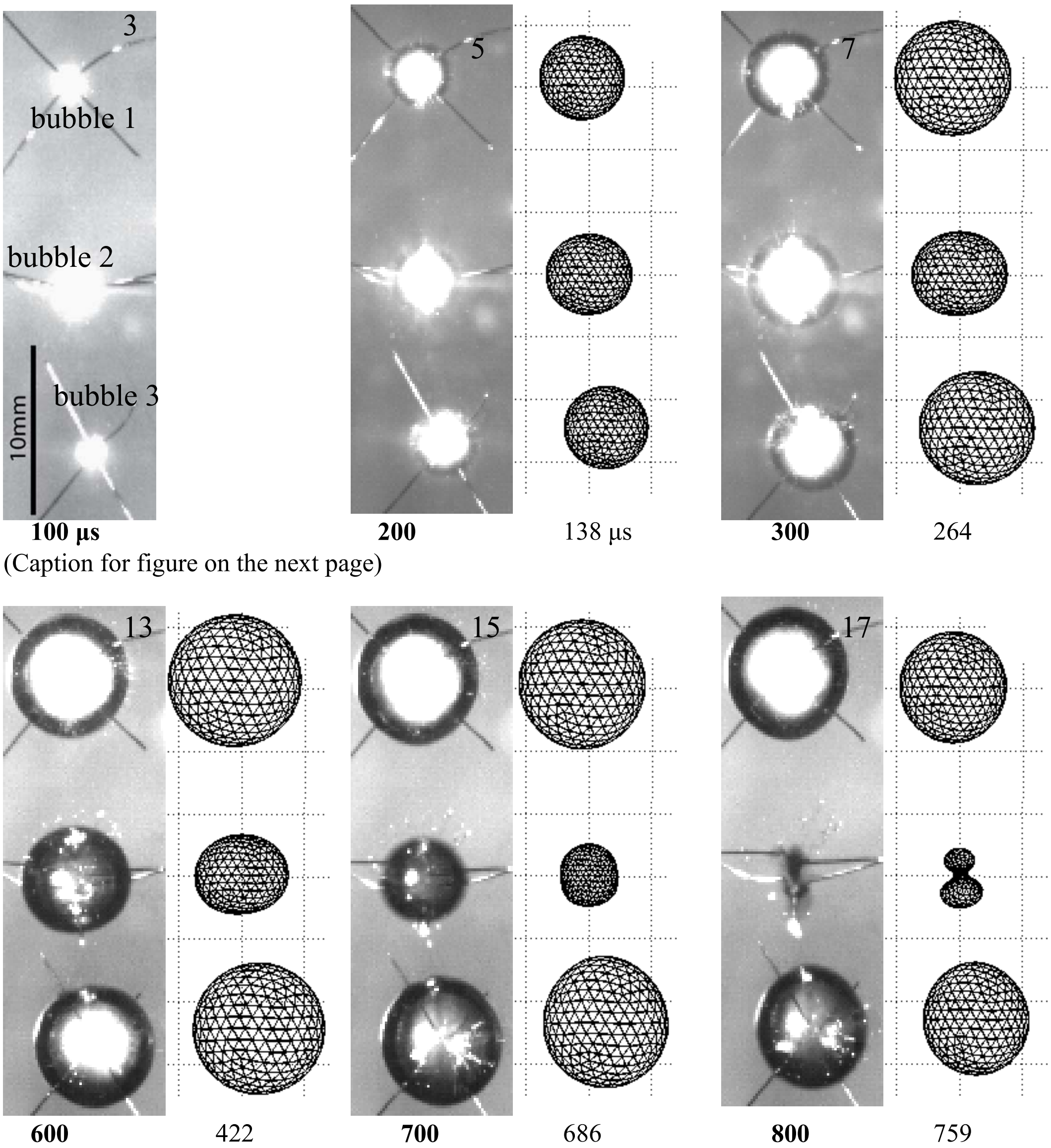

(Caption for figure on the next page)

Fig. 6.9 Case 2: Experimental results plotted together with numerical simulations (experimental results reproduced with permission from author (Adikhari, 2006)). Bubble 1 and 3 are created 25 μs after bubble 2. The center bubble 2 enters its collapse phase while bubble 1 and 3 are still expanding. Being much flattened on both the top and bottom surfaces, bubble 2 collapses along its equator forming a 'dumbbell-shaped' bubble. The left figures of the pair are experimental observations from the high speed camera filming at 20000 frames per second. Frame 1 corresponds to the frame just before the bubbles are created (frame 1 to 4 are not shown here). The frame number and time in μs are indicated on the photographs. The right figures of the pair are simulation results with the time in μs provided. They roughly correspond to the experimental results in (a). For example the last simulation result t=759 μs corresponds to Frame 17 in (a) (t=800 μs). The vapour pressure, p_v, is taken to be 0.5 bar.

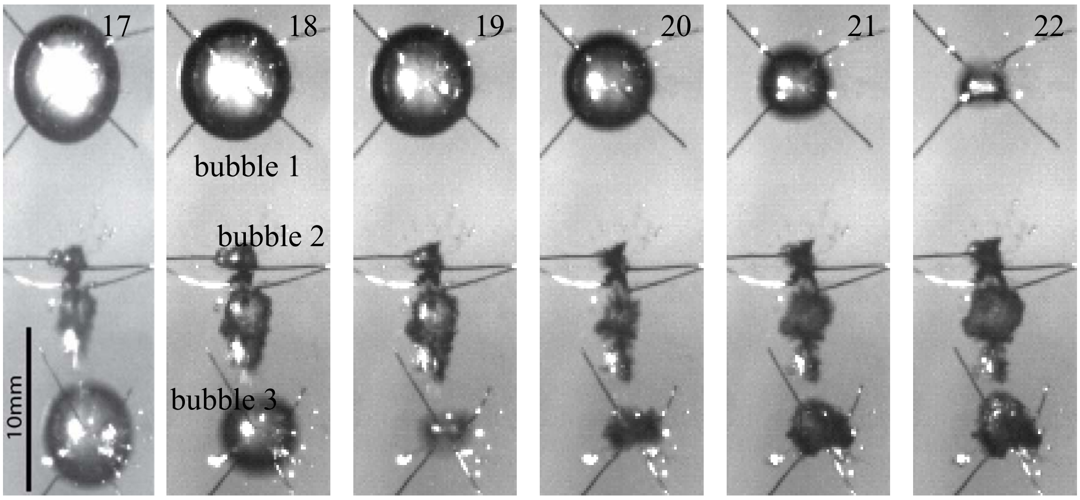

Fig. 6.10 Case 2: Experimental results after the collapse of the center bubble. The frame number continues from that in Fig. 6.9. As bubble 2 has fully collapsed while bubble 1 is still expanding (Frame 17), when it eventually collapses (Frame 22), it does so almost spherically. Bubble 3, on the other hand, collapses with a jet towards bubble 2.

As bubble 1 is still expanding when bubble 2 has collapsed (Frame 16, Fig. 6.9), and reaching its maximum size only in Frame 17 (Fig. 6.10), the upper child bubble of bubble 2 is much smaller and produces a smaller upwards jet relative to the lower child bubble. Furthermore, bubble 1 begins its collapse phase only after the upper child bubble of bubble 2 has fully collapsed, the latter's influence is negligible and thus bubble 1 collapses almost spherically with no vertical translation (Fig. 6.10). On the other hand, bubble 3 expands to its maximum radius at Frame 16 (Fig. 6.9) and has started to collapse even as the jet from bubble 2's lower child bubble is developing and directing towards bubble 3. As a consequence, bubble 3 also collapses with a jet directed towards bubble 2 (Frame 22 to 23, Fig. 6.10).

6.4.3 Case 3: Three bubbles arranged almost in-line with the center bubble being created slightly later

Similar to the previous two cases, the electrodes in Case 3 are arranged in a linear manner with $l_{1,2}$ = 8.15 mm, and $l_{2,3}$ = 8.57 mm, respectively. Again the camera is filming at 20,000 fps with a shutter speed of 1/20,000. Simulation setting of the coordinates of the bubbles is matched to the same relative physical arrangement in the experiment. Bubble 1 is placed (in mm) at (-1.64, 0.0, 7.98), bubble 2 at (0.0, 0.0, 0.0), and bubble 3 at (0.117, 0.0, -8.57). The maximum radii of bubble 1, bubble 2 and bubble 3 (which are indicated in Fig. 6.11) are 2.93, 3.46, and 2.85 mm accordingly. The bubbles are generated at a slightly different time. Bubble 3 is created first at time, t = 0 μs. Bubble 1 is generated 50 μs after that, and bubble 2 is created much later at time, t = 350 μs.

In contrast to Case 2, the center bubble (bubble 2) in this case is of larger size than the other two bubbles. But the situation is different from that of Case 1 because bubble 2 is generated much later and its expansion phase coincides with the collapse phases of both bubble 1 and bubble 3. The vapor pressure, p_v, is found to be 0.4 bar, which is slightly less than that in Cases 1 and 2. Both bubble 1 and bubble 3 collapse with a jet directed away from bubble 2 as shown in Fig. 6.12. There is an analogy between these mentioned jets and a jet in a bubble collapsing near a free surface. When a bubble collapses near a free surface, a jet directed away from this free surface is generated (Chahine (1977), Blake and Gibson (1981)).

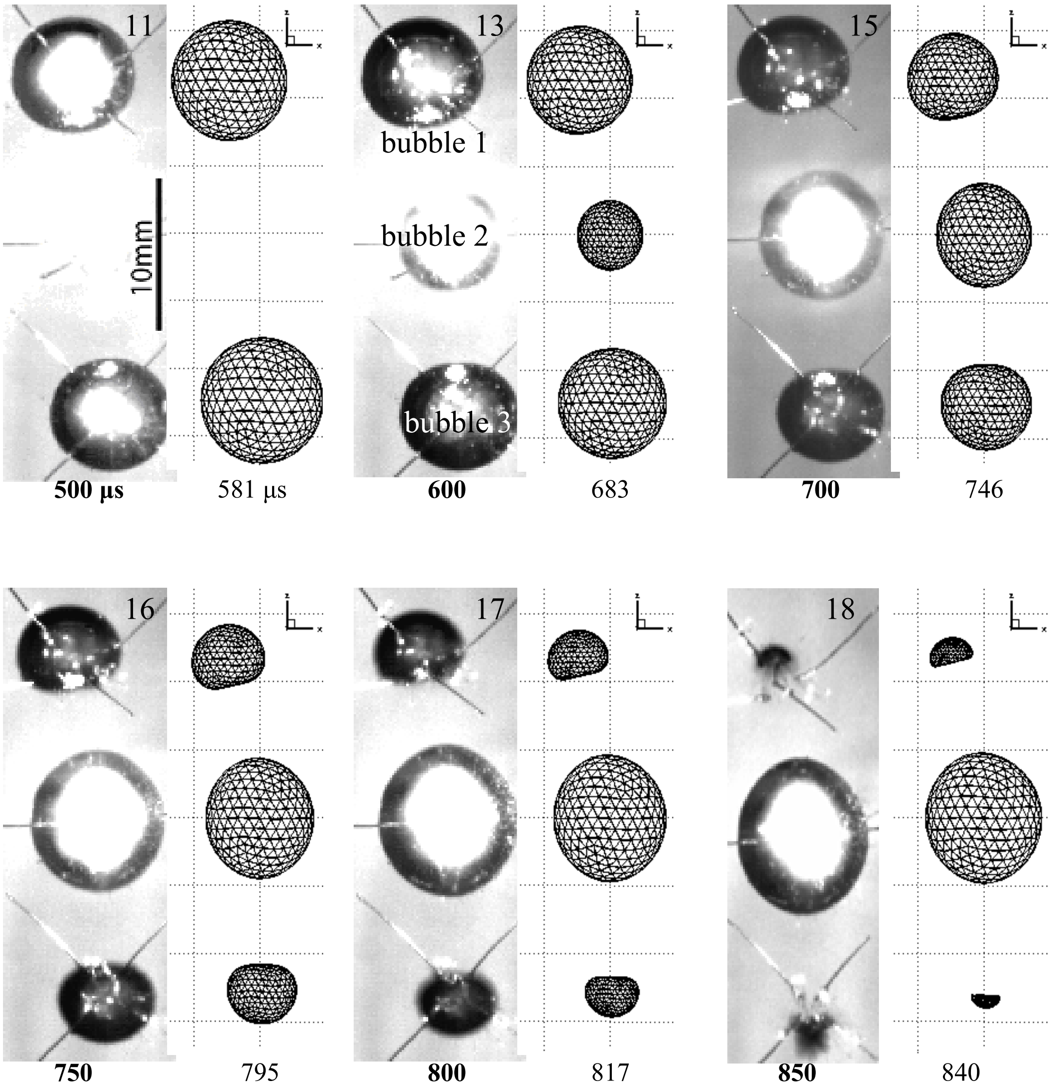

Fig. 6.11 Case 3: Experimental results plotted together with numerical simulations (experimental results reproduced with permission from author (Adikhari, 2006)). Bubble 3 is created first, followed by bubble 1 (on Frame 3, not shown here) at time = 50 µs and bubble 2 at time = 350 µs (Frame 9, not shown here). The expansion phase of bubble 2 coincides with the collapse phases of bubble 1 and 3. The resultant fluid flow causes the formation of an elliptic bubble 2. The left figures of the pair are experimental observations from the high speed camera filming at 20000 frames per second. Frame 1 corresponds to the frame just before the bubbles are created (frame 1 to 7 are not shown here). The frame number and time in µs are indicated on the photographs. The right figures of the pair are simulation results with the time in µs provided. They roughly correspond to the experimental results in (a). For example the last simulation (t=850 µs) corresponds to Frame 18 in (a) (t=840 µs). The vapor pressure, p_v, is taken to be 0.4 bar.

The flow of liquid as a result of the jets away from bubble 2 causes the bubble to be elongated at its poles (frame 20). This elliptic bubble has its maximum curvature parts at the poles. Proceeding with the same argument as stipulated in Case 2, these said parts will collapse first. As a result, an ‘elliptical-shaped’ bubble is formed (Frames 23-25, Fig. 6.12) and collapses as a flat disk shape.

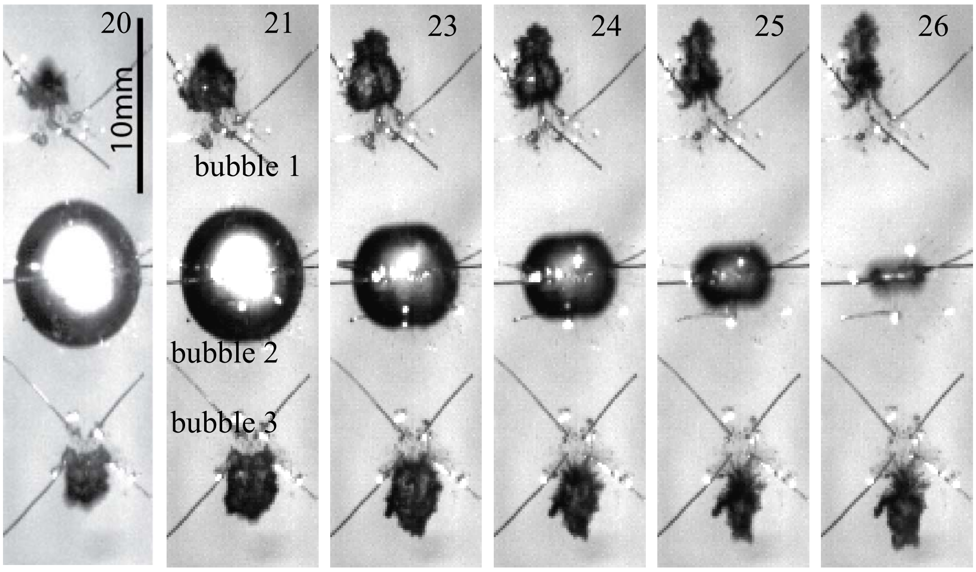

Fig. 6.12. Case 3: Experimental results after the collapse of the bottom bubble (bubble 3) (reproduced with permission from author (Adikhari, 2006)). The frame number continues from that in Fig. 6.11. Both bubble 1 and 3 collapse with a jet away from bubble 2. The elongated bubble 2 collapses with the formation of an elliptic bubble in frames 23-25.

6.4.4. Case 4: Three bubbles created in-phase but arranged at the apex of an imaginary triangle

In Case 4, the electrodes are not arranged in-line. They are placed approximately at the vertices of an imaginary triangle as shown in Fig. 6.13. The bubbles are all placed in the plane y=0. The distances between bubble 1 and bubble 2 ($l_{1,2}$), bubble 2 and bubble 3 ($l_{2,3}$), and bubble 1 and bubble 3 ($l_{1,3}$), are 6.28, 6.29, and 5.6 mm, respectively. $R_{max,1}$ is

1.93 mm, $R_{max,2}$ is 2.38 mm, and $R_{max,3}$ is 2.26 mm. The camera is filming at 15,000 fps with a shutter speed of 1/30,000.

The relative physical arrangement of the bubbles is translated into numerical input with bubble 1 placed (in mm) at (0.406, 0.0, 1.15), bubble 2 at (-2.29, 0.0, 3.76), and bubble 3 at (4.0, 0.0, -4.0). All bubbles are created at the same time as in the experiment. The vapor pressure, p_v, is found to be 0.5 in this case.

The smaller top bubble (bubble 1) collapses first with an induced jet directed approximately towards the geometrical center of the system (Fig. 6.13), analogous to a four bubbles system reported in Bui et al (2006). The development of the jet is clearly observed in the simulation figures (Fig. 6.13(b)). Both upper poles of bubble 2 and bubble 3 nearest to bubble 1 gain increasing prominence with time and are attracted towards bubble 1. For bubble 3, being nearer to bubble 1 than bubble 2, the resultant elongation is more pronounced.

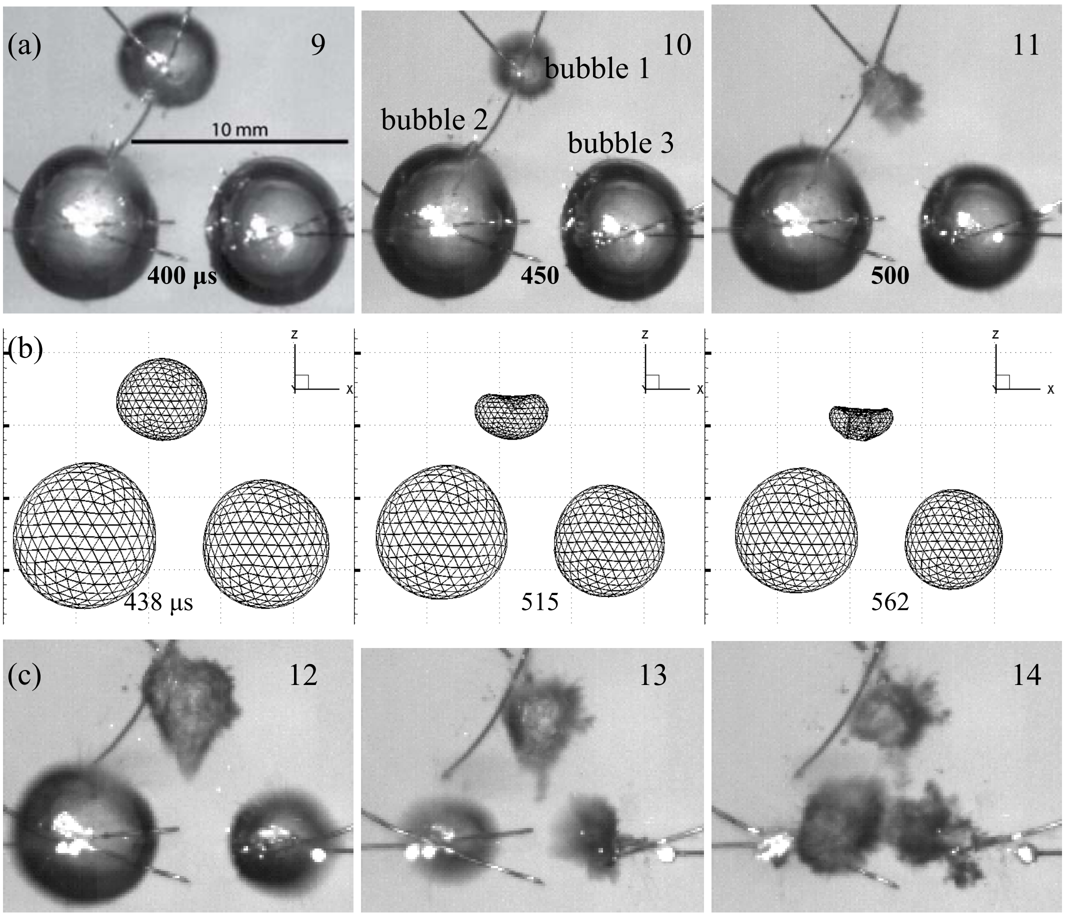

Fig. 6.13 Case 4: Experimental results plotted together with numerical simulations. All bubbles are created at the same time. Bubble 1, being smallest, collapses first with a jet towards the elongated bubble 3. (a) Experimental observations from the high speed camera filming at 15000 frames per second. Frame 1 corresponds to the frame just before the bubbles are created (frame 1 to 8 are not shown here). The frame number and time in μs are indicated on the photographs. (b) Simulation results with the time in μs as indicated. The vapor pressure, p_v, is taken to be 0.5 bar. (c) Sequence of frames after the collapse of the top bubble. Frame numbers as indicated is continued from (a). Bubble 2 and 3 collapse with two jets towards one another.

Subsequently bubble 2 and bubble 3 also collapse with induced jets (Fig. 6.13(c)). Since bubble 1 has already collapsed some time before that of bubble 2 and bubble 3, its presence does not exert much influence on the collapsing phase of bubble 2 and bubble 3. As a consequence, bubble 2 and bubble 3’s induced jets are directed towards each other as shown in Fig. 6.13(c). This is similar to the collapse of two in-phase bubbles, or a bubble near a solid wall (Tomita and Shima (1990), Timm and Hammit (1971), Lauterborn et al (1999), Blake et al (1986)).

6.4.5 Case 5: Three bubbles arranged out-of-line and close to each other

When the distances between bubbles are reduced, complex interaction phenomena are observed as in Case 5 (Fig. 6.14). Here the bubble separations are $l_{1,2}$ = 7.99 mm, $l_{1,3}$ = 5.36 mm, and $l_{2,3}$ = 3.92 mm. The maximum radii obtained for each bubble are approximately 2.01 mm ($R_{max,1}$), 2.36 mm ($R_{max,2}$), and 3.38 mm ($R_{max,3}$). The filming rate and shutter speed used are the same as that of Case 4. Again, all three bubbles are created at the same time (i.e. within one frame).

Close proximity of the physical arrangement of the bubbles renders some difficulties for the simulation. This is because the surfaces of the different bubbles tend to become too close when they are too near to one another, and this leads to numerical instability in the front-tracking calculations. Merging involves the use of an artifice or some other sophisticated methods. A code capable of automated merging of full 3D bubbles in complex or less conventional arrangement is still being developed. As such, the corresponding simulation is not performed and might be taken up in a future study with bubble 1 placed (in mm) at the origin, (0.0, 0.0, 0.0), bubble 2 at (2.30, 0.0, -7.65), and bubble 3 at (-0.829, 0.0, -5.29).

Bubble 1 and bubble 2, being smaller in size, collapse first while bubble 3 is still expanding. Due to this expansion, the bottom surface of bubble 1 is much flattened as observed in Frame 6 to 8 in Fig. 6.14. The bulged equatorial parts of bubble 1 collapse first, leading to the splitting of this bubble into two in Frame 10. The top pole of bubble 3 is attracted towards bubble 1 as bubble 1 collapses and the former forms an ‘egg-shaped’ bubble. After that, two opposite induced jets are formed in the child bubbles of bubble 1. The jet of the lower child bubble enters and penetrates bubble 3, as also observed by Tomita and Shima (1990), and Lauterborn and Hentschel (1985) for two bubbles interaction.

Bubble 2 gets very close to bubble 3 and developed into a ‘mushroom-shaped’ bubble in Frames 9 to 11 in Fig. 6.14. This is very similar to the observations reported for a bubble’s interaction with a composite surface (Tomita and Kodama, 2003), an elastic gel (Brujan et al, 2001a), and an elastic membrane (Ong et al (2005), Turangan et al (2006), Shaw et al (1999)). Bubble 2 also breaks into two parts subsequently, and its child bubble nearer to bubble 3 develops a jet that enters the latter as well. Finally bubble 3 collapses violently in Frames 13 and 14 of Fig. 6.14.

6.4.6 Case 6: Three bubble interaction showing the 'catapult' effect

The bubbles for Case 6 are arranged in a triangular manner similar to Case 4 and 5, and are initiated one after another. The separation between bubble 1 and bubble 2 is 6.55 mm, and the distance between bubble 2 and bubble 3 is 5.31 mm. The separation between bubble 1 and bubble 3 is 6.45 mm. Relatively, the orientation of the bubbles' centers are given with bubble 1 (in mm) at (-6.42, 0.0, 0.273), bubble 2 at (0.0, 0.0, -1.0), and bubble 3 at (-1.27, 0.0, 4.15). Maximum radii obtained are $R_{max,1}$ = 2.02 mm, $R_{max,2}$ = 2.94 mm, and $R_{max,3}$ = 2.9 mm. Bubble 1 is created first, followed by bubble 2 at t = 67 μs, and lastly bubble 3 which is generated 334 μs after the initiation of bubble 1. The same camera setting as that of Case 5 is used.

As bubble 1 is created before the other two bubbles, it has collapsed while bubble 2 and bubble 3 are still expanding (Frame 11, Fig. 6.15). The expansion of bubble 3 causes the top surface of bubble 2 to be much flattened in Frame 9 and 11 (Fig. 6.15). But instead of breaking into two as found in Case 5, a jet directing away from bubble 3 is developed in bubble 2. The flow of liquid due to this jetting effect brings about the elongation of the bottom part of bubble 3 downwards as it expands in its growth phase.

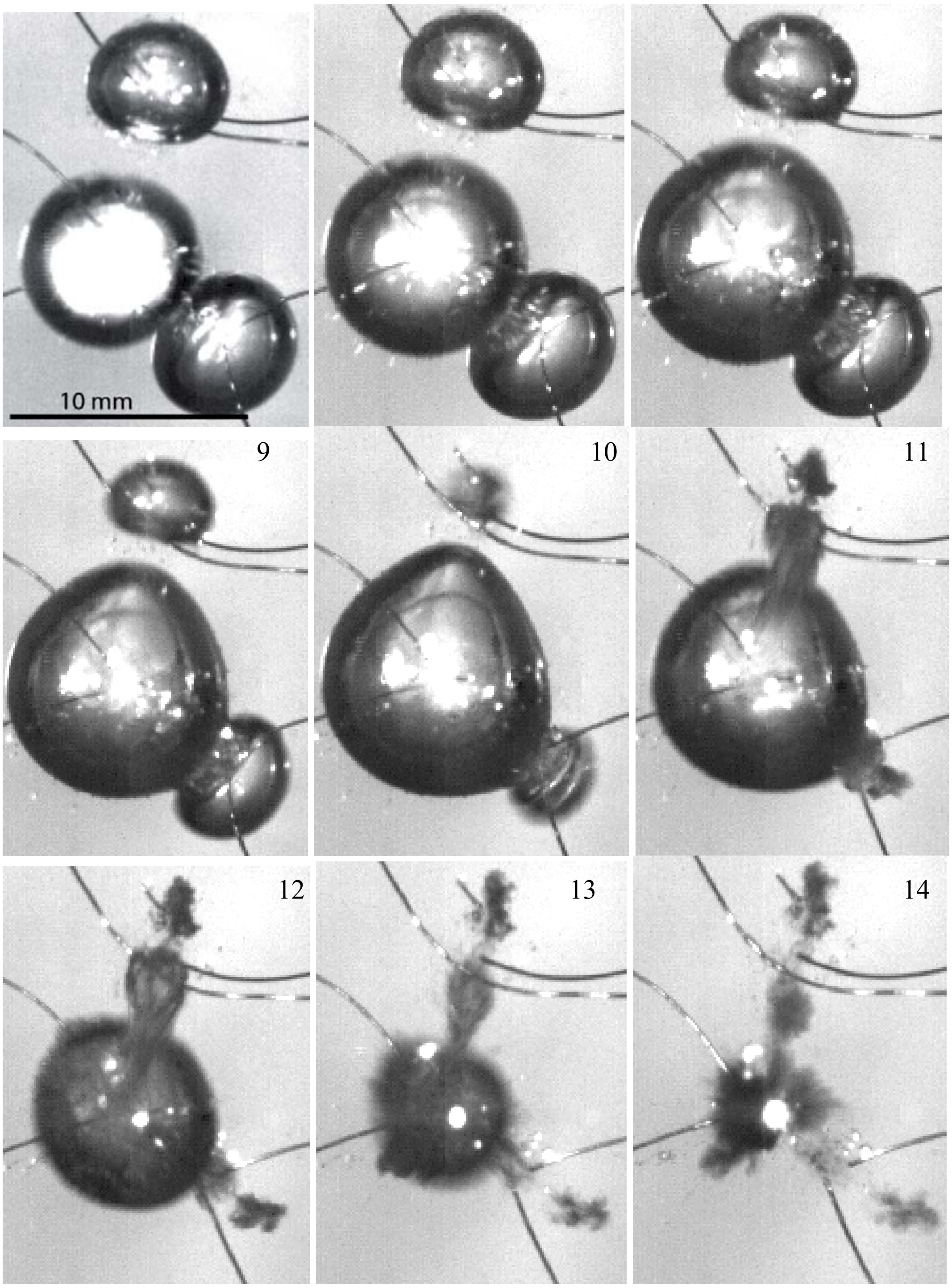

Fig. 6.14 Case 5: Sequence of frames from Frame 6 to Frame 14 from top left to bottom right (Frame 1 corresponds to the frame just before the bubbles are created, Frame 1 to 5 are not shown here). The filming rate is 15000 frames per second. All bubbles are created at the same time. Bubble 1 splits into two as it collapses. Opposite jets are developed in the resultant bubbles, and the lower bubble's jet penetrates bubble 3 which top surface is elongated towards bubble 1. Bubble 2 gets very close to bubble 3, forming a 'mushroom-shaped' bubble (Frame 7-9) before it eventually collapses by splitting into two parts.

From Frames 12 and 13 (Fig. 6.15), it is observed that the greatly elongated tip of bubble 3 downwards becomes notably squeezed. After that, a high speed jet is developed in bubble 3, directed away from bubble 2 like a ‘catapult’. The maximum jet speed obtained is more than 180 m/s. This is considerably more than the jet speed of around 50 m/s as observed in Case 1. A similar observation for two bubble interaction near a solid wall is reported by Tomita et al (1994). They postulate that the fine, high-speed jet from the larger bubble (more than 130 m/s in their case) is caused by the shock wave from the rebounding of the toroidal shaped lower bubble. In a slightly different setting in Chen et al (2006) where two microbubbles are created by laser in a thin ink sheet between two glass slices, a similar strong interaction between the bubbles is observed. The jet velocity calculated from the clear photographs in Chen et al (2006) reaches a maximum of about 75 m/s while it is still developing inside the larger bubble (although the speed drops to about 16 m/s once the jet has penetrated the bubble and moved into the liquid). The difference in velocity obtained is possibly due to the fact that the bubbles in their paper are generated in a confined space, and hence the influence of the walls to the bubble dynamics is significant. In section 6.4.7, more discussion on the physical background of this phenomenon will be given.

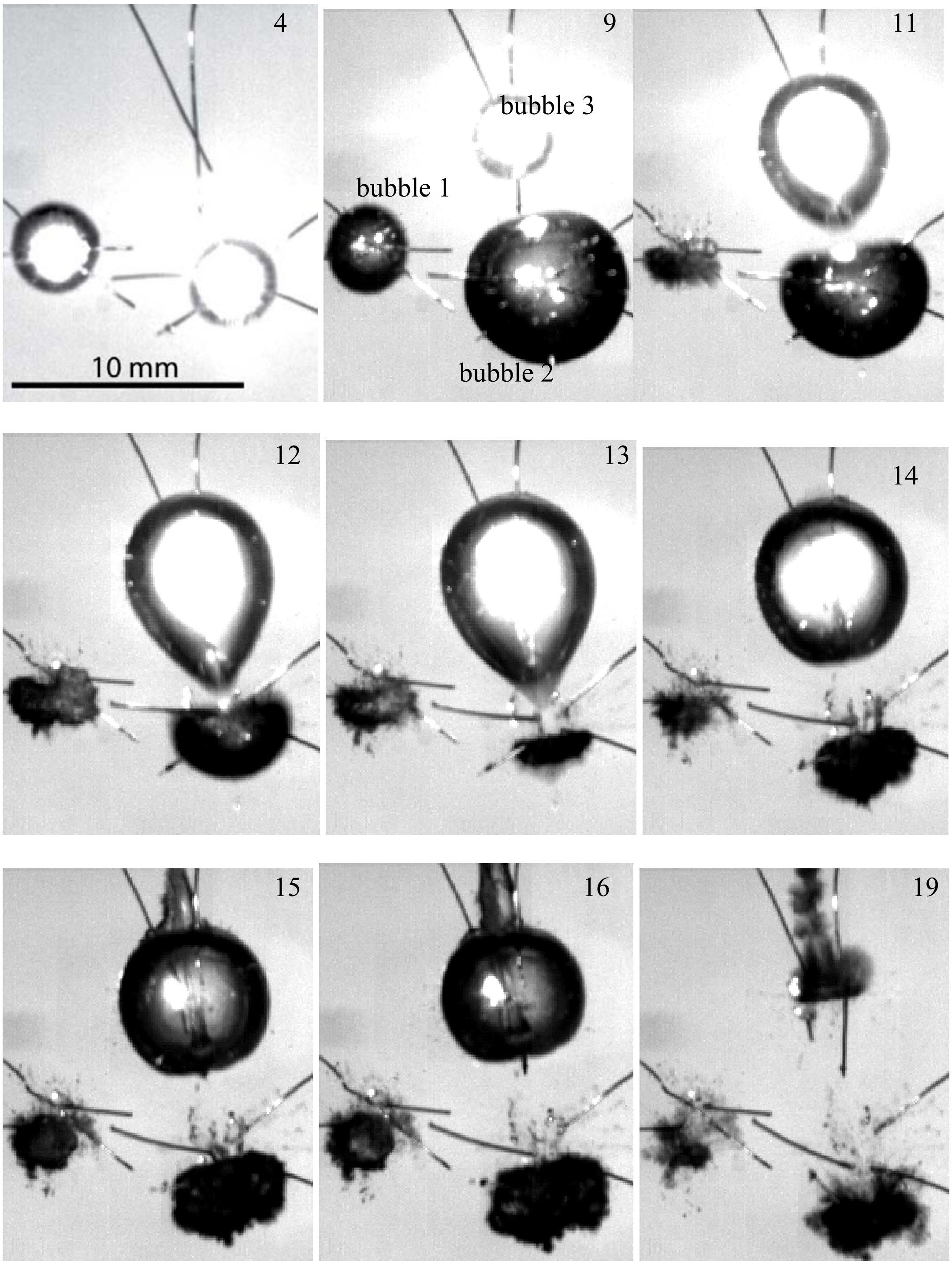

Fig. 6.15 Case 6: Selected frames from top left to bottom right with frame number as indicated. The frame rate used is 15000 frames per second. The intervals between the creation of the first (bubble 1) and the second (bubble 2), and the first and the third (bubble 3) bubbles are 66.7 μs and 267 μs respectively. Bubble 1 has collapsed, while the others are still expanding. The jet in bubble 2, directed away from bubble 3, induces the thin elongation of the tip of bubble 3 (Frame 13). As bubble 2 becomes toroidal and rebounds (Frame 14-16), a very high speed jet (greater than 180 m/s) is developed in bubble 3 that ‘catapults’ away from bubble 2.

6.4.7 Discussion on multiple bubble interactions

6.4.7.1 ‘Catapult’ effect

In this section, several important experimental and simulation results are discussed in comparison with previous works which may provide further new insights. Firstly the phenomenon of a very high speed jet in Case 6 (Fig. 6.15) is examined. This phenomenon is termed the ‘catapult’ effect because of its resemblance with the fast and forceful launch of an object winched-down on a catapult. Foreseeing possible future applications (in cases where a very high speed jet is needed), it is deemed useful to discuss more on the physics involved.

The ‘catapult’ effect seems to be basically a two-bubble interaction phenomenon (bubble 2 and 3 of Fig. 6.15). Bubble 3 is created when bubble 2 is about to reach its maximum size. Thus the internal pressure of bubble 2 is very low (much lower then ambient pressure). This causes the expanding bubble 3 to develop a protrusion on its bottom surface that is directed towards bubble 2 (frame 13). This effect has become more pronounced during the collapse of bubble 2. It almost appears as if bubble 3 is sucked into the (presumably) toroidal shaped bubble 2. Once bubble 2 has collapsed and reaches its minimum volume, it will generate a very high pressure due to the compressed gaseous contents. The possible shock wave emitted during this collapse might also contribute to a high pressure region just outside of bubble 3. Due to this high pressure, a very high speed jet develops in bubble 3. This jet originating at the lower section then penetrates and impacts on the upper portion of bubble 3 while the bubble itself is still almost in its maximum volume. The reader is also reminded of the suggestion from Lauterborn (1982) that since smaller bubbles have shorter collapse time, the highly curved parts of a bubble should collapse faster. In this case, the lower section of the enlongated bubble 3 has the highest curvature and is therefore collapsing faster, creating the high speed jet.

A possible reason for the existence of a very high speed jet may be put forward with the following considerations. Under atmospheric conditions, if a bubble collapses near a solid boundary (or two in-phase bubbles collapse in each other's vicinity), a jet is generated with a speed of 50 to 160 ms^{-1}(Blake et al (1986), Lauterborn and Hentschel (1975), Tomita and Shima (1986)), fairly regardless of the maximum size of the bubbles. It seems that the jet velocity, v_{jet}, is proportional to 5 to 10 v_{ref}, where under normal atmospheric condition (p_{ref} = 1 bar), $v_{ref} = \sqrt{p_{ref} / \rho} \approx 10\,\mathrm{ms}^{-1}$. In the current situation, however, a region with a very high pressure exists just outside bubble 3. Even though the mentioned high pressure region may exist for only a very short period of time, it is perhaps reasonable to assume that an 'effective reference pressure', much higher than p_{ref} will be generated. From Cole (1948) and Lee et al (2007), it is established that energy loss of the oscillating bubble of up to 50% of its total energy occurs during the bubble's minimum volume. This loss of energy of bubble 2 at its minimum volume is radiated outwards as a pressure pulse (or shock waves), and certainly is compatible with the suggested presence of an effective reference pressure. This higher pressure will be responsible for the higher jet velocity (assuming that the dimensionless proportionality coefficient of 5 to 10 still exists). In view of the possible application areas, and the relative ease with which such high speed jets can be generated (only two closely spaced, out-of-phase bubbles are needed), it might be a subject for future studies to analyse and optimize this effect further. Moreover, if the current difficulties in simulating the event (numerical instability due to the extreme deformation of bubble 3, and the proximity of bubbles 2 and 3) can be overcome, more insights to the physics of this phenomenon can be obtained.

6.4.7.2 Coalescence of two adjacent bubbles

When two bubbles are very near each other and they are created at the same time and have about the same dimensions, they will coalesce as shown in the experimental result given in Fig. 6.16. The first frame (Frame 2) shows the instance whereby the sparks are initiated. The initial separation between the electrodes is 1.21 mm (about half of R_{max}, which is approximately 3.4 mm). Somewhere around Frame 8, the two bubbles appear to have merged into one large bubble. From the experimental results, it cannot be determined when the coalescence occurs exactly. At Frame 15, the resulting bubble is at its maximum radius. As predicted by the equivalent numerical simulations done by Rungsiyaphornrat et al. (2003), there is a distinct and significant ‘swelling’ at the middle of the two merging bubbles, and the resultant coalesced bubble eventually collapses in an elliptical shape (Frame 25). Two jets, one directed upwards from below while the other directed downwards from above, have been observed numerically in Rungsiyaphornrat et al. (2003). However, this is not so clearly seen in the experiments (Frame 25). Nevertheless, the present experiment still confirms the earlier experimental observations of Lal and Menon (1996) regarding the broad shape and salient features like middle ‘swelling’. The exact cause of this swelling is not yet fully understood. Yet, the fact that it is also observed numerically in Rungsiyaphornrat et al. (2003), where no surface tension effects were considered, leads to the conclusion that its origin(s) may lie solely in the inertia of the fluids.

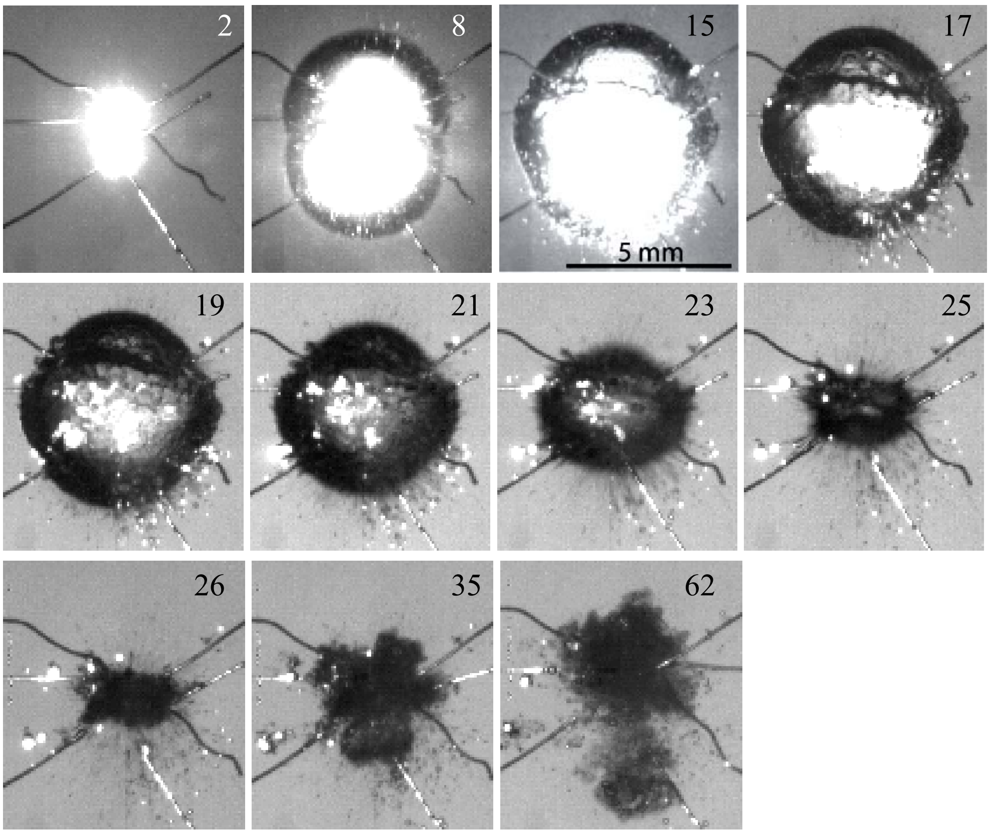

Fig. 6.16 Coalescence of two adjacent bubbles with the corresponding frame as indicated on the top left (experimental results reproduced with permission from author (Adikhari, 2006)). The inter-frame rate used is 20000 frames per second. Frame 1 corresponds to the frame just before the bubbles are created (not shown here). The bubbles are at their maximum sizes at frame 15 with the scale as provided. These two bubbles coalesced into one bubble with pronounced 'swelling' at the middle. The resultant bubble eventually collapses elliptically (frames 25 and 26). After that, the bubble fragmented into small bubbles, forming bubble clouds (frame 35). They re-expand and move away from the center of the frame (frame 62).

6.4.7.3 Symmetry considerations of multiple bubble systems

It is well-known that a single-bubble-near-a-solid-wall system can be approximated by putting an image bubble behind the wall that is located symmetrically to it with respect to the wall (Plesset and Prosperetti (1977), Krasovitski and Kimmel (2001)). The high speed jet from the physical bubble towards the solid wall is explained by Plesset and Prosperetti (1977) as follows: the portion of the real bubble farther from the wall acquires a greater velocity than the region near the wall because there is asymmetry in the velocity of the flow induced by the image bubble on the far and near portion of the real bubble. Furthermore they also explained that the sink-like flow of the image attracts the real bubble towards the wall. This translational movement of the collapsing bubble is also observed experimentally by Lauterborn and Hentschel (1985), Tomita and Shima (1990), and Lauterborn et al. (1999), among others.

A corresponding phenomenon in many-bubble system is observed by Tomita et al. (1990) using high speed photography. They show that when a small bubble is sandwiched between a larger bubble and a solid wall, a necking phenomenon appears in the small bubble. It forms a 'dumbbell-shaped' bubble and disintegrates into two parts in the end. Based on the image theory (Wang (1998), Tomita et al. (2002)), this system is equivalent to a system of four bubbles whereby the center of the system corresponds to the location of the rigid wall in the former two bubble system (Fig. 6.17). With the bubbles' radii and distances between them in agreement with that in the article (Tomita et al., 1990), we have simulated an equivalent four bubble system (as shown on the left of Fig. 6.17), and obtained results as shown in Fig. 6.18. The two bubbles are created at the same time. Bubble 1 is slightly smaller than bubble 2 (Fig. 6.18) in such a way that its maximum radius is $R_{max,1}$= 0.59 mm while $R_{max,2}$= 0.85 mm. The initial distances between the bubbles and the wall are l_{bubble1}=0.79 mm and l_{bubble2}=2.69 mm. Due to the expansion of the larger bubble 2, the north and south poles of bubble 1 are significantly flattened while it is still in its expansion phase (picture of the two bubbles at time, t = 47.43 μs, in Fig. 6.18). The much curved equator region of bubble 1 collapses first, causing the 'necking' phenomenon (as mentioned in Tomita et al., 1990) and the eventual formation of a ‘dumbbell-shaped’ bubble at t = 155.6 μs as clearly depicted in the cross-sectional picture in Fig. 6.18.

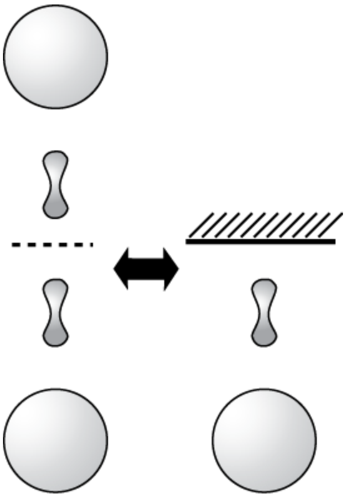

Fig. 6.17 Analogous comparison between a system of four bubbles (Fig. 6.18) and a system of two bubbles with a rigid wall (Tomita et al., 1994). According to the image theory, both systems are equivalent.

Also, from our results in Case 2 (Fig. 6.9), we notice some similarity between the three bubble system whereby the center bubble is smaller than the other two that are sandwiching it, and a single bubble between two parallel rigid walls (Fig. 6.19). From previous experimental observations of Kucherenko and Shamko (1986), and Ishida et al. (2001), it is noticed that when a bubble is formed between two narrow parallel plates, it deforms to be ‘dumbbell’ in shape before finally splitting up into two equivalent bubbles. Shima and Sato (1980) reported the same observations from their simulation results. The formation of a ‘dumbbell-shaped’ bubble in both situations could be due to the similar restriction of flow in the direction of the walls or equivalently the corresponding lower surface of the top and the upper surface of the bottom bubble in the three bubble system (see Fig. 6.19). For the latter, since the top and bottom bubbles are significantly larger, their oscillation periods are longer than that of the center bubble. Therefore, when they are expanding relatively slowly, their bottom and upper surfaces (for top and bottom bubbles, respectively) restrict fluid flow in a manner similar to that of the parallel rigid wall in the single bubble case. This restriction of flow causes the flattening of the top and bottom surfaces of the center bubble. The bulging equatorial region of the bubble will thus collapse faster, forming the 'dumbbell-shaped' bubble mentioned. In the three bubble system, the center bubble will also eventually split into two. The analogy of Fig. 6.19 is, however, not perfect, since an infinite number of bubbles would be needed to match the bubble between two flat plates. However, in a first order approximation, this consideration of only two image bubbles is important because the infinite number of other (image) bubbles are further away and therefore have less influence on the centre bubble.

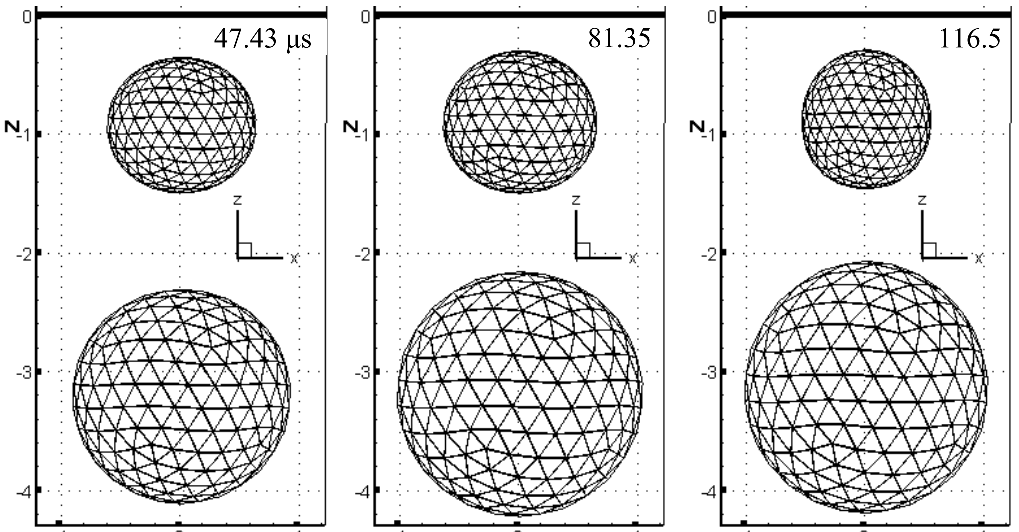

(figure to be continue next page)

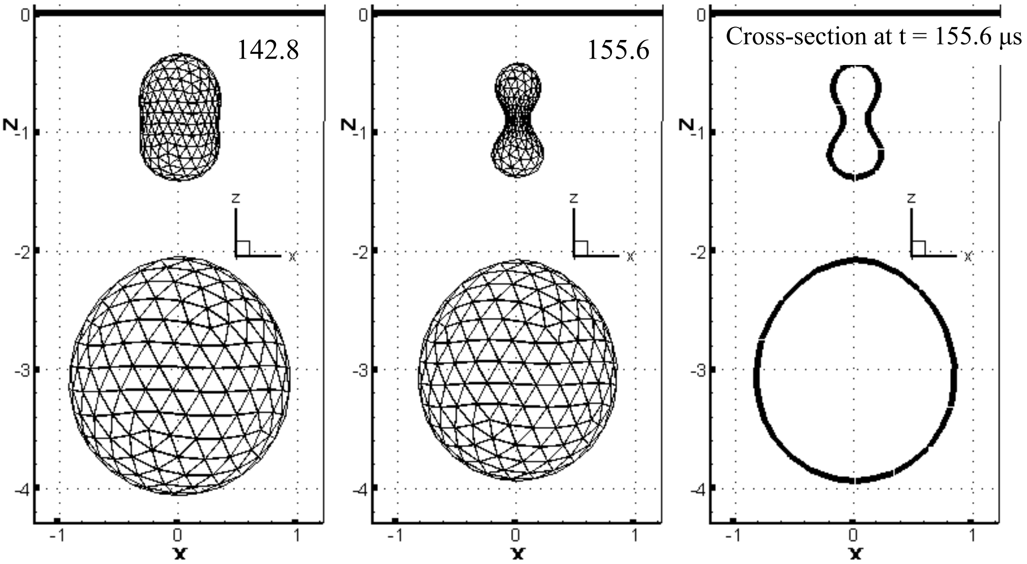

Fig. 6.18 Simulation results of four bubbles (only two are shown since the other two are symmetrically placed with exactly the same evolution in time) with the time (t) in microseconds (μs) as indicated. The center of this four bubble system is at z=0, thus it is equivalent to simulating two bubbles with a solid wall at z=0. Maximum radii of the bubbles are $R_{max,1}$=0.59 mm and $R_{max,2}$=0.85 mm. Initial distance between bubble and the wall are $l_{\text{bubble 1}}$=0.79 mm and $l_{\text{bubble 2}}$=2.69 mm. All these parameters are the same as those in the experiment performed by Tomita et al (1990). The right bottom figure shows the cross-section of the bubbles at the plane y=0 for t=155.6 μs. The flattening of the top and bottom poles of bubble 1 (t=47.43 and 81.35 μs), the necking phenomenon following that, and the elongation of top surface of bubble 2, show very close correspondence to the high speed photography results in Tomita et al. (1990).

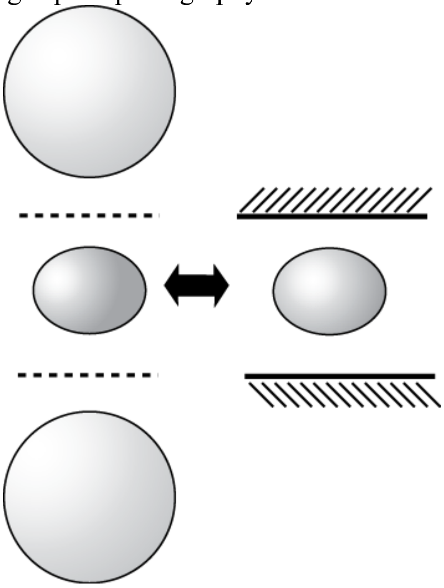

Fig. 6.19 Anologous comparison between a system of three bubbles arranged in-line with the center bubble being smaller than the top and bottom bubbles. From experimental and numerical results for Case 2 (Fig. 6.9), and the experimental results from Shima and Sato (1980), Kucherenko and Shamko (1986), and Ishida et al. (2001), the results between these systems show close correspondence in terms of the center bubble profile evolution.

6.5 Other interesting experimental results

In this section, several experimental results of significance are presented. Firstly, interaction of a spark bubble near a soft elastic material is studied. The material in use is konjac jelly. The jelly is prepared by mixing the common konjac powder with water. The mixture is heated to its boiling point and is left to cool in a container. The jelly formed has a diameter of 7.2 cm and a height of 3.5 cm. It is placed in a water tank with the same dimensions as mentioned in the previous section (17x17x17 cm^3) just a few minutes before the experiment. Another sample of the same jelly is used for the measurement of its stiffness (Young's modulus) and density. For the former, the spring coefficient (k) is obtained from the measurement done on the jelly using a compression tester where by compression force is applied on the top surface of the sample, and the resulting displacement is measured. Then Young's Modulus (E) is related to k by:

$$E = k/V, \tag{6.1}$$

where V is the volume of the sample. For the case shown in Fig. 6.20, a soft konjac jelly of E = 1.7 MPa and density comparable to water is used as the elastic material which interacts with the spark bubble. The spark is generated very close to the material, merely 0.7 mm away. The growth of the bottom half of the spark bubble is hampered by the jelly. Therefore the maximum bubble radius, R_{max}, is obtained in frame 10, by taking the distance from the top surface (which is not affected by the presence of the material) to the bubble center. R_{max} obtained is about 4.33 mm. The dark circles underneath the hemispheric bubble in frames 7 and 10 are actually stress in the gel as induced by the expanding bubble. Then the bubble collapses (as shown in frame 14 and 15). From frames 17 to 88 (t between 1.28 and 6.96 ms), a jet is seen to form from the collapsed bubble towards the material and penetrates deep into the material (depth of penetration is 0.51 cm). Due to the elasticity of the material, the trapped gas from the jet is forced out from the jelly as seen from frames 227 to 358. It forms a round gas bubble which is coated with the konjac jelly material, and rises slowly (velocity about 12 cm/s) in the fluid (tap water). The radius of the bubble is 0.74 mm. According to the numerical simulations performed by Hua et al (2007), a bubble of this size in a low viscosity fluid like water, will rise in a zig-zag manner. The path of bubble together with the wake behind it is seen as traces left behind by the konjac jelly.

In the next experiment in Fig. 6.21, the electrodes are placed between two glass plates which are placed vertically facing the camera (one behind the other). The solid wall on top is weighted down by thick aluminium block. Because of the proximity of the two vertical glass plates (about 3 mm apart), the spark bubble generated in this setting is much flattened and restricted to grow mainly in the vertical plane facing the camera. Therefore it is considered to be pseudo-2D in configuration. A similar setting (without the top solid wall) is used for experiments shown in Fig. 6.22 and 6.23. This setting has the advantage of clear visualization of the bubble dynamics involved. A similar configuration in much smaller scale is used by Chen et al (2006) to study bubble dynamics of a laser bubble in a narrow gap.

When a non-equilibrium bubble collapses near a solid wall, it will collapse with a jet towards the wall. As seen in Fig. 6.21, the bubble is created 2.9 mm away from the wall (frame 1). The bubble grows to its maximum size at frame 15, with R_{max} = 7.0 mm. It then collapses with a jet towards the wall. In frame 28, it is seen that the jet has penetrated the opposite surface of the bubble and causes it to split into two bubbles of

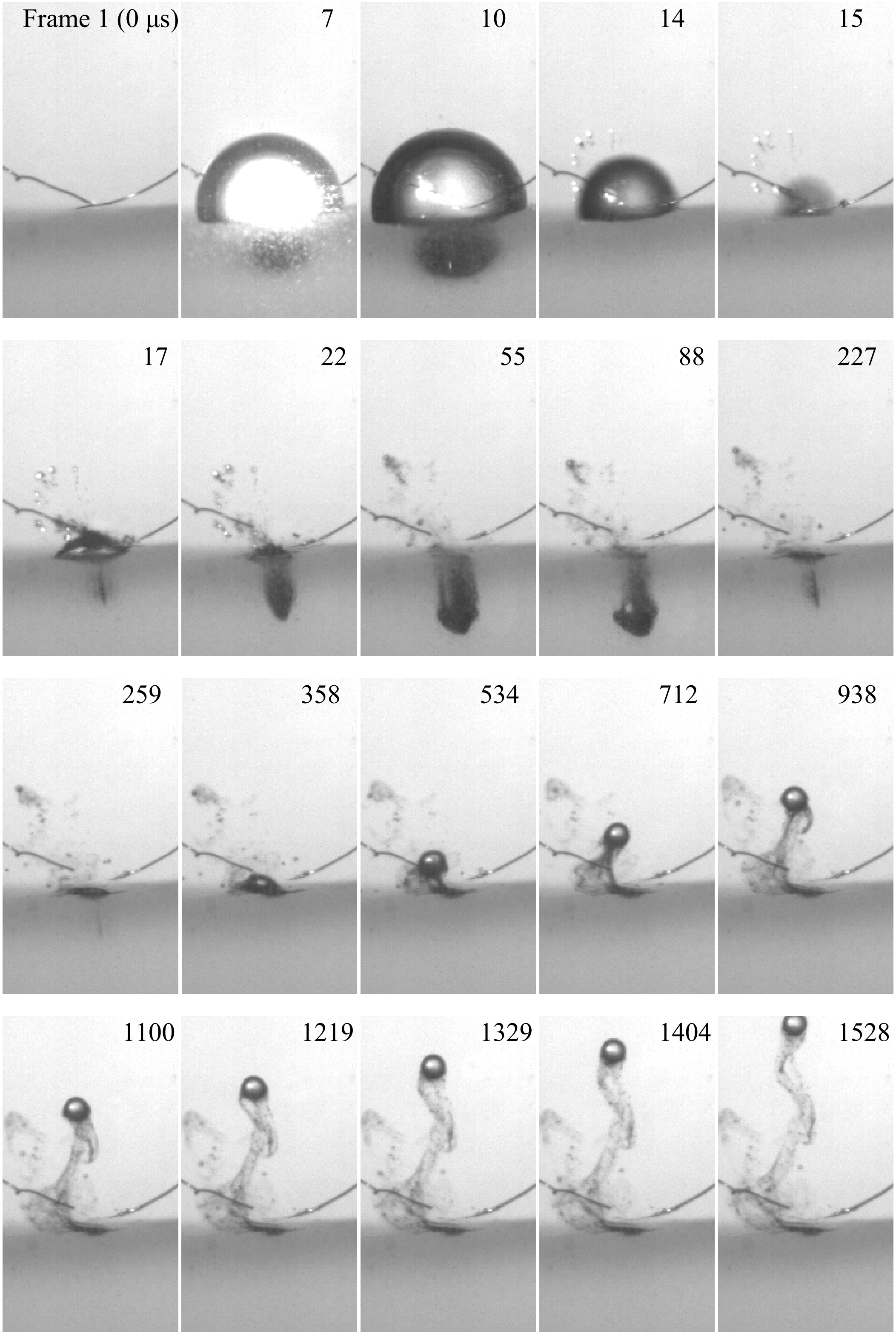

Fig. 6.20 A spark bubble near a soft elastic material (Young's modulus = 1.7 MPa). The video is taken with a high speed camera at 12,500 fps (i.e. interframe period is 80 µs). Indicated on the top right corner of each frame is the frame number starting with frame 1 (one frame before the spark

occurs). The bubble is initiated 0.7 mm away from the material, and it grows to its maximum size of 4.33 mm in radius at frame 10. Then the bubble collapses at frame 15. From frame 17 to 88, the jet from the collapsing bubble shoots into the soft material (depth of penetration at frame 88 is 0.51 cm). Then the gas trapped from the collapsed bubble forms a bubble coated with the elastic material (radius = 0.74 mm) and rises again. It rises in a zig-zag manner from frame 358 to 1528. Note the visibility of the wake at the back of the rising bubble.

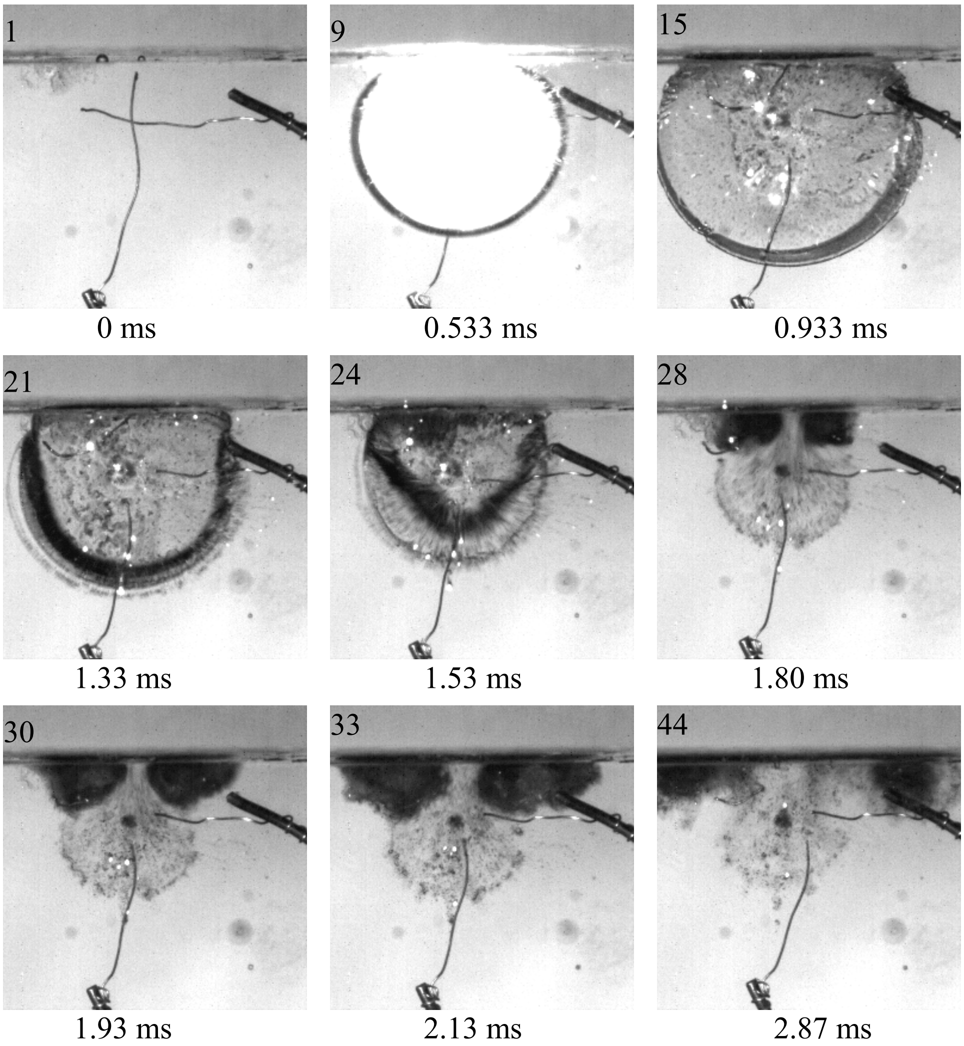

Fig. 6.21 Pseudo-2D bubble collapses near a solid wall (top of the frames). Framing rate is 15,000 fps. Selected frames up to 44 are shown, and the time after the spark has initiated is given at the bottom of each frame. Initially the crossing of the electrodes is placed 2.9 mm below the wall (frame 1). Then the bubble grows (frame 9) and achieves its maximum radius of about 7.0 mm at 0.933 ms. It then collapses with a jet towards the boundary (frames 21 to 28). The last row of frames show the interesting vortices along the solid wall as the two split bubbles roll away.

equal size. Interestingly, the two bubbles then move in a circular manner away from the jet center towards the sides of the wall. The vortices caused by this bubble movement are visualized with the help of the debris from the broken electrodes and the tiny bubbles from the bubble clouds. It is considered that this is the main cause for the shear force which is responsible for the removal of dirt on material surface as the bubbles collapse near the surface in ultrasonic cleaning. The visualization of the vortices is an advantage of this pseudo-2D experiment. They are much more difficult to visualize in three dimensional experiments.

Also in pseudo-2D configuration, the interaction of a stationary bubble with the shockwaves from a nearby spark bubble is studied in Fig. 6.22. The stationary bubble is of small size, i.e. its diameter (3.3 mm) is about the same as the gap between the glass plates (4 mm), and is therefore in a three dimensional configuration. The spark bubble, however, is much larger (R_{max} = 4.7 mm), and is considered to be in pseudo-2D configuration. Due to buoyancy, the stationary bubble is slightly elongated. Its horizontal radius is calculated to be 1.65 mm. It is placed on the surfaces between the glass plates using a syringe. The stationary bubble is 4.8 mm away from the crossing of the electrodes as shown in frame 1. As the spark bubble expands, the flow and the spherical shockwaves hit the stationary bubble. They cause the formation of a jet in the middle of the right surface of the bubble (frame 5). This jet penetrates the bubble (frame 6, t = 333 μs). As the spark bubble continues to grow to its maximum size at frame 11 (R_{max} = 4.7 mm), its expansion generates a region of low pressure around the bubble. This causes the split stationary bubbles to expand (as seen in frames 8 to 11). But as the spark bubble collapses, it ‘attracts’ the stationary bubbles towards it. Finally all the bubbles collapse as shown in the last frame at t = 1533 μs.

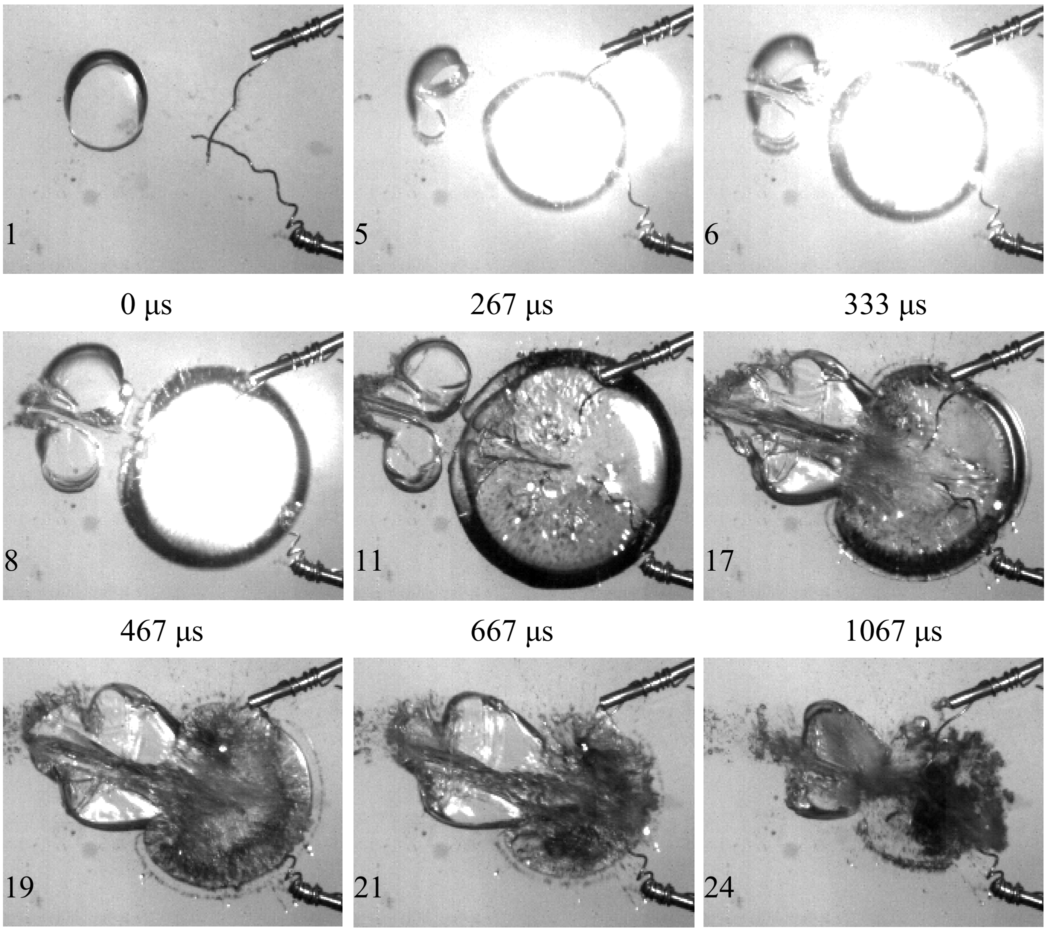

0 μs 267 μs 333 μs

467 μs 667 μs 1067 μs

1200 μs 1333 μs 1533 μs

Fig. 6.22 Interaction of a stationary 3D bubble with a pseudo-2D spark bubble that is 4.8 mm away (between the center of the stationary bubble and the crossing of the electrodes as shown in frame 1). Framing rate is 15,000 fps. Selected frames up to 24 are shown, and the time after the spark has initiated is given at the bottom of each frame. The stationary bubble has a horizontal radius of 1.65 mm. The spark bubble has a maximum radius of 4.7 mm (frame 11) at t = 667 μs. The shock waves and flow generated by the expanding spark bubble cause the stationary bubble to develop a jet and breaks into two. Then as the spark bubble collapses from frame 19 to 24, the split bubbles are attracted towards the latter and eventually breaks into many small bubbles (at last frame, t = 1533 μs).

The last experiment in this chapter shows the coalescence of two spark bubbles in the pseudo-2D configuration. The reader is advised to compare the result in Fig. 6.23

with that of a full 3D setting as given in Fig. 6.16. The crossings of the electrodes (as seen in frame 1) are placed 1.3 mm apart. The two expanding bubbles grow (frame 8) and coalesce at frame 14. Pronounced 'swelling' at the middle of the joint bubble, similar to that in Fig. 6.16, is seen. The bubble collapses radially after that.

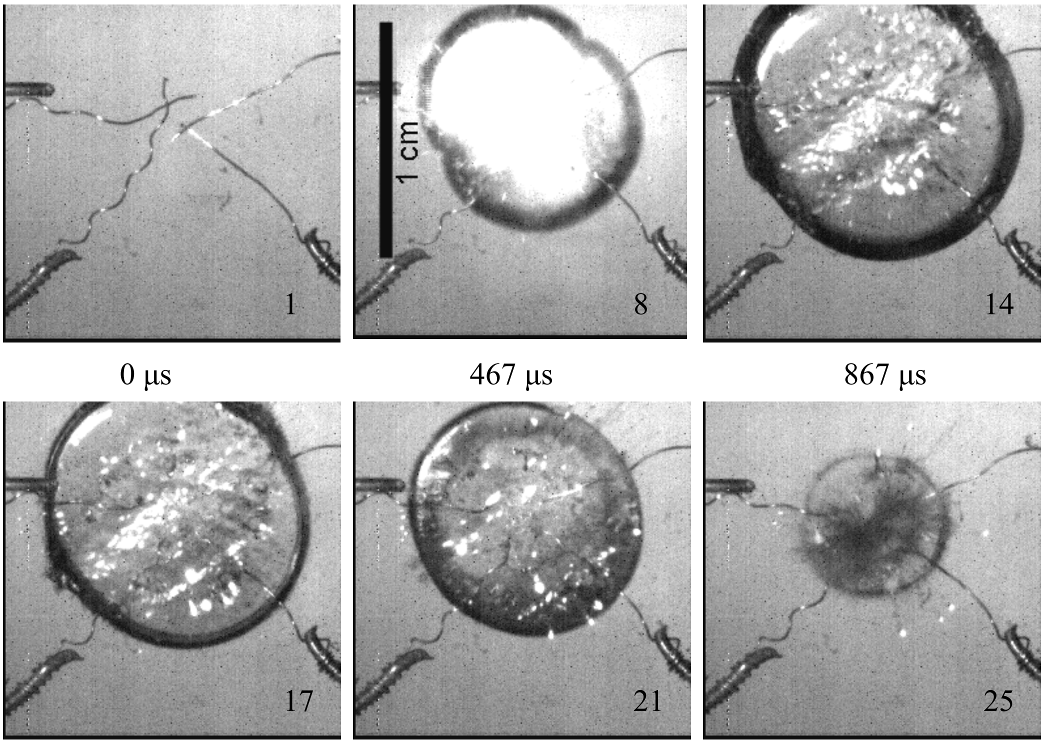

0 μs 467 μs 867 μs

1007 μs 1333 μs 1600 μs

Fig. 6.23 Two spark bubbles, 1.3 mm apart (between the crossings of the electrodes as shown in frame 1. Selected frames up to 25 are shown, and the time after the spark has initiated is given at the bottom of each frame. The scale for the image is shown as a bar in frame 8. Both bubbles expand (frame 8) and coalesce after 867 μs. Pronounced 'swelling' at the middle similar to that in Fig. 6.16 is seen. Then the joint bubble collapses almost spherically from t = 1007 μs to 1600 μs.

Chapter 7

Summary, discussions and conclusion

7.1 Summary on thesis contribution

This thesis focuses on the numerical study of bubble dynamics related to biomedical applications, namely Extracorporeal Shockwave Lithotripsy (ESWL) and therapies using ultrasound. An existing Boundary Element Method (BEM) code is extended to model the acoustic fields with temporal and spatial considerations. Strictly speaking, the model, which is based on potential flow theory, cannot be utilized to simulate shockwaves and strong ultrasound fields that require the consideration of liquid compressibility. Nevertheless through extensive validations that include both numerical and experimental results comparison with published literature (Ding and Gracewski (1996), Jamaluddin (2004), Sankin et al (2005)), the BEM simulations are deemed to be able to capture the phenomena involved well. The reason behind this could be that the bubble interaction with the acoustic field is still mainly controlled by the inertia of the fluid. The shockwave movement and reflection inside the bubble, as well as liquid compressibility are probably of secondary importance. Therefore the author argues that it is advantageous to use BEM for acoustic bubble simulation because of its inherent computational efficiency in terms of output time and storage requirement (only 51 nodes are used for the required meshing on the bubble boundary).

Also, this thesis documents the use of the BEM simulations to reveal dynamics of bubbles in extreme and very difficult to observe experimental situations, e.g. in ESWL and other ultrasonic medical treatment. For ESWL, apart from giving insights into an oscillating bubble’s interaction with the standard shockwave used in clinical treatment, an inverted shockwave which has a leading negative pressure wave followed by a much higher amplitude but shorter duration compressive wave is also simulated. This waveform was suggested by Zhong et al (2001), Bailey et al (1998), Loske and Prieto (2002) for the minimization of collateral damage during ESWL. Interesting resultant bubble dynamics are discussed.

Very often in medical applications, the ultrasonic bubbles are found in the vicinity of organs and other biomaterials such as fat, skin, and cornea. Using an elastic fluid model to represent the biomaterials, and incorporating an ultrasound field, the complex interactions between a stationary bubble and the nearby biomaterials involved in a number of common ultrasonic medical treatments (e.g. liposuction, transdermal drug delivery, and brain tumor surgery) are studied in detail. Recently, a new surgical method in development involving the use of high intensity pulsed ultrasound for localized tissue removal has been advocated by Xu et al (2005). Inspired by this study, a microbubble's interaction with the form of sound wave used in Xu et al (2005) is simulated numerically. A cancer treatment scheme similar to some previously suggested methods (Lindner (2004), Everbach (2007), Ferrara et al. (2007)) using sound wave bubble interaction can be implemented. The targeting microbubble contrast agents which will automatically attach themselves to the diseased cells when hit by these ultrasound pulses, they will collapse violently, killing the cancerous cells in vicinity and delivering drugs to other vital cells simultaneously.

Lastly, multiple bubble dynamics is studied using high speed photography and a previously developed three dimensional BEM code. Complex bubble interactions are observed and the physics involved is discussed. Other interesting experimental results are also included in this thesis as a source for future studies.

7.2 Discussions on new developments in biomedical applications involving acoustic bubbles

Since the introduction of ESWL decades ago, the use of sound waves in medical therapies has gained recognition and acceptance of the general public. The use of ultrasound for imaging is deemed so safe that it is widely used for diagnostics and obstetric scans. Based on these premises, scientific development has seen more diverse uses of sound waves in therapies being proposed. One such example is the use of ultrasound to emulsify unwanted tissue (e.g. in lipoplasty) or to pulverize unwanted solid material (e.g. in phacoemulsification). Interestingly, ultrasound is also beginning to be used for hemostasis (the stoppage of bleeding in internal organs (Vaezy et al, 1999a) such as the spleen (Vaezy et al, 1999b) and the liver (Vaezy et al, 1997)), for tumor necrosis (Bailey et al, 2003), and for immunotherapy (Bailey et al, 2003).

More adventurous use of ultrasound is also proposed. This involves the increase in the sound wave intensity by stronger vibration of the transducer and by focusing the waves generated. This form of ultrasound is termed High Intensity Focused Ultrasound (HIFU). Apart from treatments mentioned in previous chapters, HIFU is also used to treat regions that are not easily reachable by surgical means, for instance the brain (Daum et al (1998), Thomas et al (1996), Hynynen and Clement (2007)), and abdominal organs that are protected by the rib cage (Thomas et al (1996), Tanter et al (2007)). More importantly, since ultrasound can be used for imaging, HIFU presents the possibility of integrating imaging with therapy. Image-guided HIFU therapy can be an effective means for cancer treatment and drug delivery as described in Section 7.2.1.

7.2.1 Microbubbles for cancer treatment and drug delivery

To enhance the clarity of an ultrasound scan, microbubbles known as ultrasound contrast agents (UCA) are injected into the area of interest. These bubbles can be coated with receptors in such a way that they adhere only to specific cells, for example cancer tumor cells (Dayton et al (2004), Unger et al (2003), Haag et al (2006)). Not only can then the diseased area be diagnosed and imaged, the microbubbles can be utilized for the lysis of the cells when they are forced to collapse by a HIFU or shock wave. The high speed microjets from the collapsing microbubbles (Ohl and Ikink (2003), Prentice et al (2005b)) induce shear stress on the cell membrane, and cause the membrane to be permanently damaged leading to cell death. This lysing effectiveness can be further enhanced with the use of an inverted shockwave (see Section 3.3) or a pulsed HIFU (see Chapter 5). These sound waves have a leading negative tensile component which induces bubble growth, but the subsequent high pressure compressive component causes the collapse of these large bubbles. A high jet speed possibly with a large jet radius obtained can increase the area affected and number of cells lysed.

Apart from destroying the cancer cells, the targeting microbubbles can be used for drug delivery too. Instead of coating the bubbles with cancer receptors, drugs such as modified proteins and DNA can be used to cover the bubbles or be inserted into the bubbles' content. Again, sound waves are utilized to induce bubble oscillation or collapse which can in turn enhance sonoporation of the cells and facilitate the penetration of the macromolecules into the cells (Wolfrum et al (2003), Lindner and Kaul (2001), Haag et al (2006), Unger et al (2003), Lum et al (2006)).

7.2.2 Alternative waveforms for cavitation control

In Section 3.3, an inverted shockwave is introduced with the intention to reduce collateral damage to the surrounding cells. Other alternative waveforms are also suggested and studied with the same intention or to enhance and control cavitation activity. One notably effort is from Ikeda et al (2006). They make use of a dual frequency HIFU; one high frequency and high amplitude wave for the generation of cavities which is followed by a low frequency wave which enhances the violent collapse of these bubbles. They termed this method as Cavitation Control Lithotripsy (CCL) and suggested the replacement of the standard ESWL with CCL.

Another effort to improve lithotripsy treatment based on modifying the waveform used is put forward by Prieto and Loske (1995, 1998, 1999), Loske and Prieto (1996), Bailey (1997), Zhong et al (1997b, 1999a) and Sokolov et al (2001), Loske et al (2002, 2005). They suggest the use of a second shock which is sent in a few hundred microseconds after the first to enhance cavitation collapse in order to reduce treatment time. The second shock is generated either by two separate spark gaps, a modified reflector or with a piezoelectric system. Promising results obtained pave the path for continual development in lithotripsy techniques and science.

7.2.3 Ultrasonic bubbles in microfluidic devices and water treatment

Apart from medical treatments, ultrasonic bubbles are also studied for chemical and biological applications. Due to the diversity of the field, only two notable examples are mentioned here, namely the use of acoustic cavitation in microfluidic devices, and the utilization of ultrasound for water cleaning systems.

Microfluidics is the enabling technology for genomics, proteomics, and molecular drug delivery among others. The pertaining problems are related to the microscale nature of devices, especially in mixing and transport effects. The use of acoustic actuators for acoustic mixing was first reported by Moroney et al (1991). Using piezoelectric thin film to generate the vibration, Yasuda (2000) managed to generate stirring movements in micro flow channels. Yang et al (2000, 2001) used the acoustic waves for the mixing of water and ethanol, as well as, water and uranine in microchambers. Other researchers utilize cavitation microstreaming for mixing. Liu et al (2002, 2003) introduced air pockets for trapping air bubbles which are in turn vibrating to generate a streaming flow. Marmottant and Hilgenfeldt (2004) proposed to use the same phenomenon of microstreaming with microbubbles for the directional transport of particles. Recently, a different idea of utilizing cavitation bubbles in microfluidics is presented by Zwaan et al (2007). They use the collapse of a laser bubble, which is created by focusing laser light in the microchannel, to generate high speed flow in the device.

Ultrasound is suggested to be used for disinfection of wastewater effluents (Neis and Blume, 2003), and for assisting sludge disintegration (Tiehm et al (1997, 2001)). Ultrasonic treatment is done often with other disinfection methods such as using UV light. Sonochemistry effects on the microorganisms involved are believed to be the main reasons behind the treatment success. Cavitation bubbles are also important in another aspect of water technology; i.e. in the ultrasonic cleaning of the membrane filter used in water treatment. Chai et al (1999) utilized ultrasound devices to clean the polymeric membranes that have been used for water treatment. Lamminen et al (2004) suggested the use of ultrasound to clean particle-fouled ceramic membranes so as to prolong the service lifespan of the expensive membrane. They observed that cavitational microstreaming and micro-jet pitting due to the collapse of bubbles are main contributing factors that drive the cleaning process.

7.3 Assessment on possible hazards in use for medical ultrasound

There are a sizeable number of parameters for a full description of the ultrasound field. These may include the frequency, pressure amplitude in terms of peak positive and negative pressure, duty factor, temporal average power, and temporal and spatial peak intensities. Therefore to define the exposure quantity of ultrasound values deemed safe for medical applications is a complicated subject that is open to discussion and controversy.

Firstly, the effect of ultrasound on cells and genetics is of concern. As mentioned before, cell lysis can occur when a cavitation bubble collapses near it. Also degradation of DNA may happen when ultrasound of sufficiently high intensity generates cavitation. The collapse of these bubbles leads to shear stresses on the cell membrane, free radical formation in the surrounding fluid, and excessive heating (Thacker (1973), Miller and Thomas (1995, 1996)).

On a multicellular scale, ultrasound use is potentially harmful to bone and tissues. Thermal heating due to ultrasound exposure seems to be the limiting factor in physiotherapy for bones. High temperature occurs due to either prolonged exposure or high intensity ultrasound could lead to pain (Lehmann et al, 1967), and subsequently the detachment of the periosteum (a fibrous membrane which encloses the bone (Gray, 1918)) (Bruno et al, 1998).

It is known that shear stresses from collapsing cavitation bubbles are capable of causing haemolysis (the rupture of the red blood cells and the dissolution of their contents to the surrounding fluid (Allaby, 1999)). (Rooney (1970), Williams et al (1970)). However, it is reported that cavitation does not occur under the ultrasound intensity commonly used in clinical treatment, but it can be induced in blood only by high intensity ultrasound, e.g. 17 MPa at 1 MHz (Brayman et al, 1996). Nevertheless more care must be taken when ultrasound contrast agents (UCA) are introduced into the blood stream because it is demonstrated by Brayman et al (1995) and Miller and Thomas (1995, 1996) that haemolysis can occur in this case with normal ultrasound exposure levels.

Another important concern regarding the use of ultrasound is in its capacity to damage the blood vessels. Experiments with animal subjects by Dyson et al (1974) and ter Haar et al (1979) have reported damage to blood vessels due to irradiation in a standing ultrasound field. This damage was thought to be due to shear stresses from acoustic streaming. High intensity ultrasound exposure is found to be capable of creating tissue lesions (Child et al (1990), Holland et al (1996), Dalecki et al (1995)). Nevertheless this phenomenon is put to positive use by Xu et al (2005) (see Chapter 5), and Kodama et al (1997) for the removal of cerebral blood clots.

Lastly, the author wishes to mention the potential hazards for the use of ultrasound in cancer treatment. There are several possible concerns. Firstly the surrounding normal tissues could sustain collateral damage during the lysing of the cancer cells by UCA or the tissue ablation due to cavitation bubble collapse. Care must to be taken to localize the treatment area by using focused ultrasound or with integrated real time imaging techniques. Secondly, ultrasound treatment may cause the dissemination of malignant cells around the body and thus an increase in metastasis. However there is no evidence supporting the proposition that localized heating due to ultrasound may increase metastasis (Hahn (1982), Smachlo et al (1979)). Therefore, the use of ultrasound for cancer treatment may be a promising non-invasive procedure in the future.

7.4 Conclusion and future work

The research presented in this thesis addresses the need to understand the bubble dynamics involved in several biomedical applications. Details of the contributions made are given in Section 7.1. In short, a numerical method known as the Boundary Element Method (BEM) is utilized to simulate the interaction of different types of acoustic fields (planar shock, lithotripter shockwave, inverted shock, and high intensity pulsed ultrasound) with a stationary or oscillating bubble. The model is extended to include the consideration of having a biomaterial near the acoustic bubble. Details of the interactions such as the bubble shape changes in time, jet velocity at the moment of impact, translational movement of the bubble etc. are discussed in detail. These parameters are valuable because they are difficult to obtain experimentally due to temporal and spatial constrains in experiments. Complex interactions between bubble and the sound field or the biomaterials are observed and discussed to provide greater understanding to the physics behind the bubble dynamics, and a basis for future technological development. Finally, multiple bubble interactions are experimentally and numerically explored. The various interesting phenomena observed by high speed photography and calculated with a 3D BEM code are discussed.

As for future work, more experimental work for bubble dynamics utilizing the novel spark bubble technique and high speed photography can be done. For instance the study of bubbles oscillating in small tubes (mimicking blood vessels), near biomaterials, or in microfluidic devices is possible. Another promising incremental development in the current experimental setup is to incorporate ultrasound and shock waves. The various numerical studies done here can then be verified and studied further.

Numerically, several interesting areas of study can be explored. One such area being the simulation of acoustic microstreaming as mentioned in Section 1.2.2. Ultrasonic cleaning simulations, which are useful for the understanding of water treatment techniques, can be done with extension on the current code. Lastly, more simulations on other biomedical related applications, such as drug delivery and cancer treatment, can be performed to facilitate the procedural and material design in the initial stage, and to compliment the in vivo experiments or clinical trials in the final phase. The author is also currently exploring experiments on ultrasonic bubbles. A focused ultrasound transducer system has been built and it is used in several ongoing projects.

References

Adhikari, D. 2006 A study of interaction between oscillating bubbles. *UIS4932 Independent Study (ISM) Report*, Faculty of Engineering (University Scholar Program (USP)), National University of Singapore.

Allaby, M. (ed) 1999 *A Dictionary of Zoology*. Oxford University Press, New York.

Anis, A.Y. 1999. PhacoTmesis, Chapter 12 in *Atlas of Cataract Surgery* (eds. S. Masket and A.S. Crandall), 89-96, Martin Dunitz Ltd. London.

Bailey, M.R. 1997 Control of acoustic cavitation with application to lithotripsy. *PhD Dissertation*, University of Texas at Austin.

Bailey, M.R., Blackstock, D.T., Cleveland, R.O., and Crum, L.A. 1998 Comparison of electrohydraulic lithotripters with rigid and pressure-release ellipsoidal reflectors. I. Acoustic fields. *J. Acoust. Soc. Am.* **104**, 2517-2524.

Bailey, M.R., Blackstock, D.T., Cleveland, R.O., and Crum, L.A. 1999 Comparison of electrohydraulic lithotripters with rigid and pressure-release ellipsoidal reflectors. II. Cavitation fields. *J. Acoust. Soc. Am.* **106**, 1149-1160.

Bailey, M.R., Khokhlova, V.A., Sapozhnikov, O.A., Kargl, S.G. and Crum, L.A. 2003 Physical mechanisms of the therapeutic effect of ultrasound (a review). *Acoust. Phys.* **49**, 437-464.

Ball G.J., Howell B.P., Leighton T.G., and Schofield M.J. 2000 Shock-induced collapse of a cylindrical air cavity in water: a Free-Lagrange simulation. Shock Waves **10**, 265-276.

Barber, B.P., and Putterman, S.J. 1992 Light scattering measurements of the repetitive supersonic implosion of a sonoluminescing bubble. *Phys. Rev. Lett.* **69**, 3839-3842.

Bekeredjian, R., Grayburn, P.A., and Shohet, R.V. 2005 Use of ultrasound contrast agents for gene or drug delivery in cardiovascular medicine. *J. Am. Coll. Card.* **45**, 329-335.

Benjamin, T.B., and Ellis, A.T. 1966 The collapse of cavitation bubbles and the pressures thereby produced against solid boundaries. *Phil. Trans. R. Soc. Lond. A* **260**, 221-240.

Best, J.P. 1991 The dynamics of underwater explosions. *PhD Thesis*, University of Wollongong (Australia).

Blake, J.R., and Gibson, D.C. 1981 Growth and collapse of a vapour cavity near a free surface. *J. Fluid Mech.* **111**, 123-140.

Blake, J.R., Taib, B.B., and Doherty, G. 1986 Transient cavities near boundaries. Part 1. Rigid boundary. *J. Fluid Mech.* **170**, 479-497.

Blake, J.R., Taib, B.B., and Doherty, G. 1987 Transient cavities near boundaries. Part 2. Free surface. *J. Fluid Mech.* **181**, 197-212.

Blake, J.R., and Gibson, D.C. 1987 Cavitation bubbles near boundaries. *Ann. Rev. Fluid Mech.* **19**, 99-123.

Blake, J.R. 1988 The Kelvin impulse: application to cavitation bubble dynamics. *J. Australian Mathematical Soc. B Applied mathematics* **30**, 127-146.

Blake, J.R., Robinson, P.B., Shima, A., and Tomita, Y. 1993 Interaction of two cavitation bubbles with a rigid boundary. *J. Fluid Mech.* **255**, 707-721.

Blake, J.R., Keen, G.S., Tong, R.P., and Wilson, M. 1999 Acoustic cavitation: the fluid dynamics of non-spherical bubbles. *Phil. Trans. R. Soc. Lond. A* **357**, 251-267.

Bourne, N.K., and Field, J.E. 1992 Shock-induced collapse of single cavities in liquids. *J. Fluid Mech.* **244**, 225-240.

Bourne, N.K., and Field, J.E. 1999 Shock-induced collapse and luminescence by cavities, *Phil. Trans. R. Soc. Lond. A* **357**, 295-311.

Brayman, A.A., Azadniv, M., Makin, I.R.S., Miller, M.W., Carstensen, E.L., Child, S.Z., Raeman, C.H., Meltzer, R.S., and Everbach, E.C. 1995 Effect of a stabilized microbubble contrast agent on haemolysis of human erythrocytes exposed to high intensity pulsed ultrasound. *Echocardiography* **12**, 13-21.

Brayman, A.A., Azadniv, M., Cox, C., and Miller, M.W. 1996 Haemolysis of Albunex-supplemented, 40% haematocrit human erythrocytes in vitro by 1 MHz pulsed ultrasound: acoustic pressure and pulse length dependence. *Ultrasound Med. Biol.* **22**, 927-938.

Brebbia, C.A., and Dominguez, J. 1989 *Boundary Elements: An Introductory Course.* Computational Mechanics Publications, Southampton, UK.

Brennen, C.E. 1995 *Cavitation and bubble dynamics*. Oxford University Press, Great Britain.

Brennen, C.E. 2005 *Fundamentals of multiphase flows* (Chapter 3: Bubble or droplet translation, 60-72). Cambridge University Press.

Brenner, M.P., Hilgenfeldt, S., and Lohse, D. 2002 Single-bubble sonoluminescence. *Rev. Mod. Phys.* **74**, 425-484.

Brock, M., Ingwersen, I., and Roggendorf, W., 1984. Ultrasonic aspiration in neurosurgery. *Neurosurgical Review* **7**, 173-177.

Brujan, E.A., Nahen, K., Schmidt, P., and Vogel, A. 2001a Dynamics of laser-induced cavitation bubbles near an elastic boundary. *J. Fluid Mech.* **433**, 251-281.

Brujan, E.A., Nahen, K., Schmidt, P., and Vogel, A. 2001b Dynamics of laser-induced cavitation bubbles near elastic boundaries: influence of the elastic modulus. *J. Fluid Mech.* **433**, 283-314.

Brujan, E.A. 2004 The role of cavitation microjets in the therapeutic applications of ultrasound. *Ultrasound Med. Biol.* **30**, 381-387.

Brujan, E.A., Ikeda, T., and Matsumoto, Y. 2005 Jet formation and shock wave emission during collapse of ultrasound-induced cavitation bubbles and their role in the therapeutic applications of high-intensity focused ultrasound. *Phys. Med. Biol.* **50**, 4797-4809.

Bruno, G., Amadei, F., and Abbiati, G. 1998 Liposculpture with ultrasound: biomedical considerations. *Aesth. Plast. Surg.* **22**, 401-403.

Brunton, J.H. 1966 High speed liquid impact. *Philos. Trans. R. Soc. London A* **260**, 79-85.

Bui, T.T., Ong, E.T., Khoo, B.C., Klaseboer, E., and Hung, K.C. 2006 A fast algorithm for modeling multiple bubbles dynamics. *J. Comp. Phys.* **216**, 430-453.

Buogo, S., and Cannelli, B.G. 2002 Implosion of an underwater spark-generated bubble and acoustic energy evaluation using the Rayleigh model. *J. Acoust. Soc. Am.* **111**, 2594-2600.

Calvisi, M.L., Lindau, O., Blake, J.R., and Szeri, A.J. Shape stability and violent collapse of microbubbles in acoustic traveling waves. *Phys. Fluids* **19**, 047101.

Carstensen, E.L., Kelly, P., Church, C.C., Brayman, A.A., Child, S.Z., Raeman, C.H., and Schery, L. 1993 Lysis of erythrocytes by exposure to CW ultrasound. *Ultrasound Med Biol* **19**, 147-165.

Cerone, P., and Blake, J.R. 1984 A note on the instantaneous streamlines, pathlines and pressure contours for a cavitation bubble near a boundary. *J. Aust. Math. Soc.* **B26**, 31-44.

Chahine, G.L. 1977 Interaction between an oscillating bubble and a free surface. *Trans. ASME I: J. Fluids Eng.* **99**, 709-716.

Chai, X., Kobayashi, T., and Fujii, N. 1999 Ultrasound-associated cleaning of polymeric membranes for water treatment. *Separation & Purification Technology* **15**, 139-146.

Chaussy C., Brendel W., and Schmiedt E. 1980. Extracorporeally induced destruction of kidney stones by shock-waves. *Lancet* **2** (8207) 1265-1268.

Chavrier, F., Chapelon, J.Y., Gelet, A., and Cathignol, D., 2000. Modeling of high-intensity focused ultrasound-induced lesions in the presence of cavitation bubbles. *J. Acoust. Soc. Am.* **108**, 432-440.

Chen, Y.H., Chu, H.Y., and Lin, I. 2006 Interaction and fragmentation of pulsed laser induced microbubbles in a narrow gap. *Phys. Rev. Lett.* **96**, 134505.

Church, C.C. 1989 A theoretical study of cavitation generated by an extracorporeal shock wave lithotripsy. *J. Acoust. Soc. Am.* **86**, 215-227.

Clement, G.T., Sun, J., Giesecke, T., and Hynynen, K. 2000 A hemisphere array for non-invasive ultrasound brain therapy and surgery. *Phys Med Biol* **45**, 3707-3719.

Cole, R.H. 1948 *Underwater explosions*. Princeton University Press, New York.

Coleman, A.J., Saunders, J.E., Crum, L.A., and Dyson, M., 1987 Acoustic cavitation generated by an extracorporeal shockwave lithotripter. *Ultrasound Med. Biol.* **13**, 69-76.

Coleman, A.J., Choi, M.J., Saunders, J.E., and Leighton, T.G. 1992 Acoustic emission and sonoluminescence due to cavitation at the beam focus of an electrohydraulic shock wave lithotripter. *Ultrasound Med. Biol.* **18**, 267-281.

Cooter, R., Babidge, W., Mutimer, K., Wickham, P., Robinson, D., Kiroff, G., Chapman, A., and Maddern, G. 2001 Ultrasound-assisted lipoplasty. *Austral. New Zealand J. Surgery* **71**, 309-317.

Crum, L.A. 1979 Surface oscillations and jet development in pulsating bubbles. *J. De Physique* **40**, 285-288.

Crum, L.A. 1988. Cavitation microjets as a contributory mechanism for renal calculi disintegration in ESWL. *J. Urology* **140,** 1587-1590.

Dalecki, D., Raeman, C.H., Child, S.Z., and Carstensen, E.L. 1995 Intestinal haemorrhage from exposure to pulsed ultrasound. *Ultrasound Med. Biol.* **21**, 1067-1072.

Daum, D.R, Buchanan, M.T, Fjield,T., and Hynynen, K. 1998 Design and evaluation of a feedback based phased array system for ultrasound surgery. *IEEE T Ultrason Ferr Freq* **45**, 431-438.

Davidson, B.J., and Riley, N. 1971 Cavitation microstreaming. *J. Sound Vib.* **15**, 217-233.

Dayton, P.A., Pearson, D., Clark, J., Simon, S., Schumann, P.A., Zutshi, R., Matsunaga, T.O., and Ferrara, K.W. 2004 Ultrasonic Analysis of Peptide- and Antibody-targeted Microbubble Contrast Agents for Molecular Imaging of αVβ3-Expressing Cells. *Molecular Imaging* **3**, 125-134.

Dear, J.P., and Field, J.E. 1988 A study of the collapse of arrays of cavities. *J. Fluid Mech.* **190**, 409-425.

Delius M., and Brendel W. 1988 A model of extracorporeal shock-wave action - tandem action of shock-waves. *Ultrasound Med. Biol.* **14**, 515-518.

Ding, Z., and Gracewski, S.M. 1996 The behaviour of a gas cavity impacted by a weak or strong shock wave. *J. Fluid Mech.* **309**, 183-209.

Duarte, L.R. 1983 The stimulation of bone growth by ultrasound, *Arch. Orthopaedic Trauma Surg.* (Historical Archive) **101**, 153-159.

Duncan, J.H., and Zhang, S.J. 1991 On the interaction of a collapsing cavity and a compliant wall. *J. Fluid Mech.* **226**, 401-423.

Duncan, J.H., Milligan, C.D., and Zhang, S.J. 1996 On the interaction between a bubble and a submerged compliant structure. *J. Sound Vib.* **197**, 17-44.

Duck, F., 1990. Mechanical Properties of Tissue in *Physical Properties of Tissue*, (137-165). Academic Press Limited, London.

Dyson, M., Pond, J.B., Woodward, B., and Broadbent, J. 1974 The production of blood cell stasis and endothelial damage in the blood vessels of chick embryos treated with ultrasound in a stationary wave field. *Ultrasound Med. Biol.* **1**, 133-148.

Ehrlich, A., and Schroeder, C.L., 2004. *Medical Terminology For Health Professions*, pg. 542 (Appendix C), Thomson Delmar Learning.

Elder, S. A. 1959 Cavitation microstreaming. *J. Acoust. Soc. Am.* **31**, 54–64.

Everbach, C.E. 2007 Medical diagnostic ultrasound. *Physics Today*, **60**(3), 44-48.

FDA, 1996. Office of Science and Technology Annual Report Section 18. Tech. rep., U.S. Food and Drug Administration (FDA) - Center for Devices and Radiological Health. URL http://www.fda.gov/cdrh/ost/index.html

Feinstein, S.B. 2004 The powerful microbubble: from bench to bedside, from intravascular indicator to therapeutic delivery system, and beyond. *Am J Physiol Heart Circ Physiol* **287**, H450-H457.

Fermi, E 1956 *Thermodynamics* (Chapter 2 on 'The first law of thermodynamics', 24-25). Dover Publications, New York.

Ferrara, K., Pollard, R., Borden, M. 2007 Ultrasound microbubble contrast agents: fundamentals and application to gene and drug delivery. *Annu. Rev. Biomed. Eng.*, **9**, 415-447.

Flores, J., and Holt, M. 1981 Glimm's method applied to underwater explosions, *J. Comp. Phys*, **44**, 377-387.

Flynn, H.G. 1964 Physics of Acoustic Cavitation in Liquids in *Physical Acoustics*, ed. W.P. Mason, Academic Press, New York, **Vol IB**, 57-172.

Fong, S.W., Klaseboer, E., Turangan, C.K., Khoo, B.C., and Hung, K.C. 2006 Numerical analysis of a gas bubble near bio-materials in an ultrasound field. *Ultrasound Med. Bio.* **32**, 925-942.

Fong, S.W., Klaseboer, E., and Khoo, B.C. 2008 The interaction of microbubbles with high intensity pulsed ultrasound. *J. Acoust. Soc. Am.* **123**, 1784–1793.

Frenzel, H., and Schultes, H. 1934 Luminescence in ultrasound. *Z. Phys. Chem.* **B27**, 421-424.

Gracewski, S.M., Dahake, G., Ding, Z., Burns, S.J., and Everbach, E.C. 1993 Internal-stress wave measurements in solids subjected to lithotripter pulses. *J. Acoust. Soc. Am.* **94**, 652-661.

Gaitan, D.F., Crum, L.A., Roy, R.A., and Church, C.C. 1992 Sonoluminescence and bubble dynamics for a single, stable, cavitation bubble. *J. Acoust. Soc. Am.* **91**, 3166-3183.

Gibson, D.C. 1968 Cavitation adjacent to plane boundaries. In *Proc. 3rd Aust. Conf. on Hydraulic and Fluid Mechanics*, 210-214. Institution of Engineers, Sidney, Australia.

Gibson, D.C., and Blake, J.P. 1980 Growth and collapse of cavitation bubbles near flexible boundaries. In *Proc. 7th Aust. Conf. on Hydraulics and Fluid Mech.*, 283-286. Brisbane, Australia: Institution of Engineers.

Gibson, D.C., and Blake, J.P. 1982 The growth and collapse of bubbles near deformable surfaces. *Appl. Sci. Res.* **9**, 215-224.

Gilmore, F.R. 1952 The collapse and growth of a spherical bubble in a viscous compressible liquid. *Calif. Inst. of Tech. Hydrodynamics Lab. Rep. No. 26-4.*

Gray, H. 1918 *Anatomy of the human body*. Reedited by W.H. Lewis. Lea & Febiger, Philadelphia.

Guerri, L., Lucca, G., and Prosperetti, A. 1981 A numerical method for the dynamics of non-spherical cavitation bubbles. In *Proc. 2nd Int. Collog. on drops and bubbles, California*, 175-181.

Haag, P., Frauscher, F., Gradl, J., Seitz, A., Schäfer, G., Lindner, J.R., Klibanov, A.L., Bartsch, G., Klocker, H., and Eder, I.E. 2006 Microbubble-enhanced ultrasound to deliver an antisense oligodeoxynucleotide targeting the human androgen receptor into prostate tumours. *J Steroid Biochem Mol Biol.* **102**, 103-113.

ter Haar, G.R., Dyson, M., and Smith, S.P. 1979 Ultrastructure changes in the mouse uterus brought about by ultrasonic irradiation at therapeutic intensities in standing wave fields. *Ultrasound Med. Biol.* **5**, 167-179.

Hahn, G.M. 1982 *Hyperthermia and Cancer*. Plenum Press, New York.

Harris, P.J. 1992 A numerical model for determining the motion of bubble close to a fixed rigid structure in a fluid. *Intl J. Num. Methods Engng* **33**, 1813-1822.

Holland, C.K., Deng, C.X., Apfel, R.E., Alderman, J.L., Fernandez, L.A. and Taylor, K.J.W. 1996 Direct evidence of cavitation in vivo from diagnostic ultrasound. *Ultrasound Med. Biol.* **22**, 917-925.

Howard, D., and Sturtevant, B. 1997 In vitro study of the mechanical effects of shock-wave lithotripsy. *Ultrasound Med. Biol.* **23**, 1107-1122.

Howell, B.P., and Ball, G.J. 2002 A Free-Lagrange Augmented Godunov Method for the Simulation of Elastic-Plastic Solids. *J. Comp. Physics* **175**, 128-167.

Hua, J., Stene, J.F., and Lin, P. 2007 Numerical simulation of gas bubbles rising in viscous liquids at high Reynolds number. In *Proc. of 6th International Conference on Multiphase Flow (ICMF)*, Leipzig, Germany. Paper no 431.

Hynynen, K., and Clement, G. 2007 Clinical applications of focused ultrasound - the brain. *Int J Hyperther* **23**, 193-202.

Ikeda, T., Yoshizawa, S., Tosaki, M., Allen J.S., Takagi, S., Ohta, N., Kitamura, T., and Matsumoto, Y. 2006 Cloud cavitation control for lithotripsy using high intensity focused ultrasound. *Ultrasound Med. Biol.* **32**, 1383-1397.

Ishida, H., Nuntadusit, C., Kimoto, H., Nakagawa, T., and Yamamoto, T. 2001 Cavitation bubble behavior near solid boundaries. In *CAV 2001: Fourth International Symposium on Cavitation*, California Institute of Technology, Pasadena, CA USA.

Jamaluddin, A.R. 2004 Free-Lagrange Simulations of Shock-Bubble Interaction in ESWL. *PhD Thesis*, School of Engineering Sciences, University of Southampton, UK.

Jarvinen, T.A., Jarvinen, T.L., Kaariainen, M., Kalimo, H., and Jarvinen, M. 2005 Muscle injuries: biology and treatment. *Am. J. Sports Med.*. **33**, 745-764.

Klaseboer, E., and Khoo, B.C. 2004a Boundary integral equations as applied to an oscillating bubble near a fluid-fluid interface. *Comp. Mech.* **33**, 129-138.

Klaseboer, E., and Khoo, B.C. 2004b An oscillating bubble near an elastic material. *J. Appl. Phys.* **96**, 5808-5818.

Klaseboer, E., Hung, K.C. Wang, C. Wang, C.W. Khoo, B.C. Boyce, P., Debono, S., and Charlier, H. 2005 Experimental and numerical investigation of the dynamics of an underwater explosion bubble near a resilient/rigid structure. *J. Fluid Mech.* **537**, 387-413.

Klaseboer, E., and Khoo, B.C. 2006a Modified Rayleigh-Plesset model for a non-spherically symmetric oscillating bubble with applications to boundary integral methods. *Engineering Analysis with Boundary Elements* **30**, 59-71.

Klaseboer, E., Turangan, C.K., Fong S. W., Liu, T.G., Hung, K.C., and Khoo, B.C. 2006b Simulations of pressure pulse-bubble interaction using boundary element method. *Comp. Meth. Appl. Mech. Eng.* **195,** 4287-4302.

Klaseboer, E., Fong, S.W., Turangan, C.K., Khoo, B.C., Szeri, A.J., Calvisi, M.L., Sankin, G.N., and Zhong, P. 2007 Interaction of lithotripter shockwaves with single inertial cavitation bubbles. *J. Fluid Mech.* **593**, 33-56.

Klibanov, A.L. 1999 Targeted delivery of gas-filled microspheres, contrast agents for ultrasound imaging. *Adv. Drug Delivery Rev.* **37** 139-157

Kodama, T, Takayama, K., and Uenohara, H. 1997 A new technology for revascularization of cerebral embolism using liquid jet impact. *Phys. Med. Biol.* **42**, 2355-2367.

Kodama, T., and Takayama, K. 1998 Dynamics behavior of bubbles during extracorporeal shock-wave lithotripsy. *Ultrasound Med. Biol.* **24**, 723-738.

Kolb, J., and Nyborg, W. 1956 Small-scale acoustic streaming in liquids. *J. Acoust. Soc. Am.* **28**, 1237-1242.

Kornfeld, M., and Suvorov, L. 1944 On the destructive action of cavitation. *J. Appl. Phys.*, **15**, 495-506.

Krasovitski, B., and Kimmel, E. 2001 Gas bubble pulsation in a semiconfined space subjected to ultrasound. *J. Acoust. Soc. Am.* **109**, 891-898.

Kucherenko, V.V. and Shamko, V.V. 1986 Dynamics of electric-explosion cavities between two solid parallel walls. *J. Appl. Mech. Tech. Phys.* **27**, 112-115.

Lal, M.K. and Menon, S. 1996 Interaction of two underwater explosion bubbles. *Fluids Engineering Division Conference Volume 1 ASME* FED **236**, 595-600.

Lamminen, M.O., Walker, H.W., and Weavers, L.K. 2004 Mechanisms and factors influencing the ultrasonic cleaning of particle-fouled ceramic membranes. *J. Membrane Sci* **237**, 213-223.

Langer, R., 2000. Biomaterials in drug delivery and tissue engineering: one laboratory's experience. *Acc. of Chem. Res.* **33**, 94-101.

Lanza, G.M., Wallace, K.D., Scott, M.J., Cacheris, W.P., Abendschein, D.R., Christy, D.H., Sharkey, A.M., Miller, J.G., Gaffney, P.J., and Wickline S.A. 1996 A novel site-targeted ultrasonic contrast agent with broad biomedical application. *Circulation* **94,** 3334-3340.

Lask, G.P., Lee, P.K., Seyfzadeh, M., Nelson, J.S., Milner, T.E., Anvari, B., Dave, D., Geronemus, R.G., Bernstein, L.J., Mittelman, H., Ridener, L.A., Coulson, W.F., Sand, B., Baumgardner, J., Hennings, D.R., Menefee, R.F., and Berry, M. 1997 Non-ablative laser treatment of facial rhytides. In *Proc. SPIE Vol. 2970 Lasers in Surgery: Advanced Characterization, Therapeutics and Systems VII*, 338-349.

Lauterborn, W., and Bolle, H. 1975 Experimental investigations of cavitation bubble collapse in the neighbourhood of a solid boundary. *J. Fluid Mech.* **72**, 391-399.

Lauterborn, W. 1982 Cavitation Bubble Dynamics - New Tools for an Intricate Problem. *Appl. Scient. Rev.* **38**, 165-178.

Lauterborn, W., and Vogel, A. 1984 Modern optical techniques in fluid mechanics. *Ann. Rec. Fluid Mech.* **16**, 223-244.

Lauterborn, W. and Hentschel, W. 1985 Cavitation bubble dynamics studied by high speed photography and holography: part one. *Ultrasonics* **23**, 260-268.

Lauterborn, W., Kurz, T., Mettin, R. and Ohl, C.-D. 1999 Experimental and theoretical bubble dynamics. In *Advances in Chemical Physics,* **110**, 295-380. I. Prigogine and S.A. Rice (Eds).

Lehmann, J.F., DeLateur, B.J., Stonbridge, J.B., and Warren, C.G. 1967 The therapeutic temperature distribution produced by ultrasound as modified by dosage and volume of tissue exposed. *Arch. Phys. Med. Rehab.* **48**, 662-666.

Leighton, T.J. 1994 *The Acoustic Bubble*. Academic Press, Cambridge.

Lepper, W., Belcik, T., Wei, K., Lindner, J.R., Sklenar, J., Kaul, S. 2004 Myocardial contrast echocardiography. *Circulation* **109**, 3132-3135.

Lew, K.S.F., Klaseboer, E., and Khoo, B.C. 2006 A collapsing bubble-induced micropump: an experimental study. *Sensors & Actuators A: Physical*, **133**, 161-172.

Li, T.L., Tachibana, K., Kuroki, M., and Kuroki, M. 2003 Gene transfer with echo-enhanced contrast agents: Comparison between Albunex, Optison, and Levovist in mice - Initial results. *Radiology* **229**, 423-428.

Lindner, J.R. and Kaul, S. 2001 Delivery of Drugs with Ultrasound. *Echocardiography* **18**(4), 329-338.

Lindner, J.R. 2004 Microbubbles in medical imaging: current applications and future directions. *Nat Rev Drug Discov.* **3**, 527-32.

Liu, R.H., Yang, J., Pindera, M.Z., Athavale, M., and Grodzinski, P. 2002 Bubble-induced acoustic micromixing. *Lab Chip* **2**, 151-157.

Liu, R.H., Lenigk, R., Druyor-Sanchez, R., Yang, J., and Grodzinski, P. 2003 Hybridization enhancement using cavitation microstreaming. *Anal. Chem.* **75**, 1911-1917.

Lokhandwalla, M., and Sturtevant, B. 2000 Fracture mechanics model of stone comminution in ESWL and implications for tissue damage. *Phys. Med. Biol.* **45**, 1923-1940.

Longuet-Higgins, M.S. 1998 Viscous streaming from an oscillating spherical bubble. *Proc. R. Soc. Lond. A* **454**, 725-742.

Loske, A.M., and Prieto. F.E. 1996 Improving underwater shock wave focusing efficiency. In *Urolithiasis* (401-402), eds. C.Y.C. Pak, M.I. Resnick, and G.M. Preminger, Dallas TX: Millet The Printer.

Loske, A.M., Prieto, F.E., Fernández, F., Cauwelaert, J.V. 2002 Tandem shock wave cavitation enhancement for extracorporeal lithotripsy. *Phys. Med. Biol.* **47**, 3945-3957.

Loske, A.M., and Prieto, F.E. 2002 Pressure-Release versus Rigid Reflector for Extracorporeal Shockwave Lithotripsy. *J. Endourology* **16**, 273-280.

Loske, A.M., Fernandez, F., Zendejas, H., Paredes, M., and Castano-Tostado, E. 2005 Dual Pulse Shock Wave Lithotripsy: In Vitro and In Vivo Study. *J. Urology* **174**, 2388-2392.

Lum, A.F.H., Borden, M.A., Dayton, P.A., Kruse, D.E., Simon, S.I., and Ferrara, K.W. 2006 Ultrasound Radiation Force Enables Targeted Deposition of Model Drug Carriers loaded on Microbubbles. *J Control Release* **111**, 128-134.

Marmottant, P., and Hilgenfeldt, S. 2003 Controlled vesicle deformation and lysis by single oscillating bubbles. *Nature* **423**, 153-156.

Marmottant, P., and Hilgenfeldt, S. 2004 A bubble-driven microfluidic transport element for bioengineering. *Proc. Natl. Acad. Sci.* **101**, 9523-9527.

Marsh, S.P. 1980 *LASL Shock Hugoniot Data*, University of California Press, USA.

Martin, A.D., Daniel, M.Z., Drinkwater, D.T., Clarys, J.P. 1994 Adipose tissue density, estimated adipose lipid fraction and whole body adiposity in male cadavers. *Int J. Obes. Relat. Metab. Disord.* **18**, 79-83.

Mason, T.J., and Lorimer, J.P. 1988 *Sonochemistry: theory, applications and uses of ultrasound in chemistry*. Ellis Horword, Ltd., Chichester, U. K.

McCulloch, M., Gresser, C., Moos, S., Odabashian, J., Jasper, S., Bednarz, J., Burgess, P., Carney, D., Moore, V., Sisk, E., Waggoner, A., Witt, S., and Adams, D. 2000 Ultrasound contrast physics: A series on contrast echocardiography, article 3. *J Am Soc Echocardiogr*. **13**, 959-67.

Miller, D.L. and Thomas, R.M. 1995 Ultrasound contrast agents nucleate inertial cavitation in vitro. *Ultrasound Med. Biol.* **21**, 1059-1065.

Miller, D.L. and Thomas, R.M. 1996 Contrast agent gas bodies enhance haemolysis induced by lithotripter shock waves and high intensity focused ultrasound in whole blood. *Ultrasound Med. Biol.* **22**, 1089-1095.

Miller, D.L., Pislaru, S.V., and Greenleaf, J.F. 2002 Sonoporation: mechanical DNA delivery by ultrasonic cavitation. *Somat. Cell Mol. Genet.* **27**, 115-134.

Minnaert, M. 1933 On musical air bubbles and the sound of running water. *Phil. Mag.* **16**, 235-248.

Moroney, R.M., White, R.M., and Howe, R.T. 1991 Ultrasonically induced microtransport. In *Proc. MEMS'91, 3th IEEE Int. Workshop Micro Electromechanical System (Nara, Japan)*, 277-282.

Naude, C.F., and Ellis, A.T. 1961 On the mechanism of cavitation damage by nonhemispherical cavities collapsing in contact with a solid boundary. *Trans. ASME D, J. Basic Engrg.*, **83**, 648-656.

Neis, U., and Blume, T. 2003 Ultrasonic disinfection of wastewater effluents for high-quality reuse. *Water Science and Technology: Water Supply* **3**, 261-267.

Neppiras, E.A. 1980 Acoustic cavitation. *Phys. Reports* **61**, 159-251.

Nightingale, K.R., McAleavey, S.A., and Trahey, G.E. 2003 Shear-wave generation using acoustic radiation force: in vivo and ex vivo results. *Ultrasound Med. Biol.* **29**, 1715-1723.

Ohl, C.D., Lindau, O., and Lauterborn, W. 1998 Luminescence from spherically and aspherically collapsing laser induced bubbles. *Phys. Rev. Lett.* **80**, 393-396.

Ohl, C.D., and Ikink, R. 2003 Shock-wave-induced jetting of micron-size bubbles. *Phys. Rev. Lett.* **90**, 214502.

Ong, G.P. 2005 Experiments on oscillating bubbles near a free or elastic surface. *Final year project report* in partial fulfillment for the degree of Bachelor of Engineering, National University of Singapore.

Ong, G.P., Khoo, B.C., Turangan, C., Klaseboer, E. and Fong, S.W. 2005 Behavior of oscillating bubbles near elastic membranes: an experimental and numerical study. *Modern Physics Letters B* **19**, 1579-1582.

Parlitz, U., Mettin, R., Luther, S., Akhatov, I., Voss, M., and Lauterborn, W. 1999 Spatiotemporal dynamics of acoustic cavitation bubble clouds, *Phil. Trans. R. Soc. Lond.* A **357**, 313-334.

Patil, K.M., Braak, L.H., and Huson, A. 1996 Analysis of stresses in two-dimensional models of normal and neuropathic feet. *Med. Biol. Eng. Comput.* **34**, 280-284.

Payne, R.C., Veenman, P., and Wilson, A.M. 2005 The role of the extrinsic thoracic limb muscles in equine locomotion. *Journal of Anatomy* **206**, 193-204.

Pearson, A., Blake, J.R., and Otto, S.R. 2004 Jets in bubbles. *J. of Engineering Mathematics* **48**, 391-412.

Penney, D.P., Schenk, E.A., Maltby, K., Harman-Raeman, C., Child, S.Z., and Carstensen, E.L. 1993 Morphological effects of pulsed ultrasound in the lung. *Ultrasound Med. Biol.* **19**, 127-135.

Plesset, M.S., and Chapman, R.B. 1971 Collapse of an initially spherical vapour cavity in the neighbourhood of a solid boundary. *J. Fluid Mech.* **47**, 283-290.

Plesset, M. S. and Prosperetti, A. 1977 Bubble dynamics and cavitation. *Ann. Rev. Fluid Mech.* **9**, 145-85.

Prentice, P., MacDonald, M.P., Cuschieri, A., Dholakia, K., and Campbell, P. 2005a Real time observation of the ultrasound stimulated disintegration of optically trapped microbubbles in proximity to biological cells. In *Proc. SPIE Int. Soc. Opt. Eng. 5930*, 59300H.

Prentice, P., Cuschieri, A., Dholakia, K., Prausnitz, M., and Campbell, P. 2005b Membrane disruption by optically controlled microbubble cavitation. *Nature Physics* **1**, 127-110.

Prieto, F.E., and Loske, A.M. 1995 Multifocal Composite Reflectors to Concentrate Shock Waves. International Patent P.C.T./MX 95/00008.

Prosperetti, A. 1982 Bubble dynamics: a review and some recent results. *Appl. Sci. Res.* **38**, 145-164.

Power, E.D., Stitzel, J.D., West, R.L., Herring, I.P., and Duma, S.M. 2001 A nonlinear finite element model of the human eye for large deformation loading. *25th Annual Meeting of the American Society of Biomechanics*, University of California at San Diego.
URL http://asb-biomech.org/onlineabs/abstracts2001/pdf/044.pdf

Pozrikidis, C. 2005 *A Practical Guide to Boundary Element Methods with the Software Library BEMLIB.* CRC Press LLC, Florida, US.

Rayleigh, Lord 1917. On the pressure developed in a liquid during the collapse of a spherical void. *Philos. Mag.* **34**, 94-98.

Robinson, P.B., Blake, J.R., Kodama, T., Shima, A., and Tomita, Y. 2001 Interaction of cavitation bubbles with a free surface. *J. Appl. Phys.* **89**(12), 8225-8237.

Rooney, J.A. 1970 Haemolysis near an ultrasonically pulsating gas bubble. *Science* **169**, 869-871.

Rungsiyaphornrat, S., Klaseboer E., Khoo, B.C. and Yeo, K.S. 2003 The Merging of two gaseous bubbles with an application to underwater explosions. *Computers & Fluids* **32**, 1049-1074.

Sankin, G.N., Simmons, W.N., Zhu, S.L. and Zhong, P. 2005 Shockwave interaction with laser-generated single bubbles. *Physical Review Letters* **95**, 034501.

Sato, K., Tomita, Y., and Shima, A. 1994 Numerical analysis of a gas bubble near a rigid boundary in an oscillatory pressure field. *J. Acoust. Soc. Am.* **95**, 2416-2424.

Shapiro, E.M., Borthakur, A., Kaufman, J., Leigh, J.S., and Reddy, R. 2001 Water distribution patterns inside bovine articular cartilage as visualized by 1H magnetic resonance imaging. *Osteoarthritis and Cartilage* **9**, 533-538.

Shaw, S.J., Jin, Y.H., Gentry, T.P., and Emmony, D.C. 1999 Experimental observations of the interaction of a laser generated cavitation bubble with a flexible membrane. *Physics of Fluids* **11**, 2437-2439.

Shima, A., and Sato, Y. 1980 The behavior of a bubble between narrow parallel plates. *Z. angew. Math. Phys.* **31**, 691-704.

Shima, A., Tomita, Y., Gibson, D.C., and Blake, J.R. 1989 The growth and collapse of cavitation bubbles near composite surfaces. *J. Fluid Mech.* **203**, 199-214.

Smachlo, K., Fridd, C.W., Child, S.Z., Hare, J.D., Linke, C.A., and Carstensen, E.L. 1979 Ultrasonic treatment of tumors: 1. Absence of metastases following treatment of a hamster fibrosarcoma. *Ultrasound Med. Biol.* **5**, 45-49.

Snell, R.S., and Lemp, M.A. 1998. *Clinical Anatomy of the Eye*, pg. 203. Blackwell Publishers.

Soh, W.K. 1991 High-speed photographic study of a cavitation bubble. In *Proc. of SPIE – volume 1358, 19th Intl Congress on High Speed Photography and Photonics*, ed. Peter W.W. Fuller, 1011-1015.

Soh, W.K., and Willis, B. 2003 A flow visualization study on the movements of solid particles propelled by a collapsing cavitation bubble. *Experimental Thermal and Fluid Science* **27**, 537-544.

Sokolov, D.L., Bailey, M.R., and Crum, L.A. 2001. Use of a dual-pulse lithotripter to generate a localized and intensified cavitation field. *J. Acoust. Soc. Am.* **110**, 1685-1695.

Suslick, K.S., ed. 1988 *Ultrasound: Its Chemical, Physical, and Biological Effects*. VCH Publishers, New York.

Suslick, K.S. 1998 Sonochemistry, in *Kirk-Othmer Encyclopedia of Chemical Technology*, 4th Ed. J. Wiley & Sons, New York, **26**, 517-541.

Tachibana, K., and Tachibana, S. 1995 Albumin microbubble echo-contrast material as an enhancer for ultrasound accelerated thrombolysis. Circulation **92**, 1148-1150.

Taib, B.B., Doherty, G., and Blake, J.R. 1984 Boundary integral methods applied to cavitation bubble dynamics. In *Mathematical Programming and Numerical Analysis Workshop* (eds. S.A. Gustafson and R.S. Womersley) **6**, 166-186. Centre for Math, Anal. A.N.U.

Taniyama, Y., Tachibana, K., Hiraoka, K., Namba, T., Yamasaki, K., Hashiya, N., Motokuni, A., Ogihara, T., Yasufumi, K., and Morishita, R. 2002 Local delivery of plasmid DNA into rat carotid artery using ultrasound. *Circulation*, **105**, 1233-1239.

Tanter, M., Thomas, J.L., and Fink, M. 1998 Focusing and steering through absorbing and aberrating layers: Application to ultrasonic propagation through the skull. *J Acoust Soc Am* **103**, 2403-2410.

Tanter, M., Aubry, J-F, Pernot, M., Marquet, F., and Fink, M. 2007 Compensating for bone inter faces and respiratory motion in high intensity focused ultrasound. *Int J Hyperther* **23**, 141-151.

Thacker, J., 1973 The possibility of genetic hazard from ultrasonic radiation. *Curr. Top. in Radioat. Res. Q.* **8**, 235-258.

Tho, P., Manasseh, R., and Ooi, A. 2007 Cavitation microstreaming patterns in single and multiple bubble systems. *J. Fluid Mech.* **576**, 191-233.

Thomas, J.L., and Fink, M.A. 1996 Ultrasonic beam focusing through tissue inhomogeneities with a timereversal mirror: Application to transskull therapy. *IEEE Ultrason Ferr* **43**, 1122-1129.

Tiehm, A., Nickel, K., and Neis, U. 1997 The Use of Ultrasound to Accelerate the Anaerobic Digestion of Sewage Sludge. *Water Science & Technology* **36**, 121-128.

Tiehm, A., Nickel, K., Zellhorn, M., and Neis, U. 2001 Ultrasonic waste activated sludge disintegration for improving anaerobic stabilization. *Water Research* **35**, 2003-2009.

Timm, E.F., and Hammit, F.G. 1971 Bubble Collapse adjacent to a Rigid Wall, a Flexible Wall, and a Second Bubble. *Am. Soc. Mech. Eng. Cavitation Forum*, 18-20.

Tomita, Y. and Kodama, T. 2003 Interaction of laser-induced cavitation bubbles with composite surfaces. *J. Appl. Phys.* **94**, 2809-2816.

Tomita, Y., Robinson, P.B., Tong, R.P., and Blake, J.R. 2002 Growth and collapse of cavitation bubbles near a curved rigid boundary. *J.Fluid Mech.* **466**, 259-283.

Tomita, Y., Sato, K., and Shima, A. 1994 Interaction of two laser-produced cavitation bubbles near bundaries. In *Proc. IUTAM Symp. `Bubble Dynamics and Interface Phenomena' (ed. J. R. Blake et al.)*, 33-45. Kluwer.

Tomita, Y. and Shima, A. 1990 High-speed photographic observations of laser-induced cavitation bubbles in water. *Acustica* **71**, 161-170.

Tomita, Y., Shima, A., and Sato, K. 1990 Dynamic behavior of two laser-induced bubbles in water. *Appl. Phys. Lett.* **57**, 234-236.

Trosseille, X., Tarriere, C., Lavaste, F., Guillon, F., and Domont, A. 1992 Development of a F.E.M. of the human head according to a specific test protocol. *In: Proc. 36th Stapp Car Crash Conf. SAE* Paper 922527. Seattle, USA, 235-253.

Turangan, C.K., Ong, G.P., Klaseboer, E., and Khoo, B.C. 2006 Experimental and numerical study of transient bubble-elastic membrane interaction. *J. Appl. Phys.* **100**, 054910.

Tsutsui, J.M., Xie, F., Johanning, J., Lof, J., Cory, B., He, A.M., Thomas, L., Matsunaga, T., Unger, E., and Porter, T.R. 2006 Treatment of deeply located acute intravascular thrombi with therapeutic ultrasound guided by diagnostic ultrasound and intravenous microbubbles *J. Ultrasound Med.* **25**, 1161-1168.

Unger, E., Matsunaga, T.O., Schumann, P.A., and Zutshi, R., 2003. Microbubbles in molecular imaging and therapy, *Medicamundi*, **47/1**, 58-65.

Wang, Q.X. 1998 The evolution of a gas bubble near an inclined wall. *Theoret. Comput. Fluid Dynamics* **12**, 29-51.

Wang, C., Khoo, B.C., and Yeo, K.C. 2003 Elastic mesh technique for 3D BIM simulation with an application to underwater explosion bubble dynamics. *Comput. Fluids* **32**, 1195-1212.

Wang, Q.X., Yeo, K.S., Khoo, B.C., and Lam, K.Y. 1996a Nonlinear interaction between gas bubble and free surface. *Computers & Fluids* **25**, 607-628.

Wang, Q.X., Yeo, K.S., Khoo, B.C., and Lam, K.Y. 1996b Strong interaction between a buoyancy bubble and a free surface. *Theoret. Comput. Fluid Dynamics* **8**, 73-88.

Williams, A.R., Hughes, D.E., Nyberg, W.L. 1970 Haemolysis near a transversely oscillating wire. *Science* **169**, 871-873.

Wilkerson, S. 1992 A boundary integral approach for three-dimensional underwater explosion bubble dynamics. *Final rept. Nov 89-Jun 90* for Army Ballistic Research Lab Aberdeen Proving Ground MD, US.

Wolfrum, B., Mettin, R., Kurz, T., and Lauterborn, W. 2002 Observations of pressure-wave excited contrast agent bubbles in the vicinity of cells. *Appl. Phys. Lett.* **81**, 5060-5062.

Wolfrum, B., Mettin, R., Kurz, T., Lauterborn, W., and Ohl, C.-D. 2003 Cavitation induced cell detachment and membrane permeabilization. In *Proc of IEEE Symposium on Ultrasonics* **1**, 837-840.

Wu, J., and Du, G. 1997 Streaming generated by a bubble in an ultrasound field. *J. Acoust. Soc. Am.* **101**, 1899-1907.

Vaezy, S., Martin, R., Schmiedl, U., Caps, M., Taylor, S., Beach, K., Carter, S., Kaczkowski, G., Keilman, G., Helton, S., Chandler, W., Mourad, P., Rice, M., Roy, R. and Crum, L.A. 1997 Liver hemostasis using high intensity focused ultrasound. *Ultrasound in Med. and Biol.* **23**, 1413-1420.

Vaezy, S., Martin, R., Mourad, P. and Crum, L.A. 1999a Hemostasis using high intensity focused ultrasound. *European J. Ultrasound* **9**, 79-87.

Vaezy, S., Martin, R., Keilman, G., Kaczkowski, G., Chi, E., Yaziji, E., Caps, M., Poliachik, S., Carter, S., Sharar, S., Cornejo, C. and Crum, L.A. 1999b Control of splenic bleeding using high intensity ultrasound. *J. Trauma* **47**, 521-525.

Xu, Z., Fowlkes, J.B., Rothman, E.D., Levin, A.M., and Cain, C.A., 2005. Controlled ultrasound tissue erosion: The role of dynamic interaction between insonation and microbubble activity. *J. Acoust. Soc. Am.,* **117**, 424-435.

Yang, Z., Goto, H., Matsumoto, M., Maeda, R. 2000 Active micromixer for microfluidicsystems using lead-zirconate-ttitanate (PZT)-generated ultrasonic vibration. *Electrophoresis* **21**, 116-119.

Yang, Z., Matsumoto, S., Goto, H., Matsumoto, M., and Maeda, R. 2001 Ultrasonic micromixer for microfluidic systems. *Sensors Actuators A* **93**, 266-272.

Yasuda, K. 2000 Non-destructive, non-contact handling method for biomaterials in micro-chamber by ultrasound. *Sensors Actuators B* **64**, 128-35.

Young, F.R. 1989 *Cavitation* (page 17), McGraw-Hill, London.

Zhang, S.G., and Duncan, J.H. 1994 On the non-spherical collapse and rebound of a cavitation bubble. *Phys. Fluids* **6**, 2352-2362.

Zderic, V., Clark, J.L., and Vaezy, S. 2004 Drug delivery into the eye with the use of ultrasound. *J. Ultrasound Med. Biol.* **23**, 1349-1359.

Zhang, S.G., Duncan, J.H., and Chahine, G.L. 1993 The final stage of the collapse of a cavitation bubble near a rigid wall. *J. Fluid Mech.* **257**, 147-181.

Zhang, Y.L., Yeo, K.S., Khoo, B.C. and Wang, C. 2001 3D jet impact and toroidal bubbles. *J. Comput. Phys.* **166**, 336-360.

Zheng, Y., Mak, A.F.T, and Lue, B. 1999 Objective assessment of limb tissue elasticity: Development of a manual indentation procedure. *J. of Rehab. Res. Devel.* **36**, 71-85.

Zhong, P., Cocks, F.H., Cioanta, I., and Preminger, G.M. 1997a Controlled, forced collapse of cavitation bubbles for improved stone fragmentation during shock wave lithotripsy. *J. Urol.* **158**, 2323-2328.

Zhong, P., Cioanta, I., Cocks, F.H., and Preminger, G.M. 1997b Inertial cavitation and associated acoustic emission produced during electrohydraulic shock wave lithotripsy. J. Acoust Soc Am 101, 2940-2950.

Zhong, P., Lin, H.F., Xi, X.F., Zhu, S.L., and Bhogte, E.S. 1999 Shock wave-inertial microbubble interaction: methodology, physical characterization, and bioeffect study. *J. Acoust. Soc. Am.* **105**, 1997-2009.

Zhong, P., and Zhou, Y. 2001. Suppression of large intraluminal bubble expansion in shock wave lithotripsy without compromising stone comminution: Methodology and in vitro experiments. *J. Acoust. Soc. Am.* **110**, 3283-3291.

Zhong, P., Zhou, Y., and Zhu, S. 2001 Dynamics of bubble oscillation in constrained media and mechanisms of vessel rupture in SWL. *Ultrasound Med. Biol.* **27**, 119-134.

Zhu, S.L., and Zhong, P. 1999 Shock wave-inertial microbubble interaction: a theoretical study based on Gilmore formulation for bubble dynamics. *J. Acoust. Soc. Am.* **106**, 3024-3033.

Zhu, S.L., Cocks, F.H., Preminger, G.M., and Zhong, P. 2002 The role of stress waves and cavitation in stone comminution in shock wave lithotripsy. *Ultrasound Med. Biol.* **28**, 661-671.

Zwaan, E., Le Gac, S., Tsuji, K., and Ohl, C.-D. 2007 Controlled cavitation in microfluidic systems. *Phys. Rev. Lett.* **98**, 254501.